Flow and Heat Transfer Investigations in Swirl Tubes for Gas Turbine Blade Cooling

A thesis accepted by the Faculty of Aerospace Engineering and
Geodesy of the Universität Stuttgart in partial fulfillment of the
requirements for the degree of
Doctor of Engineering Sciences (Dr.-Ing.)

by

Dipl.-Ing. Christoph Biegger

born in Weingarten, Germany

Main referee:	Prof. Dr.-Ing. habil. Bernhard Weigand
Co-referee:	Prof. Ing. František Maršík, DrSc.
Co-referee:	Prof. Dr. Yu Rao
Date of defence:	7 February 2017

Institute of Aerospace Thermodynamics
University of Stuttgart
2017

Preface

This thesis was written during my time as a research assistant at the Institute of Aerospace Thermodynamics (ITLR) at the University of Stuttgart. I would like to thank all the people who contributed to its success.

First and foremost, I would like to express my gratitude to my supervisor and main referee Prof. Dr.-Ing. habil. Bernhard Weigand for all his guidance, experience and support throughout my research. Thank you very much for the scientific freedom at the ITLR, the motivating discussions and for always have been taking the time whenever I needed advice.

In appreciation of numerous discussions and for being the co-referee of this thesis, I would like to thank Prof. Ing. František Maršík, DrSc. from the Institute of Thermomechanics, Prague, Czech Republic. I am very grateful for his experience on flow stability and his advice throughout this study. I would like to express my gratitude to Prof. Dr. Yu Rao from Shanghai Jiao Tong University, China, for the fruitful cooperation on the multiple inlet swirl tube experiments. Our study and discussion were very effective and enjoyable and I greatly appreciate his ideas and vast knowledge. Throughout the years, he was not only my working colleague but became a friend. I was more than pleased that he agreed to be the co-referee of this thesis. I would also like to thank Dr.-Ing. Rico Poser for his advice and expertise conducting the heat transfer experiments.

Contents

Contents

List of Figures

Latin Characters

Symbol	Description	Unit
A	area	m^2
B	constant	$-$
c	heat capacity	$\mathrm{J\,kg^{-1}\,K^{-1}}$
c, C	constants	$-$
C_k	energy spectrum constant	$-$
C_μ	eddy-viscosity constant	$-$
C_s	Smagorinsky constant	$-$
C_{DES}	DES constant	$-$
d	diameter	m
$\tilde{d}$	DES limiter	m
D	tube diameter	m
D_{ij}	diffusivity tensor	$\mathrm{m^2\,s^{-1}}$
$E(k)$	energy spectral density	$\mathrm{J\,m^{-3}}$
f	friction factor	$-$
f, g	functions	$-$
$G(r,x)$	filter	$-$
h, H	height	m
h	heat transfer coefficient	$\mathrm{W\,m^{-2}\,K^{-1}}$
h	enthalpy	J

List of Symbols

Symbol	Description	Unit
h_c	total enthalpy	J
$\dot{I}_\phi$	angular momentum	$\mathrm{kg\,m^2\,s^{-2}}$
$\dot{I}_z$	axial momentum	$\mathrm{kg\,m\,s^{-2}}$
k	turbulence kinetic energy	$\mathrm{m^2\,s^{-2}}$
k	thermal conductivity	$\mathrm{W\,m^{-1}\,K^{-1}}$
l	lever arm	m
l, L	length	m
$\mathcal{L}$	characteristic length scale of the large eddies	m
$\dot{m}$	mass flow rate	$\mathrm{kg\,s^{-1}}$
n	number of inlet ducts	−
n	normal vector	−
N	number of samples	−
N	number of grid cells	−
N	neighboring cell center	−
Nu	Nusselt number	−
p	pressure	Pa
P	cell center	−
$\mathcal{P}$	production rate	$\mathrm{m^2\,s^{-3}}$
Pr	Prandtl number	−
Pr_t	turbulent Prandtl number	−
q	dynamic pressure	Pa
q	velocity scale	$\mathrm{m\,s^{-1}}$
$\dot{q}_w$	specific wall heat flux	$\mathrm{W\,m^{-2}}$
$\dot{q}_\Theta$	source or sink term of the scalar	$\mathrm{s^{-1}}$
r	recovery factor	−
r	mixing length	−
r	radial coordinate	m
r_a	boundary radius of the rotational fluid	m
r_b	boundary radius of the bubble	m
r_c	radius of the vortex core	m
r_t	tube radius	m
r^*	radial distance at maximum swirl velocity	m
R	tube radius	m
R	ratio of radial to tangential velocity	−
Re	Reynolds number	−
$Re_\mathcal{L}$	large eddy Reynolds number	−
Re_τ	friction Reynolds number	−
Re_z	local axial Reynolds number	−
Re_ϕ	local circumferential Reynolds number	−

Symbol	Description	Unit
Ro	Rossby number	$-$
S	swirl number	$-$
S	flow force	N
S	entropy	$\mathrm{J\,K^{-1}}$
S_{ij}	strain rate tensor	$\mathrm{s^{-1}}$
t	time	s
T	temperature	K
T_τ	friction temperature	K
u_r, u_ϕ, u_z	fluctuating velocity components	$\mathrm{m\,s^{-1}}$
u_τ	friction velocity	$\mathrm{m\,s^{-1}}$
u_η	Kolmogorov velocity scale	$\mathrm{m\,s^{-1}}$
$\mathbf{U}$	velocity vector	$\mathrm{m\,s^{-1}}$
$\mathcal{U}$	characteristic velocity scale of the large eddies	$\mathrm{m\,s^{-1}}$
U_r, U_ϕ, U_z	velocity components	$\mathrm{m\,s^{-1}}$
$\overline{U}_z$	axial bulk velocity	$\mathrm{m\,s^{-1}}$
V	volume	$\mathrm{m^3}$
w	width	m
W	axial velocity at maximum swirl velocity	$\mathrm{m\,s^{-1}}$
x, y, z	cartesian coordinates	m
y^+	dimensionless wall distance	$-$
z	axial coordinate	m

Greek Characters

Symbol	Description	Unit
Γ	circulation	$\mathrm{m^2\,s^{-1}}$
Γ	thermal diffusivity	$\mathrm{m^2\,s^{-1}}$
Γ_t	turbulent diffusivity	$\mathrm{m^2\,s^{-1}}$
δ	channel half height	m
δ_{ij}	kronecker delta	$-$
Δ	grid spacing	m
ϵ	dissipation rate	$\mathrm{m^2\,s^{-3}}$
η	Kolmogorov length scale	m
θ	fluctuating scalar	$-$
Θ	scalar	$-$
Θ	dimensionless temperature	$-$
κ	isentropic exponent	$-$

List of Symbols

Symbol	Description	Unit
κ	von Kármán constant	$-$
λ_g	Taylor microscale	m
μ	molecular dynamic viscosity	$\mathrm{kg\,m^{-1}\,s^{-1}}$
ν	molecular kinematic viscosity	$\mathrm{m^2\,s^{-1}}$
ν_t	eddy-viscosity	$\mathrm{m^2\,s^{-1}}$
$\tilde{\nu}$	modified eddy-viscosity	$\mathrm{m^2\,s^{-1}}$
ρ	density	$\mathrm{kg\,m^{-3}}$
σ	turbulent Prantdl number	$-$
τ	time	s
τ_{ij}	shear stress tensor	$\mathrm{N\,m^{-2}}$
τ_w	wall shear stress	$\mathrm{N\,m^{-2}}$
ϕ	cylindrical coordinate	rad
ϕ	variable	$-$
χ	viscosity ratio	$-$
ω	vorticity	$\mathrm{s^{-1}}$
ω	specific dissipation rate	$\mathrm{s^{-1}}$
Ω	angular velocity	$\mathrm{s^{-1}}$
Ω_{ij}	rotation rate tensor	$\mathrm{s^{-1}}$

Subscripts

Symbol	Description
0	initial
0	axial tube flow
1	state 1
2	state 2
ad	adiabatic wall
B	(vortex) breakdown
c	center
cc	curvature corrected
d	delayed
D	diameter
eff	effective
f	fluid
geo	geometrical
i, in	inlet
i, j, k	tensor indices

Symbol	Description
m	mean
N	neighboring cell center
out	outlet
p	pressure
P	cell center
r, ϕ, z	cylindrical coordinates
ref	reference
rms	root mean square
sgs	sub-grid scale
t	turbulent
tr	transient
T	temperature
w	wall
w	wire
x, y, z	cartesian coordinates
η	small scales
τ	friction
Ω	rotation
∞	far field, free stream

Superscripts

Symbol	Description
ϕ^+	dimensionless
ϕ'	fluctuation
$\overline{\phi}$	filtered
$\langle \phi \rangle$	averaged
$\tilde{\phi}$	modified
ϕ^{LES}	Large Eddy Simulation
ϕ^R	residual
ϕ^{RANS}	Reynolds-Averaged Navier-Stokes

Abbreviations

Abbreviation	Description
1D	One Dimensional
2C	Two Components
2D	Two Dimensional
3C	Three Components
3D	Three Dimensional
AFCE	Adiabatic Film Cooling Effectiveness
BD	Backward Differencing
CAD	Computer-Aided Design
CCD	Charge-Coupled Device
CD	Central Differencing
CFD	Computational Fluid Dynamics
CFL	Courant-Friedrichs-Lewy number
CMOS	Complementary Metal-Oxide-Semiconductor
CV	Control Volume
DDES	Delayed Detached Eddy Simulation
DEHS	Di-Ethyl-Hexyl-Sebacate
DES	Detached Eddy Simulation
DNS	Direct Numerical Simulation
DSC	Double Swirl Chamber
EARSM	Explicit Algebraic Reynolds-Stress Model
FV	Finite Volume
GAMG	Generalised geometric-Algebraic Multi Grid
GCI	Grid Convergence Index
ITLR	Institut für Thermodynamik der Luft- und Raumfahrt
LES	Large Eddy Simulation
MI1	One Multiple Inlet
MI3	Three Multiple Inlets
MI5	Five Multiple Inlets
MLOS	Multiplicative Line Of Sight
MRV	Magnetic Resonance Velocimetry
MSD	Modeled Stress Depletion
OpenFOAM	Open Source Field Operation and Manipulation
PANS	Partially-Averaged Navier-Stokes
PC	Personal Computer
PCG	Preconditioned Conjugate Gradient
PISO	Pressure Implicit with Splitting of Operators
PIV	Particle Image Velocimetry

Abbreviation	Description
PTV	Particle Tracking Velocimetry
RHE	Ranque-Hilsch Effect
RANS	Reynolds-Averaged Navier-Stokes
RHVT	Ranque-Hilsch Vortex Tube
RMS	Root Mean Square
RNG	Renormalization Group
RSM	Reynolds-Stress Model
RTD	Resistance Temperature Detectors
SGS	Sub-Grid Scale
SST	Shear-Stress Transport
TC	Thermocouple
THP	Thermal-Hydraulic Performance
TLC	Thermochromic Liquid Crystal
UK	United Kingdom
VB	Vortex Breakdown
VLES	Very Large Eddy Simulation
VT	Vortex Tube
YSC	Younis-Speziale-Clark

Abstract

In the present work, the flow phenomena and the heat transfer in swirl tubes are studied in detail. A swirl tube is a tube with one or more tangential inlet jets, which induce a highly 3D swirling flow. This swirling flow is characterized by large velocities near the wall and an enhanced turbulence in the tube which both increase the convective heat transfer. Therefore, a swirl tube is a very effective cooling technique for high thermal loaded components like gas turbine blades.

As a first step, a generic swirl tube with tangential inlets at the upstream end of the tube is investigated. Second, a novel application-oriented swirl tube geometry with multiple tangential inlet jets in axial direction is examined. In a comprehensive study, the flow field, the heat transfer and the pressure loss for several Reynolds numbers (mass flow rates), swirl numbers and outlet geometries are investigated experimentally and numerically. For this purpose, the flow field is measured via stereo- and tomographic-PIV (Particle Image Velocimetry) and the heat transfer is measured by applying a transient technique using thermochromic liquid crystals. The numerical simulations are performed via Detached Eddy Simulation.

In strong swirling flows, the flow field is dominated by the circumferential velocity which is characterized by a Rankine vortex with a solid body vortex in the tube center and a potential vortex in the outer region. A stability analysis reveals that the solid body vortex is unstable and hence explains the transformation of the solid body vortex into a stable potential vortex towards the tube outlet. In addition, the axial velocity shows a backflow region (vortex breakdown) in the tube center over the entire tube length. It is shown that in swirl dominated flows, a vortex breakdown is possible for Rossby numbers (ratio between axial and circumferential velocity) below 0.65. In addition, a

Abstract

comparison between the local mean axial Reynolds number and the local mean circumferential Reynolds number illustrates that a vortex breakdown occurs in flow regions with higher circumferential than axial Reynolds number. Consequently, in axial dominated flows no backflow appears.

The measurements indicate that the heat transfer in swirl tubes increases with increasing Reynolds number and swirl number, respectively. Near the inlet, the maximum heat transfer occurs due to the large circumferential velocity component. For the highest investigated swirl number, the highest heat transfer is up to ten times higher than the one in an axial tube flow. With decreasing swirl and velocity towards the tube outlet, also the heat transfer decreases continuously. The investigation of various outlet geometries (straight, tangential and $180°$ bend outlet) shows that an outlet redirection has no significant influence on the upstream flow structure and the heat transfer. Thus, the generic swirl tube is characterized by a robust design regarding inflow and outflow conditions and is well applicable for the cooling of high thermal loaded components like gas turbine blades.

The investigation of the swirl tube with multiple tangential inlet jets reveals a very complex axial velocity which changes after each inlet due to the additional mass flow. However, the circumferential velocity stays almost constant since the swirl strength is re-enhanced with each inlet jet, respectively. For each inlet jet, a high heat transfer can be observed. However, the maximum heat transfer is lower than for the swirl tube with only one inlet because of the lower inlet jet velocities. On the other hand, due to the additional tangential jets, the heat transfer distribution is more homogeneous over the entire tube length at a much lower pressure loss. For the investigated swirl tubes with one, three or five inlets, the thermal performance parameter (ratio of heat transfer to pressure loss) is in the same order of magnitude. This means that all swirl tube configurations are suitable for cooling. It strongly depends on the application, if one is interested in a maximum heat transfer paid by a high pressure loss, or a lower but more homogeneous heat transfer with a low pressure loss. For the first case, one should choose the swirl tube with only one inlet. For the second case, the swirl tube with five inlets would be the better choice.

Kurzfassung

In der vorliegenden Arbeit werden die Strömungsphänomene und der Wärme-übergang in Wirbelrohren detailliert untersucht. Ein Wirbelrohr ist ein Rohr mit einem oder mehreren tangentialen Einlässen, die eine stark dreidimension-ale Drallströmung einbringen. Diese Drallströmung ist durch hohe Geschwin-digkeiten in Wandnähe und erhöhte Turbulenz gekennzeichnet, wodurch der konvektive Wärmeübergang im Rohr erhöht wird. Daher kann ein Wirbelrohr als sehr effiziente Kühlmethode für thermisch hoch beanspruchte Bauteile wie z.B. Gasturbinenschaufeln verwendet werden.

Im ersten Schritt wird ein einfaches Wirbelrohr mit tangentialen Einlässen am Rohranfang detailliert untersucht. Des Weiteren wird eine neuartige und anwendungsorientierte Wirbelrohrgeometrie mit mehrfachen tangentialen Ein-lässen in axialer Richtung erforscht. In umfassenden Untersuchungen werden das Strömungsfeld, der Wärmeübergang und der Druckverlust für verschiedene Reynoldszahlen (Massenströme), Drallzahlen und Auslassgeometrien experi-mentell und numerisch ermittelt. Hierfür wird das Geschwindigkeitsfeld mit-tels stereo- und tomographischem-PIV (Particle Image Velocimetry) vermessen und der Wärmeübergang mit Hilfe einer transienten Messtechnik unter Verwen-dung von thermochromatischen Flüssigkristallen ermittelt. Die numerischen Simulationen werden mittels Detached Eddy Simulation durchgeführt.

Bei starkem Drall dominiert die Umfangsgeschwindigkeit das Strömungsfeld, welche durch einen Rankine-Wirbel mit Starrkörperwirbel im Rohrkern und einem Potenzialwirbel im Außenbereich gekennzeichnet ist. Eine Stabilitäts-analyse zeigt, dass der Starrkörperwirbel instabil ist, wodurch sich die Um-wandlung des Starrkörperwirbels in einen stabilen Potenzialwirbel bis zum Ende des Rohres erklärt. Darüber hinaus zeigt die Axialgeschwindigkeit ein

Rückströmgebiet (Wirbelzusammenbruch) im Rohrkern über die gesamte Rohrlänge. Es wird gezeigt, dass in dralldominierten Strömungen ein Wirbelzusammenbruch für eine Rossbyzahl (Verhältnis von Axial- zu Umfangsgeschwindigkeit) unter 0,65 möglich ist. Des Weiteren zeigt ein Vergleich zwischen der lokalen mittleren Axial-Reynoldszahl und der lokalen mittleren Umfangs-Reynoldszahl, dass ein Wirbelzusammenbruch in Strömungsgebieten mit höherer Umfangs- als Axial-Reynoldszahl auftritt. Folglich taucht in axialdominierten Strömungen keine Rückströmung auf.

Die Messungen zeigen, dass der Wärmeübergang jeweils mit der Reynolds- und Drallzahl zunimmt. Im Einlassbereich tritt wegen der hohen Umfangsgeschwindigkeitskomponente der höchste Wärmeübergang auf, welcher bei der höchsten untersuchten Drallzahl bis zu zehnmal höher als der in einer axialen Rohrströmung ist. Stromabwärts nimmt mit abnehmendem Drall und Geschwindigkeit auch der Wärmeübergang kontinuierlich bis zum Rohrende ab. Die Untersuchung verschiedener Auslassgeometrien (gerader Auslass, tangentialer Auslass und 180° Krümmer) zeigt, dass eine Auslassumlenkung keinen signifikanten Einfluss auf die stromaufwärts liegende Strömungsstruktur und den Wärmeübergang hat. Daraus folgt, dass das hier untersuchte Wirbelrohr durch ein robustes Design bezüglich Einström- und Ausströmbedingungen gekennzeichnet ist und demnach gut zur Kühlung von thermisch hochbelasteten Bauteilen wie Gasturbinenschaufeln verwendet werden kann.

Die Untersuchungen des Wirbelrohrs mit mehrfachen tangentialen Einlässen zeigen ein sehr komplexes Axialgeschwindigkeitsfeld, welches sich aufgrund des zusätzlichen Massenstroms nach jedem Einlass ändert. Die Umfangsgeschwindigkeit bleibt hingegen annähernd konstant, da sich die Drallstärke mit jedem Einlassstrahl wieder erhöht. An jedem Einlass kann ein hoher Wärmeübergang beobachtet werden. Der maximale Wärmeübergang für ein Wirbelrohr mit mehreren Einlässen ist jedoch niedriger als für eines mit nur einem Einlass aufgrund der niedrigeren Einströmgeschwindigkeiten. Allerdings ergibt sich bei mehreren Einlässen aufgrund der zusätzlichen tangentialen Strahlen eine homogenere Wärmeübergangsverteilung über die gesamte Rohrlänge bei einem deutlich niedrigeren Druckverlust als mit einem Einlass. Für alle untersuchten Wirbelrohre mit einem, drei oder fünf Einlässen liegt die thermische Effizienz (Verhältnis von Wärmeübergang zu Druckverlust) in der gleichen Größenordnung. Das heißt, alle Wirbelrohrkonfigurationen sind zur Kühlung geeignet. Dabei hängt es stark von der Anwendung ab, ob man an einem maximalen Wärmeübergang bei einem hohen Druckverlust oder an einem niedrigeren, aber dafür homogeneren Wärmeübergang bei einem niedrigeren Druckverlust interessiert ist. Für den ersten Fall sollte das Wirbelrohr mit nur einem Einlass gewählt werden. Für den zweiten Fall ist das Wirbelrohr mit fünf Einlässen die bessere Wahl.

CHAPTER 1

Introduction

1.1 Motivation

Nowadays, the gas turbine industry faces strict legal requirements concerning pollutant emissions and reduction of fuel consumption. To comply with these requirements, the thermal efficiency has to be increased for both aircraft engines and industrial gas turbines. A jet engine consists of a compressor, a combustion chamber and a turbine. The compressor increases the air pressure, in the combustion chamber fuel is added, ignited and a high temperature flow is generated. This high pressure and high temperature gas expands in the turbine producing a shaft work output. A higher thermal efficiency can be achieved by increasing the pressure ratio across the turbine and/or by increasing the combustion temperature and therefore the turbine entry temperature. Over the last decades, the turbine entry temperature increased well above the melting temperature of the turbine blade material. Due to these high thermal loads, the blades of the first turbine stages consist of an internal air cooling system as shown in the cross-section of a turbine blade in Fig. 1.1. Here, an internal serpentine cooling channel with ribs is depicted. Additionally, film cooling holes generate an air film on the outer surface of the blade to protect the material from hot gases. For the blade cooling system, the cooling air is
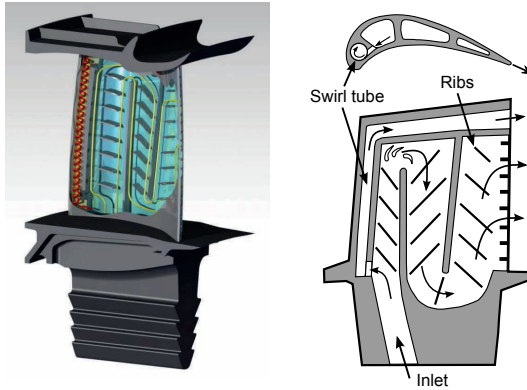
Figure 1.1: 3D turbine blade model and cross-section with leading edge swirl tube (according to [19, 219])

taken from an upstream compressor stage, which means an air loss for the combustion and thus the entire engine cycle. Consequently, a more efficient cooling method would need less cooling air from the compressor stage. This means that more air can take part in the combustion and engine cycle, which leads to a higher efficiency.

In the first turbine stages, the turbine blade leading edges are exposed to the highest temperatures and therefore they need the most effective internal air cooling system. For this purpose, a very effective cooling technique can be a swirl tube which is also shown in the cross-section of the turbine blade in Fig. 1.1. A swirl tube consists of one or more tangential inlet jets which induce a highly 3D swirling flow as shown in red in the blade leading edge on the left side of Fig. 1.1. This swirling flow is characterized by large velocities near the wall and an enhanced turbulence in the tube, which increase the convective heat transfer up to four times [115] compared to an axial unswirled tube flow. However, the complex flow field and the heat transfer in such a swirl tube are far from being completely understood and are therefore subject of this work.

1.2 Objectives of This Study

In the present work, a generic swirl tube will be investigated in detail. This is achieved by a comprehensive experimental and numerical study to analyze the

complex flow field and the heat transfer mechanisms. Moreover, the stability of swirling flows and the vortex breakdown phenomenon will be analyzed. In addition, a novel application-oriented swirl tube with multiple inlet jets will be studied in terms of flow field, pressure loss and heat transfer. Finally, the thermal performance for all investigated swirl tube configurations will be determined and quantitatively assessed.

The baseline swirl tube consists of two tangential inlets at the beginning of the tube as shown in Fig. 1.2. This means that the flow is solely induced tangentially. The rather simple geometry is designed to gain a better understanding of the complex physical mechanisms in swirl tubes. The second investigated geometry is a multiple inlet swirl tube with several tangential inlet jets in axial direction. From an engineering point of view, this geometry has the advantage that the additional tangential inlet jets downstream re-enhance the swirling flow in the tube and therefore cause a more homogeneous heat transfer over the tube length. Moreover, the mass flow is distributed over the inlets, which reduces the maximum jet velocity at the inlets and therefore the pressure loss in the tube.

In the experiments, the flow field is measured via Particle Image Velocimetry (PIV) and the heat transfer is determined with a transient technique using thermochromic liquid crystals (TLC) for various flow and geometric parameters. Additionally, the pressure loss over the tube is measured. The data are used to determine the thermal performance of the investigated swirl tube configurations and to analyze the vortex breakdown phenomenon and the stability of swirling flows. Furthermore, the experimental database will be used for the validation of numerical simulations. The performed numerical simulations allow to analyze the physical mechanisms in detail, in particular the complex flow structure and the heat transfer.
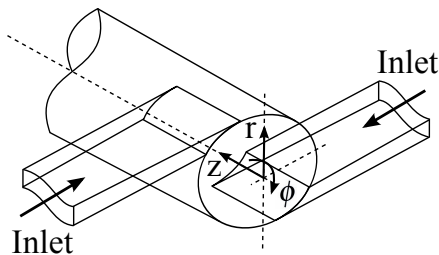
Figure 1.2: Baseline swirl tube geometry and the used coordinate system

1.3 Procedure

The single inlet and the multiple inlet swirl tube configurations are studied in
detail for various swirl numbers S and Reynolds numbers Re. The swirl num-
ber characterizes the inlet condition and the Reynolds number describes the
mass flow rate. Their definition is given in the next section. For the multiple
inlet swirl tube, three different configurations with one (MI1), three (MI3) and
five tangential inlets (MI5) in axial direction are investigated. In addition, the
influence of different outlet geometries are analyzed for the single inlet swirl
tube. The experimentally and numerically investigated swirl number range,
the Reynolds number range and the outlet geometries for both swirl tube con-
figurations are summarized in Table 1.1. For these studies, the flow field, the
temperature distribution, the heat transfer and the pressure loss are analyzed.
In the experimental investigations, the velocity field is measured via stereo-
and tomographic-PIV in a 2D laser sheet and a 3D laser volume, respectively.
For this purpose, the flow is seeded with tracer particles, which are illuminated
by two laser pulses within a short time period. The scattered light is recorded
by two cameras. Finally, the velocity vector in small interrogation windows
can be calculated from the particle shift and the time period taken. Moreover,
the temperature field in the tube is determined via thermocouples. The heat
transfer coefficients are measured applying a transient technique using TLCs.
For this purpose, the inner tube wall is sprayed with TLCs, which change their
color depending on the temperature. During the experiment, the measuring

Table 1.1: Swirl tube configurations with experimentally (exp.) and numeri-
cally (num.) investigated flow conditions (swirl number S and
Reynolds number Re, definition see next section 1.4) and outlet
geometries

		single inlet swirl tube (baseline)	multiple inlet swirl tube		
			MI1	MI3	MI5
S	exp.	$0.75 - 5.3$	5.76	1.92	1.15
	num.	$0.5 - 1.0, 5.3$		—	1.15
$Re \times 10^{-3}$	exp.	$10 - 40$	$10 - 40$		$10 - 80$
	num.	$10 - 40$		—	10, 50
outlet	exp.	straight, tangential, $180°$ bend	straight		
	num.	straight	straight		

section is exposed to a sudden temperature rise of the flow and the TLC color change is recorded on video. With the temporal fluid temperature and the time to reach a specific wall temperature (TLC color) one can determine the heat transfer coefficients from the solution of the 1D heat conduction equation into a semi-infinite wall. Additionally, the wall pressure is measured at ten axial locations over the tube length.

The temperature ratios between heated air flow and swirl tube wall examined in this study are comparably small in contrast to real technical applications. The different temperature ratios can be neglected since the results will be discussed in non-dimensional form. Moreover, Hedlund and Ligrani [84] investigated the heat transfer in swirl tubes with different temperature ratios and concluded that the temperature ratio has no influence on the heat transfer. Additionally, for an easier experimental procedure, the cold swirl tube wall is exposed to a heated air flow. This means that the direction of the wall heat flux is in the opposite direction compared to the cooling in real technical applications. Several scientists [69, 70, 84, 85, 140] investigated the influence of the wall heat flux direction and concluded that this is irrelevant for the small temperature ratios investigated here.

Furthermore, the flow field and the heat transfer in swirl tubes are numerically studied via Detached Eddy Simulation (DES) using the open-source code OpenFOAM. A DES solves the near wall region using the Reynolds-averaged Navier-Stokes (RANS) equations and the free stream region away from the wall is simulated via a Large Eddy Simulation (LES). The main advantages of this hybrid method are more accurate results than a pure RANS, especially in complex anisotropic flows, and a massive reduction of computational costs compared to a full LES.

In addition, the stability of swirling flows and the vortex breakdown phenomena in swirl tubes are investigated in detail by means of the numerical and experimental results based on selected criteria from literature. Finally, all investigated swirl tube configurations will be compared and assessed regarding their thermal performance.

1.4 Dimensionless Numbers

The flow and the heat transfer in a swirl tube can be characterized by dimensionless numbers. These numbers allow the transfer of the results at laboratory conditions to the conditions of the technical application, e.g. for gas turbine blade cooling. Furthermore, the results can be compared to different experiments or numerical simulations in literature.

Reynolds Number

The Reynolds number characterizes flow situations and is defined as the ratio of inertial forces to viscous forces. For internal flows, the Reynolds number is typically defined by the tube diameter D and the axial bulk velocity $\overline{U}_z$:

$$Re = \frac{\overline{U}_z D}{\nu} = \frac{4\dot{m}}{\pi D \mu}. \tag{1.1}$$

The Reynolds number assures the comparison of flow conditions (experiments and/or numerics) at the same mass flow rate $\dot{m}$.

Swirl Number

The swirl strength in a flow can be characterized by the swirl number which is defined as the ratio of angular momentum $\dot{I}_\phi$ divided by the tube radius R to the axial momentum $\dot{I}_z$ of the flow [73]:

$$S = \frac{\dot{I}_\phi}{R\,\dot{I}_z} = \frac{\int\limits_{r=0}^{R} \rho U_z U_\phi\, 2\pi r^2\, \mathrm{d}r}{R \int\limits_{r=0}^{R} \rho U_z^2\, 2\pi r\, \mathrm{d}r} = \frac{\int_A \rho U_z U_\phi r\, \mathrm{d}A}{R \int_A \rho U_z^2\, \mathrm{d}A}\ . \tag{1.2}$$

Here, U_z and U_ϕ denote the axial and circumferential velocity component, respectively. The swirl number depends on the local cross-section and decreases further downstream as the circumferential velocity decays over the tube length. The local value cannot be calculated in advance since the velocity distribution is unknown. Based on the inlet conditions, a geometrical swirl number can be derived to distinguish the different geometries of the investigated swirl tubes. Considering the continuity equation, the tangential inlet velocity and the axial velocity are related as follows:

$$\rho U_\phi A_{inlet} = \rho U_z A_{tube}. \tag{1.3}$$

Assuming constant velocities over the cross-sections, the swirl number yields

$$S \approx \frac{\rho U_z U_\phi \int_A l\, \mathrm{d}A}{R\, \rho U_z^2 \int_A \mathrm{d}A} \approx \frac{\rho l U_z U_\phi}{R\, \rho U_z^2} = \frac{l U_z^2 A_{tube}/A_{inlet}}{R\, U_z^2} = \frac{l}{R} \frac{A_{tube}}{A_{inlet}} \tag{1.4}$$

where l is the lever of the angular momentum as shown in Fig. 1.3. The geometrical swirl number depends only on the inlet and tube cross-sections and
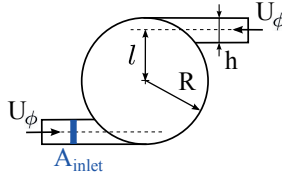
Figure 1.3: Swirl generator with tangential inlets

not on the velocities and is therefore independent of the Reynolds number. With the tube radius R, the channel height h and width w and the number of tangential inlets n, the geometrical swirl number reads

$$S_{geo} = \frac{(R - h/2)\ \pi R^2}{R\ hwn} \ . \tag{1.5}$$

In the present work, the baseline swirl tube configurations are described by the geometrical swirl number which is termed S in the following.

Nusselt Number

The Nusselt number describes the non-dimensional heat transfer and allows comparing the heat transfer from experiments, numerics and literature with various temperature differences or length scales. In tube flows the Nusselt number is based on the tube diameter D as follows

$$Nu = \frac{hD}{k} \ , \tag{1.6}$$

with the thermal conductivity k and the heat transfer coefficient h, which is defined as

$$h = \frac{\dot{q}_w}{\Delta T} = \frac{-k \left.\frac{\partial T}{\partial n}\right|_w}{T_w - T_{ref}} \ . \tag{1.7}$$

Here, $\dot{q}_w$ denotes the wall heat flux and ΔT is the driving temperature difference between the wall temperature T_w and a suitable reference temperature T_{ref} (e.g. the fluid temperature). The wall heat flux is given by Fourier's law with the thermal conductivity k and the wall normal temperature gradient. It is evident that the choice of the reference temperature has a major influ-

ence on the heat transfer coefficient and the Nusselt number. The influence of different reference temperatures is described by Moffat [159]. He investigated different experimental methods for heat transfer studies using the inlet or far field fluid temperature T_{in}, T_∞, the mean bulk temperature of the fluid T_m and the adiabatic wall temperature T_{ad}. Moffat [159] concluded that each of these reference temperatures yield a different heat transfer coefficient value for the same physical problem. For technical applications or the comparison to other experiments, it is essential to know which reference is being used. The ideal reference temperature would be the adiabatic wall temperature T_{ad} which invariably describes the heat flux under different thermal boundary conditions. In this work, the adiabatic wall temperature T_{ad} is used as a local reference temperature for the baseline swirl tube geometry. For the more complex multiple inlet swirl tube, the inlet jet temperature T_{in} is used as reference temperature.

1.5 Publications

Parts of this work have already been published in [16–20, 178]. The work has been supported by several high quality bachelor and master theses [11, 22, 28, 65, 175, 189, 191, 197, 217, 219, 222].

Flow and Heat Transfer in Swirl Tubes

In the following chapter, the most important flow phenomena in swirl tubes will be described which greatly affect the heat transfer. First, the relevant literature on the experimental and numerical investigation of swirl tubes is given. Then, the vortex breakdown phenomenon and the stability influence is discussed in detail. Finally, the Ranque-Hilsch effect and the resulting temperature separation is described by means of a literature review.

2.1 Swirl Tube

A swirl tube is characterized by an additional circumferential velocity component to the axial flow velocity. This swirling flow enhances the flow velocity near the wall and therefore the turbulence considering a constant mass flow rate. According to a comparison of different cooling techniques with enhanced heat transfer by Ligrani et al. [134], swirl tubes may have the highest heat transfer potential but also the highest pressure loss.

Experimental Swirl Tube Investigations

In the last 60 years many scientists experimentally studied swirling flow in tubes and a literature overview can be found in Table 2.1. Kreith and Margolis [115] first proposed to use swirling flow in tubes to enhance the convective heat transfer. They suggested four different methods creating a swirling flow: (1) vortex ramp, (2) tangential injection, (3) twisted strip insert, or (4) twisted tube. Their observation showed that the heat transfer in a swirling flow can be at least four times as large as heat transfer coefficients at the same mass flow rate in purely axial flow [115]. Later, different scientists studied the swirl decay in tubes either using air or water as fluid, for example, the work by [110, 116, 163, 168, 179, 206, 207, 227].

In the 1980s British and Ukrainian scientists investigated swirling flow for turbine blade cooling. These vortex technologies consisted of several tangential inlets and outlets and were first patented in 1988 as a UK patent according to Khalatov et al. [107]. These Russian and Ukrainian studies were summarized by Khalatov et al. [103, 106]. Kitoh [111] investigated swirling flows and the turbulent stresses with a free (or potential) vortex type circumferential velocity profile at the tube entrance. Dhir and Chang [40] and Chang and Dhir [34, 35] studied swirl tubes with tangential injections for two different swirl numbers ($S = 2.78, 5.23$) and a straight outlet. They identified two major mechanisms of heat transfer enhancement [35]: (1) high maximum axial velocity near the wall improves the heat flux from the wall, and (2) the enhanced turbulence level in the core region improves the mixing. Further investigations on the usage of a swirl tube for turbine blade cooling in an engine like test case were presented by Glezer et al. [69, 70]. They presented three novel cooling configurations as shown in Fig. 2.1 and investigated the heat transfer experimentally in a rotating cooling passage at a representative Reynolds number of 20,000 (based on the channel diameter). They studied the influence of realistic rotation numbers from 0 to 0.023 and concluded that Coriolis forces play an important role in enhancing the internal heat transfer. The heat transfer coefficient was determined based on an axial interpolated local fluid temperature between inlet and outlet temperature.

These studies were extended by detailed investigations by Hedlund and Ligrani [84], Hedlund et al. [85, 86], Ligrani et al. [133], Moon et al. [160], and Thambu et al. [214]. They studied the local flow structure and the heat transfer in swirling tube flows induced by tangential wall jet flows and a radial outlet at different Reynolds numbers. The heat transfer was measured using infrared thermography and a constant wall heat flux boundary condition in conjunction with thermocouple measurements. The inlet bulk temperature was used
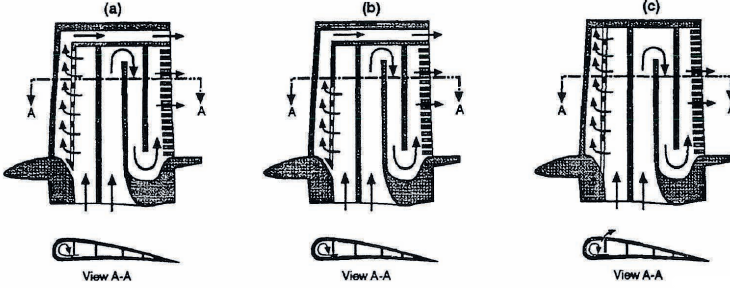
Figure 2.1: Schematic view of swirl cooling configurations by Glezer et al. [70]

as reference temperature for the heat transfer coefficient. They showed flow visualization with smoke injection and identified different-sized highly interacting Görtler vortex pairs [84]. The investigated Reynolds number based on the swirl chamber diameter ranged from 1,200 to 7,200. They found out that with increasing Reynolds number the size of the Görtler vortex pairs decreases as the flow phenomena become more unsteady.

Khalatov et al. [107–109] extensively studied a broad Reynolds number range of the cyclone cooling technique and Khalatov and Nam [105] reviewed aerothermal vortex technologies (for aerospace engineering). They used the heat transfer and pressure loss data evaluating the thermal-hydraulic performance (THP) $(\overline{Nu}/Nu_0)/(f/f_0)^{1/3}$ and provided a correlation for the averaged Nusselt number including literature data from Glezer et al. [69], Ligrani et al. [133], and Qian et al. [174]: $\overline{Nu}_D = 0.490\ Re_D^{0,56}$. Ling et al. [140] investigated the heat transfer in a swirl tube with the same geometry as Ligrani et al. [133] with two axial displaced tangential inlets and one radial outlet. They determined the heat transfer with a transient technique using thermochromic liquid crystals and used the tube inlet temperature as reference temperature. Moreover, they measured the near wall velocity on the curved surface by hotwire experiments and estimated the heat transfer using the Colburn analogy. The effect of rotation on cyclone cooling was investigated by Winter and Schiffer [221]. They found out that the flow in the channel is stabilized by the swirl and that the rotation significantly reduces the development of a pressure and suction side.

Recent swirl chamber studies by Bruschewski et al. [25], Grundmann et al. [71], and Wassermann et al. [218] used the novel magnetic resonance velocimetry (MRV) technique in water to measure the flow field with a highly 3D resolution.

The investigated swirl numbers ranged from 1 to 5. Their measurements provided an insight in the flow field for different swirl tube outlet geometries like a concentric, a ring and a eccentric outlet orifice and a round 180° bend. Their results showed that a swirl chamber is characterized by a stable flow structure, which means that swirling flows can also be used in complex geometries.

Kobiela [113] experimentally investigated the heat transfer using a transient liquid crystal technique and measured the flow field using PIV at the same experimental swirl tube rig used for the present work. The investigated swirl numbers ranged from 2.36 to 5.89 and the Reynolds numbers from 10,000 to 40,000. The outlet geometry consisted of an axial outlet. Kobiela [113] detected secondary vortex structures visible in the heat transfer pattern and estimated the appearance of Görtler vortex pairs. He concluded that no Görtler vortex pairs appear for the investigated turbulent flow at high Reynolds numbers.

A comparison of impingement and vortex cooling at the same coolant mass flow rate was shown by Ling et al. [140] and Qian et al. [174]. Qian et al. [174] used the naphthalene sublimation method measuring the heat transfer coefficients and investigated Reynolds numbers between 32,000 and 77,000 ($Re_{jet} = 127,000 - 300,00$). Both studies showed a higher maximum heat transfer coefficient for the impingement cooling but a more homogeneous heat transfer coefficient with the vortex cooling and therefore an overall higher averaged Nusselt number. Qian et al. [174] reported a heat transfer increase of 20% compared to impingement cooling with the same pressure drop.

Ling [139] investigated tapered swirl tube models with a decreasing outlet tube diameter and compared it to the baseline swirl tube with a constant diameter. The tapered models had an outlet to inlet diameter ratio of $D_{out}/D_{in} = 2/3$ and $1/2$. The comparison at $Re = 10,000$ showed that the heat transfer in the downstream region ($x/R = 7 - 8$) for the tapered model with a $1/2$ ratio is about 33% higher than for the baseline tube. The heat transfer for the other model with a $2/3$ diameter ratio increases as well about 17% compared to the basic swirl tube in the same region.

Ekkad et al. [47] measured the heat transfer inside a two-pass channel connected by series of holes on the divider wall. The combination of impingement and swirl induced by the lateral injection significantly enhances the heat transfer compared to the conventional U-bend serpentine channel design. However, a higher pressure drop penalty must be paid in this case.

Important patents about vortex cooling for gas turbine blades are by Dhir [39], Glezer et al. [68], Harvey et al. [82], and Lee [122].

Table 2.1: Literature on experimental swirl tube investigations

author	year	$Re_D \times 10^{-3}$	details
Kreith and Margolis [115]	1959	$10 - 140$	twisted strip, coiled wire, axial outlet
Nissan and Bresan [163]	1961	$5 - 25$	swirl decay
Kreith and Sonju [116]	1965	$10 - 100$	twisted tape, swirl decay
King et al. [110]	1969	$10 - 25$	water, swirl decay
Weske and Sturov [220]	1974	30	rotating tube
Hay and West [83]	1975	$10 - 49$	$S = 0.65 - 3.0$, axial outlet
Akiyama and Ikeda [4]	1986	$30 - 100$	nozzle inlet, energy loss study
Kitoh [111]	1991	$40 - 80$	$S = 1.0$, turbulent stresses, axial outlet
Dhir and Chang [40]	1992	$10 - 53$	$S = 2.78, 5.23$, tangential inlet
Kumar and Conover [117]	1993	$15 - 60$	flow visualization in water
Parchen [168]	1993	$10 - 50$	water, swirl decay
Reader-Harris [179]	1994	$10 - 10^4$	analytical swirl decay
Chang and Dhir [34]	1994	12.5	$S = 2.67, 7.84$, axial outlet
Chang and Dhir [35]	1995	12.5	$S = 2.67, 7.84$, axial outlet
Steenbergen [206]	1995	$50, 300$	$S = 0.1$, water, swirl decay
Glezer et al. [70]	1996	20	90° bend outlet
Qian et al. [174]	1997	$32 - 77$	impingement and vortex cooling
Glezer et al. [69]	1998	20	rotating channel, 90° bend outlet
Ligrani et al. [133]	1998	$1 - 18.5$	one/two inlet/s, tangential outlet
Moon et al. [160]	1998	$0.24 - 1.9$	lengthwise tangential injections
Steenbergen and Voskamp [207]	1998	$50, 300$	$S = 0.1$, water, swirl decay

Literature on experimental swirl tube investigations - continued

author	year	$Re_D \times 10^{-3}$	details
Al-Ajmi et al. [3]	1998	$1 - 14$	LDA studies of a 180° turn, tangential inlet and outlet
Alekseenko et al. [5]	1999	$6.6 - 23$	analytical study and flow visualization in water ($S = 1 - 3.8$)
Yilmaz et al. [227]	1999	$32 - 110$	swirl decay, vane angle variation
Hwang and Cheng [90]	1999	$8.6 - 21$	swirl in triangular duct
Thambu et al. [214]	1999	$0.18 - 1.1$	2D swirl tube with controlled inlet forcing
Hedlund et al. [85]	1999	$2.4 - 7.2$	$T_{in}/T_{wall} = 0.6 - 0.95$, radial outlet
Hedlund et al. [86]	1999	$2.2 - 7.2$	$T_{in}/T_{wall} = 0.62 - 0.86$, radial outlet
Hedlund and Ligrani [84]	2000	$1.2 - 7.2$	flow visualization, radial outlet
Ekkad et al. [47]	2000	$10 - 50$	crossflow swirl in cooling passage
Khalatov et al. [109]	2000	$25 - 184$	thermal-hydraulic performance (THP)
Khalatov et al. [107]	2001	$Re_{in} = 0.5 - 2.5$	$S = 0.82 - 1.58$ THP, several tangential inlets and outlets
Khalatov et al. [108]	2002	$2 - 310$	2D cyclone cooling, correlation of literature data
Khalatov and Nam [105]	2003	$-$	review of vortex technologies
Yilmaz et al. [228]	2003	$32 - 110$	swirl decay, vane angle variation
Mitrofanova [158]	2003	$-$	analytical review
Ling et al. [140]	2006	$5.4 - 9$	impingement and vortex cooling

Literature on experimental swirl tube investigations - continued

author	year	$Re_D \times 10^{-3}$	details
Gupta and Kumar [74]	2007	$9 - 18$	PTV flow visualization
Winter and Schiffer [221]	2009	$10 - 40$	effect of rotation on cyclone cooling
Lerch and Schiffer [128]	2009	5.8	adiabatic film cooling effectiveness (AFCE)
Lerch and Schiffer [129]	2011	5.8	AFCE
Lerch et al. [127]	2011	5.8	AFCE
Khalatov et al. [104]	2011	$40 - 105$	THP
Grundmann et al. [71]	2012	$10, 15$	magnetic resonance velocimetry (MRV) in water, concentric outlet orifices
Wassermann et al. [218]	2012	$10, 20$	180° bend, MRV
Kobiela [113]	2014	$10 - 40$	$S = 2.36 - 5.89$, axial outlet
Bruschewski et al. [24]	2014	$5 - 30$	$S = 1 - 5$, MRV, simple and ring orifice, 180° bend
Bruschewski et al. [25]	2015	$2 - 32$	$S = 1 - 5$, MRV, concentric, ring and eccentric outlet orifices, 180° bend

Numerical Swirl Tube Investigations

Furthermore, several numerical swirl tube investigations can be found in literature and an overview is given in Table 2.2. Hogg and Leschziner [88] numerically investigated the performance of the k-ϵ eddy-viscosity model with that of a Reynolds-stress transport closure by simulating a highly swirling confined flow. They showed that the eddy-viscosity model returns a high level of turbulent diffusion and misrepresents the flow characteristics. The Reynolds-stress model (RSM) in contrast successfully predicts velocity and turbulence fields in good agreement compared to experiments. Spall and Ashby [201] and Spall and Gatski [202] also compared the ability of the standard k-ϵ eddy-viscosity model with that of an explicit algebraic Reynolds-stress model (EARSM) and

a RSM by simulating a vortex breakdown in turbulent swirling flow. The results confirm that the k-ϵ model fails to predict the occurrence of breakdown whereas the RSM reasonably well predict the vortex breakdown. Similar work analyzing swirling flows with eddy-viscosity models and RSM was presented by [36, 94].

Ling et al. [140] numerically investigated the heat transfer in a swirl tube with the same geometry as Ligrani et al. [133] with two axial displaced tangential inlets and one radial outlet. The heat transfer coefficients from CFD show a good agreement with the transient heat transfer experiments. The flow field is well resolved in the near wall region but shows poor agreement in the core due to the used k-ϵ turbulence model.

Paik and Sotiropoulos [167] simulated turbulent swirling flows through an abrupt expansion via Detached Eddy Simulation (DES) at Reynolds numbers of 30,000 and 100,000 over a range of swirl numbers from 0.17 to 1.23. The flow field and turbulence are well resolved compared to measurements and the authors presented coherent structures visualizing the spiral vortex breakdown (see next section 2.2). Liu et al. [141, 142] simulated the flow and heat transfer of swirl cooling for the same geometry like [83] and [140] using different eddy-viscosity models. The SST model performs best compared to the k-ϵ, k-ω and RNG (Renormalization Group) model.

Kobiela [113] numerically studied swirl tubes for a swirl number range from 2.36 to 5.3 at Reynolds numbers from 10,000 to 40,000. An EARSM in conjunction with a curvature correction was applied as turbulence model and the energy equation was solved using an explicit algebraic scalar flux model (YSC) from Younis et al. [230]. Kobiela [113] extended the incompressible scalar flux model to a compressible formulation considering an additional pressure gradient term. With this model he succeeded in simulating the radial temperature separation occurring in highly swirling flows (see section 2.3).

Chang et al. [33] simulated the same swirl tube geometry from [71] via LES and the hybrid method VLES (Very Large Eddy Simulation proposed by [204]). The flow field showed good agreement with experimental data in a tube with variably-shaped outlet orifices (centered and eccentric opening).

In addition to swirling flow in cylindrical tubes, different vortex cooling techniques to enhance the heat transfer performance can be found in literature. For example, Jiang et al. [99] numerically investigated the swirl cooling heat transfer enhancement by adding water mist. They studied the effects of different parameters like the mist concentration, diameters, inlet temperature and inject velocity. They concluded that swirl cooling can take full advantage of mist addition. A double swirl chamber (DSC) is another vortex cooling concept studied by Kusterer et al. [119–121] and Lin et al. [135–137]. A DSC features two connected tubes which results in the shape of an eight. They

compared RANS CFD results in terms of heat transfer and thermal performance with single swirl chamber and impingement cooling with benefits for the DSC.

Table 2.2: Literature on numerical swirl tube investigations

author	year	$Re_D \times 10^{-3}$	approach
Hogg and Leschziner [88]	1989	−	k-ϵ, RSM
Spall and Gatski [202]	1995	10	k-ϵ, EARSM
Spall and Ashby [201]	1999	130	k-ϵ, RSM
Chen and Lin [36]	1999	$Re_{in} = 125$	k-ϵ, RSM, quadratic pressure-strain model
Jakirlić et al. [94]	2002	50	eddy-viscosity models and RSM
Kazantseva et al. [101]	2005	−	flow visualization, SST, k-ϵ
Ling et al. [140]	2006	$1.8 - 72$	FLUENT k-ϵ
Gupta and Kumar [74]	2007	$9 - 18$	FLUENT k-ϵ
Paik and Sotiropoulos [167]	2010	$30 - 100$	DES $S = 0.17 - 1.23$
Liu et al. [141]	2011	$5.4 - 24.6$	geometry from [83] and [140], SST, k-ϵ, k-ω, RNG
Liu et al. [142]	2013	$5.4 - 10$	geometry from [140], SST
Kusterer et al. [119]	2013	10.5	double swirl chamber (DSC), Star CCM+, SST, V2F, k-ϵ
Lin et al. [137]	2014	$Re_{jet} = 15$	DSC, Star CCM+ with SST, V2F, k-ϵ, Spalart-Allmaras
Chang et al. [33]	2014	15	geometry from [71], LES and VLES
Foroutan and Yavuzkurt [62]	2014	−	partially-averaged Navier-Stokes (PANS) model compared to DDES and SST
Jiang et al. [99]	2014	7.2	adding water mist, SST, k-ϵ, k-ω

Literature on numerical swirl tube investigations - continued

author	year	$Re_D \times 10^{-3}$	approach
Kobiela [113]	2014	$10 - 40$	$S = 2.36 - 5.3$, CFX EARSM with YSC scalar flux model
Scherhag et al. [187]	2014	21	$S = 3$, FLUENT LES, ring exit orifice
Kusterer et al. [121]	2015	$Re_{jet} = 15$	DSC, Star CCM+ Spalart-Allmaras
Bruschewski et al. [25]	2015	21	$S = 3$, FLUENT LES, ring exit orifice

Nusselt Number Correlations

In literature, several authors proposed a Nusselt number correlation for the heat transfer in swirl tubes, which are summarized in Table 2.3.

Hay and West [83] investigated a swirl tube with a diameter of $D = 50.8$ mm and a length of $L/D = 18$, which consists of one tangential inlet on one side. They related the heat transfer augmentation (Nu_D/Nu_0) to the local swirl number S: $Nu_D/Nu_0 = (S + 1)^{1.75}$. Here, Nu_0 is the Dittus-Boelter [42] correlation for a fully developed non-swirling turbulent flow: $Nu_0 = 0.023 \, Re_D^{0.8} Pr^{0.3}$. They also provide a correlation for the Nusselt number Nu_z in terms of the axial distance z along the tube depending on the respective Reynolds number $Re_z = Uz/\nu$: $Nu_z = 0.119 \, Re_z^{0.8}$. Furthermore, Hay and West [83] described the swirl decay with $S = 1.72 \exp(-0.04 \, z/D)$.

Hedlund et al. [85] investigated a swirl tube with two axial displaced tangential inlets and one radial outlet and studied the effect of different inlet to wall temperature ratios T_i/T_w on the heat transfer. They proposed the following relation $Nu_D = 0.63 \, (T_i/T_w)^{5.7} \, Re_D^{0.56/(T_i/T_w)}$ depending on the Reynolds number. The correlation is valid between $0.60 < T_i/T_w < 1.0$, whereby $T_i/T_w = 0.86$ for $T_i/T_w > 0.86$.

Glezer et al. [69] investigated an open swirl chamber with several evenly distributed tangential slots in the lengthwise direction. They could not measure any difference in the heat transfer for two different temperature ratios $T_i/T_w = 0.385$ and 0.465. In a later publication, Hedlund and Ligrani [84] presented a simplified correlation for the heat transfer in the same swirl tube like in their previous study [85] independent from the temperature ratio: $Nu_D = 0.27 \, Re_D^{0.65}$. This correlation is also valid for the measurements by Glezer et al. [69].

Table 2.3: Overview of Nusselt number correlations for swirl tubes

author	year	correlation
Hay and West [83]	1975	$Nu_D/Nu_0 = (S+1)^{1.75}$ for $0.65 < S < 2.15$ and $10{,}500 < Re_D < 49{,}000$ $Nu_z = 0.119 \ Re_z^{0.8}$
Hedlund et al. [85]	1999	$Nu_D = 0.63 \left(\frac{T_i}{T_w}\right)^{5.7} Re_D^{0.56/(T_i/T_w)}$ for $2000 < Re_D < 80{,}000$ and $0.60 < T_i/T_w < 1.0$
Hedlund and Ligrani [84]	2000	$Nu_D = 0.27 \ Re_D^{0.65}$ for $2000 < Re_D < 80{,}000$
Khalatov et al. [108]	2002	$Nu_D = 0.490 \ Re_D^{0.56}$ for $2000 < Re_D < 310{,}000$ (obtained for 2D configurations)
Biegger and Weigand [18]	2014	$Nu_D/Nu_0 = 1 + S^{0.73}$ for $1.5 < S < 5.3$ and $10{,}000 < Re_D < 40{,}000$

Khalatov et al. [108] investigated a 2D cyclone chamber with a diameter of 100 mm and a spanwise width of 60 mm. Since the spanwise dimension and therefore the velocity component is small, this swirl cooling design produces a 2D flow pattern. The averaged Nusselt number is well represented by an equation of the form: $Nu_D = 0.490 \ Re_D^{0.56}$. This correlation is also valid for the 2D geometry investigated by Ligrani et al. [133] and Qian et al. [174]. The 3D data from the open swirl chamber with several tangential slots by Glezer et al. [69] show higher averaged Nusselt number values. The heat transfer measurements by Moon et al. [160] lies in between the previous ones, who studied a swirl chamber using continuous tangential flow injection.

As part of this work, Biegger and Weigand [18] measured the heat transfer in a swirl tube with a diameter of $D = 50$ mm and a tube length of $L/D = 20$. The heat transfer results based on a local fluid temperature are presented for different Reynolds and swirl numbers. The Nusselt number augmentation can be described as a function of the geometrical swirl number S:
$Nu_D/Nu_0 = 1 + S^{0.73}$.

2.2 Vortex Breakdown

Originally, the vortex breakdown phenomenon was discovered in leading-edge vortices around delta wings, which influences the lift and stability of the wing. Under certain conditions, these vortices can suddenly change the aerodynamic characteristics of the wing. A similar phenomenon was observed for trailing edge wing-tip vortices, which is important in areas of dense air traffic. The vortex breakdown also occurs in swirling flows in tubes, which makes it easy to investigate it under laboratory conditions.

In swirling flows, the circumferential velocity is characterized by a Rankine vortex. This vortex consists of a solid body rotation in the core, surrounded by a potential vortex (like in tornadoes) and a boundary layer near the wall as shown in Fig. 2.2. For sufficient strong swirl, an abrupt change in the vortex structure occurs with a pronounced velocity decrease along the axis. This vortex breakdown phenomenon has been extensively studied in swirl tubes over the last decades and a literature overview is given in Table 2.4. Detailed reviews on vortex breakdown have been published almost every decade [78, 80, 123, 125] and the last and most extensive is by Lucca-Negro and O'Doherty [147]. Some of the theories, the methods to predict the vortex breakdown and the stability studies are presented in the following.

Vortex breakdowns can be characterized into three different main types according to Sarpkaya [184]: (1) double-helix vortex breakdown, (2) spiral vortex breakdown, and (3) axisymmetric (bubble) vortex breakdown. These types will be explained in the following with an additional flow visualization picture by Sarpkaya [184], where a dye filament is introduced on the vortex axis.
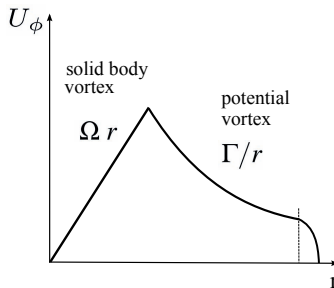
Figure 2.2: Solid body and potential vortex velocity profile [16]

Double-helix Vortex Breakdown

The double-helix vortex breakdown is characterized by a deceleration of the dye filament on the vortex axis, which expands into a slightly curved triangular sheet. The sheet halves are wrapped around each other and form a double helix as shown in Fig. 2.3.
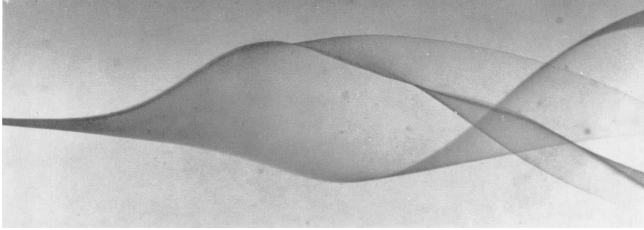
Figure 2.3: Double-helix vortex breakdown [184]

Spiral Vortex Breakdown

The dye filament marking the swirl axis is suddenly decelerated and causes a stagnation point followed by a abrupt kink into a corkscrew-shaped twisting of the dye [147]. This spiral vortex lasts for one or two turns before breaking up into large-scale turbulence depicted in Fig 2.4.
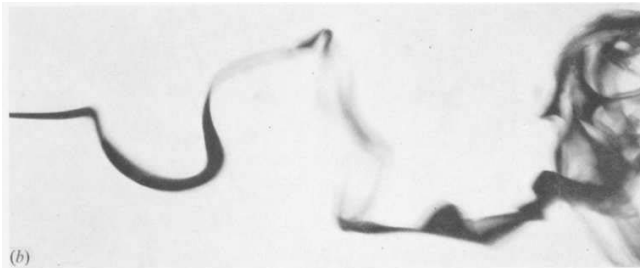
Figure 2.4: Spiral vortex breakdown [184]

Axisymmetric Vortex Breakdown

The axisymmetric (bubble) vortex breakdown is characterized by a stagnation point on the swirl axis, followed by a sudden expansion, forming a bubble of recirculating fluid shown in Fig 2.5. This bubble is nearly axisymmetric over its length and the interior is dominated by low frequency motions [147]. This could be caused by the exchange of fluid with the surrounding flow at the end of the bubble. Moreover, the bubble is quasi-steady in axial location and a tail is observed at the rear.
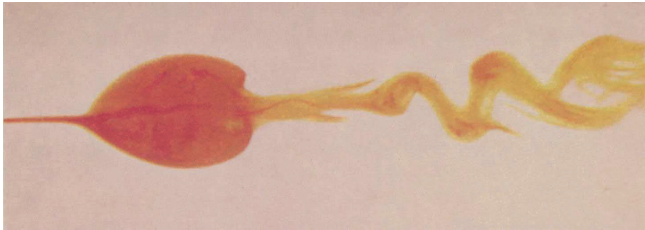
Figure 2.5: Axisymmetric vortex breakdown [184]

2.2.1 Theories of Vortex Breakdown

In the following, the most common theories on the physical mechanisms of vortex breakdown are presented [80]: (1) quasi-cylindrical approximation, (2) supercritical/subcritical states, and (3) hydrodynamic instability.

(1) The quasi-cylindrical approximation introduced by Hall [79] is analogous to the failure of the boundary layer approximation at separation. For large Reynolds numbers the viscous, incompressible cylindrical equation system is obtained by neglecting the gradients in axial direction, which are much smaller than in radial direction. Hall [79] found that the solution of the parabolic equation could not be continued beyond some downstream point for certain upstream conditions. He assumed that this was due to the violation of the neglect of gradients in axial direction and that a breakdown occurs nearby. Thus, vortex breakdown is regarded analogous to boundary-layer separation.

(2) Benjamin [12] defined the existence of standing waves in a swirling flow to be the critical state. He proposed that vortex breakdown is a transition from supercritical to subcritical flow between two steady states of axisymmetric swirling flow. This is analogous to the hydraulic jump in an open-channel

flow [155] or a shock wave in a compressible flow [57]. If the flow is supercritical, the waves are swept away downstream from the originated disturbances [57]. While in a subcritical flow, the waves are spread upstream against the flow and transport information about the downstream conditions and geometry. Squire [205] established a convenient estimation that a flow is subcritical if the maximum swirl velocity exceeds the axial velocity. This criterion will be investigated for the present swirl tube flow in section 5.9.1.

(3) Ludwieg [148] proposed that vortex breakdown arises from the amplification of small spiral disturbances. He studied an inviscid swirling flow in a narrow annulus and found a necessary condition for the stability of a vortex core at sufficiently large Reynolds numbers [155]. Several experiments by Sarpkaya [184–186] and Faler and Leibovich [60] support this theory, at least if spiral breakdown is concerned. Ludwieg's hydrodynamic stability condition is described in more detail in section 5.9.2 and applied to the swirl tube flow in this work.

2.2.2 Prediction of Vortex Breakdown

Different attempts to predict vortex breakdown can be found in [56, 149, 186]. Mager [149] solved the momentum-integral equations of the viscous core of an incompressible swirling flow through a nozzle. The equation system is solved for the circumferential and axial velocities both inside and outside the core. The system has a singularity which results in two possible solutions: (1) mass flow dominated core, or (2) swirl dominated core. At low swirl, the core is mass flow dominated and characterized by a high discharge coefficient. The swirl dominated core flow sustains very large pressure losses and has regions of reverse axial velocity. Sarpkaya [186] examined the effect of adverse pressure gradient on a vortex breakdown and analyzed the breakdown location using the integral method proposed by Mager [149]. Sarpkaya [186] extended Mager's analytical model and predicted the location of the breakdown fairly well.

Kobiela [113] analytically estimated a swirl number limit for the occurrence of an axial backflow based on a momentum balance. The reverse flow on the axis is caused by a pressure gradient in the tube center in the opposite direction of the main flow. Over the tube length, the pressure decreases due to friction and at the same time, the swirl strength and the centrifugal forces decrease. For low swirl, the axial pressure loss is dominant and in the entire tube a negative axial pressure gradient $\partial p/\partial z$ occurs and with it an axial forward flow. For strong swirl, the swirl decrease dominates and in the vortex core, a positive axial pressure gradient arises and causes a reverse flow. For the backflow limitation, the pressure gradient on the tube axis has to be zero: $\partial p/\partial z = 0$.

(a) Considered pressure path in a tube segment

(b) Pressure distribution for a low swirl number

(c) Pressure distribution for a high swirl number
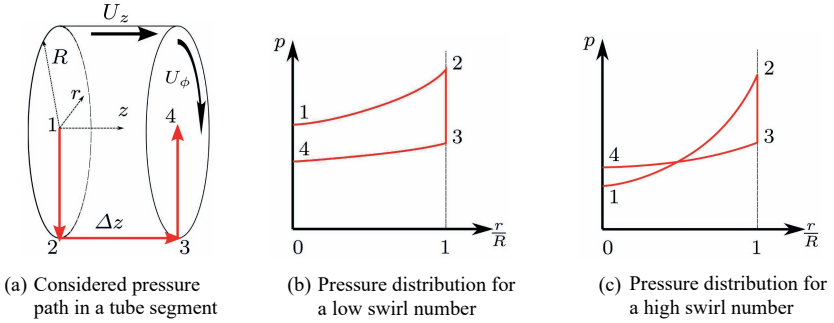
Figure 2.6: Pressure distribution in a swirl tube (adapted from [113])

The pressure distribution is exemplarily illustrated in a short tube segment as shown in Fig. 2.6 according to Kobiela [113]. The pressure distribution is discussed along the path from 1 to 4 and is shown for a low (b) and a high swirl number (c), respectively. Position 1 is located in the tube center and the path leads radially outwards to the tube wall (2), whereby the pressure increases due to centrifugal forces. Between 2 and 3 the pressure decreases along the tube segment length Δz due to friction. On the radially inward path from 3 to 4, the pressure decreases in turn due to the centrifugal forces. Since the swirl has decreased, the pressure decrease is smaller than the increase from 1 to 2. For sufficient strong swirl, the pressure in 4 is higher than in 1, for weak swirl vice versa.

With this approach, Kobiela [113] analytically estimated a swirl number limit S_{limit} for which the axial pressure gradient in the tube center vanishes. For this purpose, he assumed a solid body rotation in the swirl tube and neglected the narrow band potential vortex in the outer tube. Therefore, the circumferential velocity can be described as

$$U_\phi = \omega r \tag{2.1}$$

with a constant angular velocity ω over the radius r. The radial pressure distribution then yields

$$p(r) = p_{center} + \int_0^r \rho\, \omega^2 \tilde{r}\, \mathrm{d}\tilde{r} = p_{center} + \frac{1}{2}\rho\, \omega^2 r^2\ . \tag{2.2}$$

In the limiting case, the axial velocity in the tube center is zero and increases approximately linear to an axial velocity near the wall $U_{z,w}$:

$$U_z(r) = \frac{U_{z,w}}{R}r \ .$$

(2.3)

It is assumed that the axial velocity is constant in the axial direction. Based on an angular and axial momentum balance over the tube segment considering the swirl decay and the pressure loss due to wall friction, the axial velocity near the wall results in [113]

$$U_{z,w} = R\ \omega \ .$$

(2.4)

For details about the momentum balance and the straightforward calculation, the reader is referred to the original work by Kobiela [113]. Finally, the velocity components are inserted in the swirl number according to Eqn. 1.2 and $U_{z,w}$ is replaced by Eqn. 2.4:

$$S = \frac{\int\limits_{r=0}^{R} \rho\ \frac{U_{z,w}}{R}r\ \omega r\ 2\pi r^2\ \mathrm{d}r}{R\ \int\limits_{r=0}^{R} \rho\left(\frac{U_{z,w}}{R}r\right)^2\ 2\pi r\ \mathrm{d}r} = \frac{\int\limits_{r=0}^{R} \rho\ 2\pi\omega^2 r^4\ \mathrm{d}r}{R\ \int\limits_{r=0}^{R} \rho\ 2\pi\omega^2 r^3\ \mathrm{d}r} \ .$$

(2.5)

Thus, the limitation swirl number for reverse flow on the tube axis yields

$$S_{limit} = 0.8 \ .$$

(2.6)

For higher swirl numbers, an axial backflow occurs in the vortex core.
If one assumes a parabolic axial velocity profile

$$U_z(r) = \frac{U_{z,w}}{R^2}r^2$$

(2.7)

instead of a linear distribution, the limitation swirl number results in [113]

$$S_{limit} = \sqrt[3]{\frac{4}{5}} = 0.928 \ .$$

(2.8)

In the present work, swirl tubes with low swirl numbers ($S = 0.5, 0.75$ and 1.0) around the limitation swirl number are numerically investigated in detail and presented in section 5.3.7.
Spall et al. [203] proposed a criterion for the onset of vortex breakdown over a wide range of Reynolds numbers. Based on the investigation of previous
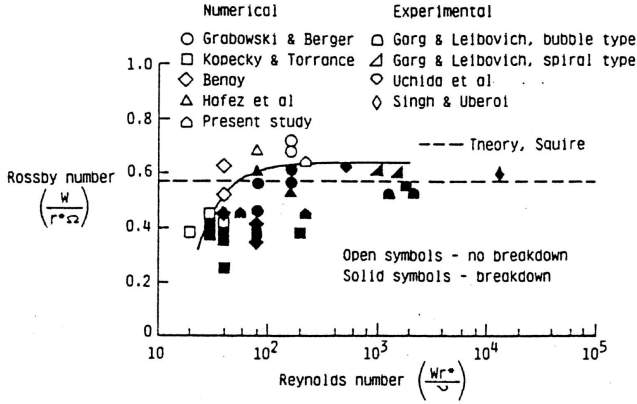
Figure 2.7: Rossby number dependence of wing-tip vortices (according to [203])

studies, he defined a local Rossby number (or inverse swirl ratio) to describe the region where breakdown occurs:

$$Ro = W/r^*\Omega \tag{2.9}$$

where W, r^* and Ω represent a characteristic velocity, length and rotation rate, respectively. Spall et al. [203] defined r^* as the radial distance at which the swirl velocity is maximum. W is the axial velocity at this position, which is a consistent velocity scale for both uniform and radially varying velocity profiles and for the swirl velocity scale $r^*\Omega$. Here, Ω is the rotation rate of the solid body rotation. For consistency, Spall et al. [203] defined the Reynolds number in terms of the same characteristic length scale r^* and velocity scale W. The results of their study as well as other numerical and experimental investigations are presented in Fig. 2.7. It is apparent that for Reynolds numbers greater than 100, the critical Rossby number for the vortex breakdown is about 0.65. For lower Reynolds numbers, the increased damping effects of the viscosity are dominant and lower the critical Rossby number. The theoretical analysis about the existence of axisymmetric standing waves by Squire [205] suggests a critical Rossby number of 0.57. Spall et al. [203] emphasized that the established Rossby number-Reynolds number parameter can be applied for both confined and unconfined vortical flows due to the characteristic scales related to the vortex itself.

Escudier and Keller [56] discussed the isentropic force-free transition in a Rankine vortex to determine the occurring flow conditions. Their analysis is based on a radial momentum balance to determine the flow force between two different flow states. With this flow-force difference, one can analyze the critical flow states and determine the vortex breakdown region. This flow state analysis is explained in more detail in section 5.9.2 and thus will be applied to the here investigated swirl tube flow.

2.2.3 Stability Criteria

In literature, there exist many stability investigations on vortex breakdown and different stability criteria are proposed, for example, by Escudier [54], Escudier and Zehnder [59], Howard and Gupta [89], Leibovich and Stewartson [125], Ludwieg [148], and Maršík et al. [153].

Escudier [54] visualized a typical flow structure development of a vortex breakdown in a laminar swirling flow in a closed cylinder with rotating endwalls as shown in Fig. 2.8. Between two critical rotation Reynolds numbers $Re_\Omega = \Omega R^2/\nu$, which increase with the dimensional cylinder height $H/(2R)$, vortex breakdown occurs. Here, H is the cylinder length, R its radius and Ω the angular velocity of the endwall. For larger cylinder heights, there can be several vortex breakdown bubbles. The obtained stability region for a single and a double breakdown is given in Fig. 2.9 according to Escudier [54]. For smaller Reynolds numbers the flow is steady, for larger unsteady (oscillatory).

Escudier and Zehnder [59] proposed a simple criterion for the occurrence of vortex breakdown at a fixed location based on the tube Reynolds number: $Re_B \sim \Omega^{-3}R^{-1}$, where $\Omega = D\,\Gamma/\overline{U}_z$ is the circulation number and R the ratio of the radial velocity to the tangential velocity in the inflow region [147]. The correlation is valid over a wide range of Reynolds numbers $(5 \times 10^2 - 10^5)$, but deviates for high circulation numbers are shown in the diagram in the original paper [59]. It should be mentioned that the correlation is limited to small values of the parameter R due to the experimental arrangement.

Escudier and Keller [57] analyzed the influence of outlet contractions on the vortex breakdown in swirling flows according to the critical state theory by Benjamin [12]. In this theory, the vortex breakdown is a transition zone from a supercritical to a subcritical flow state. In a subcritical flow, the geometry and conditions downstream affect the upstream flow and the vortex breakdown region. Escudier and Keller [57] showed that a strong contraction of 55% of the diameter has no influence on supercritical flows, but has a significant influence on subcritical flows with vortex breakdown. In the case of no contraction, the backflow is observed along the entire tube axis, while for a strong contraction
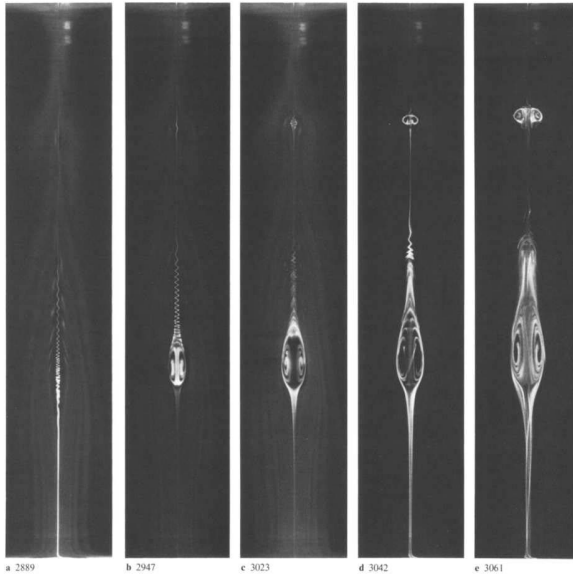
Figure 2.8: Visualization of vortex structure in a cylinder with increasing rotation Reynolds number Re_Ω (according to [54])
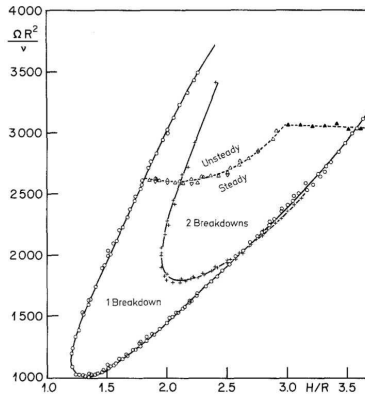
Figure 2.9: Stability boundaries for single and double breakdowns, and boundary between unsteady and steady flow (according to [54])

the vortex core becomes strongly jet like [57].

In section 5.9.2, four stability criteria by Howard and Gupta [89], Leibovich and Stewartson [125], Ludwieg [148], and Maršík et al. [153] will be introduced and used to analyze the present swirl tube flow. The studies by Howard and Gupta [89], Leibovich and Stewartson [125], and Ludwieg [148] are more general forms of Rayleigh's stability criterion. These stability criteria are against axisymmetric disturbances of flows, against spiral disturbances of inviscid swirling flows or for an unbounded columnar vortex embedded in an inviscid flow, respectively. Maršík et al. [153] investigated swirling annular flow. Their stability approach follows from the thermodynamic stability condition based on the second law of thermodynamics and considers the attenuation of the kinetic energy of disturbances. All stability criteria will be described in detail in section 5.9.2.

Table 2.4: Literature on vortex breakdown (VB) and stability in swirl tubes

author	year	investigation
Squire [205]	1960	theoretical analysis of VB
Harvey [81]	1962	visualization of VB
Benjamin [12]	1962	theory of VB
Ludwieg [148]	1962	stability criterion for flows with helical streamlines
Howard and Gupta [89]	1962	stability criterion for swirling flows
Chanaud [31]	1965	oscillatory motion in swirling flows
Benjamin [13]	1965	significance of VB
Hall [78]	1966	review on vortex cores
Hall [79]	1967	theory of VB
Benjamin [14]	1967	theory of VB
Cassidy and Falvey [30]	1970	unsteady flow after VB
Sarpkaya [184]	1971	visualization of various types of VB in a diverging cylindrical tube
Sarpkaya [185]	1971	VB in swirling conical flows
Mager [149]	1971	analytical model for VB prediction
Hall [80]	1972	VB review
Sarpkaya [186]	1974	effect of adverse pressure gradient on prediction of VB location
Faler and Leibovich [60]	1977	states of VB
Leibovich [123]	1978	VB review
Garg and Leibovich [67]	1979	spectral characteristics of VB

Literature on VB and stability in swirl tubes - continued

author	year	investigation
Escudier et al. [55]	1982	dynamics of confined vortices
Escudier and Zehnder [59]	1982	criterion for VB
Escudier [53]	1983	VB without endwall
Escudier and Keller [56]	1983	VB prediction
Leibovich and Stewartson [125]	1983	instability condition of columnar vortices
Leibovich [124]	1984	vortex stability survey
Escudier [54]	1984	flow visualization in a cylinder with rotating endwall
Escudier and Keller [57]	1985	VB with exit contraction
Keller et al. [102]	1985	VB prediction
Spall et al. [203]	1987	criterion for VB
Escudier [52]	1988	VB overview
Lopez [143]	1990	numerical axisymmetric VB
Brown and Lopez [23]	1990	physical mechanism of axisymmetric VB [143]
Neitzel and Watson [162]	1991	numerical study of VB
Lopez and Perry [145]	1992	VB with rotating endwall
Lopez [144]	1994	numerical axisymmetric VB
Althaus et al. [6]	1994	experimental and numerical study of VB transition
Jeong and Hussain [98]	1995	vortex identification (Q-criterion)
Spall and Gatski [202]	1995	numerical study of VB (k-ϵ, EARSM)
Gursul [75]	1996	non-axisymmetric forcing on swirling jet
Okulov [165]	1996	symmetry transition of VB
Spall and Ashby [201]	1999	numerical study of VB (k-ϵ, RSM), slightly diverging tube
Murakhtina and Okulov [161]	2000	topology and symmetry changes of vorticity field
Lucca-Negro and O'Doherty [147]	2001	VB review (numerical and experimental)
Mitchell and Délery [157]	2001	review on VB control
Escudier et al. [58]	2006	influence of outlet geometry on swirling flow

Literature on VB and stability in swirl tubes - continued

author	year	investigation
Maršík et al. [152]	2010	thermodynamic stability condition of swirl tube flow
Maršík et al. [153]	2010	thermodynamic stability condition of swirling annular flow
Foroutan and Yavuzkurt [62]	2014	numerical study of swirling flow (PANS)
Kobiela [113]	2014	analytical VB estimation

2.3 Ranque-Hilsch Effect

In 1933, Ranque [177] first discovered the phenomenon of temperature separation in a swirling vortex flow. Later, Hilsch [87] extensively studied the geometrical parameters and the performance optimization of such a vortex tube. Since then, the device is called Ranque-Hilsch vortex tube (RHVT). A vortex tube consists of a hollow cylinder, in which a compressed gas is tangentially induced and separated in a low and high total temperature flow region as schematically shown in Fig. 2.10. On one side the cold gas in the center exits through a central nozzle, whereas on the other side the hot gas flows through a ring orifice. One would expect that the colder and therefore specifically heavier fluid would be on the outside of the tube and the hot fluid in the center due to the centrifugal force. This somehow surprising temperature or energy separation is referred to as the Ranque-Hilsch effect. Its temperature effect is controversially discussed in literature and is therefore still subject of research. A literature overview on the studies of RHVTs is listed in Table 2.5. Detailed reviews on the Ranque-Hilsch effect can be found in Eiamsa-ard and Promvonge [46], Gutsol [76], Thakare et al. [213], Xue et al. [224], and Yilmaz et al. [229].

Different studies experimentally investigated the exit temperatures in vortex tubes depending on the tube geometry, inlet conditions and mass flow distribution between cold and hot exit [41, 72, 169, 192]. For example, for an inflow pressure of 7 bar, a total temperature separation of 80 K is achievable. The largest temperature differences can be achieved, if the gas inlet is close to the cold exit. With a higher inflow pressure and thus mass flow and swirl strength, the temperature at the cold exit can be further reduced, whereas the hot gas temperature increases. An overview of important design criteria for vortex tubes are summarized by Behera et al. [10] and Yilmaz et al. [229].
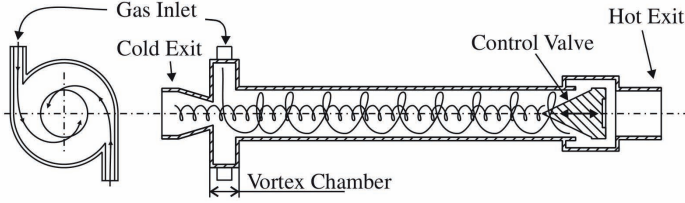
Figure 2.10: Schematic design and flow in a Ranque-Hilsch vortex tube (according to [130])

In literature, several explanations of the energy separation phenomenon can be found, for example, by Deissler and Perlmutter [38], Erdélyi [51], Gutsol and Bakken [77], Knoernschild [112], Liew et al. [130], and Stephan et al. [208]. Knoernschild [112] observed that an element of compressible fluid cannot be treated like an incompressible fluid, which is transported through a pressure gradient without any interactions with the fluid through which it moves. In contrast, a compressible fluid particle interacts with its surrounding and will be compressed on moving radially outwards to a region of higher pressure or expanding on moving inwards [180]. Thus, the interaction work through mixing of the fluid results in the cooling of the inwards-moving particles and heating of those moving outwards.

Deissler and Perlmutter [38] analyzed the flow and energy separation in a turbulent compressible vortex and confirmed the explanation by Knoernschild [112]. They proposed that the most important factor affecting the total temperature separation is the turbulent shear work done on or by a fluid element. They stated that the importance of turbulence for energy separation has two reasons: first, the turbulent viscosity is several orders of magnitude higher than the molecular viscosity. Secondly, the energy separation occurs due to the expansion and contraction of the eddies as they move radially in a pressure gradient [38]. Thus, Deissler and Perlmutter [38] found out that most of the total temperature change of a fluid element as it moved towards the center is due to the shear work done on the element (positive in the outer region, negative in the core). They analytically calculated the thermal radial stratification based on a theory which has been used to explain effects in the atmosphere and obtained the turbulent heat flux as

$$-\rho c_p \overline{u'T'} = \rho c_p \Gamma_t \left(\frac{\partial T}{\partial r} - \frac{1}{\rho c_p} \frac{\partial p}{\partial r} \right) \qquad (2.10)$$

with the turbulent thermal diffusivity Γ_t. It follows that the turbulent heat flux is a function of the pressure gradient as well as of the temperature gradient. For the case of no radial heat transfer and assuming isentropic expansion (or contraction of eddies), the temperature distribution should be isentropic rather than isothermal [38]. Thus, the relation between pressure and temperature yields

$$T \propto p^{\frac{\kappa-1}{\kappa}}, \text{ or } \frac{\partial T}{\partial r} = \frac{1}{\rho c_p}\frac{\partial p}{\partial r} \tag{2.11}$$

which is consistent to Eqn. 2.10 and analogous to an adiabatic change of state over a radial pressure distribution.

Recently, Kobiela [113] proposed to model the turbulent heat flux with an additional pressure gradient term based on the gradient-transport hypothesis with a turbulent diffusivity tensor (D_{ij}):

$$-\rho c_p \overline{u_i' T'} = D_{T,ij}\frac{\partial T}{\partial x_j} + D_{p,ij}\frac{\partial p}{\partial x_j}. \tag{2.12}$$

From a comparison with the exact compressible conservation equation for the turbulent heat fluxes, Kobiela [113] used a linear approach analogous to the turbulent scalar flux model by Younis et al. [230]. With it, he described the turbulent diffusivity tensor $D_{p,ij}$ by means of the Reynolds stresses:

$$C\,\frac{k}{\epsilon}\,\overline{u_i' u_j'}\frac{\partial p}{\partial x_j} \tag{2.13}$$

where C is a constant, k the turbulence kinetic energy and ϵ the dissipation rate. This is a similar relation between the turbulent heat flux and the pressure gradient as Eqn. 2.10, but it explicitly considers the Reynolds stresses and therefore the turbulence anisotropy instead of the turbulent diffusivity. In numerical simulations, this model showed a radial static temperature distribution according to an adiabatic change of state [113].

Furthermore, Kobiela [113] analyzed the radial path of a fluid element in a vortex and considered a solid body vortex (forced vortex) and a potential vortex (free vortex). As discussed before, the static temperature is lowest in the vortex core according to an adiabatic change of state over a radial pressure distribution. For a solid body vortex ($U_\phi \sim r$), where viscous forces dominate, the increasing velocity along the radius causes an additional dynamic temperature distribution. Hence, the total temperature in the vortex core is lower than in the outer vortex. Considering a potential vortex ($U_\phi \sim 1/r$), where inertial forces dominate, the velocity distribution is highest in the vortex core. Therefore, the dynamic temperature distribution is in the opposite direction

as the static temperature distribution. This results in a constant total temperature over the radius and hence no separation is possible. Consequently, the Ranque-Hilsch effect only occurs in a solid body vortex.

This means that Kobiela [113] confirmed the explanation of the Ranque-Hilsch effect by Deissler and Perlmutter [38]. He showed analytically that the temperature separation is caused by an adiabatic change of state in a compressible fluid along a radial pressure distribution. So the heat transport is also possible against the existing temperature gradient. The effect is additionally enhanced by the difference in static and total temperature due to the velocity distribution in a solid body vortex. Both cause the observed total temperature separation in a vortex tube.

Table 2.5: Literature on the Ranque-Hilsch effect (RHE) in vortex tubes (VT)

author	year	investigation
Ranque [177]	1933	first temperature separation in VT
Hilsch [87]	1946	first detailed parameter study of temperature separation in VT
Knoernschild [112]	1948	explanation of the RHE
Elser and Hoch [48]	1951	separation of gases in VT
Deissler and Perlmutter [38]	1960	analysis of energy separation
Reynolds [180]	1961	mechanism of energy separation
Erdélyi [51]	1962	explanation of the RHE
Sibulkin [194]	1962	unsteady, viscous, circular flow
Gulyaev [72]	1965	RHE at low temperatures
Bruun [26]	1969	experimental energy separation in VT
Linderstrøm-Lang [138]	1971	3D calculations of velocity and temperature in VT
Takahama and Yokosawa [210]	1981	energy separation in divergent VT
Kurosaka [118]	1982	acoustic streaming in swirling flow
Stephan et al. [208]	1983	experimental investigation of energy separation
Stephan et al. [209]	1984	mathematical formulation of energy separation
Eckert [43]	1986	energy separation in VT
Balmer [7]	1988	RHE in liquids
Ahlborn et al. [2]	1994	temperature separation limits

Literature on the Ranque-Hilsch effect in VT - continued

author	year	investigation
Ahlborn and Groves [1]	1997	secondary flows in VT
Gutsol [76]	1997	RHE review
Gutsol and Bakken [77]	1998	explanation of RHE
Mischner and Bespalov [156]	2002	entropy production in RH-tube
Shannak [192]	2004	temperature separation in VT
Behera et al. [10]	2005	numerical study of RHVT (RNG k-ϵ)
Gao et al. [66]	2005	experimental study of RHVT
Piralishvili and Fuzeeva [169]	2005	analytical and experimental study of RHVT
Piralishvili and Fuzeeva [170]	2006	criteria for energy separation
Sohn et al. [196]	2006	experimental and numerical study of VT
Eiamsa-ard and Promvonge [44]	2006	numerical study of VT
Eiamsa-ard and Promvonge [45]	2007	numerical study of RHVT
Eiamsa-ard and Promvonge [46]	2008	review of RHVT
Dincer et al. [41]	2008	experimental study of RHVT
Behera et al. [9]	2008	numerical study of RHVT (RNG k-ϵ)
Xue and Arjomandi [223]	2008	effect of vortex angle in RHVT
Yilmaz et al. [229]	2009	review on design criteria for VT
Secchiaroli et al. [190]	2009	numerical study of RHVT (RANS and LES)
Zin et al. [231]	2010	numerical study of VT (RNG k-ϵ)
Xue et al. [224]	2010	review of temperature separation
Liew et al. [131]	2012	experimental study of RHVT
Liew et al. [130]	2012	theory of energy separation in RHVT (Maxwell's demon)
Xue et al. [225]	2013	experimental study of temperature separation
Xue et al. [226]	2014	energy analysis in VT

Literature on the Ranque-Hilsch effect in VT - continued

author	year	investigation
Kobiela [113]	2014	analytical derivation of the RHE from the conservation equations
Thakare et al. [213]	2015	review of experimental, numerical and optimization studies of VT

Experimental Methods

In this chapter, the experimental methods to investigate the flow field, the pressure loss, the temperature field and the heat transfer in swirl tubes will be explained. The velocity field is measured using Particle Image Velocimetry (PIV) and the heat transfer is investigated using a transient liquid crystal technique. Finally, the measurement uncertainty will be presented.

3.1 Experimental Apparatus

The measurements are conducted in the experimental swirl tube apparatus at the ITLR as shown in a CAD sketch in Fig. 3.1. The open loop facility is driven by a central vacuum pump not shown in the figure. The air enters a laminar flow element (1) determining the mass flow rate. After the inlet plenum (2) the air is tranquilized through a honeycomb structure and is then heated in an inhouse designed mesh heater (3) for the heat transfer experiments or seeded with tracer particles for the PIV measurements. In the swirl generator (4) the air enters through two tangential ducts into the swirl tube (5). Finally, the air exits the measuring section through an outlet tube (6) into the outlet plenum (7), which is connected to the vacuum pump.
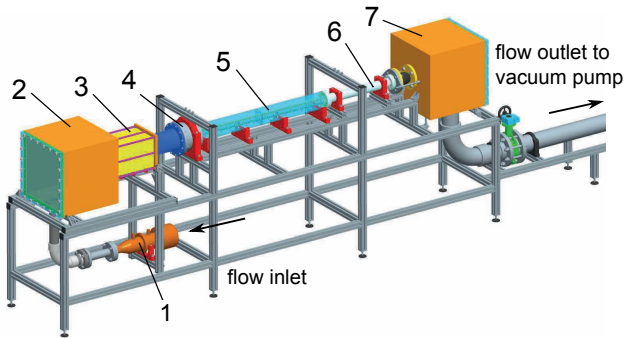
Figure 3.1: Experimental apparatus (CAD) with (1) laminar flow element, (2) inlet plenum, (3) mesh heater/seeding chamber, (4) swirl generator, (5) swirl tube, (6) outlet tube (changeable section) and (7) outlet plenum [19]

3.2 Mass Flow Measurements

The mass flow rate in the measuring section is determined using a laminar flow element (LFE 50MC2-2F) from TetraTec Instruments. It consists of a tube segment with several long thin tubes where the Reynolds number is small and the flow can be assumed as laminar. So the mass flow rate depends linearly on the pressure drop over the tubes. Furthermore, the ambient pressure, temperature and humidity are measured to calculate the viscosity. With it, the volume and mass flow rate can be determined. The manufacturer guarantees an uncertainty of the volume flow rate of less than 1% of the measured value. According to the calibration protocol the maximum deviation of the volume flow rate was below 0.33% in the measured range from 4 to 40 dm^3/s.

3.3 Particle Image Velocimetry

PIV is an optical method for flow visualization and measurement to obtain instantaneous velocity distributions. For this, light scattering particles are added to the flow. A laser light sheet illuminates the particles with two pulses within a short time period Δt. The scattered light is recorded onto two consecutive frames of a CCD camera. For evaluation the image is split into small interrogation windows. For each window the velocity vector can be calculated

from the particle shift between both frames by cross-correlation methods and the time period Δt. For stereo-PIV (2D-3C) two cameras are used to determine all three velocity components in a 2D plane.

Elsinga et al. [50] recently developed a tomographic-PIV technique, which calculates the three-dimensional velocity field in a 3D volume using four cameras (3D-3C). The working principle is shown in Fig. 3.2. As for stereo-PIV, the flow is seeded with tracer particles, but illuminated with a laser volume generated by an optical lens system. The particle distribution in the measuring section is then recorded on double frames from multiple point of views using four CCD cameras. Since the camera viewing is not perpendicular to the measuring section the Scheimpflug criterion is applied for all cameras to focus the whole object plane. The Scheimpflug condition says that the object plane, the lens plane and the image plane have to intersect in a common point [176]. Then, the particle distribution is reconstructed in the captured volume as a light intensity map with the tomography algorithm MLOS (Multiplicative Line Of Sight). Finally, the instantaneous velocity field is obtained
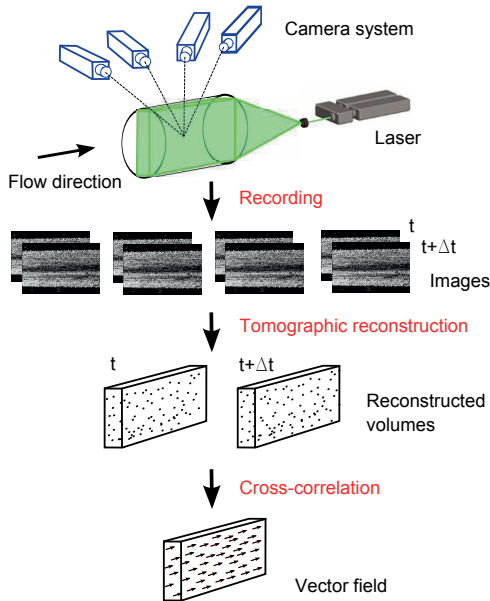
Figure 3.2: Illustration of tomographic-PIV in the swirl tube [16]

from analyzing the first and second exposure by 3D cross-correlation of the reconstructed volumes.

PIV Procedure

For the here performed measurements a PIV system from LaVision with the software DaVis 8 is used. The laser from New Wave Research is a double pulse Nd:YAG laser with a wavelength of 532 nm. The laser frequency is set to 3 or 10 Hz depending on the recording frame rate of the cameras. The time interval between the double frames is set to $\Delta t = 4 - 50 \ \mu$s depending on the measuring position and the investigated Reynolds number (flow velocity). The laser sheet or volume is adjusted by an optical lens system to 1 mm for stereo-PIV and around 8 mm for tomographic-PIV measurements. The flow is seeded with light scattering tracer particles, which have to be small enough to ensure a good tracking, but large enough for a sufficient light scattering [176]. Here, the oil di-ethyl-hexyl-sebacate (DEHS) is used with the Atomizer Aerosol Generator ATM 210 from Topas, which generates droplets with a mean diameter of around 1 μm. The camera is adjusted to achieve a particle density between 0.02 and 0.05 particles per pixel and a particle diameter around 5 pixels.

Two different CCD cameras from LaVision are available, an Imager ProX 2M (frame rate 15 Hz, resolution 1600×1200) and a Flowmaster 3S (frame rate 4 Hz, resolution 1280×1024). Both are fully synchronized with the laser. The cameras are mounted in a symmetrical arrangement on one side of the measuring section either horizontal or vertical. Due to the backscatter effect the vertical arrangement is recommended to ensure the same illumination for both cameras. For stereo-PIV the camera angle to the direction perpendicular to the tube axis is set to $\pm 30°$. For tomographic-PIV the same angle is set to $\pm 20°$ for the inner and $\pm 40°$ for the outer cameras. The magnification factor varies between 0.13, 0.12 and 0.1 for the camera angles 20°, 30° and 40°, respectively and is defined as the ratio of the distance between image plane and lens to the distance between object plane and lens [176].

The camera arrangement has to be calibrated to define the relation of the image section and the physical dimensions before starting the PIV measurements. For this purpose, each camera records a calibration plate with a defined grid of dots on two levels, which is placed in the measuring section. Then, the DaVis software identifies the dots in each plane and merges the images to an ideal grid using a mapping function with a third order polynomial. For stereo-PIV the rms fit of the polynomial should be less than 1 pixel, ideally below 0.5 and for tomographic-PIV less than 0.4 pixel for a good volume reconstruction [49]. For the here performed stereo-PIV measurements the desirable value is

usually obtained. However, for tomographic-PIV a value between 0.3 and 0.6 is achieved depending on the inner or outer camera due to the larger viewing angle and therefore stronger refraction through the tube glass wall. Therefore, an additional self-calibration process is carried out to eliminate potential errors in the vector calculation due to misalignment of the calibration plate position and the light sheet position.

One measuring range contains the tube diameter in height and two diameters in length. So at least ten positions are necessary to measure the entire tube, which is achieved with the stereo-PIV technique. For the complex tomographic-PIV technique, an area of $z/D = 4 - 10$ is captured to obtain an insight in the 3D turbulent structures in the tube. For each stereo-PIV measurement 2,000 images are recorded, processed and ensemble averaged. For the tomographic-PIV technique 1,000 images are captured and processed due to the immense post-processing time. The accuracy of the sample size is shown in the next section. The post-processing is performed in four passes. For the first two passes an interrogation window size of 64 x 64 pixels is chosen with a 50% overlap of the adjacent windows. The final pass is processed with a 32 x 32 pixels window size and a 25% overlap with a Gaussian weighting function. The window size and overlap determine the spatial resolution of the 2D vector field and the number of planes in depth for the tomographic-PIV measurements.

Sample Size Validation

The PIV measurement allows to take instantaneous velocity fields, which have to be ensemble averaged to obtain the mean flow field. It is evident that the number of samples used for averaging has a significant influence on the experimental accuracy. Uzol and Camci [215] proposed a method to evaluate the sample size accuracy. For this statistical analysis 2,000 instantaneous velocity fields are measured. Then, 100 randomly selected statistically independent averages of 5 to 1,000 ensembles are calculated at a specific point. Here, two points at characteristic positions are considered: one on the tube axis ($z/D = 16.4$ and $r/D = 0$) for the axial velocity component and one at the tube border ($z/D = 16.4$ and $r/D = 0.39$) for the circumferential velocity component. The mean velocity component is then calculated as follows:

$$U_{z,N} = \frac{1}{N} \sum_{i=1}^{N} U_{z,i} \qquad U_{\phi,N} = \frac{1}{N} \sum_{i=1}^{N} U_{\phi,i} \ , \qquad (3.1)$$

where N is the number of samples used for averaging. The results of the statistical analysis is exemplarily shown for $Re = 10,000$ in Fig. 3.3. The solid horizontal line represents the mean value of all 2,000 samples. With increasing samples the scatter around the mean value is decreasing. The maximum deviation for 1,000 samples for the axial velocity component U_z is 1.9% and for the circumferential velocity component U_ϕ 0.9%. For the higher Reynolds numbers $Re = 20,000$ and $40,000$, the statistical analysis shows similar values for the deviation. Based on this analysis a sample size of 1,000 ensembles is chosen for an adequate accuracy for the complex and time-consuming tomographic-PIV measurements.
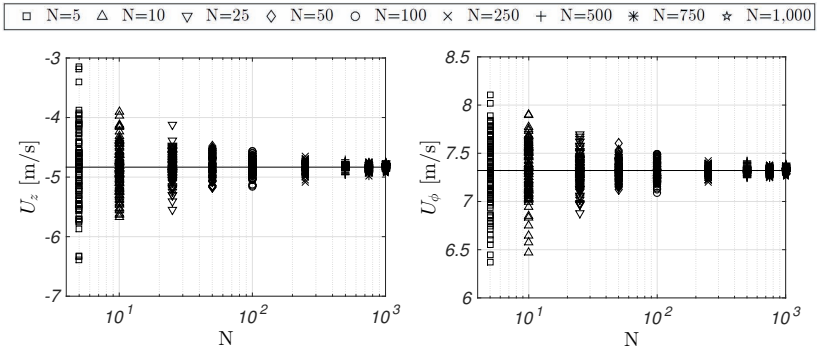
Figure 3.3: Statistical analysis of the PIV sample size [16]

3.4 Pressure Measurement

The pressure difference to the ambient (or to the reference pressure at the tube outlet) is measured along the tube wall using Scanivalve Corp. DSA pressure modules. The bore holes have a diameter of 1 mm and are placed perpendicular to the wall surface. Depending on the investigated Reynolds number (mass flow rate) the module with a range of 2,500 Pa (10 inch H_2O) or 17,200 Pa (2.5 psid) is used with an accuracy of 0.12% or 0.2% of the full scale (F.S.), respectively. The exact measurement positions are presented in the relevant chapter of the baseline single inlet swirl tube and the multiple inlet swirl tube, respectively.

3.5 Transient Liquid Crystal Technique

The heat transfer in the swirl tube is measured with the well established transient technique using thermochromic liquid crystals (TLC) see, for example, Ireland and Jones [92] and Poser et al. [173]. For this purpose, the liquid crystals are sprayed onto the inner tube surface and change their color depending on their temperature, so that they indicate the wall temperature. Before the experiment begins, the entire swirl tube model has a constant initial temperature. The measurement starts with a sudden temperature step and heated fluid is exposed to the measuring section. The TLC color play on the surface is recorded on video and the time to reach a specific color (temperature) can be determined. With the initial temperature T_0, the fluid temperature T_f and the time t to reach the calibrated TLC temperature at the wall T_w, the local heat transfer coefficient h can be calculated with the analytical solution of the 1D transient heat conduction problem. The fluid temperature T_f is approximated by a series of ideal temperature steps based on Duhamels superposition principle [100]. With that the 1D Fourier equation for a semi-infinite wall with a homogeneous initial temperature distribution and a convective boundary condition (Carslaw and Jaeger [29]) yields

$$
T_w - T_0 = \sum_{j=1}^{N} \left[1 - e^{\beta^2} \operatorname{erfc}(\beta) \right] \Delta T_{f(j,j-1)}
$$

$$
\text{with} \quad \beta = h \sqrt{\frac{t - \tau_j}{\rho_w c_w k_w}} \ .
$$

(3.2)

Here $t - \tau_j$ is the local indication time and $\rho_w c_w k_w$ are the wall material properties: density, specific heat capacity and conductivity. The swirl tube model is made of Perspex with a wall thickness of 22 mm, which very well satisfies the assumption of a semi-infinite wall due to a low thermal conductivity. More details about the underlying assumptions for the measurement technique can be found in Vogel and Weigand [216]. Additionally, the curved surface of the tube is taken into account considering an analytical expression for transient heat transfer experiments given by Buttsworth and Jones [27]. For a concave cylinder with a curvature radius R the expression yields

$$
h_{cc} = h - \frac{k}{2R} \quad \text{and} \quad \Theta_{cc} = \Theta \frac{1}{1 - \dfrac{k}{2Rh}} \ .
$$

(3.3)

The index cc means the curvature corrected variables of the heat transfer coefficient h and the dimensionless temperature $\Theta = (T_w - T_0)/(T_f - T_0)$.

The experimental TLC setup with the CMOS camera (IDS uEye UI-1460-C, resolution 2048×1536) and a cross-section of the swirl tube model is shown in Fig. 3.4. The inner surface of the tube is first sprayed with a TLC layer and then a black coating for a defined contrast. Here, narrow bandwidth TLCs (SPN/R38C1W by Hallcrest Ltd.) are used with a color bandwidth of 1 K for a high accuracy and a maximum green intensity at 38.4°C. The maximum green intensity of the TLCs is calibrated in advance on a copper plate with a flat temperature gradient to an accuracy of 0.1 K [172]. The fluid temperature is measured on the tube centerline with type K thermocouples (Omega 5SC-TT-KI-40-2M) in combination with the temperature measurement instrument TEMPpoint DT8871U-16 from DataTranslation. This device has a cold junction compensation for each thermocouple channel and a precision reference current source for each RTD channel. The accuracy for a type K thermocouple with the TEMPpoint given by the manufacturer is $\pm 0.16\%$. Due to the necessary fast response time, thermocouples with an exposed junction are used with a wire diameter of $d_w = 0.08$ mm. The response time for this thermocouple type in a flow speed of 18 m/s is around 0.02 s given by the manufacturer.
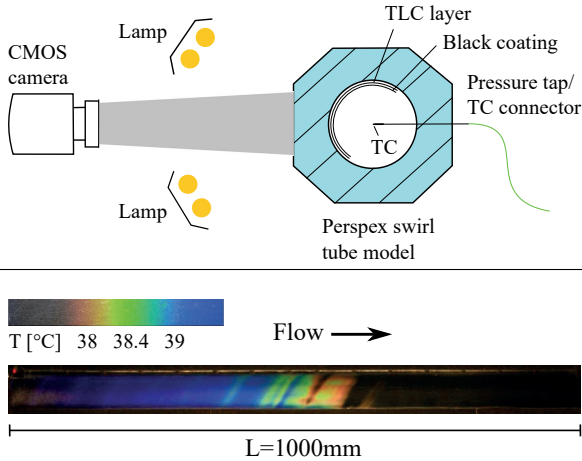
Figure 3.4: Top: TLC measurement setup with thermocouple (TC) and pressure tap position, bottom: liquid crystal color play in the swirl tube [19]

The temporal sample frequency for the TEMPpoint is 10 Hz, which is needed to capture the sudden temperature step with a high accuracy. The thermocouples are placed in the tube center through capillary tubes with an outer diameter of 1.2 mm, so that the flow is not affected much. A quarter of the swirl tube is recorded due to the camera viewing angle. A typical liquid crystal color play is depicted in Fig. 3.4, which starts from unchanged (black due to the background) to red, yellow, green and blue. For post-processing the data are averaged in circumferential direction due to rotational symmetry.

For each measurement the heater power, and with it the fluid temperature, is adjusted in such a way that the TLC color change occurs between 3 s and 90 s after the heater has been turned on. For a shorter color change, the time measurement error increases as well as the discretization error of the temperature step function. For a longer measurement the lateral heat conduction strongly influences the wall temperature indicated by the TLCs and the assumption of a semi-infinite heat conduction in the wall is not valid anymore.

Ranque-Hilsch Effect and Reference Temperature

In section 2.3 the Ranque-Hilsch effect has been extensively discussed, which causes a radial temperature separation in a sufficient strong swirling flow in tubes. This effect makes the determination of the fluid temperature rather difficult, which is necessary for the calculation of the heat transfer coefficient. The radial temperature separation increases with higher swirl numbers and Reynolds numbers, respectively. For the highest swirl number ($S = 5.3$) and Reynolds number ($Re = 40{,}000$) investigated here, the radial temperature difference near the inlet reaches 9 K. The radial temperature profiles at four axial locations for $Re = 20{,}000$ and $Re = 40{,}000$ will be shown in Fig. 5.20 in section 5.5, which highlights the difficulties to determine a local reference temperature in swirl tubes. As explained in section 2.3, Kobiela [113] described the radial temperature distribution by an adiabatic change of state in a compressible fluid along a radial pressure distribution. In the vortex core, the velocity is relatively small and the static temperature is equal to the total temperature. Especially in the outer vortex, the circumferential velocity is significantly large and causes an additional difference between the static and the total temperature. Hence, the radial temperature distribution between adiabatic wall (ad) and center (c) yields

$$T_{ad} = T_c \left(\frac{p_w}{p_c}\right)^{\frac{\kappa-1}{\kappa}} + r\frac{\mathbf{U}^2}{2c_p} \tag{3.4}$$

where κ is the isentropic exponent, r is a recovery factor, $\mathbf{U}$ is the velocity vector outside the boundary layer and c_p is the specific heat capacity [113]. Bernhard [15] recommends a recovery factor between $\sqrt{Pr} \leq r \leq \sqrt[3]{Pr}$, which results in 0.85 and 0.9 for $Pr = 0.72$. In the here performed experiments, the main part of the radial temperature separation is due to the pressure distribution. As an example, for the largest temperature difference of 9 K ($S = 5.3$, $Re = 40{,}000$), two third is due to the pressure distribution and one third due to the dynamic temperature.

In the experiments, the measurement of the adiabatic wall temperature T_{ad} according to Eqn. 3.4 is not possible, because the pressure distribution is unknown and the PIV velocity measurement would be too time-consuming for each TLC experiment. Kobiela [113] showed an easier approach to determine the adiabatic wall temperature T_{ad}. Before each measurement, the center temperature is measured with eight thermocouples on the tube axis and at each position the ratio between wall and center temperature is calculated. This ratio depends mainly on the pressure and velocity distribution and does not change with the temperature, if the Reynolds number is constant. After the TLC experiment, the adiabatic wall temperature $T_{ad,tr}$ during the transient measurement is obtained from the measured center temperature $T_{c,tr}$ during the transient measurement and the temperature ratio obtained during the initial adiabatic conditions. If one neglect the dynamic temperature $r\mathbf{U}^2/(2c_p)$, the temperature ratio yields

$$
\underbrace{\left.\frac{T_{ad}}{T_c}\right|_{\dot{q}=0}}_{\text{initial adiabatic flow}} = \underbrace{\left.\frac{T_{ad,tr}}{T_{c,tr}}\right|_{\dot{q}\neq0}}_{\text{transient heated flow}} . \tag{3.5}
$$

The adiabatic wall temperature $T_{ad,tr}$ is then used as fluid temperature for the calculation of the heat transfer coefficient. This determination of the adiabatic wall temperature according to Eqn. 3.5 contains a small error. The ratio between the static and total temperature is not constant, but its difference $r\mathbf{U}^2/(2c_p)$ is constant. It can be shown that this influence is small and the neglect is justified. The maximum deviation occurs for the highest velocities, where the dynamic temperature reaches 3 K. For an initial temperature of 295 K and a maximum fluid temperature of 320 K, the deviation in the adiabatic wall temperature results in 0.26 K. For smaller velocities and therefore all other cases, the dynamic temperature part decreases rapidly as it is proportional to the velocity square. For a medium swirl number and Reynolds number the dynamic temperature is only 0.5 K with a maximum fluid temperature of 335 K. With it, the uncertainty for the adiabatic wall temperature is rather small with 0.07 K.

3.6 Measurement Uncertainty

The measurement uncertainties are based on the root-sum-square method described by Moffat [159] and on a 95% confidence level. Details about the error propagation are well summarized by Kobiela [113]. The production tolerance of the tube diameter is ±1.0% and the uncertainty of the mass flow rate of the calibrated laminar flow element is ±0.33%. With it, the uncertainty of the Reynolds number yields ±1.07%. The Scanivalve Corp. DSA pressure measurement gives an uncertainty of the here used modules of ±0.2% (2500 Pa) or ±0.12% (17,200 Pa) of the full scale, which results in an uncertainty of 5 Pa or 20.64 Pa, respectively. The uncertainty of the dimensionless temperature Θ depending on the thermocouple measurement (±0.16 K) and the narrowband TLC temperature indication (±0.1 K) gives ±1.0%. The Perspex wall material properties density ρ, specific heat capacity c and conductivity k have an uncertainty of ±0.8%, ±0.7% and ±5.3%, respectively. All together with the temporal resolution of 0.1 s and an uncertainty of ±3.33% the overall uncertainty of the heat transfer coefficient h yields $\pm 8 - 13\%$ depending on space and time. At the tube inlet, the uncertainty is highest where the temporal uncertainty dominates due to a fast TLC color change. Further downstream, the temperature measurement is the main component of the uncertainty. The typical range and the measurement error for the relevant experimental parameters are summarized in Table 3.1.

In addition to the uncertainty of the heat transfer coefficient, the Reynolds number varies in space and time during a transient experiment and has to

Table 3.1: Experimental parameters, their typical range and the measurement error

parameter	unit	typical range	measurement error
D	[m]	0.05	±1.0%
$\dot{m}$	[kg/s]	$0.007 - 0.028$	±0.33%
Re	[−]	$10,000 - 40,000$	±1.07%
p	[Pa]	2,500 or 17,200	±0.2% or ±0.12%
Θ	[−]	$0.5 - 0.7$	±1.0%
ρ	[kg/m^3]	1,190	±0.8%
c	[J/(kg K)]	1,470	±0.7%
k	[W/(m K)]	0.19	±5.3%
t	[s]	$3 - 90$	±3.33%
h	[W/(m^2 K)]	$15 - 500$	$\pm 8 - 13\%$
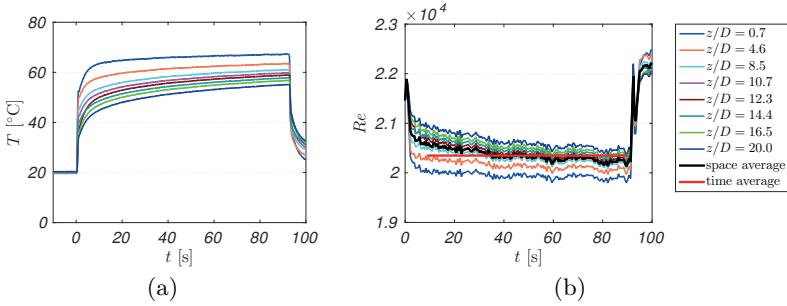
Figure 3.5: Temporal evolution of the local temperatures in the swirl tube (a) and the corresponding local and averaged Reynolds numbers (b) for a transient TLC experiment with $S = 2.95$ and $Re = 20,000$

be considered accordingly. In Fig. 3.5 (a) the temporal evolution of the local temperature in the swirl tube is shown for a transient TLC experiment with a medium swirl number $S = 2.95$ and $Re = 20,000$. The temperatures are measured with thermocouples in the tube center during the experiment and illustrate the sudden temperature step at the beginning and the decrease after the measurement time of around 90 s. One can see that the temperature near the inlet at $z/D = 0.7$ is highest, while the temperatures further downstream stay lower than the upstream ones due to the upstream wall heat flux. The temperature step at the beginning is also lower for the downstream positions. Based on the measured temperatures, the dynamic viscosity for each position is calculated using Sutherland's law [100] and with it the local Reynolds number is determined see Eqn. 1.1. Additionally, the mass flow change is considered due to the temperature depending density. In Fig. 3.5 (b) the local, the space averaged and the time averaged Reynolds numbers are shown for the same transient TLC experiment. The local Reynolds number differs up to 3% from the mean value depending on space and time. As the Nusselt number in the experiment depends approximately on $Re^{0.8}$, this results in an uncertainty in the Nusselt number of 2.4%.

Numerical Methods

In recent years, the numerical modeling and simulation have become an important analyzing tool for technical and scientific problems. Thereby, Computational Fluid Dynamics (CFD) is dealing with numerical fluid dynamics, turbulence and heat transfer. It can be used to investigate complex engineering problems, where experiments on models might be difficult or too expensive. Due to more and more powerful PCs and supercomputers numerical simulations are often faster and cheaper than experiments. Nowadays, CFD is well established as a standard tool in the design process in industry.

In this chapter the numerical methods used for the here performed simulations are presented. The first section introduces the governing equations followed by a brief introduction into the simulation of turbulent flows. Next, the turbulence modeling and the numerical methods in the open-source CFD code OpenFOAM are described. Finally, the validation of the numerical setup simulating a turbulent channel flow is presented.

4.1 Governing Equations

The 3D fluid dynamics for laminar and turbulent flows can be described by the exact conservation equations. These transport equations, derived by means of a control volume, describe the temporal change of mass, momentum (x, y, z coordinates) and energy in a fluid. In the following, the conservation equations are summarized for an unsteady, incompressible fluid with constant fluid properties. Here, the tensor notation will be used $U_i = (U, V, W)$ with the Cartesian coordinates $i = (x, y, z)$. The continuity and momentum equation reads in Einstein notation

$$\frac{\partial U_i}{\partial x_i} = 0 \tag{4.1}$$

$$\frac{\partial U_i}{\partial t} + \frac{\partial (U_i U_j)}{\partial x_j} = -\frac{1}{\rho}\frac{\partial p}{\partial x_i} + \frac{\partial}{\partial x_j}\left(\nu \frac{\partial U_i}{\partial x_j}\right) \tag{4.2}$$

in combination with the appropriate initial and boundary conditions. Here, p is the pressure and ρ is the density. These equations are also known as the Navier-Stokes equations. The momentum conservation (4.2) comprises the local variation of U_i in time, a convection term, a pressure term and a diffusion term.

According to the transport equation of a scalar Θ (e.g. temperature) the conservation of energy reads

$$\frac{\partial \Theta}{\partial t} + \frac{\partial (U_j \Theta)}{\partial x_j} = \frac{\partial}{\partial x_j}\left(\Gamma \frac{\partial \Theta}{\partial x_j}\right) + q_\Theta, \tag{4.3}$$

where Γ is the diffusivity of Θ (e.g. the thermal diffusivity for the energy equation) and q_Θ is a source or sink term of the scalar (e.g. heat source).

4.2 Simulation of Turbulent Flows

Flows can be either laminar or turbulent. Both flow conditions are characterized by completely different behavior. Laminar flows have a uniform distribution and no disturbances. Turbulent flows are irregular with an intensive mixing, this means that there exists an enhanced momentum and heat exchange. Generally, turbulence is unsteady, three-dimensional and consists of eddies. The large eddies are dominated by the geometry and mostly anisotropic. These large eddies break up and transfer their energy to successively smaller and

smaller eddies [171], which are dominated by viscous effects. The small eddies have no preferred direction and are thus locally isotropic. They dissipate the turbulence kinetic energy into internal energy of the fluid. The eddy disintegration and its energy transfer from large eddies to small eddies is called the energy cascade introduced by Richardson [181] and complemented and quantified by Kolmogorov [114]. The energy cascade as shown in Fig. 4.1 is divided in three zones: the production zone dominated by the large scales, the inertial subrange and the dissipation range containing the small dissipative scales. In the production zone large eddies are generated and obtain energy from the mean flow with the production rate $\mathcal{P}$. These eddies are characterized by the same length $\mathcal{L}$ as the macroscopic mean flow. With a characteristic velocity $\mathcal{U}$ a representative Reynolds number analogous to the mean flow yields

$$Re_{large\_eddies} = \frac{\mathcal{U}\mathcal{L}}{\nu}. \tag{4.4}$$

The large eddies itself depend on the geometry, are highly anisotropic and are therefore difficult to describe in universal models. As one can see in the energy spectrum in Fig. 4.1, the large eddies contain most of the energy.

The dissipation takes place only at low Reynolds numbers where the viscous part is dominant. The dissipation effect is therefore limited to the smallest scales of turbulent eddies. The kinetic energy is dissipated into internal energy of the fluid and is described by the dissipation rate ϵ. With the length scale of the smallest eddies $\eta \ll \mathcal{L}$ and their velocity scale $u_\eta \ll \mathcal{U}$ the local Reynolds number reads

$$Re_{small\_eddies} = \frac{u_\eta \eta}{\nu} \ll Re_{large\_eddies}. \tag{4.5}$$

Under the assumption that the smallest eddies only depend on the dissipation rate ϵ and the viscosity ν, the Kolmogorov scales can be derived by using dimensional analysis as [171]:

$$\eta = \left(\frac{\nu^3}{\epsilon}\right)^{1/4} \qquad u_\eta = (\epsilon\nu)^{1/4} \qquad \tau = \left(\frac{\nu}{\epsilon}\right)^{1/2}. \tag{4.6}$$

The Reynolds number based on the Kolmogorov scale is 1, which is consistent that the kinetic energy is dissipated by the effects of viscosity at the smallest scales. The smallest eddies show an isotropic behavior due to their independence of the geometrical scales and therefore can be better described with universal models.

In the inertial subrange, there is no production or dissipation of turbulence and the energy is just transferred to smaller and smaller eddies. So the dissipa-
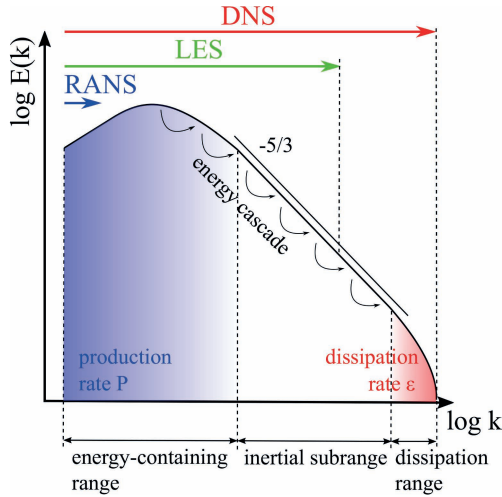
Figure 4.1: Turbulent energy spectrum and energy cascade

tion rate ϵ also represents the rate of energy transport from larger to smaller eddies. Thus, the kinetic energy of eddies depend on the dissipation rate ϵ and the energy spectrum can be associated to each wave number k, which is inversely proportional to the turbulent length scale. The energy spectrum function can then be derived from dimensional analysis of the inertial subrange [171]:

$$E(k) = C_k \epsilon^{2/3} k^{-5/3}. \tag{4.7}$$

The slope of the energy is called the Kolmogorov spectrum with the exponent $-5/3$ and is shown in Fig. 4.1 for a high Reynolds number flow and therefore a wide inertial subrange.

In 1935 Taylor [211] marked the start of the study of isotropic turbulence and defined a microscale λ_g as a measure of the diameter of the smallest eddies, which are responsible for dissipation [171]. Taylors derivation incorrectly supposes that the velocity fluctuation u' is the characteristic velocity of the dissipative eddies. Later, the Taylor microscales are determined from the Kolmogorov scales η and u_η as the characteristic scales of the smallest eddies. Thus, the microscales are given by [171]

$$\lambda_g/\mathcal{L} = \sqrt{10}\, Re_{\mathcal{L}}^{-1/2} \qquad \eta/\mathcal{L} = Re_{\mathcal{L}}^{-3/4} \qquad \lambda_g = \sqrt{10}\, \eta^{2/3}\mathcal{L}^{1/3} \tag{4.8}$$

where $\mathcal{L}$ is the characteristic length scale of the large eddies and $Re_{\mathcal{L}}$ the respective Reynolds number. At high Reynolds number, the Taylor microscale λ_g represents an intermediate size between η and $\mathcal{L}$ at which the viscosity of the fluid significantly affects the turbulent eddies. Thus, λ_g can be used to estimate the dissipation range of a flow.

Simulation Methods

There are different possibilities with different effort and accuracy describing turbulent flows. The exact solution of the Navier-Stokes equations describing the turbulence in all details can be solved using the Direct Numerical Simulation (DNS). For that, a very fine mesh is needed in the order of the Kolmogorov length scale to resolve the turbulence spectrum as shown in Fig. 4.1. For high Reynolds numbers the dissipative eddies become smaller and smaller and the DNS mesh would need an infinite fine resolution. It can be shown that the number of grid cells N raise with $Re^{11/4}$ [171], which makes it impossible to simulate most of engineering problems at high Reynolds numbers even with present supercomputers. As a result, different approaches have been developed to model the effects of turbulence instead of fully resolving them.

One alternative is the Large Eddy Simulation (LES) [183], where the large scale turbulence is resolved and just the small eddies are modeled. The LES filter usually cuts somewhere in the inertial subrange as shown in Fig. 4.1, so that the large eddies, which are larger than the grid size, are simulated with the exact equations. The small dissipative eddies, which are smaller than the grid size, are not resolved. These small eddies have almost isotropic properties and their effect can be modeled using a so called sub-grid scale (SGS) model. The simplest method simulating turbulent flows is solving the Reynolds-Averaged Navier-Stokes equations (RANS), which model the entire turbulence. Thereby, the equations are solved for the mean flow field and the effects of turbulent fluctuations are modeled. So the computational grid has to resolve just the large motion of the mean flow field as shown in the spectrum in Fig. 4.1 and can be chosen rather coarse. Because of this, RANS is a relatively fast and cheap simulation method, which is sufficient for most engineering problems and the standard in industry until now. Moreover, a RANS simulation is not suitable for highly anisotropic 3D flows and has problems with recirculation areas and flow reattachment due to its simplification of the turbulence and time-averaged solution of the flow variables.

A recent method is the coupling of LES with statistical RANS models to drastically reduce computational cost for making LES affordable in a wide range
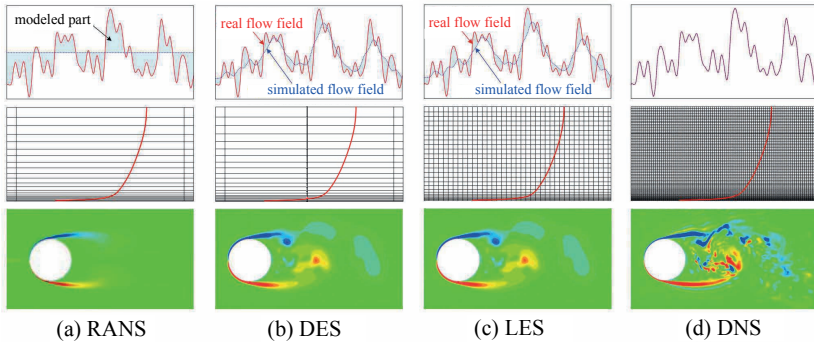
Figure 4.2: Comparison of simulation methods (adapted from [63] and [199])

of complex industrial applications [64]. This hybrid RANS-LES approach described by Spalart et al. [199] is called Detached Eddy Simulation (DES) and solves the near wall region with the RANS equations, whereas the free stream region is simulated via LES. So the wall does not need such a fine resolution as in a full LES and nevertheless the simulation provides more reasonable results especially in complex 3D problems than RANS.

Figure 4.2 shows an overview of the presented approaches simulating turbulent flows. On the top, the real flow field is shown in red, the resolved flow field simulated with LES and the averaged and modeled flow variable with RANS. In the middle a typical resolution of the computational mesh of the boundary layer is depicted. On the bottom a typical result for a turbulent flow (vorticity) around a cylinder is illustrated highlighting the achievable resolution of turbulence for each simulation method.

Characteristics of Swirl Tube Flow

The flow in a swirl tube is characterized by a recirculation zone on the tube axis due to the large swirl number investigated here. As a result of the geometry, the simulation is dealing with strong curvatures and a complex 3D flow field. This anisotropic turbulence of swirling flows cannot be reproduced satisfactorily by RANS simulations [217]. Therefore, the here presented simulations are performed using DES as a compromise of computational time and accuracy.

4.3 Turbulence Modeling

In this section, the aforementioned approaches to model the effect of turbulence are presented in detail. First, the RANS concept is introduced followed by the LES method. Finally, the here used hybrid DES method is described extensively and the near wall treatment is explained.

4.3.1 Reynolds-Averaged Navier-Stokes Equations

In most cases, engineers are more interested in the mean flow field instead of instantaneous snapshots of the flow. The Reynolds-averaged approach time-averages all of the unsteadiness, which is regarded as part of the turbulence. So the RANS equations are based on the Reynolds decomposition of the flow variables (U, p, T), e.g. the velocity is decomposed into its time-averaged value $\langle U_i \rangle$ and the turbulent fluctuation u_i about that value

$$U_i = \langle U_i \rangle + u_i. \tag{4.9}$$

The so decomposed and averaged Navier-Stokes equations yield equations which describe the mean motion of the flow:

$$\frac{\partial \langle U_i \rangle}{\partial x_i} = 0 \tag{4.10}$$

$$\frac{\partial \langle U_i \rangle}{\partial t} + \frac{\partial (\langle U_i \rangle \langle U_j \rangle)}{\partial x_j} = -\frac{1}{\rho} \frac{\partial \langle p \rangle}{\partial x_i} + \frac{\partial}{\partial x_j} \left(\nu \frac{\partial \langle U_i \rangle}{\partial x_j} - \langle u_i u_j \rangle \right) . \tag{4.11}$$

The Reynolds decomposition of the non-linear convection term $\langle U_i U_j \rangle$ becomes $\langle U_i \rangle \langle U_j \rangle + \langle u_i u_j \rangle$, where the last term is unknown. This is the closure problem of turbulence as the fluctuations cannot be represented by the mean quantities. This term is known as the Reynolds stress tensor $-\rho \langle u_i u_j \rangle$ due to its effect on the mean flow like a stress term.

The energy equation is decomposed and averaged in the same way and yields

$$\frac{\partial \langle \Theta \rangle}{\partial t} + \frac{\partial (\langle U_j \rangle \langle \Theta \rangle)}{\partial x_j} = \frac{\partial}{\partial x_j} \left(\Gamma \frac{\partial \langle \Theta \rangle}{\partial x_j} - \langle u_j \theta \rangle \right), \tag{4.12}$$

with the unknown turbulent scalar flux $-\rho c_p \langle u_j \theta \rangle$, which has to be modeled as well. As the conservation equations are not closed because they contain more unknowns than equations, it requires approximations to describe the Reynolds stresses and the turbulent scalar fluxes in terms of the mean quantities. For these terms, higher order correlations can be derived, but they

still contain unknown correlations of higher order which require additional approximations. So it is impossible to close the equation system and therefore turbulence models are needed to approximate the Reynolds stresses and scalar fluxes.

Simple Turbulence Models

In the following, simple turbulence models are introduced to close the conservation equations. The first idea to model turbulence is proposed by Boussinesq in 1877 [21], in which the effect of turbulence can be represented by an increased viscosity [61]. So the eddy-viscosity model based on the Boussinesq hypothesis describes the Reynolds stresses as follows:

$$\langle u_i u_j \rangle = 2\nu_t S_{ij} - \frac{2}{3}\delta_{ij}k \tag{4.13}$$

with the turbulent viscosity ν_t, the turbulence kinetic energy $k = 1/2\langle u_i u_j \rangle$ and the Kronecker delta δ_{ij}. The strain rate tensor is defined as

$$S_{ij} = \frac{1}{2}\left(\frac{\partial \langle U_i \rangle}{\partial x_j} + \frac{\partial \langle U_j \rangle}{\partial x_i}\right). \tag{4.14}$$

Equation 4.13 represents the definition of the turbulent viscosity ν_t as the ratio of the Reynolds stresses to the mean rate of strain. It should be noted that the turbulent viscosity varies in space and time and depends on the local turbulence. So it is not a fluid property in contrast to the molecular viscosity ν.

For the turbulent scalar fluxes the same analogy can be used to relate the fluctuations to the gradient of the transport quantity. Then, the gradient diffusion hypothesis for a scalar reads:

$$\langle u_j \theta \rangle = \Gamma_t \frac{\partial \langle \Theta \rangle}{\partial x_j}, \tag{4.15}$$

with the turbulent diffusivity Γ_t.

Considering the Boussinesq hypothesis the RANS momentum and energy equations yield

$$\frac{\partial \langle U_i \rangle}{\partial t} + \frac{\partial(\langle U_i \rangle \langle U_j \rangle)}{\partial x_j} = -\frac{1}{\rho}\frac{\partial \langle p \rangle}{\partial x_i} + \frac{\partial}{\partial x_j}\left(\nu_{eff}^{RANS}\frac{\partial \langle U_i \rangle}{\partial x_j}\right) \tag{4.16}$$

$$\frac{\partial \langle \Theta \rangle}{\partial t} + \frac{\partial (\langle U_j \rangle \langle \Theta \rangle)}{\partial x_j} = \frac{\partial}{\partial x_j} \left(\Gamma_{eff}^{RANS} \frac{\partial \langle \Theta \rangle}{\partial x_j} \right) \ . \tag{4.17}$$

Here, the effective viscosity is $\nu_{eff}^{RANS}(x,t) = \nu + \nu_t(x,t)$ and the effective thermal diffusivity $\Gamma_{eff}^{RANS}(x,t) = \Gamma + \Gamma_t(x,t)$.

The idea of eddy viscosity turbulence models is to determine ν_t. Dimensional analysis shows that the eddy viscosity can be described by two parameters: a velocity scale q (e.g. the turbulence kinetic energy k) and a length scale l. This yields the following expression for ν_t with a dimensionless constant c_μ:

$$\nu_t = c_\mu \ q \ l. \tag{4.18}$$

There are different options with different complexity determining a characteristic velocity, e.g. with an algebraic expression or with a transport equation for itself. In general, the number of equations is used to characterize the turbulence models. The simplest ones are the zero-equation models with an algebraic expression for the turbulent viscosity (e.g. Prandtl's mixing length model [164]). More complex models have one or two-equations for either the characteristic velocity or length scale. The most famous and widely-used two-equation models are the k-ϵ and k-ω model and a combination of both, the SST turbulence model. Here, one equation for the turbulence kinetic energy k as the velocity scale is solved and either the dissipation rate ϵ or the specific dissipation rate ω is used to estimate the length scale. For all these models the Reynolds stresses depend linearly from the velocity gradients, which is not valid for highly three-dimensional flows. More complex turbulence models are the Reynolds stress models (RSM), which are not based on the Boussinesq eddy-viscosity hypothesis. These higher order models solve a transport equation for each Reynolds stress and hence have the advantage to account for anisotropic flow behavior. However, with an additional length scale seven partial differential equations have to be solved in addition to the equations for the mean flow, which makes the equation system stiffer and convergence difficult to achieve.

4.3.2 Large Eddy Simulation

One alternative dealing with turbulent flows is the Large Eddy Simulation (LES), where the large scale turbulence is resolved and just the small eddies are modeled. Here the separation of turbulence scales is the basis of the filtered equations, which were formulated by Smagorinsky in 1963 [195]. According to the theory of Kolmogorov, the small scales are uniform and universal and can

be approximated by a sub-grid scale (SGS) model. The large scales containing most of the energy are simulated, which are most important for the transport of the conserved properties.

The filtered equations are structural similar to the RANS equations, but instead of the Reynolds decomposition a low pass frequency filter is used to separate the large and small scales of the velocity field, for example, as follows:

$$U = \overline{U} + u', \tag{4.19}$$

where $\overline{U}$ represents the resolved scales and u' the modeled sub-grid scales. Important difference to the Reynolds decomposition is that the filtered residual is not zero: $\overline{u'} \neq 0$. The general filtering operation (introduced by Leonard in 1974 [126]) is obtained mathematically in physical space as the convolution product [171]:

$$\overline{U}(x,t) = \int G(r,x)U(x-r,t)\mathrm{d}r \ . \tag{4.20}$$

Here G is a random filter, for example, a box (or top-hat) or a Gaussian filter. The simplest filter is the box filter, where $\overline{U}(x)$ is the average of $U(x')$ in the interval $x - 1/2\Delta < x' < x + 1/2\Delta$, and associated with a length scale Δ, which is proportional to the wavelength of the smallest scales. In practice, the flow field is not filtered explicitly and for the here performed simulations the implicit box filter is used. So the filtering process is due to the inability of the grid to resolve all scales of turbulence. The mathematical description is

$$G(x-r) = \begin{cases} \frac{1}{\Delta} & \text{if } |x - r| \leq \frac{\Delta}{2} \\ 0 & \text{otherwise} \end{cases} \tag{4.21}$$

with the grid size Δ.

Filtered Conservation Equations

The filtered Navier-Stokes equations describe the filtered velocity field $\overline{U}$. For a spatially uniform filter, the continuity equation is

$$\frac{\partial \overline{U}_i}{\partial x_i} = 0. \tag{4.22}$$

Since the differentiation and filtering operator are commutative, the sub-grid scale field u' is divergence-free as well. The filtered momentum equation yields

$$\frac{\partial \overline{U}_i}{\partial t} + \frac{\partial \overline{U_i U_j}}{\partial x_j} = -\frac{1}{\rho}\frac{\partial \overline{p}}{\partial x_i} + \frac{\partial}{\partial x_j}\left(\nu\frac{\partial \overline{U}_i}{\partial x_j}\right) \tag{4.23}$$

with the filtered pressure field $\overline{p}$. This equation differs from the Navier-Stokes equation due to the non-linear convection term, because the filtered product differs $\overline{U_i U_j} \neq \overline{U}_i \overline{U}_j$. The difference is the residual stress tensor

$$\tau_{ij}^R = \overline{U_i U_j} - \overline{U}_i \overline{U}_j \tag{4.24}$$

which is analogous to the Reynolds stress tensor [171]. With this residual stress tensor the filtered momentum equation yields

$$\frac{\partial \overline{U}_i}{\partial t} + \frac{\partial \overline{\overline{U}_i \overline{U}_j}}{\partial x_j} = -\frac{1}{\rho}\frac{\partial \overline{p}}{\partial x_i} + \frac{\partial}{\partial x_j}\left(\nu\frac{\partial \overline{U}_i}{\partial x_j}\right) - \frac{\partial \tau_{ij}^R}{\partial x_i} \tag{4.25}$$

which is structural similar to the one obtained for the RANS equations and like them, the filtered equations for $\overline{U}$ are unclosed as well. The residual shear stress tensor can be again expressed based on the Boussinesq hypothesis with a sub-grid scale eddy viscosity ν_{SGS}:

$$\tau_{ij}^R = -\nu_{SGS}2\overline{S}_{ij}, \tag{4.26}$$

with the strain rate tensor for the filtered velocity

$$\overline{S}_{ij} = \frac{1}{2}\left(\frac{\partial \overline{U}_i}{\partial x_j} + \frac{\partial \overline{U}_j}{\partial x_i}\right). \tag{4.27}$$

Then, the final form of the filtered momentum equation reads

$$\frac{\partial \overline{U}_i}{\partial t} + \frac{\partial \overline{U_i U_j}}{\partial x_j} = -\frac{1}{\rho}\frac{\partial \overline{p}}{\partial x_i} + \frac{\partial}{\partial x_j}\left(\nu_{eff}^{LES}\frac{\partial \overline{U}_i}{\partial x_j}\right) \tag{4.28}$$

where the effective viscosity is $\nu_{eff}^{LES}(x,t) = \nu + \nu_{SGS}(x,t)$. The derivation is structural similar to the RANS formulation.

The scalar transport is filtered in the same way and split into a resolved part and a sub-grid scale:

$$\Theta = \overline{\Theta} + \theta'. \tag{4.29}$$

With the filtered scalar the energy equation using the gradient diffusion hypothesis reads

$$\frac{\partial \overline{\Theta}}{\partial t} + \frac{\partial (\overline{U_j \Theta})}{\partial x_j} = \frac{\partial}{\partial x_j} \left(\Gamma_{eff}^{LES} \frac{\partial \overline{\Theta}}{\partial x_j} \right) \tag{4.30}$$

with the effective diffusivity $\Gamma_{eff}^{LES}(x,t) = \Gamma + \Gamma_{SGS}(x,t)$.

The Boussinesq approximation is a suitable and simple closure for the averaged and filtered equations. The fact that both equations have the same form makes the implementation of a hybrid RANS/LES method easier. So a single turbulence model can be used treating both formulations, which will be introduced in the next section 4.3.3.

The Smagorinsky Model

In the following, the Smagorinsky model as one of the simplest and most used algebraic sub-grid scale models is introduced. The model is based on the Boussinesq hypothesis and provides an expression for the sub-grid scale eddy viscosity, which is needed in Eqn. 4.26. From dimensional analysis the viscosity ν_{SGS} is the product of a length scale l and a velocity scale q analogous to the RANS mixing length model (Eqn. 4.18):

$$\nu_{SGS} = l \, q. \tag{4.31}$$

The length scale l is taken to be proportional to the filter width Δ through the Smagorinsky constant C_S. It should be mentioned that for smaller filter width or grid size ($\Delta \to 0$) the SGS shear stress tensor goes to zero and a LES merges into a DNS. The velocity scale is expressed through $q = l|\overline{S}|$ with the filtered rate of strain $|\overline{S}| = \sqrt{2\overline{S}_{ij}\overline{S}_{ij}}$ [63]. As a result, the sub-grid scale eddy viscosity yields

$$\nu_{SGS} = (C_s \Delta)^2 |\overline{S}| \tag{4.32}$$

and the SGS shear stress tensor becomes

$$\tau_{ij}^R = -2(C_S \Delta)^2 |\overline{S}|\overline{S}_{ij}. \tag{4.33}$$

The Smagorinsky constant C_S is not a constant, but depends on the specific flow problem and lies between 0.065 and 0.24 in general [63].

4.3.3 Detached Eddy Simulation

The DES is a hybrid RANS-LES method, where the near wall is solved with RANS equations and the free stream region away from the wall is simulated via LES. The main advantage of coupling both techniques is a drastic reduction of the computational costs compared to a full LES and that it provides more reasonable results than RANS especially for complex 3D flow problems. As already seen, the RANS and LES conservation equations show a structural similarity, which is used to model the turbulence with the eddy viscosity concept. Spalart and Allmaras [198] proposed the following expression for the turbulent viscosity:

$$\nu_t = \tilde{\nu} f_{v1} \quad \text{with} \quad f_{v1} = \frac{\chi^3}{\chi^3 + c_{v1}^3} \quad \text{and} \quad \chi = \frac{\tilde{\nu}}{\nu}. \tag{4.34}$$

The function f_{v1} is constructed in such a way that the modified eddy viscosity $\tilde{\nu}$ maintains its log-layer behavior all the way to the wall. The parameter χ is the ratio of $\tilde{\nu}$ to the molecular viscosity ν. The modified eddy viscosity $\tilde{\nu}$ is described by the transport equation

$$\frac{D\tilde{\nu}}{Dt} = c_{b1}\tilde{S}\tilde{\nu} + \frac{1}{\sigma}\left[\frac{\partial}{\partial x_j}\left((\nu + \tilde{\nu})\frac{\partial\tilde{\nu}}{\partial x_j}\right) + c_{b2}\left(\frac{\partial\tilde{\nu}}{\partial x_j}\right)^2\right] - c_{w1}f_w\left(\frac{\tilde{\nu}}{d}\right)^2. \tag{4.35}$$

The left side is the substantial derivative of the eddy viscosity. The first term on the right side is the production term, the second term is the diffusion term and the last term is the destruction term for the modified eddy viscosity $\tilde{\nu}$. In the production term, $\tilde{S}$ is given by

$$\tilde{S} = S + \frac{\tilde{\nu}}{\kappa^2 d^2} f_{v2} \quad \text{with} \quad f_{v2} = 1 - \frac{\chi}{1 + \chi f_{v1}}. \tag{4.36}$$

The function f_{v2} is also constructed like f_{v1}, so that $\tilde{S}$ preserves its behavior all the way to the wall.
The function f_w in the destruction term is inspired by algebraic models, in which the mixing length plays a major role near the wall [198]:

$$f_w = g\left[\frac{1 + c_{w3}^6}{g^6 + c_{w3}^6}\right]^{1/6} \tag{4.37}$$

with the function g and the mixing length r:

$$g = r + c_{w2}(r^6 - r) \qquad r = \frac{\tilde{\nu}}{\tilde{S}\kappa^2 d^2}. \tag{4.38}$$
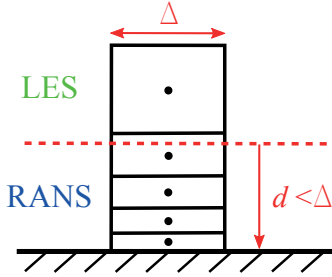
Figure 4.3: Behaviour of the DES limiter switching between RANS and LES (according to [63])

In the log layer both f_w and r are equal 1 and decrease in the outer region. The model constants are $c_{v1} = 7.1$, $c_{b1} = 0.1355$, $c_{b2} = 0.622$, $\kappa = 0.41$, $\sigma = 2/3$, $c_{w1} = c_{b1}/\kappa^2 + (1 + c_{b2})/\sigma$, $c_{w2} = 0.3$ and $c_{w3} = 2$ [198].

In the destruction term for $\tilde{\nu}$ in Eqn. 4.35, d is the distance to the nearest wall. Spalart et al. [200] replaced d by a length scale $\tilde{d} = C_{DES}\Delta$ involving the grid spacing Δ and the model constant C_{DES}. Thus, the Spalart-Allmaras model transforms into a LES one-equation sub-grid scale model. Reducing the length scale enhances the destruction term, which results in a reduced eddy viscosity. The length $\tilde{d}$ is the DES limiter and defined as follows

$$\tilde{d} = \min(d, C_{DES}\Delta). \tag{4.39}$$

If $d < \Delta$ the Spalart-Allmaras model act as a turbulence viscosity model and in regions where $d > \Delta$ as a sub-grid scale model. Spalart et al. [200] recommend the grid spacing

$$\Delta = \max(\Delta_x, \Delta_y, \Delta_z) \tag{4.40}$$

and the constant C_{DES} is calibrated to 0.65 by means of the isotropic turbulence spectrum [193]. Depending on the distance d from the wall, the DES limiter switches between RANS in the near wall region and LES in the free stream region as illustrated in Fig. 4.3.

4.3.4 Delayed Detached Eddy Simulation

The DES requires that the grid spacing in the boundary layer is much larger in the direction parallel to wall than perpendicular to the wall. As a result,

the wall-parallel grid spacing (Δ_x and Δ_z) should exceed the boundary layer thickness, so that the DES limiter ensures the RANS approach in the entire boundary layer as intended. If the grid spacing is much smaller than the boundary layer thickness, the outer boundary layer switches too early to LES and reduces the eddy viscosity and consequently the Reynolds stress. This behavior is known as Modeled Stress Depletion (MSD) since the beginning of the DES and different proposals have been made to create a more robust formulation. Menter and Kuntz [154] proposed a solution using the F_2 or F_1 functions of the SST (shear-stress transport) two-equation RANS model to identify the boundary layer and rejecting the switch to LES in this region. The Delayed Detached Eddy Simulation (DDES) proposed by Spalart et al. [199] is derived from the proposal from Menter and Kuntz, but is not limited to the SST model. The DDES is applicable to any turbulence model which involves the eddy viscosity. The authors added a function f_d to the definition of the length scale and described the DES limiter as follows:

$$\tilde{d} = d - f_d \max(0, d - C_{DES}\Delta), \tag{4.41}$$

where

$$f_d = 1 - tanh([8r_d]^3) \quad \text{and} \quad r_d = \frac{\nu_t + \nu}{\sqrt{\frac{\partial \langle U_i \rangle}{\partial x_j} \frac{\partial \langle U_i \rangle}{\partial x_j} \kappa^2 d^2}}. \tag{4.42}$$

The function f_d is designed to be 1 in the LES region, where $r_d \ll 1$, and 0 elsewhere. The function r_d distinguishes, if a point is in the boundary layer or not. It also depends on the eddy viscosity field and is time-dependent and thus independent of the grid size in contrast to the first DES limiter. The subscript d means "delayed" as it prevents the DES from a too early switch to the LES mode. The DDES is used for the here presented simulations and will be referred to as DES in the following sections.

4.3.5 Near Wall Turbulence

Turbulent wall bounded flows are greatly influenced by the wall, where the variables exhibit strong gradients. Depending on the wall distance, different turbulent transport mechanisms dominate and affect the velocity profile. The profile can be divided into three regions as shown in Fig. 4.4: the viscous sublayer, the buffer layer and the logarithmic layer. The non-dimensional

velocity U^+ and the non-dimensional wall distance y^+ in 2D are defined as follows:

$$U^+ = \frac{\langle U \rangle}{u_\tau} \qquad y^+ = \frac{u_\tau y}{\nu}. \tag{4.43}$$

Here, the coordinate y represents the distance from the wall and u_τ is the friction velocity, which depends on the wall shear stress τ_w:

$$u_\tau = \sqrt{\frac{|\tau_w|}{\rho}} \qquad \tau_w = \rho\nu \left.\frac{\partial \langle U \rangle}{\partial y}\right|_{y=0}. \tag{4.44}$$

With the friction velocity, a friction Reynolds number can be defined as

$$Re_\tau = \frac{u_\tau \delta}{\nu}, \tag{4.45}$$

where δ is a characteristic length, e.g. the channel half height for a channel flow.

In the viscous sublayer ($y^+ < 5$) the molecular viscosity is dominant and the Reynolds stresses vanish, which results in a laminar behavior and the velocity depends linearly on the wall distance

$$U^+ = y^+. \tag{4.46}$$

For larger y^+ the effects of viscosity are negligible and the turbulent transport dominates. In this logarithmic layer ($y^+ > 30$), the velocity shows a logarithmic relation to the wall distance and can be written as [171]

$$U^+ = \frac{1}{\kappa}ln\ y^+ + B \tag{4.47}$$

with the von Kármán constant $\kappa = 0.41$ and $B = 5.2$ (for a smooth wall). In the buffer layer ($5 < y^+ < 30$) the molecular and the turbulent transport have the same magnitude. The turbulent velocity profile highlighting the viscous sublayer and the logarithmic law of the wall is exemplarily shown in Fig. 4.4 by means of DNS data for a turbulent channel flow at $Re_\tau = 395$ from Kasagi [93]. The turbulent temperature profile near the wall can be described with a law of the wall analogous to the velocity profile. The friction temperature is formulated as

$$T_\tau = -\Gamma \left.\frac{\partial \langle T \rangle}{\partial y}\right|_{y=0} \frac{1}{u_\tau} \tag{4.48}$$
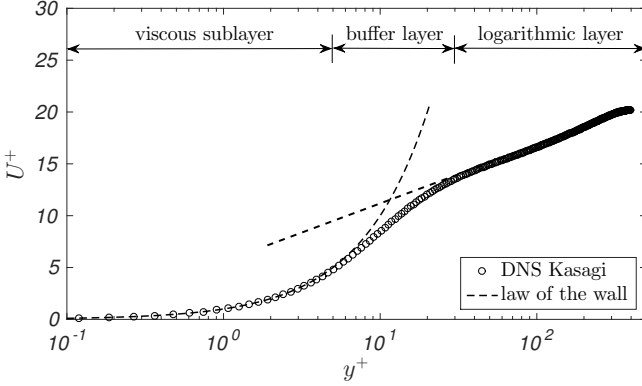
Figure 4.4: Non-dimensional velocity profile of a viscous fluid near the wall

which yields the non-dimensional temperature

$$T^+ = \frac{\langle T \rangle}{T_\tau}. \tag{4.49}$$

In the viscous sublayer the temperature profile shows a linear relation to the wall distance analogous to the velocity profile

$$T^+ = Pr \ y^+. \tag{4.50}$$

The turbulent temperature profile in the logarithmic layer depends on the Reynolds number and on the temperature boundary condition [212].

4.4 Numerical Solution Methods

The numerical solution of the coupled non-linear partial differential equation set is approximated by a system of algebraic equations. In fluid dynamics, the finite volume (FV) method is usually used as a discretization method based on the integral form of the governing equations [61]. Therefore, the computational domain is subdivided into a finite number of small control volumes (CV), and the conservation equations are applied and integrated over each CV. The computational node lies in the center and the variables on the surfaces are

interpolated between the CV-center values. The result is an algebraic equation for each CV and the overall solution consists of the discrete solutions at all discrete points. One advantage is that the FV method is conservative by construction, which means that the conservation laws hold in each individual CV as well as in the entire computational domain.

The numerical grid is a discrete representation of the geometric domain at which the variables are calculated. The solution domain is divided into a finite number of subdomains and thus specifies the boundaries of the CVs. In general, discretization errors can occur with an insufficient mesh resolution. For example, in regions where large gradients are expected (as the boundary layer) a sufficient number of computational points is needed to resolve the shape of the solution. In finite volume calculations, the accuracy strongly depends on the mesh resolution [95]. The grid quality can be measured in terms of mesh non-orthogonality, cell aspect ratio and skewness [166]. The mesh non-orthogonality describes the angle between the line connecting two cell centers and the normal of their common face, 0 would be the best. The cell aspect ratio in 2D is the ratio between the biggest and the smallest areas of the bounding box of the cell. In 3D, it is the maximum of the previous ratio or the following expression:

$$\text{cell aspect ratio} = \frac{1}{6} \frac{|A_x| + |A_y| + |A_z|}{V^{2/3}}, \tag{4.51}$$

where A_x, A_y and A_z are the areas of the cell's bounding box and V is the cell volume. An aspect ratio of 1 is best. The skewness describes the distance between the intersection of the line connecting two cell centers with their common face and the center of that face. A smaller skewness is better [166]. For the present investigation, block structured O-grids with hexahedral elements are used. The grid quality for all investigated grids is summarized in appendix A.

OpenFOAM

The numerical simulations are performed with the open-source finite volume code OpenFOAM (Open Field Operation and Manipulation) [97] in the version 2.2.x. As pressure corrector for the Navier-Stokes equations the Pressure-Implicit Split-Operator (PISO) algorithm is used. This unsteady solver involves one predictor step guessing the pressure field and two corrector steps between momentum and continuity equation while adjusting the velocity and pressure field for each time step. The pressure is corrected with the PCG (Preconditioned Conjugate Gradient) solver in combination with the GAMG

(Generalized geometric-Algebraic Multi-Grid) preconditioner [96]. The GAMG solver generates a quick solution on a coarse mesh and maps this solution onto a finer mesh as an initial guess to obtain the solution on the fine mesh faster. For the presented simulations the GAMG solver is used for the momentum, temperature and modified eddy viscosity equations.

For the time discretization a second-order backward differencing (BD) scheme is applied, which uses three time levels of the variable ϕ:

$$\phi^{n-2} = \phi^{t-\Delta t} \qquad \phi^{n-1} = \phi^{t} \qquad \phi^{n} = \phi^{t+\Delta t} \tag{4.52}$$

The time levels can be expressed with Taylor series, see Ferziger and Perić [61]. With these, the BD scheme approximates the temporal derivative with

$$\frac{\partial \phi}{\partial t} \simeq \frac{1}{\Delta t} \left(\frac{3}{2} \phi^{n} - 2\phi^{n-1} + \frac{1}{2} \phi^{n-2} \right), \tag{4.53}$$

which is a second order accurate implicit discretization method. For stability of convection dominated problems, the Courant-Friedrichs-Lewy or just Courant number has to be considered

$$CFL = \frac{u \Delta t}{\Delta x} < 1, \tag{4.54}$$

where u is the local flow velocity, Δt the iteration time step and Δx the grid size. The Courant number describes the ratio of time Δt to the characteristic convection time $\Delta x / u$, which is the time needed for a disturbance to be transported for a distance Δx (e.g. a grid cell). In OpenFOAM the time step can be adjusted automatically to set a maximum Courant number [166]. For the here presented DES the maximum Courant number is set <0.9.

The viscous and convective fluxes are approximated with a second-order accurate central differencing scheme (CD). It is based on the assumption of a linear variation of the variable ϕ between the current cell center P and the neighboring cell center N

$$\phi_f = f_x \phi_P + (1 - f_x) \phi_N \tag{4.55}$$

where the subscript f denotes the face value and the interpolation factor f_x is the ratio between the distances fN and PN. The CD scheme is second order accurate [61], but is unbounded, which means that the variable ϕ is not bounded by the neighboring cell values and may introduce non-physical oscillations. This issue of the CD scheme can be overcome only with a mesh refinement. On the other hand, bounded schemes usually introduce false diffusion to the system.

Numerical Errors

Numerical solutions of the discretized equations of flow and heat transfer problems are only approximate solutions and should not be considered exact. Numerical simulations always include three kinds of systematic errors [61]:

- Modeling errors, which are the difference between the real flow and the exact solution of the used mathematical model,

- Discretization errors, which are the difference between the exact solution of the conservation equations and the exact solution of the algebraic system of discretized equations,

- Iteration errors, which are the difference between the iterative and exact solutions of the algebraic equation system.

Modeling errors depend on the made assumptions deriving the transport equations. These errors may be introduced by simplifying the geometrical domain, by simplifying boundary conditions and/or by the choice of the turbulence model. The modeling errors can be evaluated by comparing the solution with exact analytical solutions, with accurate experimental data or with more accurate models like direct numerical simulations. For the presented simulations the numerical setup and turbulence model is validated by simulating a turbulent channel flow and compared with DNS data. Moreover, the swirl tube simulations are compared to own experimental results.

Discretization errors are introduced by the discretization approximation which decrease, if the mesh or the time step are refined. Additionally, the order of discretization scheme defines the accuracy. A typical analysis investigating the grid resolution is the determination of the grid convergence index (GCI) [182]. Here, at least three different grids (coarse, medium and fine) are constructed and the simulation results are compared in terms of interesting variables of the problem (e.g. velocity, friction, heat transfer). As the grid is refined, the spatial discretization errors should asymptotically tend to zero. The GCI is usually used for steady state problems and difficult to apply for transient simulations like LES or DES as the computational costs comparing mean values are enormous. In the present study, the baseline swirl tube case ($S = 5.3$ and $Re = 10,000$) is performed with two different fine meshes to analyze grid dependency. Furthermore, the chosen discretization schemes are second order accurate in time and space and therefore provide a good accuracy for LES and DES.

The iteration error can be controlled by the convergence of the iterative solution method and depend on the residual criterion. In the present transient simulations, a low iteration error is achieved by setting the final residual tolerance to 10^{-7} for all variables at each iteration. The used schemes and solution settings are summarized in appendix A for the performed simulations.

4.5 Turbulent Channel Flow Validation

In this section, the validation of the numerical method including the code and the setup is presented simulating a turbulent channel flow at $Re_\tau = 150$. Furthermore, a grid study is performed to analyze a sufficient and accurate mesh resolution for a DES. The results are compared to DNS data from Iida and Kasagi [91]. The flow is homogeneous in streamwise x- and spanwise z-direction and the statistics depend only on the wall normal y-direction. The walls are set with a no-slip condition and different constant temperatures as shown in Fig. 4.5. The inlet and outlet are defined with a cyclic boundary condition, which results in an infinite channel flow. The flow is driven by an imposed pressure gradient between inlet and outlet.

The size of the computational domain is $6.3h \times h \times 4.7h$ with the channel height h, which is an appropriate dimension for turbulent channel flows [37]. The wall boundary is resolved with a non-dimensional wall distance $y_1^+ = 1$ for the first cell. The cell size in the intermediate flow between the walls is estimated with the Taylor microscale λ_g in Eqn. 4.8 and used as a base size for subsequent refinements. The investigated meshes and their resolution in
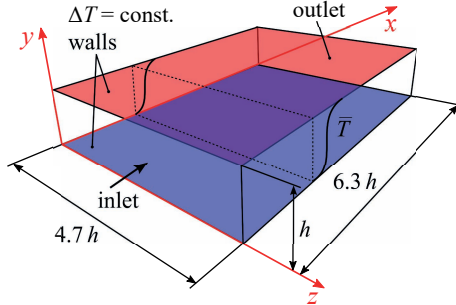
Figure 4.5: Computational domain of the channel flow

Table 4.1: Computational grids for the channel flow validation

mesh	$n_x \times n_y \times n_z$	Δx^+	Δy^+	Δz^+	cells
base	$96 \times 48 \times 101$	19.6	$\in [1,14]$	14	465,408
fine	$135 \times 60 \times 141$	14	$\in [1,10]$	10	1,142,100
refined	$96 \times 48 \times 135$	19.6	$\in [1,14]$	10.5	622,080
stretched	$67 \times 48 \times 135$	28	$\in [1,14]$	10.5	434,160
DNS	-	18.4	$\in [0.08,4.91]$	7.36	-

x-, y- and z-direction are listed in Table 4.1. According to the DES guidelines provided by Spalart et al. [199], three additional meshes to the baseline mesh with different non-dimensional distances are investigated to study the behavior of the DES formulation: (1) a fine mesh with a refinement factor of $\sqrt{2}$ in all directions, (2) a refined mesh with an increased resolution in spanwise direction only, and (3) a stretched mesh with a refinement in spanwise direction and a stretching in streamwise direction.

The results for the channel flow simulations are shown in Fig. 4.6 in terms of the non-dimensional variables: velocity U^+ (Eqn. 4.43), shear stress in streamwise and wall normal direction $-(uv)^+$, temperature T^+ (Eqn. 4.49) and temperature fluctuation T_{rms}^+. All variables are compared to DNS data from Iida and Kasagi [91]. The non-dimensional velocity and temperature show a slight overestimation for all meshes compared to the DNS, but an overall good prediction of the viscous sublayer and buffer layer can be observed. The error slightly decreases with the mesh refinement in spanwise direction. The overestimation in the channel center is typical for LES channel flows according to Fröhlich [63]. The shear stress $-(uv)^+$ is well resolved for the fine, refined and stretched mesh. The fine mesh provides the best approximation of the temperature fluctuations which are the most difficult ones to reproduce. The initial baseline mesh again shows the largest deviation starting from the buffer layer, which highlights that the mesh is inadequately resolved and higher order variables cannot be simulated sufficiently. A good approximation of the DNS data can be obtained by an independent mesh refinement, in particular by an increase of the mesh resolution in spanwise direction. The refined mesh and the stretched mesh perform sufficiently well like the fine mesh and a mesh reduction in streamwise direction proves to be a good choice as the turbulent structures are stretched by the strong convection. The stretched mesh shows overall good results and is a good compromise of number of cells and accuracy. Figure 4.7 shows the turbulent energy spectrum based on the streamwise velocity component at the channel mid-plane for all investigated meshes and the
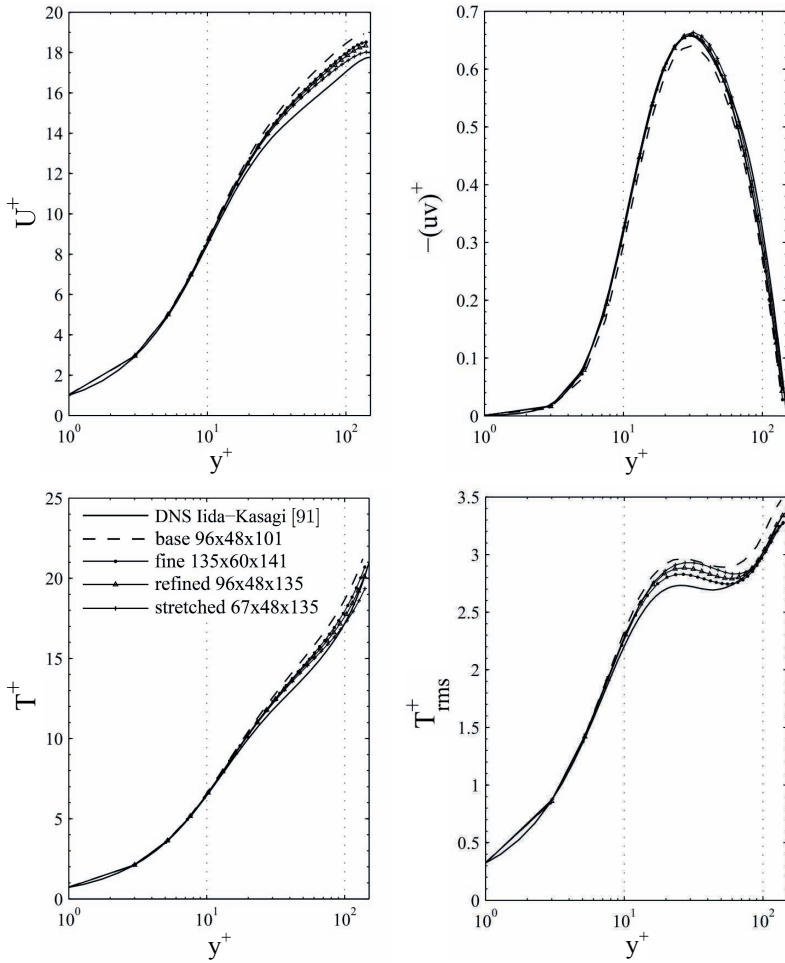
Figure 4.6: Channel flow validation results in non-dimensional form for a mesh variation. Top left: velocity, top right: shear stress in the xy-plane, bottom left: temperature, bottom right: temperature fluctuations (rms) [17]
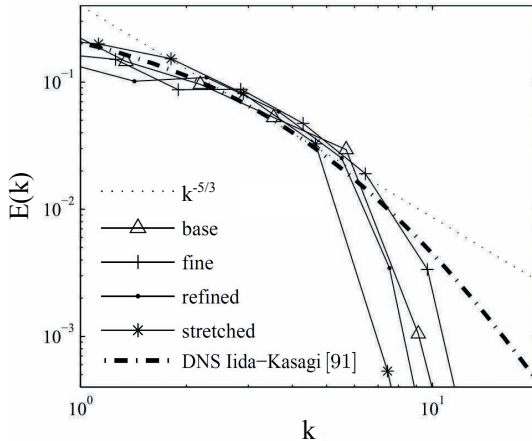
Figure 4.7: Turbulent energy spectrum in the channel flow based on the streamwise velocity component at the channel mid-plane [17]

DNS from Iida and Kasagi [91]. All simulations nicely follow the Kolomogorov spectrum with the $k^{-5/3}$ slope. The plot highlights the frequency (wavenumber) cut-off of the LES filter by the mesh resolution. As expected, the stretched mesh is poorest resolved and the energy is cut at the lowest wavenumber and thus at the largest scale. This means that all smaller scales are treated with the sub-grid scale turbulence model. The difference in spanwise resolution between the base and refined mesh has no effect on the energy cut-off as the spectrum is analyzed for the streamwise velocity component. The fine mesh is clearly best resolved.

The investigation on different meshes reveals that the solution is greatly affected by the different resolution in each direction and the mesh density in the buffer layer, which has an important influence on the DES limiter. In terms of global accuracy the stretched mesh performs best although it has the lowest number of grid cells. This confirms the fact that a DES has a non-monotonic convergence with the mesh density [199]. From the analysis it can be concluded that a streamwise grid size of $\Delta x^+ = 28$ and a wall normal size of $\Delta y_c^+ = 15$ in the center provide a reasonable mesh resolution for DES. Furthermore, the validation of a turbulent channel flow shows that the here used numerical method very well reproduces wall bounded flows [17].

Single Inlet Swirl Tube

In this chapter, the baseline single inlet swirl tube will be discussed in detail. The swirl tube is characterized by two tangential inlet jets at the upstream end of the tube. The term single inlet means that there is only one inlet position along the tube length. First, details about the experimental and numerical setup are given. Then, the results of the flow field, heat transfer and pressure loss are discussed. Finally, the thermal performance and the stability of swirl flows are analyzed and discussed.

5.1 Experimental Details

The geometry and the coordinate system of the baseline swirl tube is shown in Fig. 5.1. The swirl tube is closed on one side and the fluid solely enters via tangential rectangular inlets. The tube has an inner diameter of $D = 50$ mm and a length of $L/D = 20$. The inlets have a width of $w/D = 0.67$ and the height h can be varied with different inserts to vary the swirl number S. The here investigated swirl numbers range between 0.75 and 5.3 and the respective inlet heights are listed in Table 5.1. Furthermore, the investigated Reynolds
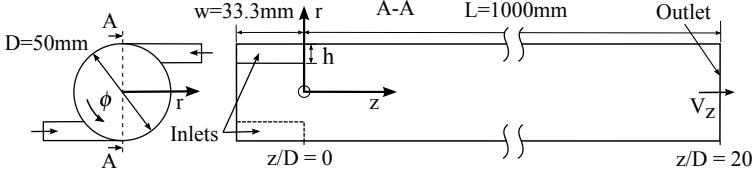
Figure 5.1: Baseline swirl tube geometry

Table 5.1: Investigated swirl numbers ($n = 2$ and $w = 0.67D$)

h/D [-]	0.1	0.13	0.17	0.2	0.28	0.32	0.37	0.44
S [-]	5.3	3.83	2.95	2.36	1.5	1.25	1.0	0.75

number range is between 10,000 and 40,000 and the corresponding bulk veloci-
ties and mass flow rates are summarized in Table. 5.2. The axial bulk velocity
will be used to show all results in a non-dimensional form.
The wall pressure is measured at ten equally distributed pressure taps in ax-
ial direction. The bore holes have a diameter of 1 mm and are placed per-
pendicular to the wall surface. The measurement positions are at $z/D =$
1.08, 3.20, 5.26, 7.32, 9.42, 11.50, 13.58, 15.64, 17.72, 19.80. In order to use
a more accurate pressure module, the relative pressure difference to the most
downstream tap at $z/D = 19.80$ is measured.
The fluid temperature in the tube center is measured with eight type K ther-
mocouples through capillary tubes with an outer diameter of 1.2 mm. The
thermocouple positions are at $z/D = 0.7, 4.6, 8.5, 10.7, 12.3, 14.4, 16.5, 20.0$.
These thermocouples are also used to measure the radial temperature distribu-
tion due to the Ranque-Hilsch effect. For this purpose, the thermocouples are
traversed in radial direction in the tube. The inflow temperature is measured

Table 5.2: Axial bulk velocity and mass flow rate for all investigated Reynolds
numbers

Reynolds number	$\overline{U}_z$ [m/s]	$\dot{m}$ [kg/s]
10,000	3.225	0.00706
20,000	6.486	0.01418
30,000	9.736	0.02122
40,000	12.990	0.02829

in the center of the tube cross-section upstream of the swirl generator. The diameter of this intermediate tube is rather large and the flow velocity is small, which means that the thermocouple measures the inflow total temperature at this position. On the outside, an additional thermocouple is taped onto the Perspex wall to monitor the wall temperature between the heat transfer measurements.

Furthermore, different outlet geometries are studied to investigate their influence on the flow field and the heat transfer in the swirl tube. The baseline swirl tube consists of a straight outlet tube as shown in the experimental apparatus in Fig. 3.1 (6). The effect of a flow redirection is investigated with a tangential and a 180° bend outlet as depicted in Fig. 5.2. The tangential outlet channel has a width of $w/D = 1.33$ and a height of $h/D = 0.2$. The round cross-section of the 180° bend has the same area than the actual swirl tube [19].
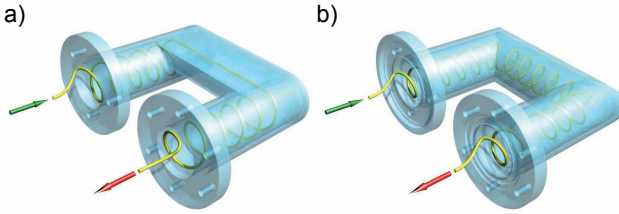
Figure 5.2: Outlet geometries. a) Tangential, b) 180° bend [19]

5.2 Computational Details

The computational domain of the swirl tube simulations is shown in Fig. 5.3. It represents the experimental geometry as close as possible. The swirl tube (2) has a diameter of $D = 50$ mm and a length of $L = 20D$. The swirl generator (1) consists of two 180° displaced inflow boundary sections (red hatched area) with the height h and the width $w = 0.67D$. In accordance with the experimental setup an additional outlet tube (3) and outlet plenum (4) are simulated to reduce the influence of the outlet boundary condition and to assure numerical stability.

The simulations for the highest swirl number $S = 5.3$ are performed at three different Reynolds numbers $Re = 10,000$, $20,000$ and $40,000$. Furthermore,
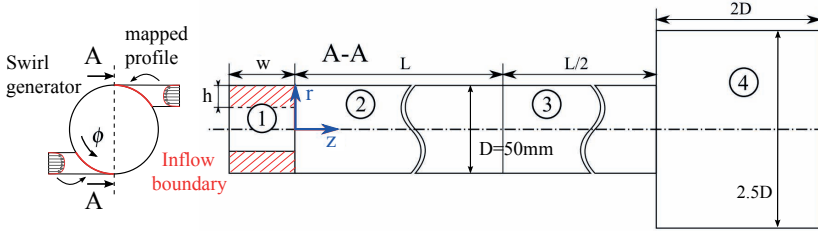
Figure 5.3: Computational domain with swirl generator (1), swirl tube (2), outlet tube (3) and outlet plenum (4)

swirl tubes with lower swirl numbers of $S = 1.0$, 0.75 and 0.5 are simulated at the lowest Reynolds number $Re = 10,000$ due to the computational time. Details about these simulations regarding the respective inflow section height and the inlet velocity for the different swirl numbers at $Re = 10,000$ are listed in Table 5.3.

The computational meshes for the three Reynolds numbers are hexahedral O-grids with a total mesh size of 9, 15 and 34 million cells, respectively. A cross-section of the swirl tube mesh and a detailed view of the wall resolution is shown in Fig. 5.4. The wall is resolved to provide a dimensionless wall distance of $y_1^+ < 1.5$ for the first cell near the wall. As a reference scale the Kolmogorov length scale is used, which can be approximated by $\eta = D\,Re^{-3/4}$ with the tube diameter D as the characteristic length [171]. The details about the meshes for the three Reynolds numbers are listed in Table 5.4 regarding number of cells, Kolmogorov length scale η, the first wall cell size and the center cell sizes in all directions. The meshes for the different swirl numbers at $Re = 10,000$ are the same according to Table 5.4, but differ from the

Table 5.3: Numerically investigated swirl numbers and inlet velocities for $Re = 10,000$

S [-]	5.3	1.0	0.75	0.5
h/D [-]	0.1	0.37	0.44	0.54
U_{in} [m/s]	19.02	5.14	4.32	3.52
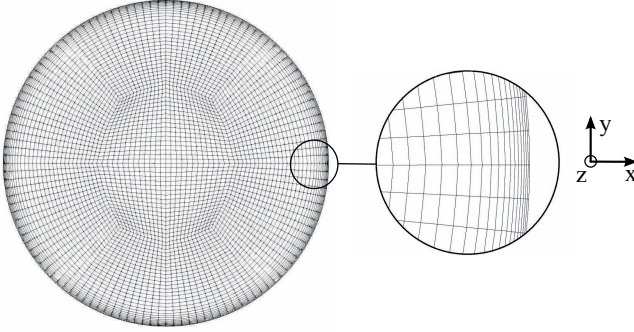
Figure 5.4: Cross-section of the hexahedral tube mesh and a detailed view of the wall resolution [17]

inflow boundary section height as summarized in Table 5.3. The time step is automatically adjusted with a Courant number limit of max. 0.9 which occurs exclusively in the inlet part. The simulations are run for $3\Delta t_{domain}$, before starting averaging over $15\Delta t_{domain}$. Here $\Delta t_{domain} = L/\overline{U}_z$ is the domain flow time.

The wall boundaries are set with a no-slip condition. A turbulent velocity profile is mapped onto the inflow boundary section as shown in Fig. 5.3. Here a uniform inlet temperature is given of $T_{in} = 333K$ and the wall temperature is defined constant at $T_{wall} = 293K$. At the outlet, a fixed pressure value is set and Neumann boundary conditions are applied for all other variables [20]. For completeness, an overview of the here used discretization schemes and the solution settings is given in appendix A together with the specific boundary conditions.

Table 5.4: Summary of number of cells, Kolmogorov length scale η and used wall and center cell sizes for the computational meshes

mesh	cells	η [m]	Δy_1 [m]	$(\Delta x,\ \Delta y,\ \Delta z)_{center}$ [m]
$Re = 10{,}000$	$9 \cdot 10^6$	$5 \cdot 10^{-5}$	$3 \cdot 10^{-5}$	$(9.4,\ 7.9,\ 11.0) \cdot 10^{-4}$
$Re = 20{,}000$	$15 \cdot 10^6$	$3 \cdot 10^{-5}$	$1.5 \cdot 10^{-5}$	$(8.3,\ 7.1,\ 9.6) \cdot 10^{-4}$
$Re = 40{,}000$	$34 \cdot 10^6$	$1.7 \cdot 10^{-5}$	$0.9 \cdot 10^{-5}$	$(5.3,\ 4.5,\ 6.8) \cdot 10^{-4}$

5.3 Flow Field

In this section, the flow field of the baseline swirl tube is discussed in detail. First, the axial and circumferential velocities and their fluctuations are presented. It follows the turbulence kinetic energy, the vorticity and the helical vortex structure in the swirl tube. Then, the influence of the tube outlet geometry on the flow field is presented. Finally, the flow field of different swirl numbers is shown investigating the axial backflow region.

5.3.1 Axial Velocity

The non-dimensional axial velocity in the baseline swirl tube ($S = 5.3$ and $Re = 10,000$) is shown in Fig. 5.5 at seven axial positions z/D comparing experimental and numerical data. Additionally, a contour plot from the numerics is presented to visualize the flow field. The flow direction is from left to right and the velocity scale is exemplarily shown on top of the first position $z/D = 2.5$. The axial velocity has its maximum velocity in the near wall region and a backflow in the tube center also known as vortex breakdown. The swirling flow is strong enough that the backflow occurs across the entire tube length. The magnitude of the backflow even increases towards the tube outlet, whereas the axial velocity in the outer region decreases slightly due to wall friction. The numerical data show a good agreement to the experimental data, only slight differences occur for the backflow region in the tube center.

The experimentally measured axial velocity for higher Reynolds numbers $Re = 20,000$ and $40,000$ are shown in the contour plots in Fig. B.3 in the appendix. The non-dimensional axial velocity slightly increases with increasing Reynolds number especially in the outer region. In the tube center the backflow region expands for higher Reynolds numbers. One can see that the backflow in the center shows some discontinuous green areas in particular for the high Reynolds number $Re = 40,000$, which is due to a low seeding density during the PIV measurements due to the large velocity and the difficulty of the tracer particles to follow the flow.

Tomographic-PIV results in the measured range from $z/D = 4 - 10$ are presented in Fig. B.1 in the appendix. The axial velocity in the outer region and the increasing backflow in the tube center show a good agreement to the stereo-PIV results.
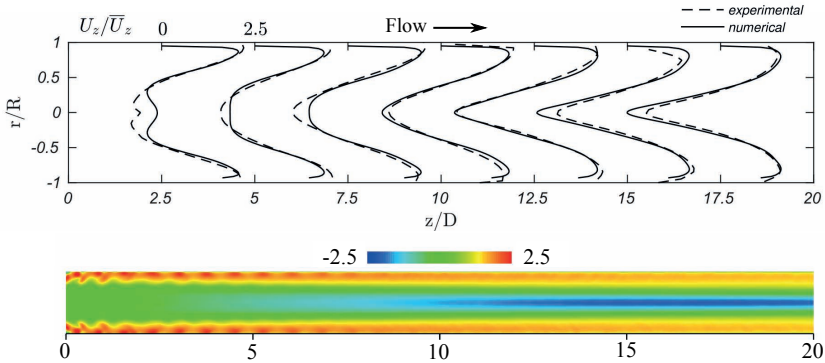
Figure 5.5: Comparison of experimental and numerical non-dimensional axial velocity and DES contour plot for $S = 5.3$ and $Re = 10,000$

5.3.2 Circumferential Velocity

Figure 5.6 shows experimental and numerical non-dimensional circumferential velocity profiles in combination with a contour plot from the numerics for the baseline swirl tube ($S = 5.3$ and $Re = 10,000$). Due to the high swirl number investigated, the circumferential velocity component is the largest velocity component and more than two times larger than the axial velocity U_z. The velocity magnitude and therefore the angular momentum decrease significantly towards the tube outlet due to viscous and turbulent dissipation. Moreover, the maximum shifts closer towards the tube center. It is evident that the flow is axisymmetric over the length of the tube. The circumferential velocity profile can be characterized by a Rankine vortex (see Fig. 2.2) with a solid body vortex ($U_\phi = \Omega r$) in the tube center, a potential vortex ($U_\phi = \Gamma/r$) in the outer region and a boundary layer near the wall according to Maršík et al. [152]. Here, Ω is the angular velocity, Γ the circulation and r the radius measured from the center of the vortex. Near the inlet at $z/D = 2.5$ the solid body vortex is dominant. Further downstream, the solid body region shrinks and the velocity magnitude decreases, but the angular velocity Ω increases with a steeper velocity gradient in the tube center. Near the tube outlet the potential vortex extends and dominates the circumferential velocity profile. Again, the experimental and numerical profiles show good agreement, only the circumferential velocity maximum is slightly overestimated by the numerical simulation in the second half of the tube.

Figure 5.6: Comparison of experimental and numerical non-dimensional circumferential velocity and DES contour plot for $S = 5.3$ and $Re = 10,000$

The experimental results for the higher Reynolds numbers $Re = 20,000$ and 40,000 are presented for completeness in Fig. B.6 in the appendix. The non-dimensional circumferential velocity slightly increases with higher Reynolds numbers as already seen for the axial velocity. Comparing the stereo-PIV and the tomographic-PIV results in Fig. B.2, a good agreement of the circumferential velocity can be seen.

5.3.3 Velocity Fluctuations

The numerically simulated axial, radial and circumferential velocity fluctuations in the tube mid-plane are shown in Fig. 5.7 at the same axial positions z/D as the velocity. All three non-dimensional fluctuations are in the same order of magnitude. In the tube center they increase towards the tube outlet especially after $z/D = 10$. This is due to the increasing axial backflow on the tube axis and the increasing angular velocity of the solid body vortex in the center. Due to rotational symmetry, two symmetric maxima appear on both sides in the outer region especially for the radial component. Near the wall the axial and circumferential velocity fluctuations show a distinct increase, which demonstrates a strong turbulent mixing and fluid exchange near the wall. These effects are more pronounced near the inlet and might be responsible for the high heat transfer in this region.
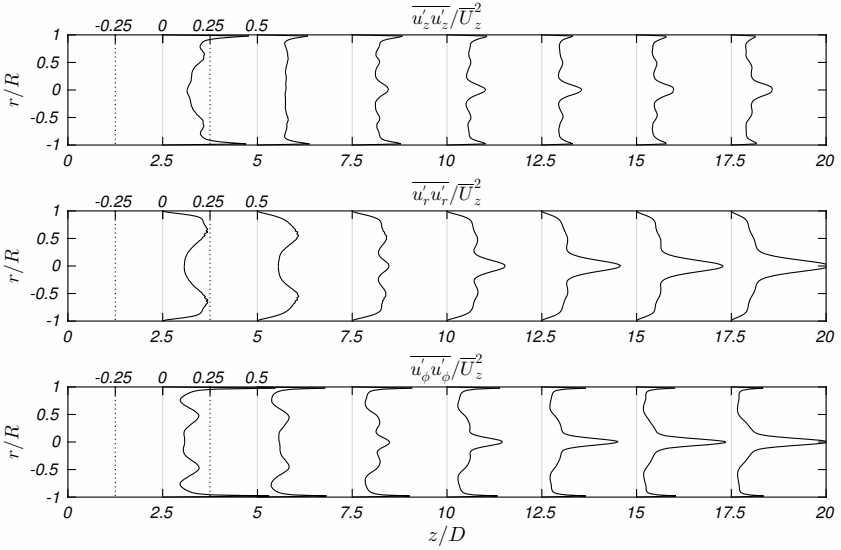
Figure 5.7: DES non-dimensional velocity fluctuations for $S = 5.3$ and $Re = 10,000$

5.3.4 Turbulence Kinetic Energy

The turbulence kinetic energy k describes the energy of the turbulent fluctuations and the production rate $\mathcal{P}$ and dissipation rate ϵ are responsible for the redistribution of the kinetic energy in turbulent flows. These quantities are defined as follows:

$$k = \frac{1}{2}\overline{u'_i u'_i} \tag{5.1}$$

$$\mathcal{P} = -\overline{u'_i u'_j}\frac{\partial \overline{U}_i}{\partial x_j} \tag{5.2}$$

$$\epsilon = \nu\,\overline{\frac{\partial u'_i}{\partial x_j}\frac{\partial u'_i}{\partial x_j}} \tag{5.3}$$

The production rate describes the production of turbulence kinetic energy from the main flow energy. The dissipation rate describes the dissipation of turbulence kinetic energy due to turbulent fluctuations into internal energy and is always positive due to its definition.

81

A comparison of the turbulence kinetic energy between the experimental PIV results and the numerical simulation is shown in Fig. 5.8 with an additional contour plot from the numerics for a better visualization. The turbulence kinetic energy shows a local maximum close to the wall, which decreases towards the tube outlet as the flow velocity decreases. In the tube center a global maximum develops within the tube length, which correlates with the increasing axial backflow. The distribution of k provides a detailed view where the turbulent structures occur in the swirl tube. Here two main regions can be detected: (1) the outer region of the tube near the tangential inlets and (2) on the tube axis mainly in the second half of the tube. In these regions the turbulent structures are responsible for a high fluid mixing.

Figure 5.9 shows the production and the dissipation rate of the turbulence kinetic energy in the swirl tube. The radial profile of the production $\mathcal{P}$ reveals that the production of turbulence kinetic energy appears mostly in the outer and near wall region, where the highest velocities occur. The profile of the dissipation ϵ is similar to the one of k with a high dissipation rate near the wall and an increasing value on the tube axis further downstream in the second half of the tube. It is evident that the highest turbulence kinetic energy dissipates the most. In summary, the turbulence kinetic energy is produced in the outer and near wall region, where the highest velocities occur, is transferred towards the tube center and dissipates. Consequently, the turbulence kinetic energy and its dissipation process coincides with the axial backflow in the tube center.
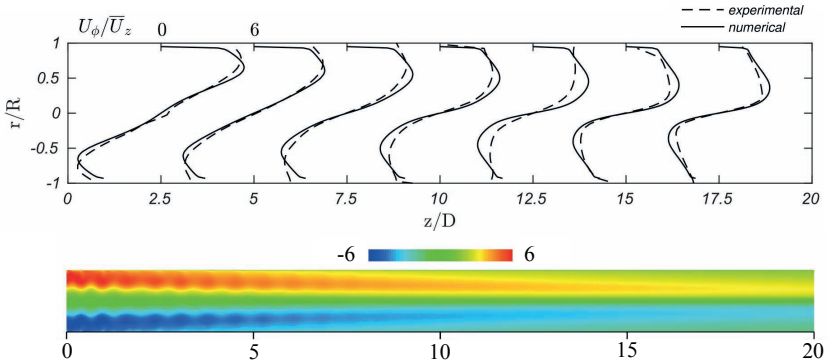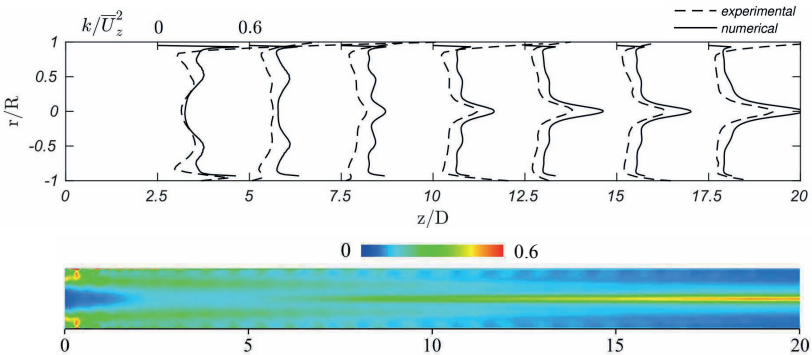

Figure 5.8: Comparison of experimental and numerical non-dimensional turbulence kinetic energy and DES contour plot for $S = 5.3$ and $Re = 10,000$
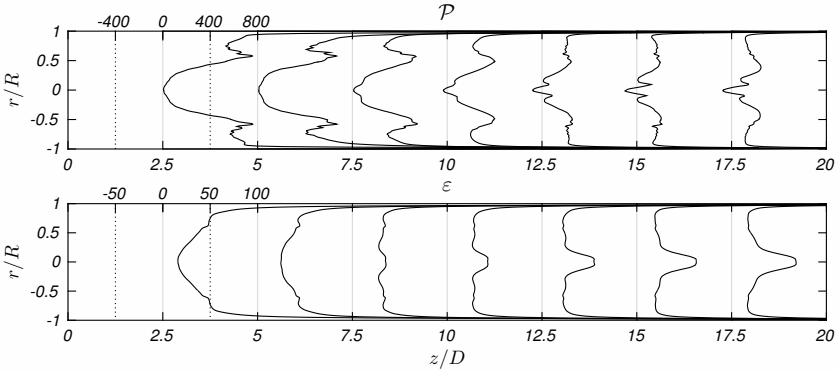
Figure 5.9: DES production $\mathcal{P}$ and dissipation ϵ for $S = 5.3$ and $Re = 10,000$

5.3.5 Vorticity

The rotation of a fluid can be described by its vorticity, which is defined in the general vector form as $\omega = \nabla \times \mathbf{U}$. Here, ∇ is the nabla or partial derivative operator and $\mathbf{U}$ the velocity vector. Figure 5.10 shows the vorticity in circumferential direction $\omega_\phi (= \partial U_r/\partial z - \partial U_z/\partial r)$ in the swirl tube simulated via DES. The experimental PIV results are consistent with the numerics and summarized in Fig. B.12 in the appendix for the investigated Reynolds numbers 10,000, 20,000 and 40,000. One can see two co-rotating vortices by means of the vorticity dots near the tube inlet with higher magnitude (blue and orange). These vortices indicate a helix vortex structure around the axis of the swirl tube. Both vortices shrink to the core moving further downstream towards the tube outlet while the magnitude slightly increases. This process is driven by the conversion of solid body to potential vortex as already shown for the circumferential velocity profile in Fig. 5.6. Thus, high velocity fluid moves closer to the axis and the fluid in the outer tube is slowed down due to friction. So the angular velocity increases in the tube core and the circulation of the potential vortex expands.

In the following, 3D instantaneous vorticity snapshots are presented in form of iso-surfaces obtained from tomographic-PIV measurements. The vorticity in circumferential direction ω_ϕ is shown in Fig. 5.11, which show the same behavior of two co-rotating vortices around the tube axis (blue and orange). Furthermore, the 3D vorticity snapshot visualizes the axisymmetric turbulent structures in the swirl tube. Near the wall the vorticity changes sign of the

83
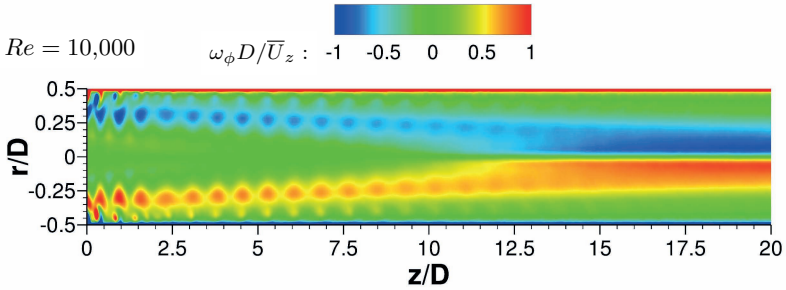
Figure 5.10: DES non-dimensional vorticity for $S = 5.3$ and $Re = 10,000$
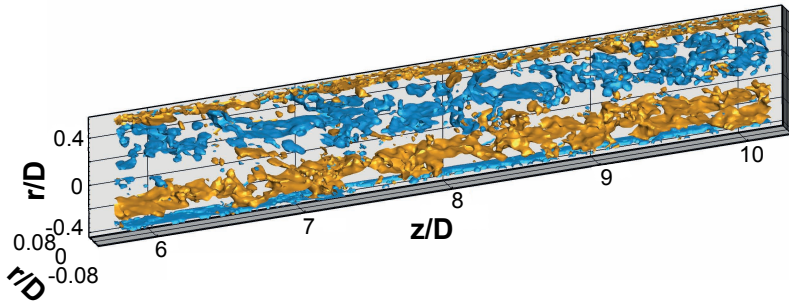
Figure 5.11: Tomographic-PIV instantaneous vorticity ω_ϕ at $Re = 10,000$, color coding: blue $\omega_\phi < 0$, orange $\omega_\phi > 0$

rotation and reveals small scale vortices besides the main vortex structure in the tube. These small scale vortices are responsible for an enhanced fluid mixing in the boundary layer.

In Fig. 5.12 the instantaneous vorticity in axial direction $\omega_z (= 1/r \ \partial(rU_\phi)/\partial r -1/r \ \partial U_r/\partial\phi)$ is presented. Here, two counter-rotating vortices are visible, one in the outer tube region with negative vorticity (green) and one in the tube center with positive vorticity (orange). The number of vortices in the tube center (orange) increases further downstream at $z/D = 7$ and reveals an enhanced turbulence. This is due to the increasing axial backflow on the tube axis and the increasing angular velocity of the solid body vortex in the
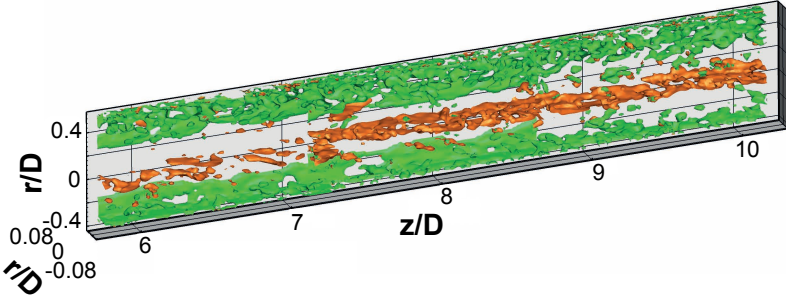
Figure 5.12: Tomographic-PIV instantaneous vorticity ω_z at $Re = 10,000$, color coding: green $\omega_z < 0$, orange $\omega_z > 0$

center as already seen for the velocity fluctuations. The vortices around the center (green) emphasize the axial turbulence due to the main flow in the outer tube. In summary, the tomographic-PIV measurement technique can provide detailed flow data in a complex flow like the one investigated here, which are useful for comparison with transient numerical simulations like DES.

In the following, the vortex structure in the swirl tube is shown by the Q-criterion defined as $Q = 1/2 \ (\Omega_{ij}^2 - S_{ij}^2)$. Here, S_{ij} and Ω_{ij} are the symmetric and antisymmetric velocity gradient tensors. Occurring vortices are visualized with iso-surfaces of $Q > 0$, where the rotation dominates the shear rate. To depict the vortex structure in the present work, the vorticity tensor Ω_{ij} is modified in a way that only the vorticity part which lies in orthogonal planes to the axial direction is shown. This means that the dominant rotation around the tube axis is neglected ($\Omega_{r\phi} = \Omega_{\phi r} = 0$) and the vortex structure in circumferential direction can be revealed as shown by iso-surfaces in Fig. 5.13. The flow structure in the swirl tube is characterized by a double-helix vortex with the highest intensity near the tangential inlets, where the highest velocities occur. The diameter of the helical structure shrinks towards the tube outlet. This is due to the shrinking of the solid body vortex and the shift of the maximum circumferential velocity towards the tube center. This stability phenomenon will be further analyzed in section 5.9.2. In the inlet region, a smaller inner double-helix vortex is visible. Here, the axial backflow (colored in blue) reaches the tangential inlets of the tube, turns and mixes with the axial flow in the outer tube. This double helix vortex is in accordance with the already presented vorticity in circumferential direction in Fig. 5.11.
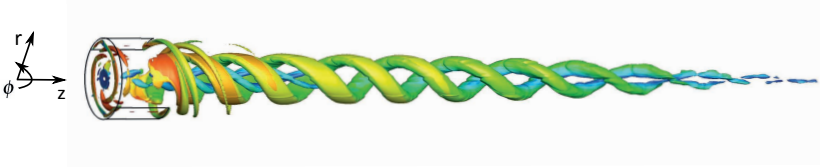
Figure 5.13: DES double helix vortex in the swirl tube for $S = 5.3$ and $Re = 10,000$, iso-surfaces of $Q = 1$, color represents axial velocity [17]

5.3.6 Influence of the Tube Outlet Geometry

In literature, most of the experimental investigations about swirling tube flows for gas turbine blade cooling used different outlet geometries. Table 5.5 gives an overview of selected studies with different outlet geometries such as an axial outlet, a 90° or 180° bend outlet, a tangential or radial outlet.

Moreover, Escudier and Keller [57] analyzed the influence of outlet contractions on the vortex breakdown and showed that a strong contraction of 55% of the diameter has no influence on axial (supercritical) flows, but has a significant influence on subcritical flows with vortex breakdown. In the case of no contraction, the backflow is observed along the entire tube axis, while for a strong contraction the vortex core becomes strongly jet like [57].

As part of this work and mentioned in section 5.1, different outlet geometries

Table 5.5: Literature on experimental swirl tube investigations with different outlet geometries

author	year	$Re_D \times 10^{-3}$	outlet
Chang and Dhir [35]	1995	12.5	axial outlet
Glezer et al. [69]	1998	20	90° bend outlet
Ligrani et al. [133]	1998	$1 - 18.5$	tangential outlet
Hedlund et al. [86]	1999	$2.2 - 7.2$	radial outlet
Khalatov et al. [107]	2001	$Re_{in} = 0.5 - 2.5$	tangential outlet
Ling et al. [140]	2006	$5.4 - 9$	radial outlet
Bruschewski et al. [25]	2015	$2 - 32$	concentric, ring and eccentric outlet orifices, 180° bend outlet

are studied to investigate their influence on the flow field and the heat transfer in the swirl tube. The flow field of the baseline swirl tube with a straight outlet has been discussed extensively at the beginning of this chapter. In the following, the effect of a flow redirection is investigated with a tangential and a 180° bend outlet as shown in Fig. 5.2. It should be mentioned that the round cross-section of the 180° bend is consistent with the cross-section of the actual swirl tube.

The dimensionless axial and circumferential velocity profiles at $Re = 10,000$ and $S = 5.3$ for all investigated geometries are presented in Fig. 5.14. For a more detailed view, only the upper half of the tube $r/D = 0 - 0.5$ is shown due to symmetry. As already discussed, the axial flow is characterized by a strong backflow on the tube axis, whereas the circumferential velocity is the largest component and dominates the flow field in the swirl tube. Comparing the flow field for all geometries, there is almost no difference evident between the straight, the tangential and the 180° bend outlet. The axial velocities with the backflow in the tube core show nearly the same profile. The same is evident for the circumferential velocity profiles, which show a general agreement. Furthermore, the maximum circumferential velocity is indicated by a circle and coincides for all geometries.
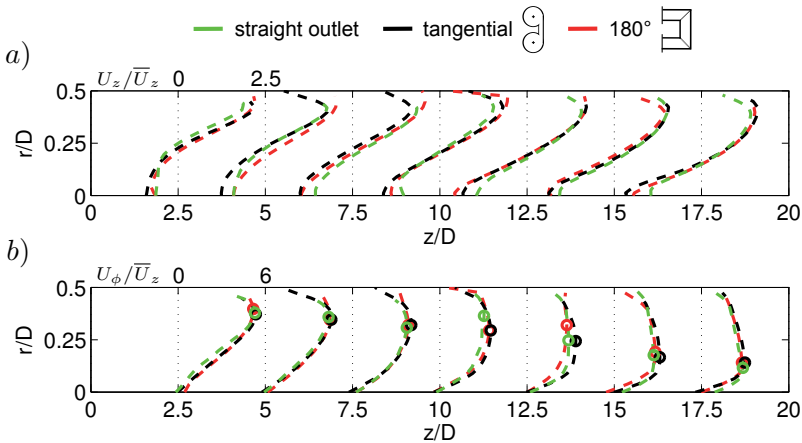
Figure 5.14: PIV flow field for $Re = 10,000$, $S = 5.3$ and all three investigated outlet geometries (straight, tangential and 180° bend). a) Axial velocity, b) circumferential velocity

So, it can be concluded that an outlet redirection (without contraction) has no significant influence on the swirling flow field in a tube. This is an interesting result, because one would expect influences of the tube outlet geometries on the observed backflow and the helix vortex system in the tube. Thus, the here investigated basic swirl tube is characterized by a robust design regarding inflow and outflow conditions.

For completeness, the detailed PIV contour plots regarding the velocity field, the turbulence kinetic energy and the vorticity for all investigated outlet geometries are presented in appendix B.

5.3.7 Swirl Number Variation

The swirl strength in the tube flow has a major impact on the vortex structure and on the axial backflow in the tube center. Moreover, Kobiela [113] analytically estimated a swirl number limit $S_{limit} = 0.928$ for which the axial pressure gradient in the tube center vanishes and backflow may occur. Therefore, lower swirl numbers $S = 1.0$, 0.75 and 0.5 have been numerically simulated. Here, the results for $S = 1.0$ and 0.5 will be compared to the high swirl number case $S = 5.3$ in terms of the mean and instantaneous velocity field, the velocity fluctuations and the local swirl number.

5.3.7.1 Velocity Field

The mean axial and circumferential velocity profiles for the high swirl number $S = 5.3$ ($\triangle$) and the two lower swirl numbers $S = 1.0$ ($\diamond$) and 0.5 ($\circ$) are plotted in Fig. 5.15. For the highest swirl number $S = 5.3$ the maximum axial velocity is in the near wall region and a backflow occurs in the tube center, which increases towards the tube outlet. The swirl is strong enough that this axial backflow appears over the entire tube length as already shown in section 5.3.1. The axial velocity for the lower swirl number $S = 1.0$ reveals a lower maximum near the wall and a reduced velocity on the tube axis, but no backflow for the mean velocity. The axial velocity for the lowest swirl number $S = 0.5$ shows almost a constant profile over the tube radius. Near the wall the axial velocity is similar to the one for $S = 1.0$, but in the tube center only a slightly reduced velocity is apparent.

For the highest swirl number $S = 5.3$, the circumferential velocity is more than two times larger than the axial component due to the large tangential inflow velocity. As explained in section 5.3.2, the profile is characterized by a solid body vortex in the core and a potential vortex in the outer tube. The lower
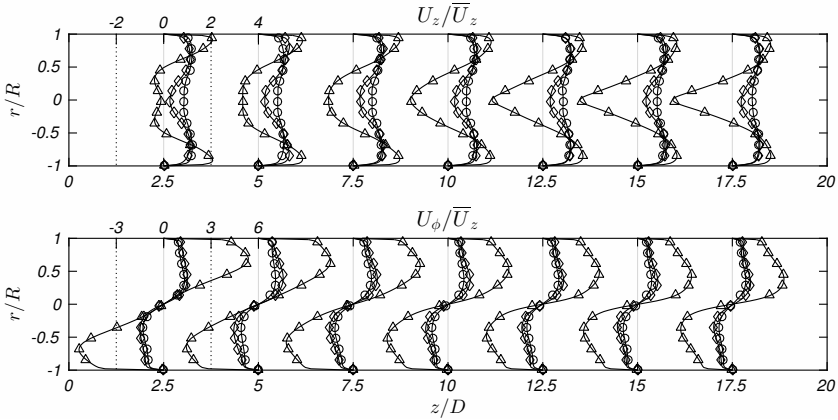
Figure 5.15: DES non-dimensional axial (top) and circumferential (bottom) velocity for three different swirl numbers $S = 5.3$ ($\triangle$), 1.0 ($\diamond$) and 0.5 ($\circ$) at $Re = 10{,}000$

swirl numbers show a much lower velocity magnitude due to the smaller inflow velocity listed in Table 5.3. Two major differences between the higher and lower swirl numbers are visible. First, for the high swirl number the angular velocity of the solid body vortex (slope) in the core increases within the tube length, whereas for the lower swirl number the slope reduces. Second, the maximum of the circumferential velocity for $S = 5.3$ moves from the near wall region at the inlet closer to the center at the tube outlet. For the lower swirl numbers, the radial position is almost constant at $r/R = 0.4$ over the entire tube. This means that in strong swirling flows the solid body vortex has to be somehow transformed into a more stable flow. Further investigations on the flow stability follow in section 5.9.2.

The data suggest that the swirl is the main driver for the axial backflow in the tube center. Consequently, the occurrence of the backflow may be estimated by the swirl number. Kobiela [113] analytically estimated a swirl number limit $S_{limit} = 0.928$ for the occurrence of an axial backflow based on a parabolic axial velocity profile as shown in section 2.2.2. For a further analysis, the instantaneous axial velocity for the three investigated swirl numbers $S = 5.3, 1.0$ and 0.5 is shown in Fig. 5.16. The black color represents negative velocity and thus backflow regions. For a better visualization, it is also marked by a white line surrounding those areas. For the highest swirl number, a large backflow region over the entire tube is evident. For the swirl number $S = 1.0$, which

89
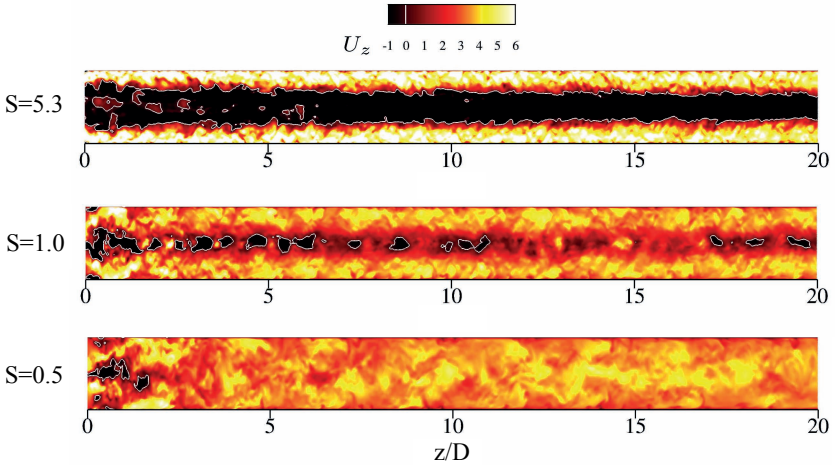
Figure 5.16: DES instantaneous axial velocity for three different swirl numbers $S = 5.3$, 1.0 and 0.5, the white line represents zero axial velocity

means that the inlet area is equal to the tube cross-section, just a few backflow areas occur. With a further reduction of the swirl strength, no axial backflow areas can be observed after the inlet section for $S = 0.5$. This confirms the analytically estimated swirl number limit $S_{limit} = 0.928$ for the occurrence of an axial backflow. A more profound analysis on the occurrence of vortex breakdown will be given in section 5.9.1.

5.3.7.2 Velocity Fluctuations

The axial, radial and circumferential velocity fluctuations in the tube mid-plane are shown in Fig. 5.17 for the same three swirl numbers $S = 5.3$ ($\triangle$), 1.0 ($\diamond$) and 0.5 ($\circ$). All three fluctuations are in the same order of magnitude. For $S = 5.3$ the fluctuations in the tube center increase towards the tube outlet especially from the middle of the tube $z/D = 10$. This correlates with the increasing axial backflow on the tube axis. In the inlet region at $z/D = 2.5$, two symmetric maxima appear near the wall especially for the radial component. This demonstrates a strong radial mixing and fluid exchange near the wall, which is responsible for the high heat transfer near the inlet. For
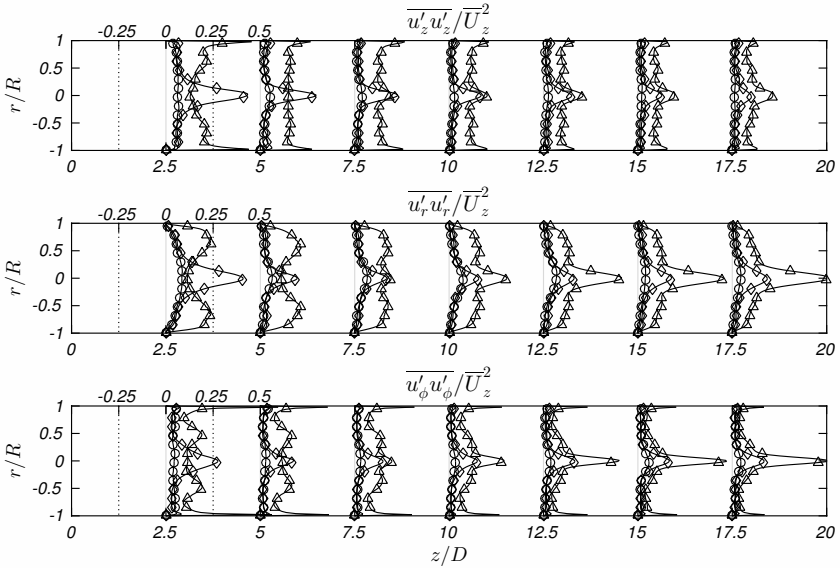
Figure 5.17: DES velocity fluctuations for three different swirl numbers $S = 5.3$ ($\triangle$), 1.0 ($\diamond$) and 0.5 ($\circ$) at $Re = 10{,}000$

the lower swirl numbers, the fluctuations are much smaller as well, but on the axis near the inlet at $z/D = 2.5$ a high peak is conspicuous for $S = 1.0$. These high fluctuations correspond to the axial backflow areas as shown in the instantaneous axial velocity contour in Fig. 5.16. They are preserved up to the middle of the tube and then, they are damped further downstream in contrast to the high swirl number case. The fluctuations for the lowest swirl number $S = 0.5$ are definitely the lowest and almost constant along the radius. In summary, for a higher swirl number also higher velocity fluctuations occur which corresponds to a higher turbulence level.

5.3.7.3 Swirl Number

The local swirl numbers of the performed simulations are presented in Fig. 5.18 for the three geometrical swirl numbers $S = 5.3$, 1.0 and 0.5. The swirl number definition is already given in section 1.4 as the ratio of the angular momentum to the axial momentum of the flow. For the highest swirl number case $S = 5.3$,

91

the local swirl number near the inlet is much smaller than the geometrical one. This is due to the reason that a complete transformation of the circumferential to the axial velocity component is considered for the idealized geometrical swirl number. However, the highest losses occur at the inlet. It is evident that these losses increase with higher inlet velocities and therefore geometrical swirl numbers. In addition, the tangential inflow is already partly converted to the axial velocity.

For the lower swirl number cases, the local and geometrical swirl number near the inlet matches apart from the oscillating behavior. Here, the losses are not as dominant as in the strong swirling flow. For all cases, the local swirl number decreases further downstream towards the tube outlet due to dissipation and decreasing circumferential velocity. Moreover, the local swirl number distribution gives insight about the dominant flow characteristics. For $S = 5.3$ the local swirl number is higher than one over the entire tube, which means that the flow is swirl dominated by the circumferential velocity component. On the other hand, for $S = 0.5$ the local swirl number is smaller than one, which means that the flow field is axial dominated. It will be shown in section 5.9.1 that the dominant flow characteristics can be used to estimate the occurrence of the axial backflow in swirling flows.
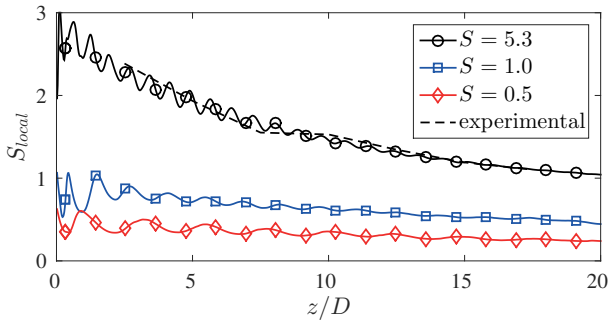
Figure 5.18: DES local swirl number for three different geometrical swirl numbers $S = 5.3$ ($\triangle$), 1.0 ($\diamond$) and 0.5 ($\circ$) at $Re = 10,000$

5.4 Wall Shear Stress

The instantaneous wall shear stress on the tube wall is shown in Fig. 5.19 for the high swirl number $S = 5.3$. The wall shear stress along a boundary

surface is defined as the velocity gradient in normal direction introduced in Eqn. 4.44. The instantaneous snapshot shows swirling stripes of the streamwise flow near the wall. It is evident that the highest shear stresses occur in the inlet region and decrease slowly towards the tube outlet according to the dominant circumferential velocity.
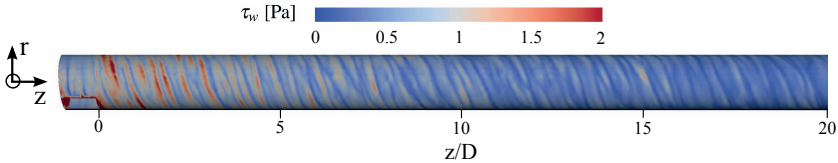
Figure 5.19: DES instantaneous wall shear stress for $S = 5.3$ and $Re = 10,000$

5.5 Temperature

In this section, the temperature distribution in the swirl tube is presented for two different cases, first for adiabatic wall boundary conditions and second for a heat transfer case with a cooled wall with different inlet and wall temperatures.

If the wall is kept adiabatic, the Ranque-Hilsch effect with a radial temperature separation can be observed in a swirling tube flow. This radial temperature distribution is measured experimentally and shown in Figure 5.20 for two different Reynolds numbers $Re = 20,000$ and $Re = 40,000$, respectively. For this purpose, four thermocouples at the locations $z/D = 0.7$, 4.6, 8.5 and 16.5 are traversed in millimeter steps in radial direction. Each radial position is measured and averaged over 60 s with a sample rate of 10 Hz. During the measurement the wall temperature is almost constant. It is evident that near the inlet at $z/D = 0.7$ the highest radial temperature separation occurs due to the highest swirl and thus highest circumferential velocity. For $Re = 20,000$ the temperature difference between the tube center and the wall is around 2 K, whereas for the higher Reynolds number $Re = 40,000$ the temperature separation reaches up to 9 K. Further downstream, the temperature difference becomes smaller as the swirl decreases. Near the tube outlet at $z/D = 16.5$ the temperature difference between the center and the wall is approximately one quarter of the one near the inlet.
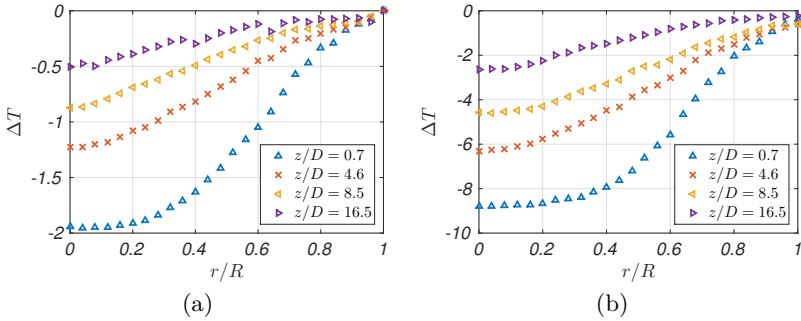
Figure 5.20: Experimental radial temperature distribution $\Delta T = T_c - T_w$ for $S = 5.3$. (a) $Re = 20{,}000$, (b) $Re = 40{,}000$

Moreover, a compressible flow simulation with adiabatic wall boundary conditions has been performed for $S = 5.3$ and $Re = 20{,}000$. The compressibility is important to capture the Ranque-Hilsch effect mentioned in section 2.3. The mean temperature contour in the tube mid-plane is presented in Fig. 5.21. The inlet temperature is set to 300 K and the contour clearly shows the radial temperature separation with the cold fluid in the tube core. This is in accordance to the already shown temperature profiles.

For the heat transfer case with a cooled wall, the phenomena of a wall boundary layer and an axial temperature change occur in addition to the Ranque-Hilsch effect. The mean contour plot is shown in Fig. 5.22 for the same case $S = 5.3$ and $Re = 20{,}000$. For this compressible flow simulation the wall temperature is set constant at $T_w = 293$ K and the fluid inlet temperature is $T_{inlet} = 333$ K. The temperature direction is analogous to the experiments. For a better visual reference of the temperature contour, the scale has been adjusted from 303 K to 333 K. It should be noted that only in the wall boundary layer the temperature decreases to 293 K.

In the tube core the radial separation from the adiabatic investigations is still visible and the temperature on the axis is reduced compared to the region next to the wall. So the temperature slightly increases moving radial outwards and decrease in the boundary layer to the constant wall temperature of 293 K. Over the tube length the temperature decrease drastically due to convection.

Thus, a DES for a compressible flow is capable to predicting the Ranque-Hilsch effect for adiabatic conditions as well as for a cooled wall. It is evident that this temperature separation has be taken into account for the determination of the reference temperature for the heat transfer coefficient. For the

$\overline{T}$ [K]: 298.5   299   299.5   300   300.5   301

z/D
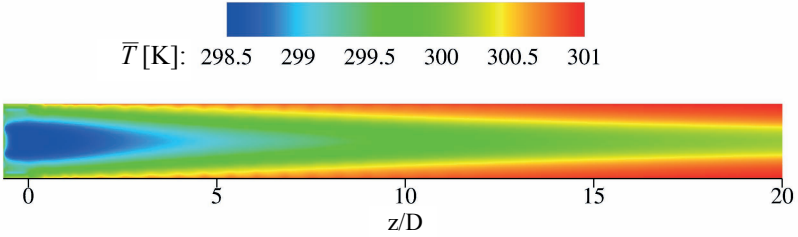
Figure 5.21: Mean temperature from a DES for a compressible flow with adiabatic wall boundary conditions, $S = 5.3$ and $Re = 20,000$

$\overline{T}$ [K]: 303 313 323 333

z/D
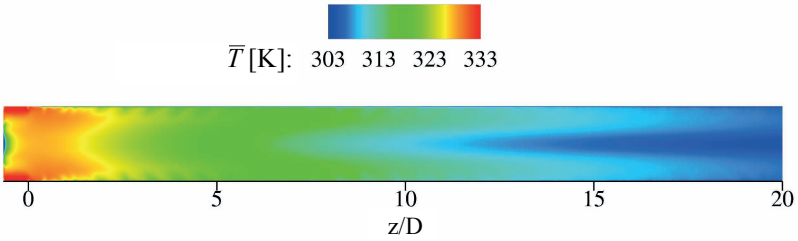
Figure 5.22: Mean temperature from a DES for a compressible flow with $T_{in} = 333K$ and $T_{wall} = 293K$, $S = 5.3$ and $Re = 20,000$

experiments, this radial temperature difference influences the measured center temperature and the desired adiabatic wall temperature. Therefore, the adiabatic wall temperature during the transient measurement is obtained from the measured center temperature during the transient measurement and the temperature ratio obtained during the initial adiabatic conditions. This procedure has already been explained in detail in section 3.5.

5.6 Heat Transfer

In the following, the heat transfer results in terms of circumferentially averaged Nusselt numbers are presented. The Nusselt numbers are normalized by the Nusselt number Nu_0 for a fully developed axial tube flow. Here, the Dittus-Boelter correlation is used given by $Nu_0 = 0.023 \, Re^{0.8} Pr^{0.3}$ [42] also

mentioned for the Nusselt number correlations in section 2.1. For the normalization the mean Reynolds number from each experiment is used for the correlation as described in section 3.6. The heat transfer results are compared for the four investigated Reynolds numbers $(10{,}000 - 40{,}000)$, eight different swirl numbers $(0.75 - 5.3)$ and three outlet geometries (straight, tangential and $180°$ bend outlet).

A detailed overview on the local wall heat flux distribution is given in Fig. 5.23. It shows the numerical results for the swirl number $S = 5.3$ and the Reynolds number $Re = 10{,}000$. One can see that the wall heat flux decreases continuously over the length of the tube. The influence of the helical vortex structure on the wall heat flux is clearly visible in the spiral stripes around the tube.
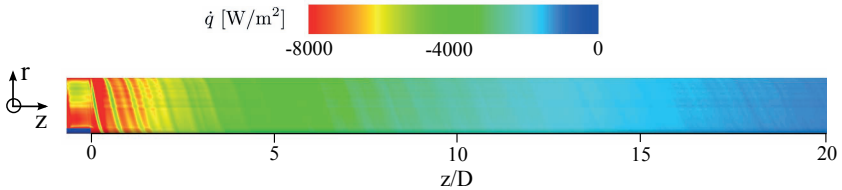
Figure 5.23: DES wall heat flux for $S = 5.3$ and $Re = 10{,}000$

Figure 5.24 shows the Nusselt numbers including error bar for the highest swirl number $S = 5.3$ (a) and for $S = 2.95$ (b). The error bar of the Nusselt number is $\pm 13\%$ in the inlet region and $\pm 8\%$ in the outlet region as already described in section 3.6. The normalized heat transfer results overlap for all investigated Reynolds numbers, so that the swirling flow is proportional to $Re^{0.8}$ analogous to an axial tube flow. This is a very important result as it allows to scale the obtained heat transfer data. Near the inlet the maximum Nusselt numbers are up to 10 times higher than the one for an axial tube flow due to the large circumferential velocity component in this region. For $S = 2.95$ the heat transfer enhancement still reaches a factor of 5. With decreasing swirl and velocity, the heat transfer continuously decreases towards the tube outlet. At the outlet, for $S = 5.3$ the Nusselt number is still two and a half times higher and for $S = 2.95$ two times higher than the one for an axial flow. The circumferential velocity with large gradients near the wall is the major mechanism for the high heat transfer observed in the swirl tubes. Near the wall, the velocity decreases by a factor of 3 over the tube length as shown in the velocity distribution in Fig. 5.6, which is in accordance to the Nusselt number decrease.

Next, the influence of different swirl numbers on the heat transfer is presented
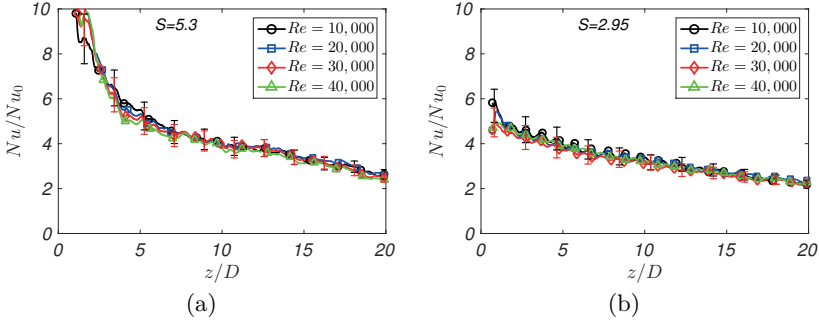
Figure 5.24: Experimental normalized Nusselt numbers for different Reynolds numbers. (a) $S = 5.3$, (b) $S = 2.95$

in Fig. 5.25 (a). The investigated swirl numbers range from 5.3 to 0.75. It is evident that with higher swirl number and therefore higher circumferential velocity near the wall, the heat transfer increases. Near the inlet, the Nusselt numbers range from 3 to 10 for the investigated swirl numbers and decrease towards the tube outlet. At the outlet, the heat transfer enhancement for the lowest swirl number $S = 0.75$ is around 1.2. Consequently, over the entire tube all Nusselt numbers are still higher than the one in an axial tube flow. This confirms that swirling flows enhance the heat transfer in tubes.

Figure 5.25 (b) shows the heat transfer comparison for the three investigated outlet geometries: straight, tangential and 180° bend outlet. Here the Nusselt numbers are plotted for $S = 5.3$ and $Re = 30,000$. The heat transfer profile is almost unchanged compared to the one in Fig. 5.24 (a) with the maximum Nusselt number enhancement of 10 near the inlet and the decrease towards the tube outlet. Regarding the different outlet geometries, there is nearly no difference visible in the Nusselt numbers. This is in accordance to the already discussed flow field in section 5.3.6. So it can be confirmed that the here investigated outlet redirection has no significant influence on the upstream heat transfer. Thus, the here investigated swirling flow in tubes is characterized by a robust design regarding different swirl strengths and outlet conditions and therefore well applicable for cooling of high thermal loaded components.

The experimental globally averaged normalized Nusselt numbers $\overline{Nu}/Nu_0$ are summarized in Table 5.6 for all investigated Reynolds and swirl numbers. For the lowest swirl number $S = 0.75$, the average heat transfer is around 1.5 times higher than in a purely axial tube flow. With increasing swirl, the heat transfer enhancement increases up to 4.5 compared to the one in an axial flow for
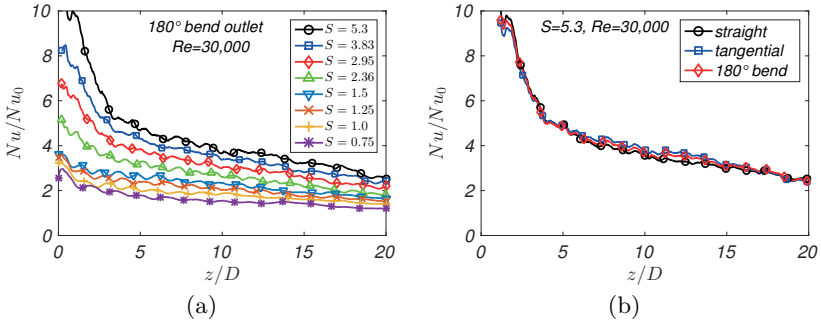
Figure 5.25: Experimental normalized Nusselt numbers for (a) all investigated swirl numbers at $Re = 30,000$, and (b) different outlet geometries for $S = 5.3$ and $Re = 30,000$

the highest swirl number $S = 5.3$. Comparing different Reynolds number for a constant swirl number, it is noteworthy that the heat transfer enhancement is almost constant, which means that the Nusselt number $\overline{Nu}$ for swirling flows is proportional to $Re^{0.8}$ analogous to an axial tube flow. This is a very important result as it allows to scale the obtained heat transfer data.

In the following, the numerical results for $S = 5.3$ and three Reynolds numbers are compared to the experiments in Fig. 5.26 (a). It should be mentioned that the results are obtained from DES simulations for an incompressible flow with segregated momentum and energy equations. One can see a good agreement for the higher Reynolds numbers $Re = 20,000$ and $40,000$. However, deviations

Table 5.6: Experimental globally averaged Nusselt numbers $\overline{Nu}/Nu_0$

$S \setminus Re$	10,000	20,000	30,000	40,000
0.75	1.62	1.54	1.57	1.50
1.0	1.90	1.78	1.80	1.78
1.25	2.08	2.05	2.03	1.99
1.5	2.24	2.29	2.29	2.27
2.36	-	2.95	2.81	-
2.95	3.36	3.32	3.38	3.28
3.83	-	3.71	3.89	-
5.3	4.47	4.58	4.47	4.50

of 25% are evident for the lower Reynolds number $Re = 10{,}000$ near the inlet region. This is due to an underestimated heat flux which might be caused by an insufficient turbulence level for the lowest Reynolds number $Re = 10{,}000$. However, difficulties to simulate the heat transfer for high swirl numbers are often reported in literature, for example, for RANS simulations by Kobiela [113] or LES simulations by Scherhag et al. [187].

In Fig. 5.26 (b) the Nusselt numbers from a simulation for an incompressible and a compressible flow are compared for $Re = 20{,}000$. For a compressible flow simulation, the momentum and energy equation are coupled and solved iteratively. Since the Spalart-Allmaras DDES model for the simulation of compressible flows is not available in the standard OpenFOAM 2.2.x library, the compressible formulation has been implemented as part of this work. The OpenFOAM code is given in appendix A. It is evident that the Nusselt number curve from the compressible flow simulation agrees well with the experiments compared to the incompressible flow simulation. Only a slight underestimation in the inlet region occurs up to $z/D = 6$. This can be also the uncertainty in the experiments since in the inlet region the highest uncertainty occur due to a fast color change of the TLCs. Considering the simulation for an incompressible flow, the Nusselt numbers are in the same order of magnitude but the curve shows a different slope and seems not correct. This is due to the reason, that the momentum and energy equations are segregated. This shows that the occurring Ranque-Hilsch effect explained in section 2.3 can only be described by the compressible conservation equations. Therefore, it can be
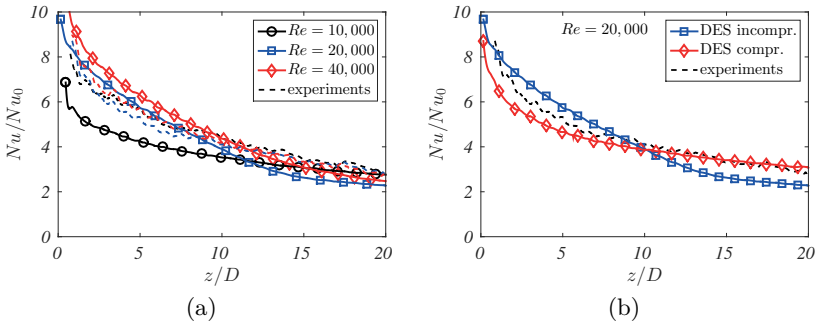
Figure 5.26: Comparison of normalized Nusselt numbers from DES and experiments for $S = 5.3$ and (a) different Reynolds numbers, and (b) a comparison between a simulation for an incompressible and a compressible flow at $Re = 20{,}000$

concluded that the heat transfer for strong swirling flows has to be solved by a compressible flow simulation although the Mach number is below 0.3.

For the here performed simulations, the computational time increases by a factor of four between an incompressible and a compressible flow simulation since the coupled equation system needs four additional inner iterations for a converged solution. Therefore, just one case could be exemplarily performed by a compressible flow simulation for $S = 5.3$ and $Re = 20,000$ as shown in Fig. 5.26 (b). The choice of an incompressible or a compressible flow simulation only affects the energy equation and therefore has almost no influence on the already shown flow characteristics.

5.7 Pressure Loss

For a comparison of different cooling methods, not only the absolute heat transfer is important, but rather the ratio of heat transfer to pressure loss is decisive. So the pressure loss in cooling channels in gas turbine blades has to be considered as well to optimize the heat transfer for a given pressure.

The pressure distribution in the swirl tube with $S = 5.3$ and $Re = 20,000$ is presented in Fig. 5.27 and characterized by two mechanisms. First, the total pressure in axial direction decreases due to wall friction. Second, a radial pressure distribution occurs due to the centrifugal forces of the swirling flow. The pressure in the tube center is lower than at the wall. As the swirl decreases further downstream, also the radial pressure distribution becomes smaller towards the tube outlet. Both mechanism overlap and cause an axial pressure gradient on the tube axis depending on the swirl number as explained in section 2.2.2 according to Kobiela [113]. For strong swirl, the swirl decrease dominates, the axial pressure gradient is positive and a backflow occurs. For low swirl, the axial pressure loss dominates and the axial pressure gradient on
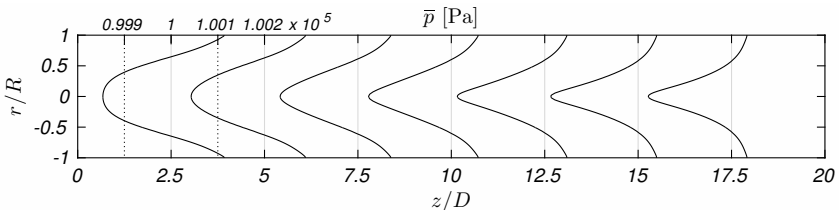
Figure 5.27: DES pressure distribution in the swirl tube with $S = 5.3$ and $Re = 20,000$

the axis is negative.

Figure 5.28 shows the wall pressure distribution over the tube length to the wall pressure at the outlet $p_{w,0}$ in dimensionless form with the dynamic pressure $q = 1/2\rho\overline{U}_z^2$. In Fig. 5.28 (a) the pressure is plotted for $S = 5.3$ and all investigated Reynolds numbers whereas in (b) the distribution for various swirl numbers between 0.75 and 5.3 is shown. It is evident that the wall pressure decreases over the tube length. The pressure decrease is stronger for higher swirl numbers. The maximum pressure loss occurs in the inlet region where the highest velocities appear. Comparing the different Reynolds numbers, the dimensionless pressure losses coincide. For lower swirl numbers, the pressure is drastically reduced compared to a strong swirling flow.

The pressure loss for the three investigated outlet geometries (straight, tangential and 180° bend outlet) overlap for the same flow conditions as already shown in the Nusselt number plot in Fig. 5.25 (b). Therefore, this plot is not shown additionally but the agreement is evident comparing the highest swirl number $S = 5.3$ in Fig. 5.28 (a) and (b) between the straight and the 180° bend outlet. Thus, there is no influence on the upstream pressure loss for the investigated outlet geometries.

Next, the numerical results for $S = 5.3$ and three Reynolds numbers are presented and compared to the experiments in Fig. 5.29 analogous to the Nusselt number plot in Fig. 5.26 (a). The plot shows that the simulations underestimate the pressure loss over the tube up to 20% at the beginning of the tube. The curve is not as steep as the experimental data, but the overall pressure loss shows a good agreement for all Reynolds numbers.
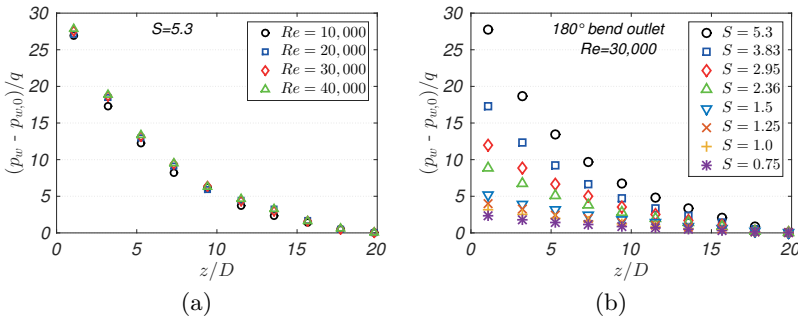
Figure 5.28: Experimental normalized pressure loss for (a) different Reynolds numbers and $S = 5.3$, and (b) all investigated swirl numbers at $Re = 30{,}000$
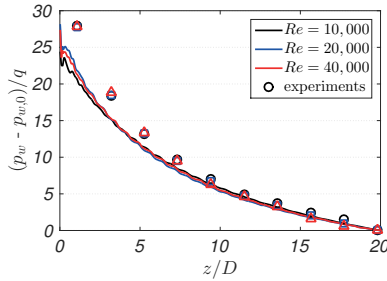
Figure 5.29: Comparison of normalized pressure loss from DES simulations for an incompressible flow and experiments for $S = 5.3$

For a comparison with the heat transfer enhancement, the pressure loss of the swirling tube flows will be compared to the one in an axial tube flow. Therefore, Table 5.7 summarizes the experimental friction factor enhancement f/f_0 over the tube length for all investigated Reynolds and swirl numbers. The friction factor is defined as

$$f = \frac{\Delta p}{1/2\rho \overline{U}_z^2} \frac{D}{L} \tag{5.4}$$

and normalized by the friction factor correlation for an axial tube flow $f_0 = 0.3164\ Re^{-0.25}$ by Blasius [188]. The high heat transfer observed in swirl tubes is paid by a high friction factor, which varies between 4.7 and 64 times the one in an axial tube flow for all investigated Reynolds and swirl numbers. This high pressure loss is related to the high local velocities compared to the low mean axial velocity used for the correlation. With increasing swirl also the friction factor increases. For swirl dominated flows ($S \geq 1.0$), the friction factor increases with higher Reynolds numbers. This means that the Reynolds number dependency by the Blasius correlation of $Re^{-0.25}$ is not valid for swirling flows.

In addition to the pressure loss over the tube length, the swirling flow has to be generated in the swirl generator, which causes an additional pressure loss. In the following, the experimental friction factor enhancement f/f_0 over the tube length including the tangential inlets is listed in Table 5.8. Here the same correlation for an axial tube flow by Blasius is used for an easier comparison. It is evident that the pressure loss over the tangential inlets is higher than the pressure loss over the tube length. This is due to the smaller cross-section and the higher velocity in the inlets.

Table 5.7: Experimental friction factor enhancement f/f_0 over the tube length

$S \setminus Re$	10,000	20,000	30,000	40,000
0.75	5.53	5.05	4.87	4.73
1.0	6.45	6.47	6.53	6.65
1.25	7.82	7.93	8.19	8.44
1.5	8.74	9.45	10.54	11.04
2.36	15.06	16.92	18.16	19.39
2.95	19.74	22.65	24.89	26.50
3.83	27.73	32.70	35.99	38.65
5.3	43.93	52.31	57.96	64.00

Table 5.8: Experimental friction factor enhancement f/f_0 over the tube length including inlets

$S \setminus Re$	10,000	20,000	30,000	40,000
0.75	13.82	12.21	11.79	11.71
1.0	16.84	15.47	15.41	15.42
1.25	17.29	17.27	17.93	18.33
1.5	20.44	20.63	20.97	21.74
2.36	33.36	35.92	37.85	39.67
2.95	43.19	48.27	52.56	56.76
3.83	65.41	74.36	83.28	91.61
5.3	113.28	131.18	149.55	167.50

5.8 Thermal Performance

For an interpretation of the obtained heat transfer and the respective pressure loss, the thermal performance parameter is a useful quantity for a comparison with other cooling methods presented, for example, by Ligrani [132] and Ligrani et al. [134] for several heat transfer augmentation techniques. The thermal performance parameter $(\overline{Nu}/Nu_0)/(f/f_0)^{1/3}$ is the ratio between the heat transfer enhancement and the friction factor increase. A thermal performance parameter greater than 1 indicates a higher efficiency than in an axial tube flow. Table 5.9 summarizes the experimental thermal performance for all investigated Reynolds and swirl numbers based on the experimental globally averaged Nusselt numbers in Table 5.6 and the experimental friction factor en-

hancement over the tube in Table 5.7. The thermal performance parameters range between 0.9 and 1.27 for all investigated cases. One can see that the thermal performance increases with higher swirl number although the pressure loss drastically increases as shown in Table 5.7. Considering the different Reynolds numbers, the parameters indicate a better thermal performance for a lower Reynolds number. The highest performance appears for $S = 5.3$ and $Re = 10,000$. In summary, swirl tubes show a high heat transfer potential and are therefore well applicable for cooling of high thermal loaded components such as turbine blades for a given pressure loss.

Table 5.9: Thermal performance parameter $(\overline{Nu}/Nu_0)/(f/f_0)^{1/3}$ (experiments)

$S \setminus Re$	10,000	20,000	30,000	40,000
0.75	0.92	0.90	0.93	0.89
1.0	1.02	0.95	0.96	0.95
1.25	1.05	1.03	1.01	0.98
1.5	1.09	1.08	1.04	1.02
2.36	-	1.15	1.07	-
2.95	1.24	1.17	1.16	1.10
3.83	-	1.16	1.18	-
5.3	1.27	1.22	1.16	1.13

Figure 5.30 shows experimental data of the globally averaged Nusselt numbers $\overline{Nu}/Nu_0$ (a) and the thermal performance parameters $(\overline{Nu}/Nu_0)/(f/f_0)^{1/3}$ (b) over the friction factor f/f_0 for all investigated Reynolds and swirl numbers, respectively. The globally averaged Nusselt numbers visualize the obtained heat transfer enhancement and the paid pressure loss. With increasing swirl also the heat transfer and the pressure loss increase. The experimental thermal performance parameters from Table 5.9 scatter around one and show the best performance for $Re = 10,000$.

All experimentally obtained normalized Nusselt numbers are plotted in Fig. 5.31 (a) as a function of the geometrical swirl number S. The globally averaged Nusselt numbers correlate with the swirl number and are well presented by the following equation:

$$\frac{Nu}{Nu_0} = 1 + S^{0.76} \tag{5.5}$$

for $0.75 < S < 5.3$ and $10,000 < Re < 40,000$.
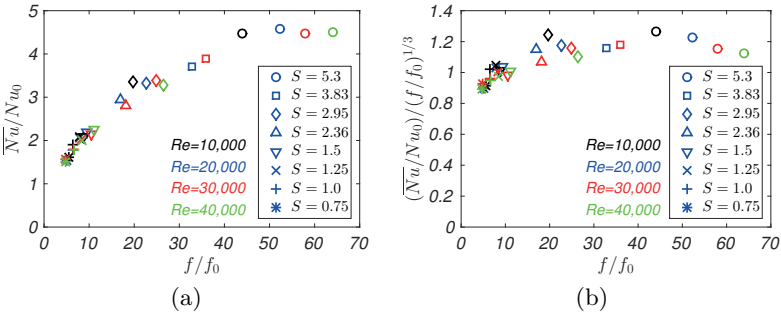
Figure 5.30: Experimental globally averaged Nusselt numbers $\overline{Nu}/Nu_0$ (a) and thermal performance parameters $(\overline{Nu}/Nu_0)/(f/f_0)^{1/3}$ (b) over the friction factor f/f_0 for all investigated Reynolds and swirl numbers

This correlation is plotted in Fig. 5.31 first over the swirl number S (a) and second over the Reynolds number Re (b). Additionally, the Nusselt number for an axial tube flow by Dittus and Boelter [42] and the correlations for swirl tube flows by Hedlund and Ligrani [84] ($Nu = 0.27 \, Re^{0.65}$) and by Khalatov et al. [108] ($Nu = 0.490 \, Re^{0.56}$) are added for comparison in Fig. 5.31 (b). It is evident that the globally averaged Nusselt numbers increase as S or Re increases. In the present study, the increase has been determined by $Re^{0.8}$ in
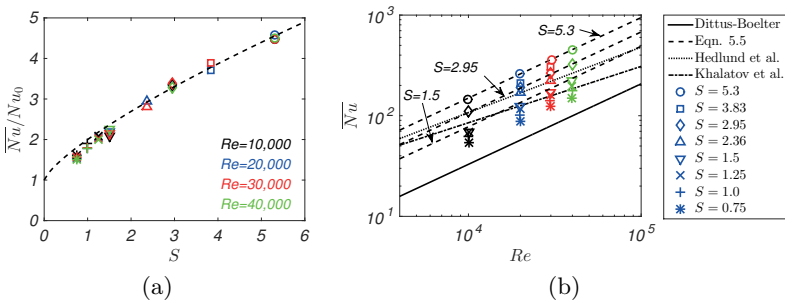
Figure 5.31: Experimental Nusselt numbers for all investigated cases and the correlation from Eqn. 5.5 over the swirl number S (a) and the Reynolds number Re (b)

accordance to the Dittus-Boelter correlation. The difference in the power of Re between Eqn. 5.5 and the correlations by Hedlund and Ligrani [84] and Khalatov et al. [108] might be due to the used reference temperature for the heat transfer coefficient. In the present work, the local fluid temperature is used as reference temperature whereas the other researchers used the mean temperature at the inlet.

5.9 Analysis of Flow Phenomena

For a technical application the flow stability is important for a reliable operation. The already shown complex flow field in the swirl tube is characterized by an axial backflow in the tube center known as vortex breakdown and a strong circumferential velocity component depending on the swirl number. Hereafter, the numerical swirl tube results in terms of velocity and temperature field will be used to analyze the flow field with regard to vortex breakdown and stability using different criteria from literature. For this, the DES results of the high swirl number case $S = 5.3$ for the Reynolds number $Re = 20,000$ will be considered.

5.9.1 Vortex Breakdown Analysis

In section 2.2, the vortex breakdown phenomenon with the main types and the most common theories have been introduced. In the present swirl tube an axisymmetric vortex breakdown occurs with a pronounced axial backflow on the tube axis for sufficient strong swirl. Such a breakdown is a transition from a supercritical to a subcritical flow state, in which the flow is spread upstream and transports information about the downstream conditions. Moreover, different approaches to predict vortex breakdown have been presented in section 2.2 and the two most suitable will be analyzed in the following: the flow force analysis by Escudier and Keller [56] and a criterion based on the Rossby number proposed by Spall et al. [203].

Escudier and Keller Criterion

As mentioned in section 2.2.2, Escudier and Keller [56] discussed the isentropic force-free transition in a Rankine vortex as depicted in Fig. 5.32. A complete force-free transition consists of a first (discrete) force- and loss-free transition
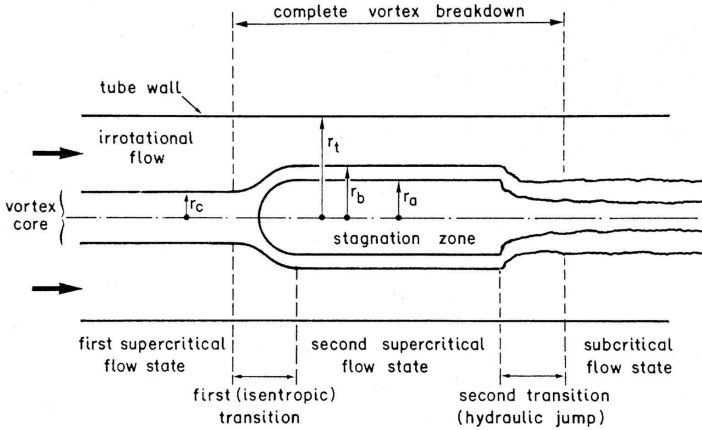
Figure 5.32: Transition of a vortex core in a rotational tube flow [56]

followed by a force-free dissipative transition (hydraulic jump), which is determined by the downstream boundary condition [56]. To determine the flow conditions, Escudier and Keller [56] mentioned it is sufficient to consider the first transition. It is supposed that the flow can be represented as a Rankine vortex and consists of a solid-body rotation of radius r_c surrounded by a potential vortex. The velocity components are defined as follows with a uniform axial velocity w_1:

$$v_1(r) = \begin{cases} \omega r & \text{if } r \leqq r_c \\ \omega r_c^2/r & \text{otherwise} \end{cases}, \quad w_1(r) = W_1 , \tag{5.6}$$

where r_c is the radius of the vortex core and the angular velocity ω and W_1 are constants. It is assumed that the static pressure along the bubble surface is constant. To formulate the momentum balance Escudier and Keller [56] defined the flow force S by

$$S = 2\pi \int\limits_0^{r_c} (\rho w^2 + p)r \, \mathrm{d}r , \tag{5.7}$$

where ρ is the density and p the pressure. Assuming that Bernoulli's theorem is valid along the axis down to the stagnation point at the front of the bubble, the pressure on the axis yields $p_1(0) = -1/2\rho W_1^2$. Additional to the radial

momentum equation, the flow force can be determined for the first and second flow state [56]:

$$S_1 = \frac{1}{2}\rho W_1^2 \pi r_t^2 \left\{ 1 + \frac{1}{2}k^2 r_c^2 - \frac{3}{8}k^2 r_c^2 \frac{r_c^2}{r_t^2} - \frac{1}{4}k^2 r_c^2 \frac{r_c^2}{r_t^2} \ln\left(\frac{r_t^2}{r_c^2}\right) \right\} \quad (5.8)$$

$$S_2 = \frac{1}{2}\rho W_1^2 \pi r_t^2 \left\{ 1 + \frac{1}{2}k^2 r_c^2 - \frac{1}{2}k^2 r_c^2 \frac{r_b^2}{r_t^2} + \frac{1}{8}k^2 \frac{r_b^4 - r_a^4}{r_t^2} \right.$$
$$\left. - \frac{1}{4}k^2 r_c^2 \frac{r_c^2}{r_t^2} \ln\left(\frac{r_t^2}{r_b^2}\right) \right\} \quad . \tag{5.9}$$

Here k is defined as $k = 2\omega/W_1$, r_c is the radius of the vortex core, r_t is the tube radius and r_a and r_b are the boundary radii of the rotational fluid and the bubble as shown in the schematic diagram in Fig. 5.32. Further details on the lengthy calculation of the flow states can be found in the original paper by Escudier and Keller [56]. The flow-force difference between the first and second flow state can now be obtained:

$$S_2 - S_1 = \frac{\pi}{4}\rho W_1^2 k^2 r_c^2 \left\{ -r_b^2 + \frac{1}{4}\frac{r_b^4 - r_a^4}{r_c^2} + \frac{3}{4}r_c^2 + \frac{1}{2}r_c^2 \ln\left(\frac{r_b^2}{r_c^2}\right) \right\} \quad . \tag{5.10}$$

Escudier and Keller [56] mentioned that it can be shown by considering the second variation of the flow force that the downstream state is supercritical for $r_b/r_t < 1$, as must be the case after an isentropic transition, and becomes critical at $r_b/r_t = 1$. For every value of r_c/r_t (< 1) of a Rankine vortex, there exists an isentropic transition to a second flow state. After the first transition the flow changes gradually under the influence of viscous effects and the flow condition is closer to critical.

In the following, it is assumed that the boundary radii of the rotational fluid and the bubble are almost the same $r_a \approx r_b$. This approximation is valid for the confined swirl tube flow investigated here. With it, Eqn. 5.10 yields

$$S_2 - S_1 = \pi\rho\omega^2 r_c^2 \left\{ -r_b^2 + \frac{3}{4}r_c^2 + \frac{1}{2}r_c^2 \ln\left(\frac{r_b^2}{r_c^2}\right) \right\} \quad . \tag{5.11}$$

Finally, from the momentum balance the flow-force difference is set to zero $S_2 - S_1 = 0$. So the numerically obtained flow field can be analyzed using the angular velocity ω and the vortex core radius r_c from the solid body region to calculate the vortex breakdown radius r_b. This analytically obtained bubble radius is then compared to the numerically simulated bubble radius in Table 5.10. Both radii show a good agreement between the calculated and

Table 5.10: Comparison of analytically calculated and numerically simulated radius r_b of the vortex breakdown bubble in the swirl tube ($S = 5.3$) for two Reynolds numbers

	position z/D	2.5	10	17.5
$S = 5.3$	r_b/D (analytical)	0.246	0.196	0.182
$Re = 10{,}000$	r_b/D (numerical)	0.247	0.207	0.177
$S = 5.3$	r_b/D (analytical)	0.254	0.211	0.168
$Re = 20{,}000$	r_b/D (numerical)	0.237	0.227	0.207

simulated breakdown bubble region over the entire tube length (inlet, middle and outlet). For the higher Reynolds number slight differences occur, but for the lower Reynolds number the radii agree well. In summary, the flow field analysis according to Escudier and Keller [56] is suitable to determine the vortex breakdown region in the swirl tube flow, which is characterized by a Rankine like vortex.

Spall Criterion

Spall et al. [203] proposed a criterion for the onset of vortex breakdown based on the Rossby number (inverse swirl number). The local Rossby number is defined as the ratio of the axial velocity to the circumferential velocity $Ro = U_z^*/(r^*\Omega) = U_z^*/U_{\phi,max}$. Spall et al. [203] defined r^* as the radial distance at which the swirl velocity is maximum. U_z^* is then the axial velocity at this position. These characteristic scales are also used to calculate the local Reynolds number Re_z^*. The results of their study and other numerical and experimental investigations reveal a critical Rossby number for vortex breakdown of 0.65 as shown in Fig. 2.7. For lower Rossby numbers the circumferential velocity is dominant and vortex breakdown occurs.

Figure 5.33 shows the local Rossby numbers over the local Reynolds number for the three different swirl numbers $S = 0.5$, 1.0 and 5.3 at the same global Reynolds number $Re = 10{,}000$. The same global Reynolds number means at the same mass flow rate. The Rossby number limit of 0.65 by Spall et al. [203] is also shown. Open symbols indicate no breakdown, whereas solid symbols refer to vortex breakdown. It is evident that for the highest swirl number $S = 5.3$ vortex breakdown occurs over the entire tube. On the other hand, for the lowest swirl number $S = 0.5$, the circumferential velocity is too weak for vortex breakdown and no axial backflow exists in the tube as already shown
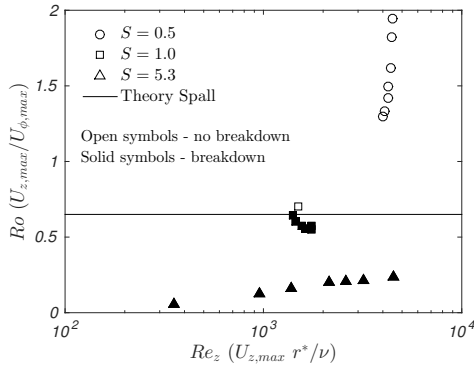
Figure 5.33: Local Rossby number over local Reynolds number obtained from DES for different swirl numbers at the same global Reynolds number $Re = 10{,}000$

in Fig. 5.16. For the intermediate swirl number $S = 1.0$, most of the local Rossby number points are below the limit and vortex breakdown may occur. Only one position near the outlet is above 0.65 and reveal that there is no breakdown anymore (open square). For comparison we again consider the instantaneous velocity contour for $S = 1.0$ in Fig. 5.16. In the first half of the tube, some backflow areas are evident, whose number decreases moving further downstream to the end of the tube. This means that near the outlet the flow field is at the onset of vortex breakdown, which can be also identified by the local Rossby number shown here.

For a further analysis, two different local Reynolds numbers are considered, the axial and the circumferential Reynolds number Re_z and Re_ϕ. Both are defined with the mean velocity $\overline{U}_z$ and $\overline{U}_\phi$ at each axial position, respectively. These Reynolds numbers are used to compare the influence of the mean velocities in contrast to the maximum circumferential velocity like in the previous Rossby number criterion. The calculated local Reynolds numbers Re_z and Re_ϕ for different axial positions are plotted in Fig. 5.34 for the same swirl numbers as before. The solid line indicates the axial Reynolds number, whereas the dashed line represents the circumferential Reynolds number.

For the highest swirl number $S = 5.3$ it is evident that the circumferential Reynolds number Re_ϕ is much higher than the axial one and therefore dominates the flow field. Here vortex breakdown occurs according to the instantaneous velocity in Fig. 5.16. For the lowest swirl number $S = 0.5$ it is the
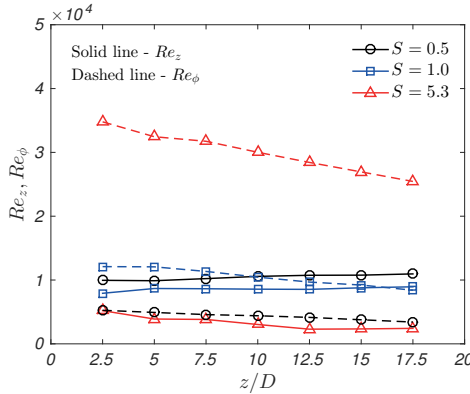
Figure 5.34: Comparison of local axial and circumferential Reynolds number obtained from DES for different swirl numbers at the same global Reynolds number $Re = 10{,}000$

other way around. The axial Reynolds number Re_z is twice the circumferential one, which means that the flow field is axial dominated, where no breakdown appears. Regarding the intermediate swirl number $S = 1.0$, both Reynolds numbers intersect near the tube outlet. At the beginning of the tube the circumferential velocity dominates, where a few backflow areas can be detected as shown in Fig. 5.16. Moving towards the tube outlet, the axial velocity becomes more dominant and almost no backflow occurs anymore.

This comparison indicates that the flow field for $S = 1.0$ is at the onset of vortex breakdown analogous to the results of the Rossby number criterion. This is in accordance with the estimation by Squire [205] that a flow is subcritical (vortex breakdown), if the maximum swirl velocity exceeds the axial velocity as stated in section 2.2.1. Consequently, this analysis shows that the maximum velocities (for the Rossby number) or the mean velocities (for the Reynolds numbers) are suitable flow characteristics to determine vortex breakdown regions in swirling flows.

5.9.2 Stability Analysis

Several authors studied the stability of vortex flows including Lord Rayleigh [146], Howard and Gupta [89], Ludwieg [148], Leibovich and Stewartson [125] and Maršík et al. [152, 153]. The first important stability criterion by Rayleigh

stated that a circular inviscid flow is stable, if the angular momentum Ω increases monotonically outward [32]:

$$\frac{d}{dr}(r^2\Omega)^2 > 0 , \tag{5.12}$$

where the circumferential velocity is described as $U_\phi = r\Omega$. In wall bounded flows like in tubes, the swirl velocity goes to zero. This means that an initial instability always occurs near the wall, if the Reynolds number is high enough. For most of the following criteria, the Rayleigh stability serves as a starting criterion and has been extended for different kind of flows or disturbances.

Howard and Gupta Criterion

Howard and Gupta [89] derived a more general form of Rayleigh's criterion for the stability against axisymmetric disturbances of flows considering the axial velocity component U_z as well:

$$\frac{d}{dr}\left(r^2 U_\phi^2\right) - \frac{1}{4}r^3\left(\frac{dU_z}{dr}\right)^2 > 0 . \tag{5.13}$$

This stability condition is evaluated for the investigated swirl tube flow and is plotted at seven axial positions z/D in Fig. 5.35. In the tube core, the flow is at the onset of stability. The stability then increases with increasing angular velocity before it becomes unstable in the near wall region. Here, instabilities occur due to viscous damping. The peak stability moves slightly towards the tube axis, which might be due to the transformation of solid body to potential vortex. It is evident that the axial disturbances are not crucial for the stability of a strong swirling flow investigated here.

Ludwieg Criterion

Ludwieg [148] proposed a criterion for the centrifugal instability of inviscid swirling flows in a narrow annulus. Again, it is a generalized form of Rayleigh's criterion for instability to spiral disturbances:

$$(1-h)(1-h^2) - (5/3-h)g^2 < 0 \quad \text{with} \tag{5.14}$$

$$g = \frac{r}{U_\phi}\frac{dU_z}{dr} \quad \text{and} \quad h = \frac{r}{U_\phi}\frac{dU_\phi}{dr} \tag{5.15}$$
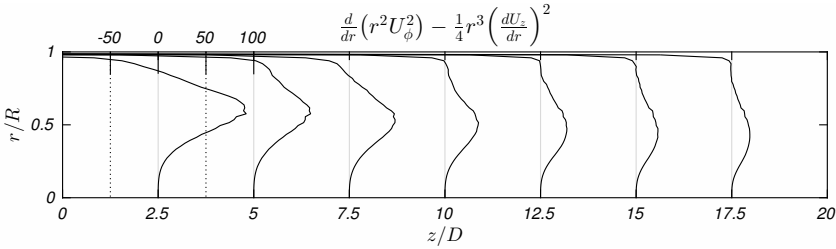
Figure 5.35: Stability condition by Howard and Gupta [89] for $S = 5.3$ and $Re = 20{,}000$ (DES data)

Figure 5.36 shows the instability condition by Ludwieg for the swirl tube flow. Unstable regions are shown with light red bars. On the tube axis the flow is at the onset of stability. Moving outwards the flow becomes unstable to spiral disturbances where the circumferential velocity has its maximum. The magnitude of the centrifugal instability (in red) decreases towards the tube outlet and almost stabilizes. Moving further outwards, a stable region again appears where the potential vortex is dominant. It follows an instability near the wall as expected.

Sarpkaya [185] commented that this criterion is not able to explain the axisymmetric vortex breakdown and remarked that the condition predicts instability for a wide range of quasi-cylindrical flows, which some of them show no vortex breakdown. Later, Escudier [52] stated that vortex flows are much less stable to spiral disturbances than to axisymmetric disturbances, which is also reported here.
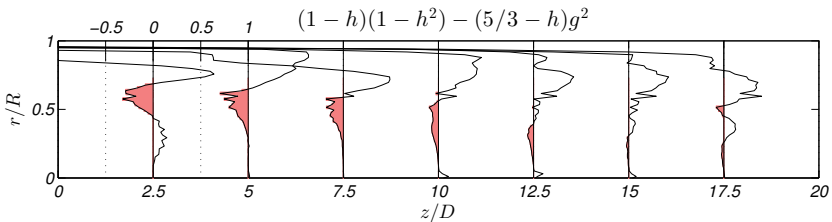
Figure 5.36: Stability condition by Ludwieg [148] for $S = 5.3$ and $Re = 20{,}000$ (DES data)

Leibovich and Stewartson Criterion

Leibovich and Stewartson [125] proposed a more general criterion for the instability of symmetric disturbances of an unbounded columnar vortex in an inviscid flow as follows:

$$U_\phi \frac{d\Omega}{dr} \left[\frac{d\Omega}{dr} \frac{d\Gamma}{dr} + \left(\frac{dU_z}{dr} \right)^2 \right] < 0 \qquad (5.16)$$

Here Ω is the angular velocity and can be expressed by the circumferential velocity as U_ϕ/r and Γ is the circulation given by $U_\phi r$. The instability condition applied to the swirl tube flow is presented in Fig. 5.37. In the tube center the flow is at the onset of stability where the circumferential velocity is characterized by a solid body vortex. Further outwards the flow is stable according to this criterion with a peak where the maximum circumferential velocity occurs. Near the wall, the flow becomes unstable as the criterion is derived for unbounded flows. Comparing this criterion to the stability condition by Howard and Gupta [89] in Fig. 5.35, both show a similar trend and reveal the same flow stability as both consider the axial velocity as well.
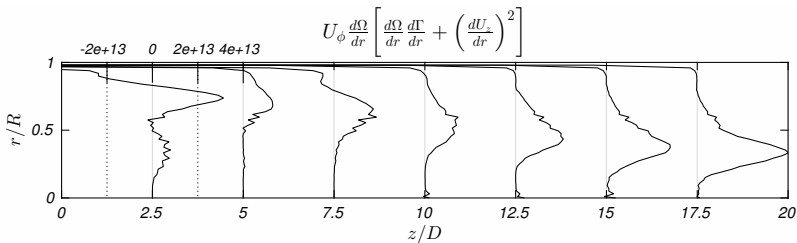
Figure 5.37: Stability condition by Leibovich and Stewartson [125] for $S = 5.3$ and $Re = 20{,}000$ (DES data)

Total Enthalpy Condition

Maršík [150] derived a thermodynamic stability condition based on the analysis of the second law of thermodynamics and the attenuation of the kinetic energy of disturbances. This condition is valid for steady cases and processes as well. Additionally, Maršík [150] showed the generality of this approach by studying the thermoviscous fluid with convection and by investigating the

classical Couette flow between two cylinders [153].
From this stability criterion, a condition for steady state flows is derived based on the minimum of the total enthalpy [151]. The total enthalpy is defined as

$$h_c = \frac{\mathbf{U}^2}{2} + h(T, p) \tag{5.17}$$

depending on the temperature and pressure. In a strong swirling flow, the radial and axial velocity components can be neglected, so that only the circumferential velocity $U_\phi(r)$, the temperature $T(r)$ and the pressure $p(r)$ depend on the radius r. Then, the total enthalpy change for an isentropic and steady flow in differential form yields

$$\frac{dh_c}{dr} = \frac{1}{2}\frac{U_\phi^2}{dr} + \left(\frac{\partial h}{\partial T}\right)_p \frac{dT}{dr} + \left(\frac{\partial h}{\partial p}\right)_T \frac{dp}{dr} = 0 \ . \tag{5.18}$$

This equation is the necessary condition of the extremum (minimum) of the thermodynamic quantity h_c. For equilibrium conditions, the thermodynamic derivatives are as follows [151]:

$$\left(\frac{\partial h}{\partial T}\right)_p = c_p \ , \quad \left(\frac{\partial h}{\partial p}\right)_T = \frac{1}{\rho} - T\left(\frac{\partial(1/\rho)}{\partial T}\right)_p \tag{5.19}$$

and with it the total enthalpy change in Eqn. 5.18 yields

$$\frac{dh_c}{dr} = \frac{1}{2}\frac{U_\phi^2}{dr} + \frac{1}{\rho}\frac{dp}{dr} + c_p\frac{dT}{dr} - T\left(\frac{\partial(1/\rho)}{\partial T}\right)_p \frac{dp}{dr} = 0 \ . \tag{5.20}$$

For incompressible flows the last term is zero, but it plays an important role for compressible flows. So this term is decisive for analyzing the Ranque-Hilsch effect in a swirl tube flow with a radial temperature separation. For a perfect gas the last term in Eqn. 5.20 yields the form $1/\rho$, which is valid for small radial temperature differences ($\rho \neq f(T)$). From the balance of momentum the pressure gradient for the rotational flow is

$$\frac{U_\phi^2}{r} = \frac{1}{\rho}\frac{dp}{dr} \ . \tag{5.21}$$

After inserting the above expression in Eqn. 5.20 together with the perfect gas approximation, one obtains the necessary condition for a corresponding steady state:

$$\frac{dh_c}{dr} = \frac{1}{2}\frac{dU_\phi^2}{dr} + \frac{U_\phi^2}{r} + c_p\frac{dT}{dr} - \frac{1}{\rho}\frac{dp}{dr} = \tag{5.22}$$

$$\underbrace{\frac{d(rU_\phi)^2}{2r^2dr}}_{\text{mechanical stability}} + \underbrace{c_p\frac{dT}{dr} - \frac{U_\phi^2}{r}}_{\text{thermal stability}} = 0 \tag{5.23}$$

This condition can be split into two parts, the mechanical and the thermal stability, which can be satisfied separately. From the derivation, it directly follows the Rayleigh criterion see Eqn. 5.12. The flow is stable, if both criteria are fulfilled

$$\text{Rayleigh criterion} \quad \frac{d(rU_\phi)^2}{2r^2dr} \geq 0 \tag{5.24}$$

$$\text{thermal criterion} \quad c_p\frac{dT}{dr} - \frac{U_\phi^2}{r} \geq 0 \; . \tag{5.25}$$

Figure 5.38 shows the total enthalpy condition in blue and separately the Rayleigh ($\triangle$) and the thermal criterion ($\circ$) for the swirl tube flow. The mechanical condition is positive and becomes only negative near the wall. The maximum coincides with the maximum of the circumferential velocity. In contrast, the thermal condition is slightly negative highlighted in red. The minimum appears in the solid body vortex region. This means that the solid body vortex is unstable according to the thermal criterion by Maršík [150] and therefore explains the transformation of the solid bod vortex into the stable potential vortex. However, the thermal instability is compensated by the mechanical criterion, which means that the vortex system is entirely stable in terms of minimum total enthalpy analogous to the Rayleigh criterion.

In addition, the second differential of the total enthalpy condition will be used to analyze the stability condition. Considering the mechanical and the thermal criterion, the second differential of the condition in Eqn. 5.23 yields

$$\frac{d}{dr}\left(\frac{d(rU_\phi)^2}{2r^2dr} + c_p\frac{dT}{dr} - \frac{U_\phi^2}{r}\right) \geq 0 \tag{5.26}$$

The evaluation of this equation is presented in Fig. 5.39. In the tube core the second differential is positive, which means that the fluctuations are attenuated in a correct way here. This positive region in the core is shrinking towards the tube outlet and is in accordance with the shrinking vorticity in Fig. 5.10. This means that the swirl tube flow is characterized by a stable vortex structure. Moving radial outwards the second differential of the total enthalpy condition becomes negative indicating a local enthalpy maximum. In this region the flow
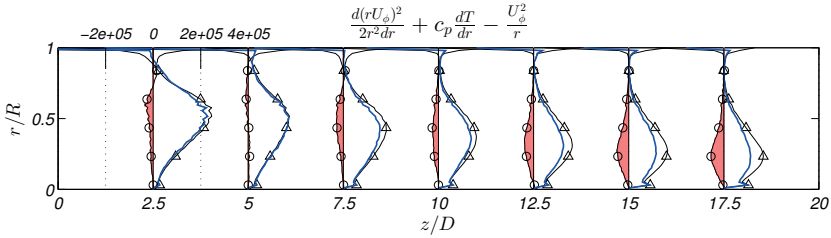
Figure 5.38: Total enthalpy condition by Maršík [151] for $S = 5.3$ and $Re =$ 20,000 (DES data): mechanical criterion ($\triangle$), thermal criterion ($\circ$) and sum of stability ($-$)
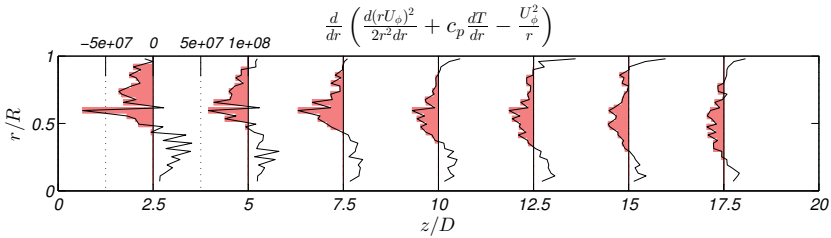
Figure 5.39: Second differential of total enthalpy condition for $S = 5.3$ and $Re = 20,000$ (DES data)

structure changes from a solid body vortex to a potential like vortex, which may initiate flow instabilities in this region.

Application

In the following, the mechanical and thermal condition for a flow state will be applied analytically to the typical flow structures in a swirl tube, the solid body vortex and the potential vortex.

Solid Body Vortex

The flow field of a solid body vortex is defined as

$$U_r = 0, \quad U_\phi = \Omega r, \quad U_z = 0, \quad T = T(r), \quad p = p(r) \tag{5.27}$$

117

with a constant angular velocity Ω. With it, the mechanical condition 5.24 is satisfied

$$\frac{d(\Omega r^2)^2}{2r^2 dr} = 2\Omega^2 r \geq 0 \ . \tag{5.28}$$

The thermal criterion 5.25 yields

$$\int\limits_{1}^{2} c_p dT - \int\limits_{r_1}^{r_2} \frac{\Omega^2 r^2}{r} dr \geq 0 \tag{5.29}$$

and results after calculation in

$$c_p(T_2 - T_1) - \left(\frac{U_{\phi 2}^2}{2} - \frac{U_{\phi 1}^2}{2}\right) \geq 0 \ . \tag{5.30}$$

This inequality can be satisfied, if the first term is greater than the second one. For the here investigated swirl tube flow the temperature in the tube core is lower due to the Ranque-Hilsch effect, which means that $T_2 > T_1$ and for a solid body vortex follows that $U_{\phi 2} > U_{\phi 1}$. As a consequence, both terms are positive, so for the inequality it depends which term is greater.

As an example, the thermal condition for a solid body vortex is analyzed for the swirl tube case $S = 5.3$ and $Re = 20,000$ considering the inlet region ($z/D = 2.5$). Here, the largest solid body vortex region occurs. The circumferential velocity and the temperature difference between the radial positions of the solid body vortex are as follows:

- Solid body vortex region: $r_1/R = 0$, $r_2/R = 0.6$
  $\Delta T_{12} = 0.67 \ K$, $U_{\phi 1} = 0 \ m/s$, $U_{\phi 2} = 44.3 \ m/s$

  $\Rightarrow \ 1007 \ J/(kgK) \cdot 0.67 \ K - (44.3 \ m/s)^2/2 = -307 \ m^2/s^2 \leq 0$

One can see that the thermal condition is negative for a solid body vortex flow. This confirms that the solid body vortex is unstable according to the thermal criterion also shown in Fig. 5.38.

Potential Vortex

The flow field of a potential vortex is defined as

$$U_r = 0, \quad U_\phi = \Gamma/r, \quad U_z = 0, \quad T = T(r), \quad p = p(r) \tag{5.31}$$

with a constant circulation Γ. For this vortex flow, the Rayleigh criterion gives marginal stability:

$$\frac{d(\Gamma)^2}{2r^2 dr} = 0 \geq 0 \ . \tag{5.32}$$

The thermal condition reads

$$\int\limits_1^2 c_p dT - \int\limits_{r_1}^{r_2} \frac{\Gamma^2}{r^3} dr \geq 0 \tag{5.33}$$

and results in

$$c_p(T_2 - T_1) - \left(\frac{U_{\phi 1}^2}{2} - \frac{U_{\phi 2}^2}{2} \right) \geq 0 \ . \tag{5.34}$$

In a potential vortex, the inner circumferential velocity $U_{\phi 1}$ is larger than the outer velocity $U_{\phi 2}$, which means that the second term is positive. This means that the temperature in the vortex core has to be lower than in the outer region to satisfy this condition. So again, due to the Ranque-Hilsch effect and a lower temperature in the tube center both terms are positive and for the inequality it depends which term is greater.

As an example, the thermal condition for a potential vortex is analyzed for the same swirl tube case $S = 5.3$ and $Re = 20,000$. The largest potential vortex region occurs in the outlet region ($z/D = 17.5$), which will be considering in the following. The respective circumferential velocities and temperatures at the radial positions of the potential vortex are as follows:

- Potential vortex region: $r_1/R = 0.53$, $r_2/R = 0.98$
  $\Delta T_{12} = 0.39 \ K$, $U_{\phi 1} = 29.1 \ m/s$, $U_{\phi 2} = 18.9 \ m/s$

  $\Rightarrow 1007 \ J/(kgK) \cdot 0.39 \ K - (29.1^2 - 18.9^2)/2 \ m^2/s^2 = 148 \ m^2/s^2 \geq 0$

For a potential vortex flow the thermal condition is satisfied. This confirms that the potential vortex is stable according to the thermal criterion also shown in Fig. 5.38.

Crocco Theorem

Besides the total enthalpy condition by Maršík, a different approach is used in this section to analyze the total enthalpy in the swirl tube. Crocco (1937)

first found the relation of total enthalpy in terms of entropy and velocity field, which is given as follows [8]:

$$\nabla h_c = T\nabla S + \mathbf{U} \cdot \nabla \mathbf{U} . \tag{5.35}$$

This theorem represents the momentum equation, where S is the entropy and $\mathbf{U}$ the velocity field. In vector form, the last term is the curl (rotational) of the velocity $\nabla \times \mathbf{U}$ and can be rewritten as the vorticity ω. If we assume a flow field in which the entropy S is uniform over the fluid, the Crocco theorem 5.35 then becomes

$$\nabla h_c = \mathbf{U} \times \omega . \tag{5.36}$$

Such a flow is termed homentropic. In cylindrical coordinates, the vorticity is given as

$$\omega(r,\phi,z) = (\omega_r, \omega_\phi, \omega_z) = \left(\frac{\partial U_z}{r\partial\phi} - \frac{\partial U_\phi}{\partial z}, \frac{\partial U_r}{\partial z} - \frac{\partial U_z}{\partial r}, \frac{1}{r}\frac{\partial(rU_\phi)}{\partial r} - \frac{\partial U_r}{r\partial\phi} \right) . \tag{5.37}$$

In a swirling tube flow the radial velocity is small in comparison to the axial and circumferential velocity components and thus can be neglected, such that the total enthalpy differential in radial direction results in

$$\frac{\partial h_c}{\partial r} = U_\phi \omega_z - U_z \omega_\phi \tag{5.38}$$

$$= \frac{U_\phi^2}{r} + U_\phi \frac{\partial U_\phi}{\partial r} + U_z \frac{\partial U_z}{\partial r} . \tag{5.39}$$

Figure 5.40 shows the total enthalpy change in the swirl tube along the radius. For the entire tube, the total enthalpy change is positive with the maximum according to the maximum circumferential velocity as it is derived from the velocity field. In the potential vortex region, the value decreases until near the wall, where the total enthalpy change becomes negative. Overall, the profile is similar to Howard and Gupta's criterion.

Comparing Fig. 5.40 and the mechanical criterion in Fig. 5.38 indicated by the triangles ($\triangle$), the curve progression is very similar. Both approaches show the same trend from the mechanical point of view, although there are differences in their derivation. The Crocco theorem does not consider temperature effects like in the thermal criterion as there is no information about the entropy change. On the other hand, it takes the axial and the circumferential velocity
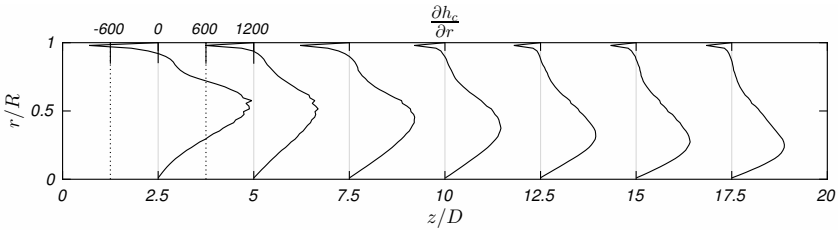
Figure 5.40: Total enthalpy differential $\partial h_c/\partial r$ for $S = 5.3$ and $Re = 20,000$ (DES data)

component into account compared to the total enthalpy condition by Maršík, which considers only the dominant circumferential velocity.

5.9.3 Conclusions

In summary, the swirl tube flow is analyzed in terms of vortex breakdown and flow stability. It has been shown that the flow force analysis by Escudier and Keller [56] is suitable to determine the vortex breakdown region in a swirling tube flow, which is characterized by a Rankine like vortex. Moreover, the criterion based on the Rossby number by Spall et al. [203] is capable to predicting the occurrence of vortex breakdown considering the maximum circumferential velocity. It follows that vortex breakdown is possible in swirl dominated flows below a Rossby number of 0.65. In addition, the comparison between axial and circumferential local Reynolds numbers confirms Spall's criterion and illustrates that vortex breakdown occurs in flows with higher circumferential than axial Reynolds number. Consequently, in axial dominated flows no backflow appears.

Furthermore, the swirl tube flow has been investigated regarding the stability criteria by Howard and Gupta [89], Ludwieg [148] and Leibovich and Stewartson [125]. All are based on Rayleigh's criterion and consider different disturbances. The stability condition by Howard and Gupta and Leibovich and Stewartson are quite similar with a stable region over the entire tube, but near the wall initial instabilities occur. The stability criterion to spiral disturbances by Ludwieg indicates instabilities where the circumferential velocity has its maximum.

Moreover, two conditions regarding the total enthalpy for steady state flows have been analyzed and have been proven to be capable of stability analysis.

The condition according to Maršík [150] considers the mechanical and the thermal stability. Whereas Crocco's theorem has been derived for a homentropic flow and does not consider temperature effects, but additionally takes the axial velocity into account. Both approaches are more or less the same from mechanical point of view. However, Maršík's condition has the advantages that it can be evaluated directly by measured quantities and that it considers temperature effects as well. This is necessary due to the Ranque-Hilsch effect in strong swirling flows investigated here. The stability analysis revealed that the solid body vortex is unstable according to the thermal criterion by Maršík [150] and hence explains the transformation of the solid body vortex into the stable potential vortex. However, the thermal instability is compensated by the mechanical criterion, which means that the vortex system is entirely stable in terms of minimum total enthalpy.

Multiple Inlet Swirl Tube

In this chapter, the detailed investigations for the multiple inlet swirl tubes are presented. These swirl tubes are characterized by maximum five tangential inlet jets along the tube, which again increase the swirl strength and thus the heat transfer. The advantage of this concept is a more homogeneous heat transfer distribution over the entire tube with a lower pressure loss due to lower inlet jet velocities. First, the experimentally measured flow field, the heat transfer and the pressure loss are shown for all configurations with one (MI1), three (MI3) and five (MI5) tangential inlet jets. Then, the thermal performances of the different multiple inlet swirl tubes are determined and quantitatively assessed. Additionally, results of DES simulations for the MI5 configuration are shown to allow deeper insights into the occurring flow structures.

6.1 Experimental Details

For the multiple inlet swirl tube experiments the existing rig as shown in Fig. 3.1 was modified. The measuring section was exchanged with a multiple inlet swirl tube and an additional plenum as depicted in Fig. 6.1. For the
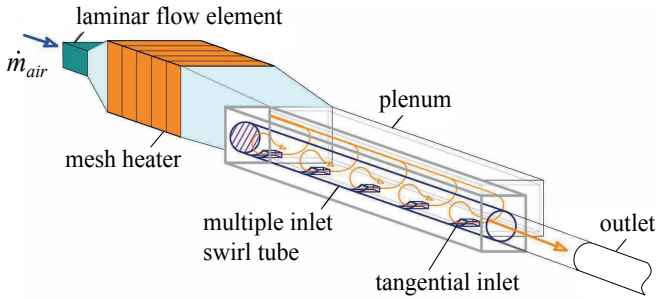
Figure 6.1: Experimental rig for the multiple inlet swirl tubes

heat transfer measurements the air can be heated by the same mesh heater providing a sudden temperature step. The following additional plenum enables to supply up to five tangential inlets. It is directly attached to the swirl tube. The air flow path through the tangential inlets is sketched with orange arrows. Each inlet section can be closed separately by a curved fitting block to maintain the cylindrical tube cross-section. Finally, the air exits the measuring section into an outlet tube connected to the vacuum pump. The entire model is made of Perspex because of its low thermal conductivity for the heat transfer experiments and to provide optical access for the PIV and TLC measurements.

The dimensions of the multiple inlet swirl tube and the positions of the measurement probes are shown in Fig. 6.2. The tube diameter is $D = 50$ mm with a length of $L/D = 20$ analogous to the baseline swirl tube. In axial direction eight thermocouples (TC) are positioned equidistantly in the tube center through capillary tubes. Additionally, five thermocouples are placed in the tangential inlet channels. At the same axial coordinates, pressure taps are placed to measure the static pressure along the tube wall. The respective geometrical swirl numbers according to Eqn. 1.5 are $S_1 = 5.76$ for the one inlet case, $S_3 = 1.92$ for the three inlets case and $S_5 = 1.15$ for the five inlets swirl tube. The investigated Reynolds numbers are based on the tube diameter and the axial bulk velocity in accordance with the baseline swirl tube. The PIV measurements are conducted at $Re = 10{,}000$ and $20{,}000$ for MI1, at $Re = 10{,}000$ and $30{,}000$ for MI3 and at $Re = 10{,}000$ and $50{,}000$ for MI5 to obtain one case with the same inlet mass flow rate and thus inlet jet velocity. The heat transfer coefficients are measured for a Reynolds number range from $10{,}000$ to $40{,}000$ for MI1 and MI3, respectively, and for a range from $10{,}000$ to $80{,}000$ for MI5.
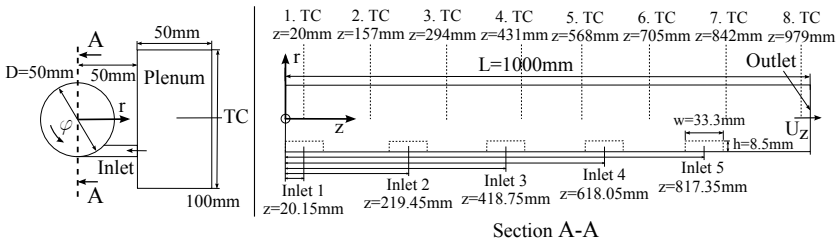
Figure 6.2: Multiple inlet swirl tube geometry and thermocouple (TC) position
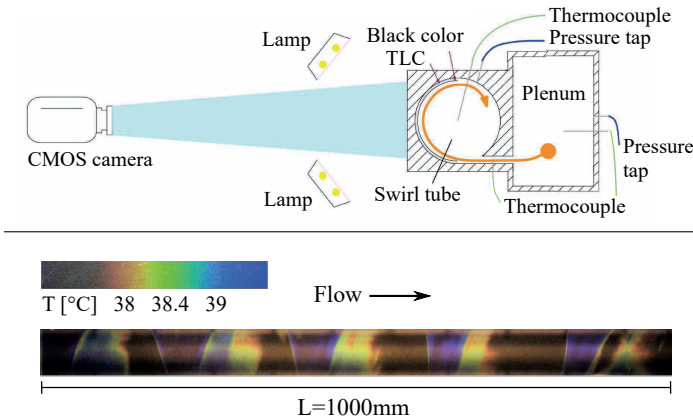
Figure 6.3: Top: TLC measurement setup with thermocouple and pressure tap positions, bottom: liquid crystal color play for the MI5 swirl tube

The measurement setup for the heat transfer experiments and a typical liquid crystal color play for the MI5 swirl tube is presented in Fig. 6.3. The setup explains the position of the thermocouples and the pressure taps in the swirl tube, in the inlet section and in the plenum. For the TLC measurements, the inner tube wall is sprayed with layers of TLC and black paint. The Perspex model is illuminated with two lamps. The TLC color play in the bottom figure emphasizes the early color change in regions where the tangential jets impinge on the curved wall and the further development of the flow in a screw-shape. The typical TLC color change starts from unchanged (black due to the background) to red, yellow, green and blue.

6.2 Computational Details

The numerical setup for the multiple inlet swirl tube simulations is chosen in accordance with the simulation setup for the baseline swirl tube described in section 5.2. Here, only the MI5 swirl tube is exemplarily simulated. The computational domain consists of five inflow boundary sections, the actual tube, an outlet tube and a plenum. The computational grid for the MI5 configuration is a hexahedral O-grid with 9 and 12 mio cells for the Reynolds numbers 10,000 and 50,000, respectively. More details about the mesh, the Kolmogorov length scale η and the wall and center cell sizes are listed in Table 6.1.

The inflow conditions for each tangential inlet are obtained from a preliminary RANS simulation for the entire domain with additional inlet plenum [178]. A DES simulation of the entire swirl tube and plenum would be too time-consuming. The mass flow distribution and the respective velocity through each inlet for the investigated Reynolds numbers are summarized in Table 6.2. The mass flow rate through the first two inlets is almost the same, but for the following three inlets the mass flow rate increases due to an increasing relative pressure loss over the subsequent inlets. Comparing the first and the last inlet, 30% more mass flow goes through the fifth inlet.

Table 6.1: Summary of number of cells, Kolmogorov length scale η and used wall and center cell sizes of the computational meshes for the investigated MI5 swirl tubes

mesh	cells	η [m]	Δy_w [m]	$(\Delta x, \, \Delta y, \, \Delta z)_c$ [m]
$Re = 10,000$	$9 \cdot 10^6$	$5 \cdot 10^{-5}$	$3 \cdot 10^{-5}$	$(9.4, \, 7.9, \, 11.0) \cdot 10^{-4}$
$Re = 50,000$	$12 \cdot 10^6$	$1.5 \cdot 10^{-5}$	$2.5 \cdot 10^{-5}$	$(7.5, \, 6.8, \, 10.4) \cdot 10^{-4}$

Table 6.2: Mass flow and inlet velocity distribution of the MI5 swirl tube simulations

inlet number	1	2	3	4	5
$\dot{m}_i/\dot{m}_{ges}$	18.0%	17.8%	19.2%	21.3%	23.7%
U_{in} [m/s] ($Re = 10,000$)	4.03	3.97	4.30	4.78	5.30
U_{in} [m/s] ($Re = 50,000$)	20.14	19.87	21.48	23.89	26.49

6.3 Flow Field

In the following section, the flow field for the different multiple inlet swirl tubes is discussed in detail. First, the axial and circumferential velocity components are presented followed by the turbulence kinetic energy, the vorticity and the local swirl number. Again, the axial bulk velocity $\overline{U}_z$ will be used to show all results in a non-dimensional form.

6.3.1 Axial Velocity

The contour plots of the experimental non-dimensional axial velocity $U_z/\overline{U}_z$ for the swirl tubes with one, three and five inlets for $Re = 10{,}000$ are presented in Fig. 6.4 a) - c). For comparison, the numerical results for the five inlets configuration is shown in d). The contour legend from the one inlet and the multiple inlet swirl tubes differ for a clearer display. The respective inlet sections are displayed with black rectangles.

The axial velocity for the one inlet configuration is similar to the results of the baseline swirl tube with a strong axial flow in the near wall region and an axial backflow in the tube center. The backflow strength increases towards the tube outlet. A major difference to the baseline swirl tube is that the axial backflow in the tube center is characterized by a standing wave, which is caused by an unsymmetrical flow field due to only one tangential inlet.

The multiple inlet configurations show a completely different axial flow structure, which changes between each inlet jet due to the additional mass flow. Thus, the swirl tube can be divided into three or five different sections, respectively, highlighted with the black dashed lines. In the first section several alternating recirculation areas occur, indicated by the blue color and a black contour line representing zero velocity. These recirculation areas are caused by an unsymmetrical inlet jet. In front of each subsequent inlet, a recirculation zone occurs near the opposite wall (blue zones) and thus reduces the cross-sectional area of the tube. Due to this reduction, the flow from the previous section is accelerated in the center. The axial flow in the second section for MI3 is characterized by a maximum axial velocity in the tube center and no axial backflow occurs anymore. In the last and third region of the MI3 configuration the largest axial velocity component appears in the outer region accompanied with a low velocity in the tube center. Regarding the configuration with five tangential inlet jets, five different flow regions occur, respectively. At the first inlet, recirculation areas are evident, whereas further downstream the enhanced mass flow is responsible for an axial flow towards the tube outlet.
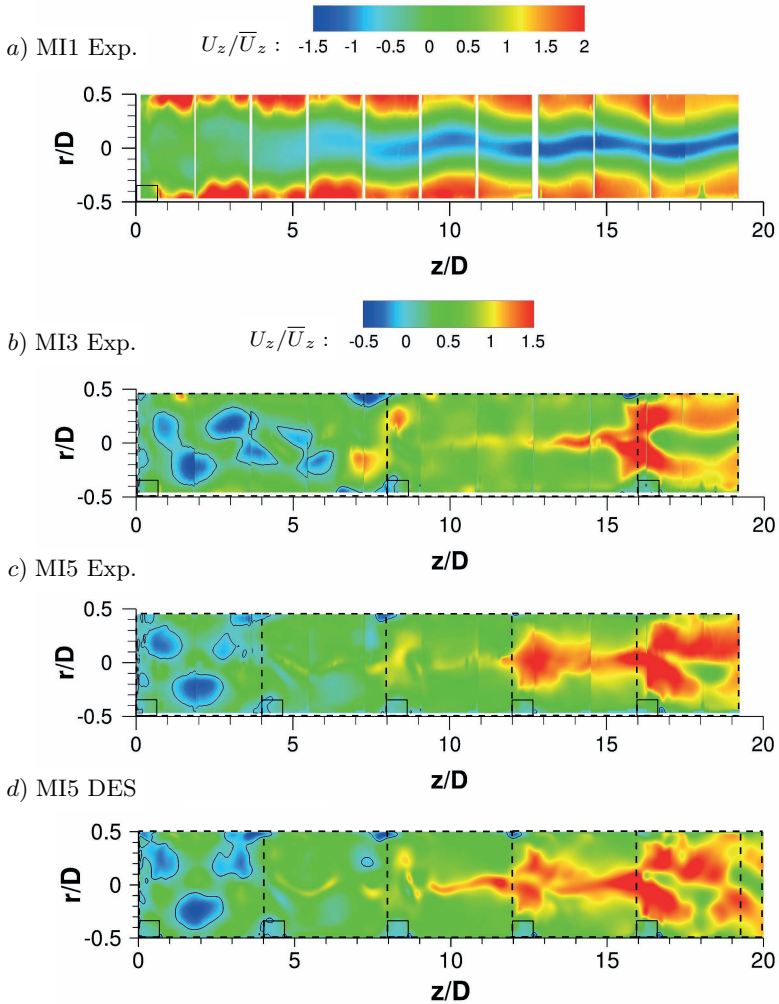
Figure 6.4: Experimental non-dimensional axial velocity for MI1, MI3 and MI5 and DES results for MI5 at $Re = 10{,}000$

With increasing number of inlets the axial flow becomes stronger, first in the center of the tube and after the fifth inlet also in the outer region of the tube, analogous to the three inlet configuration.

Comparing the experimental and the numerical axial contours of the MI5 configuration in Fig. 6.4 c) and d), one can see a good agreement for the entire tube. In front of each inlet, a recirculation zone near the opposite wall is evident, which shrinks the cross-sectional area for the upstream flow and accelerates it in the tube center. Thus, the DES simulation is capable to predicting such a complex flow field with five tangential jets with a good accuracy.

6.3.2 Circumferential Velocity

In the following, the contour plots of the experimental non-dimensional circumferential velocity $U_\phi / \overline{U}_z$ for all configurations with one, three and five tangential inlet jets for $Re = 10,000$ are shown in Fig. 6.5 a) - c). For comparison, the numerical results of the MI5 configuration is presented in d). Again, the inlets are displayed with a black rectangle and the contour legend for the one inlet case and the multiple inlet cases are different for a clearer presentation.

The circumferential velocity for the one inlet configuration $U_{\phi,max} / \overline{U}_z = \pm 6$ is clearly the largest velocity component and three times larger than the related axial velocity component $U_{z,max} / \overline{U}_z = 2$. Near the tangential inlet the circumferential velocity is largest and decreases continuously towards the tube outlet, which is in accordance to the baseline swirl tube shown in section 5.3.2.

Figure 6.5 b) shows the circumferential velocity for the MI3 configuration. From the contour color it is evident that the absolute velocity value is almost constant over the entire tube. The additional tangential inlet jets in axial direction induce additional swirl and keep the circumferential velocity of around $U_{\phi,max} / \overline{U}_z = \pm 2$ on a constant level. The same appears for the MI5 configuration. The overall circumferential velocity component of around $U_{\phi,max} / \overline{U}_z = \pm 1.5$ is lower than for MI3, but almost constant over the entire tube. For both configurations, the vortex core is not directly in the tube center as already shown for the MI1 swirl tube. It scatters around the center in a wave-like form. This is due to the unsymmetrical tangential inlet jets from one side of the tube.

Comparing the experimental and the numerical results in Fig. 6.5 c) and d), the DES slightly overestimates the circumferential velocity by maximum 20% especially in the first inlet section. This might be due to an overestimated tangential inlet velocity distribution from the preliminary RANS simulation.
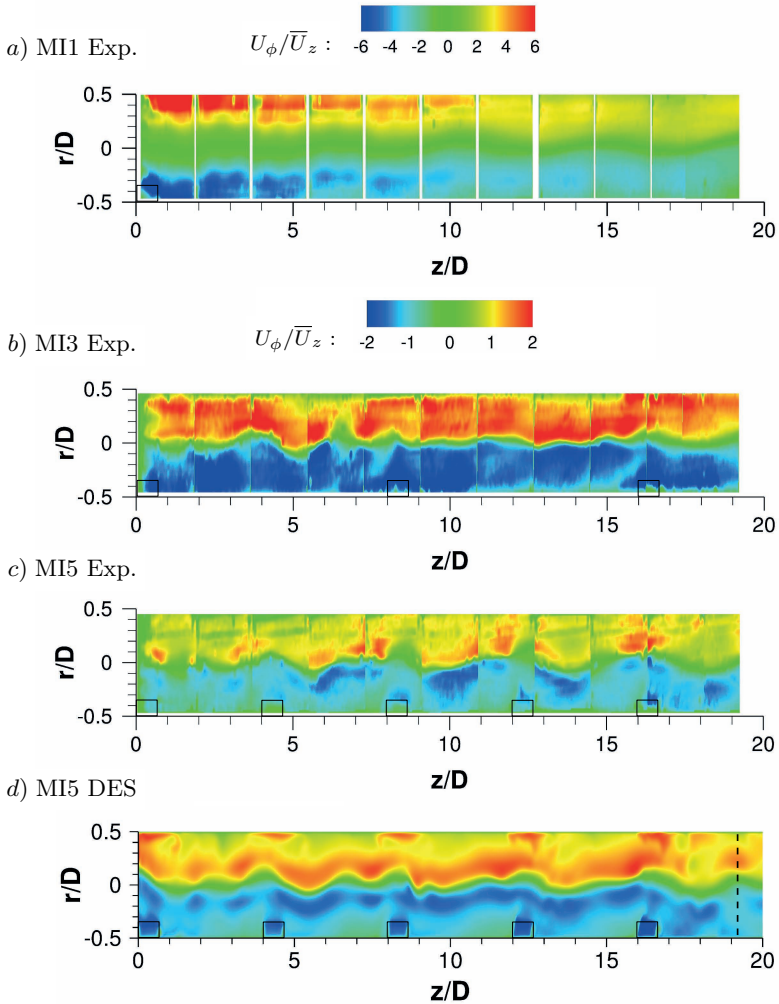
Figure 6.5: Experimental non-dimensional circumferential velocity for MI1, MI3 and MI5 and DES results for MI5 at $Re = 10{,}000$

However, the overall circumferential velocity distribution shows a good agreement. The simulation provide a more detailed view into the occurring flow structures. The wave-like form in the vortex core becomes clearer and a larger circumferential velocity component near the wall on the other side of the inlet is evident. The enhanced impinging swirl flow might be responsible for the high heat transfer in the inlet jet regions, which will be shown later in the heat transfer section 6.5.

6.3.3 Turbulence Kinetic Energy

The turbulence kinetic energy $k/\overline{U}_z^2$ gives insight in the energy of the turbulent fluctuations in swirl tubes. It is shown for the experimentally investigated multiple inlet configurations in Fig. 6.6 a) - c). Again, the numerical results for MI5 is presented in d).

For the one inlet case, the highest kinetic energy occurs near the inlet in the outer region of the tube. Here, the largest circumferential velocity occurs which causes high turbulent fluctuations. Further downstream near the tube outlet, the turbulence kinetic energy increases in the tube center similar to the baseline swirl tube.

The main part of the turbulence kinetic energy for the multiple inlet configurations appears in the tube center in contrast to the one inlet swirl tube. For the MI3 configuration, the kinetic energy occurs also at each inlet jet and along the opposite wall of the tube, besides the high turbulence in the center. The turbulence kinetic energy distribution for MI5 is quite similar to the MI3 configuration, but the magnitude is slightly lower due to the overall lower velocity components.

Comparing the experimental and numerical results in Fig. 6.6 c) and d), one can see a good agreement. The highest turbulence in the tube center is evident especially near the tube outlet. Moreover, the high kinetic energy opposite of the inlet jets is clearer in particular for the fourth and fifth jet. Here, the DES simulation gives an additional insight into the occurring flow structures.

6.3.4 Vorticity

The vorticity is useful to analyze the rotation of a fluid as already introduced in section 5.3.5 and is therefore predestined for swirling flows. In the following, the experimental non-dimensional vorticity $\omega_\phi D/\overline{U}_z$ is presented in Fig. 6.7 for all investigated configurations MI1, MI3 and MI5. The contour legend for
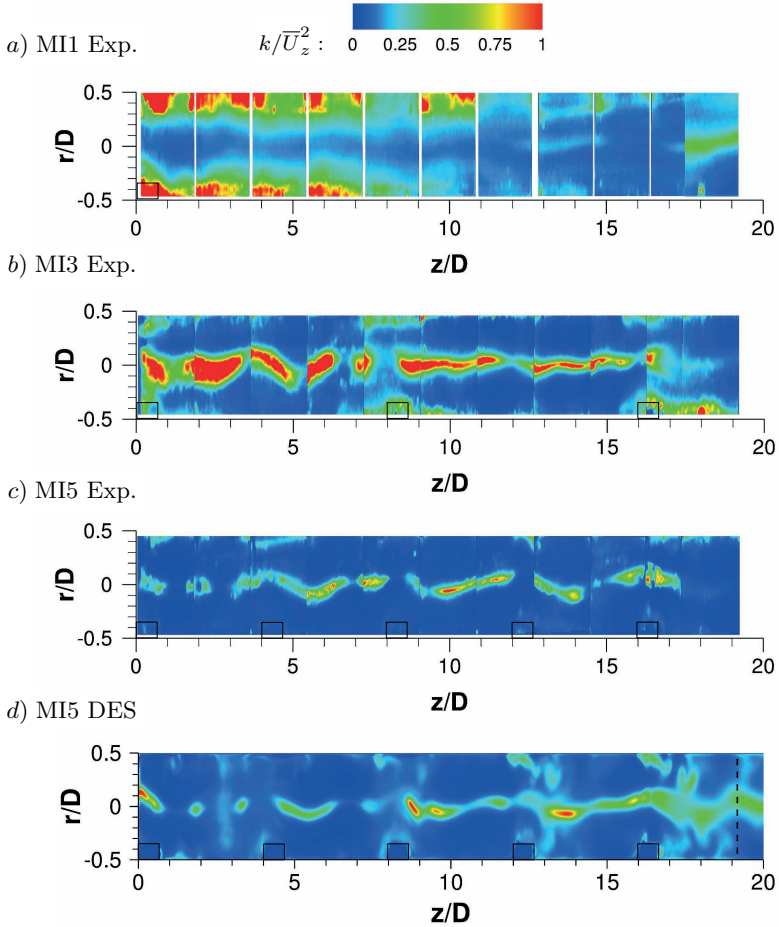
Figure 6.6: Experimental non-dimensional turbulence kinetic energy for MI1, MI3 and MI5 and DES results for MI5 at $Re = 10,000$

the multiple inlet cases is again adjusted for a clearer presentation.

For the configuration with one inlet jet, a dominant vortex system is evident indicated by a large positive and negative vorticity band on each half of the tube. It is also noteworthy that this vortex structure describes a wave-like form similar to the axial flow as shown in Fig. 6.4 due to the unsymmetrical inlet jet.

The vorticity for the swirl tube configurations with multiple inlet jets becomes more complex as shown in Fig. 6.7 b) and c). In the tube center, one can see periodically changing positive and negative vorticity areas over the entire tube. Near the inlet jets, dominant vortex structures are evident as well as on the opposite side of the tube. This indicates that these vortex structures are spread over the tube circumference.

For a more detailed insight in the occurring vortices, the Q-criterion is presented in Fig. 6.8 for the swirl tube with five inlet jets. The definition of the Q-criterion is given in section 5.3.5. One can see two main structures in the swirl tube that are already indicated by the vorticity contour. First, a vortex in the tube center with a wave-like form. Second, large spiral vortices around the tube axis especially near the inlet jets. The strong tangential momentum induced by the jets causes these turbulent structures, which, in turn, cause the enhanced heat transfer in the inlet regions. The detailed heat transfer distribution will be shown later in section 6.5.

6.3.5 Swirl Number

The local swirl number for the five inlets swirl tube is exemplarily shown in Fig. 6.9 obtained from numerical simulations. The swirl number definition as the angular momentum to the axial momentum of the flow is already given in section 1.4. The vertical lines indicate the tangential inlets.

The previously shown flow field for the MI5 swirl tube is characterized by an almost constant circumferential velocity and a rather complex axial velocity distribution, which changes after each inlet jet. This strongly influences the local swirl number in Fig. 6.9. It shows a peak value at each inlet. Between the inlets, the local swirl number decreases in each case. The highest local swirl number occurs for the first two inlets due to the low axial velocity in these regions. Further downstream, the axial velocity and therefore the axial momentum increase due to the increasing mass flow. As a consequence, the local swirl number decreases because the circumferential velocity and its momentum keep almost constant.

a) MI1

$\omega_\phi D/\overline{U}_z :$ -0.5 -0.25   0   0.25   0.5

b) MI3

$\omega_\phi D/\overline{U}_z :$ -0.2 -0.1   0   0.1   0.2

c) MI5
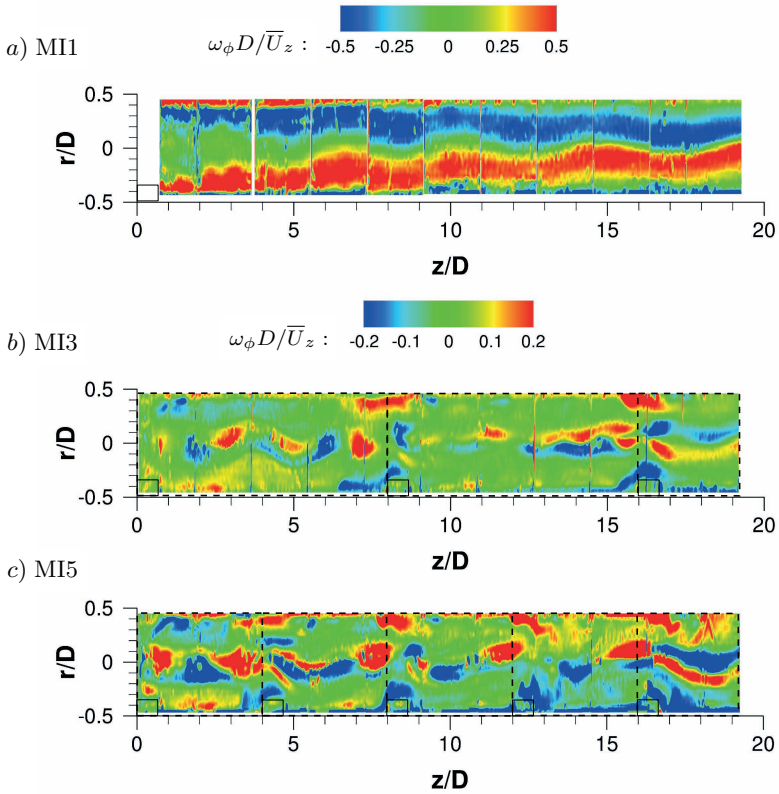
Figure 6.7: Experimental non-dimensional vorticity for MI1, MI3 and MI5 at $Re = 10,000$

Figure 6.8: DES vortex structure in the MI5 swirl tube for $Re = 10,000$, iso-surfaces of $Q = 1$, color represents axial velocity
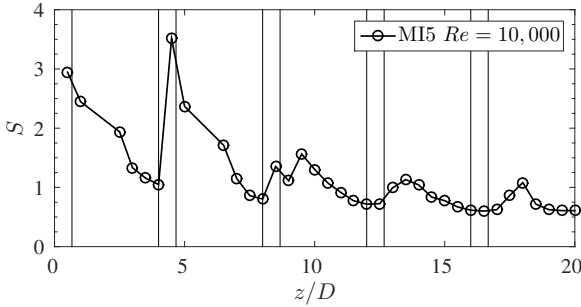
Figure 6.9: DES local swirl number for MI5 at $Re = 10,000$

6.4 Temperature

The previous sections highlighted the complexity of the flow field in swirl tubes with multiple inlet jets. It is evident that the flow field influences the temperature field, which on the other hand is needed for the evaluation of the heat transfer. To determine a reasonable reference temperature for the heat transfer coefficient, the mean temperature field in the swirl tube with five inlet jets obtained from DES simulations is shown in Fig. 6.10 for $Re = 10,000$ and 50,000. The inlet fluid temperature is set to 333 K and the wall temperature is constant at 293 K. For a clearer temperature contour, the range of the legend has been adjusted from 303 K to 333 K, because only in the wall boundary layer the temperature decreases to 293 K.

Both temperature contours show an almost homogeneous temperature distribution over the entire tube. The tangential inlet jets induce a high temperature which develops over the tube circumference and is still visible on the opposite tube wall. At the beginning of the tube, a low temperature area is located in the center. Here, the measured thermocouple temperature in the tube center would not be a suitable reference temperature for the heat transfer coefficient because it strongly differs from the temperature near the wall.

From the temperature distribution, two possible reference temperatures for the heat transfer coefficient could be evaluated. First, the jet inlet temperature which impinges on the curved wall and is therefore responsible for the enhanced heat transfer at the inlets. For the sections between the inlets, this temperature would be too high and thus underestimates the local heat transfer coefficient. Second, the local bulk temperature measured in the tube center which would give a reasonable heat transfer in the sections between the inlets.
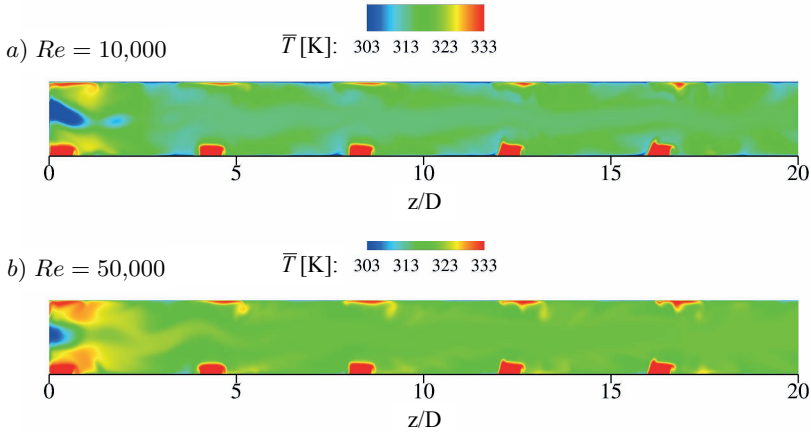
Figure 6.10: DES mean temperature for MI5 at $Re = 10,000$ (a) and $Re = 50,000$ (b) with $T_{in} = 333K$ and $T_{wall} = 293K$

However, the local bulk temperature at the inlets would be too low and over-estimates the heat transfer coefficient in this regions.

In the following, the inlet jet temperature is used as a conservative reference temperature for the evaluations of the heat transfer coefficients. As just mentioned, this reference temperature will underestimate the heat transfer in regions without inlets. Therefore, the largest influence will be on the MI1 configuration and the lowest influence will be for the MI5 configuration. However, the conservative inlet jet temperature seems a more reasonable reference temperature than the bulk temperature, which would be too low in the inlet region and thus overestimates the heat transfer coefficient.

Finally, the experimentally measured radial temperature distribution for two configurations with three and five inlets for $Re = 40,000$ under adiabatic conditions is presented in Fig. 6.11. Depending on the number of inlets, a different inlet jet velocity occurs for the same Reynolds number. It is evident that the inlet jet velocity for MI3 is higher than the one for MI5. For a higher inlet jet velocity and therefore a higher swirl strength, a larger radial temperature difference can be observed. For MI3 a radial temperature difference of around 0.4 K for all axial positions has been measured. For MI5 and a lower inlet jet velocity, a temperature difference between 0.1 K and 0.3 K occurs, which depends on the thermocouple position next to an inlet or away from it. These measurements indicate that the temperature distribution under adiabatic con-
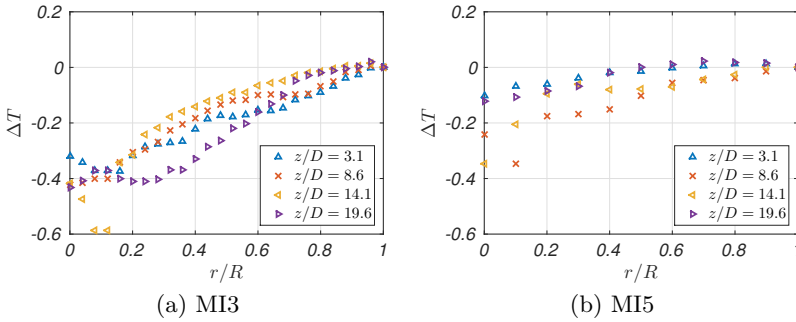
Figure 6.11: Experimental radial temperature distribution $\Delta T = T_c - T_w$ for $Re = 40{,}000$ for MI3 (a) and MI5 (b)

ditions is almost homogeneous over the swirl tube with multiple inlet jets and that the Ranque-Hilsch effect is not present anymore. The lower circumferential velocity through the multiple inlet is not strong enough and the additional inlet jets suppress a radial temperature separation.

6.5 Heat Transfer

In this section, the results for the experimentally and numerically obtained heat transfer for the swirl tubes with multiple inlet jets will be presented. First, a wall heat flux contour for MI5 obtained from DES is exemplarily shown. Then, the experimental circumferentially averaged Nusselt numbers for the configurations with one, three and five inlet jets are presented, respectively. The heat transfer coefficients are measured in a Reynolds number range from 10,000 to 40,000 for MI1 and MI3, respectively, and from 10,000 to 80,000 for MI5. For an easier comparison of the different swirl tube configurations, the heat transfer coefficient is based on the conservative inlet jet temperature as discussed in the previous section.

Figure 6.12 shows the numerically obtained wall heat flux in the swirl tube with five inlet jets for $Re = 10{,}000$. One can clearly see the enhanced heat flux from each inlet jet. Between the inlets, the wall heat flux continuously decreases until the next inlet jet. The highest wall heat flux occurs for the last inlet due to the increasing mass flow rate and therefore highest inlet jet velocity compared to the upstream inlets. An overview of the respective inlet jet velocities has already been given in Table 6.2.
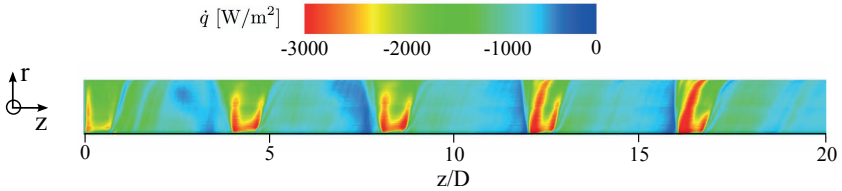
Figure 6.12: DES wall heat flux in the MI5 swirl tube for $Re = 10,000$

In the following, the circumferentially averaged Nusselt numbers for various Reynolds numbers are presented. First, the experimental Nusselt numbers for one tangential jet is shown in Fig. 6.13. It is evident that the highest heat transfer occurs in the inlet jet region. It increases with increasing Reynolds number. For the highest investigated Reynolds number of 40,000 the maximum Nusselt number reaches a value of around 1000. With increasing axial distance z/D from the inlet jet, the heat transfer continuously decreases.
Figure 6.14 shows the experimental Nusselt numbers for the MI3 (a) and the MI5 (b) swirl tube configuration. For each inlet jet an increased heat transfer is observed. Between the tangential jets the Nusselt numbers decrease until the next inlet as already shown in the wall heat flux contour in Fig. 6.12. With increasing Reynolds number, also the Nusselt number increases. For the Reynolds number of 40,000, the maximum Nusselt number is around 300 for the three inlet configuration and around 200 for the five inlets configuration. It is evident that the maximum Nusselt number for the multiple inlet jets is lower than for the swirl tube with only one inlet jet ($Nu = 1000$), but due
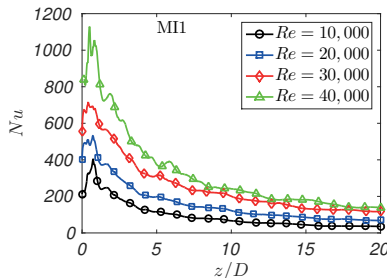
Figure 6.13: Experimental Nusselt numbers for the one inlet swirl tube for different Reynolds numbers

(a) MI3

(b) MI5
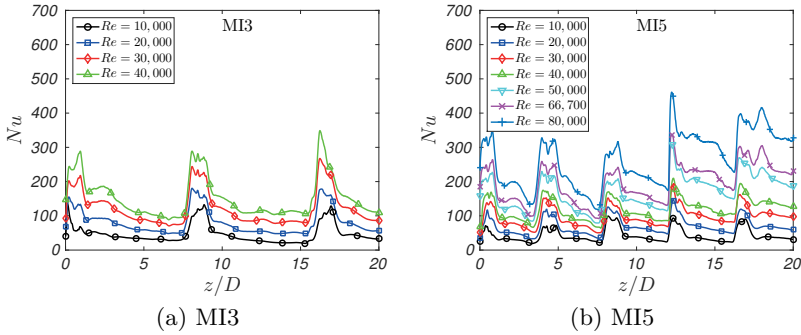
Figure 6.14: Experimental Nusselt numbers for the MI3 and the MI5 swirl tube for different Reynolds numbers

to the additional tangential jets and enhanced swirl strength the heat transfer distribution is more homogeneous over the entire tube length as shown in Fig. 6.14.

It can be concluded that two major mechanisms are responsible for the homogenous heat transfer in the MI5 swirl tube. At the inlets, the tangential jets impinge on the concave wall, cause an enhanced turbulence and consequently an enhanced convective heat transfer. This can be also seen in the large spiral vortices at the inlets in Fig. 6.8, which become stronger for the inlets further downstream due to a higher inlet mass flow rate. Moreover, with increasing number of inlets and therefore mass flow rate in the swirl tube, the axial velocity becomes stronger as shown in Fig. 6.4. This causes an enhanced heat transfer between the inlet jets and therefore a more homogeneous heat transfer distribution over the entire tube.

Next, a comparison between the experimental and the numerical obtained heat transfer is presented. In Fig. 6.15 the results for the MI5 swirl tube and a Reynolds number of 10,000 (a) and 50,000 (b) are depicted. The axial position of the tangential inlet jets is indicated by vertical lines. The Nusselt number comparison between experiment and numerics shows a good agreement for such a complex flow in a multiple inlet jet swirl tube for both a low and a high Reynolds number. For both Reynolds numbers, slight deviations between the first and second jet can be seen. This might be due to the overestimated tangential inlet velocity distribution and therefore overestimated circumferential velocity in this region as already discussed in section 6.3.2. However, this comparison confirms that the DES is capable to predicting the heat transfer for a multiple inlet swirl tube very well.

(a) $Re = 10,000$

(b) $Re = 50,000$
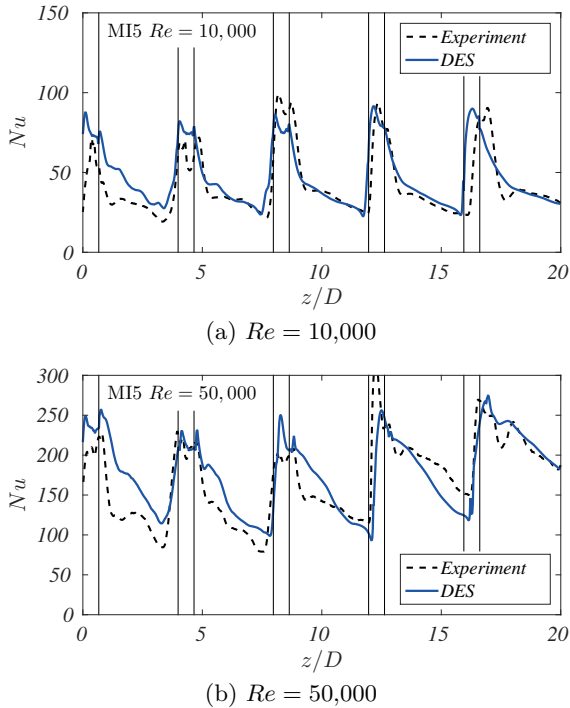
Figure 6.15: Comparison of Nusselt numbers from experiments and DES for the MI5 swirl tube

Finally, the experimental globally averaged Nusselt numbers for all swirl tube configurations and all investigated Reynolds numbers are presented in Table 6.3. It is evident that the globally averaged heat transfer increases with increasing Reynolds number. The highest heat transfer can be achieved with only one inlet jet. With more tangential inlet jets the maximum Nusselt numbers decrease.

For completeness, the globally averaged normalized Nusselt numbers for all swirl tube configurations and Reynolds numbers are summarized in Table 6.4. The Nusselt numbers are again normalized with the Dittus-Boelter correlation for an axial tube flow given by $Nu_0 = 0.023 \ Re^{0.8} Pr^{0.3}$ [42]. It has to be mentioned that the mass flow rate and consequently the Reynolds number increase along the tube length due to the additional inlet jets. This makes

a comparison of the normalized heat transfer difficult as the Dittus-Boelter correlation is based on a constant Reynolds number.

Table 6.3: Experimental globally averaged Nusselt numbers $\overline{Nu}$

Re	10,000	20,000	30,000	40,000	50,000	66,700	80,000
MI1	96.1	162.6	255.0	327.0	-	-	-
MI3	46.7	81.0	121.6	153.0	-	-	-
MI5	42.3	68.7	97.3	119.4	166.4	197.1	261.5

Table 6.4: Experimental globally averaged normalized Nusselt numbers $\overline{Nu}/Nu_0$

Re	10,000	20,000	30,000	40,000	50,000	66,700	80,000
MI1	2.89	2.83	3.13	3.31	-	-	-
MI3	1.48	1.47	1.50	1.55	-	-	-
MI5	1.28	1.23	1.23	1.17	1.34	1.32	1.47

6.6 Pressure Loss

The pressure loss for the three multiple inlet swirl tubes along the axial coordinate z/D for $Re = 10,000$ is presented in Fig. 6.16 (a). Additionally, a more detailed plot for the MI3 and MI5 configuration is shown in Fig. 6.16 (b). Again, the pressure loss is normalized with the dynamic pressure $q = 1/2\rho\overline{U}_z^2$. The overall pressure loss for one inlet jet is much higher compared to the multiple inlet jets configurations. Near the inlet jet, the largest pressure loss occurs and decreases continuously along the tube length. For MI3 shown in Fig. 6.16 (b), the pressure drops after the first inlet jet, is then slightly enhanced at the second inlet jet and again decreases at the last jet. For MI5 the pressure drop at the beginning of the tube is quite low due to a low mass flow rate. With axial tube length the pressure difference between each measurement position increases due to an increasing mass flow further downstream.

The detailed experimental friction factor enhancement over the tube length is listed in Table 6.5. It is normalized with the friction factor for an axial tube flow. Here, the Blasius equation $f_0 = 0.3164\ Re^{-0.25}$ [188] is used as already

(a) all MI

(b) MI3 and MI5 detail
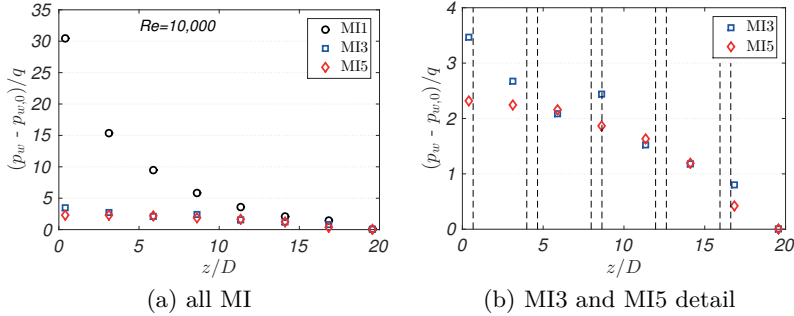
Figure 6.16: Experimental normalized pressure loss for all investigated multiple inlet configurations and $Re = 10{,}000$

introduced in section 5.7. It is evident that the friction factor increases with increasing Reynolds number. The highest pressure loss occurs for only one inlet jet. Depending on the Reynolds number, it is between 49 and 66 times higher compared to an axial tube flow. With increasing number of tangential inlet jets, the friction factor enhancement drastically decreases to around 10% for MI3 and 7.5% for MI5. This is due to lower inlet jet velocities compared to the MI1 swirl tube configuration.

Table 6.6 shows the experimental friction factor enhancement including the pressure drop over the tangential inlets. For this purpose, the static pressure in the tube is measured against the pressure in the plenum. It is clear that the inlet jets cause a large pressure loss. For the MI1 and MI3 configuration, the pressure drop over the inlets is the decisive part, which is around 2 to 3 times the pressure drop over the tube. For MI5 the pressure drop over the inlets and over the tube are in the same order of magnitude. The friction factor enhancement over the tube including inlets is around twice the one over the tube.

Table 6.5: Experimental friction factor enhancement f/f_0 over the tube

Re	10,000	20,000	30,000	40,000	50,000	66,700	80,000
MI1	48.95	54.93	61.42	66.12	-	-	-
MI3	5.14	5.43	6.52	6.74	-	-	-
MI5	3.59	4.35	4.71	4.84	5.36	5.57	5.80

Table 6.6: Experimental friction factor enhancement f/f_0 over the tube in-
cluding inlets

Re	10,000	20,000	30,000	40,000	50,000	66,700	80,000
MI1	152.81	173.74	195.84	214.85	-	-	-
MI3	16.78	19.13	23.27	27.74	-	-	-
MI5	6.46	7.81	8.62	8.87	9.87	10.34	10.89

6.7 Thermal Performance

In this section, the thermal performance of the investigated multiple inlet swirl
tubes is used to compare and rate the different configurations. For this purpose,
the globally averaged normalized Nusselt numbers $\overline{Nu}/Nu_0$ and the thermal
performance parameters $(\overline{Nu}/Nu_0)/(f/f_0)^{1/3}$ for all experimentally investi-
gated configurations are presented in Fig. 6.17 (a) and (b), respectively. For
each inlet configuration, the heat transfer enhancement compared to an axial
flow is almost constant over the investigated Reynolds number range. Only for
the MI1 swirl tube, the Nusselt number enhancement slightly increases with
higher Reynolds numbers. Moreover, it is evident that the highest globally
averaged Nusselt number enhancement is obtained for the MI1 configuration.
It decrease with increasing number of inlet jets. This is caused by the differ-
ent swirl strengths in the tube. For the same Reynolds number and therefore
same mass flow rate, the swirl strength and consequently the circumferential
velocity near the wall decrease because the mass flow rate is distributed to
multiple inlet jets.
For a comparison of the thermal performances of the investigated configura-
tions in Fig. 6.17 (b), the friction factor enhancement will be considered as
well. It becomes clear that the thermal performance for all configurations and
all Reynolds numbers are in the same order of magnitude. This means that
all swirl tube configurations are suitable for cooling. It strongly depends on
the application, if one is interested in a maximum heat transfer paid by a
high pressure loss or a lower but more homogeneous heat transfer with a low
pressure loss. For the first case, one should choose the MI1 swirl tube config-
uration. For the second case, the MI5 swirl tube configuration would be the
best choice.
It should be mentioned that the presented thermal performance for the multi-
ple inlet swirl tubes differ from the thermal performance for the baseline swirl
tube given in Table 5.9 in the previous chapter. This is due to a different
reference temperature for the Nusselt number. For the multiple inlet swirl
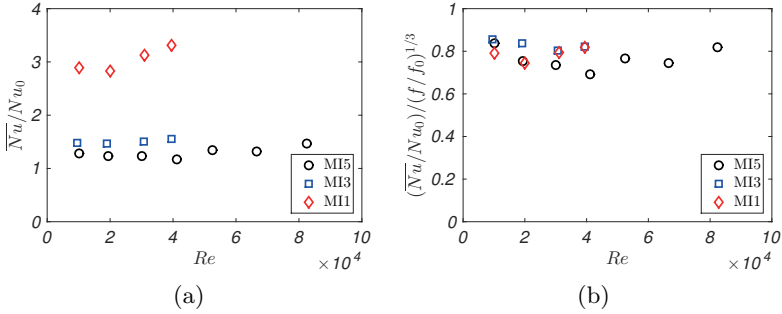
Figure 6.17: Globally averaged Nusselt numbers $\overline{Nu}/Nu_0$ (a) and thermal performance parameters $(\overline{Nu}/Nu_0)/(f/f_0)^{1/3}$ (b) over the Reynolds number Re for all experimentally investigated multiple inlet configurations

tubes the jet inlet temperature is used to determine the Nusselt number which is higher than the local fluid temperature, and therefore causes a lower heat transfer and thermal performance, respectively. For completeness, the experimentally obtained thermal performance parameters $(\overline{Nu}/Nu_0)/(f/f_0)^{1/3}$ are listed in Table 6.7 for all investigated configurations and Reynolds numbers.

Table 6.7: Thermal performance parameter $(\overline{Nu}/Nu_0)/(f/f_0)^{1/3}$ (experiments)

Re	10,000	20,000	30,000	40,000	50,000	66,700	80,000
MI1	0.79	0.75	0.79	0.82	-	-	-
MI3	0.86	0.84	0.81	0.82	-	-	-
MI5	0.83	0.76	0.73	0.69	0.77	0.74	0.82

Conclusions

In the present work, the flow phenomena and the heat transfer in swirl tubes were studied in detail. A swirl tube features one or more tangential inlet jets which induce a highly 3D swirling flow. This swirling flow is characterized by large velocities near the wall and an enhanced turbulence in the tube which both increase the convective heat transfer. Therefore, a swirl tube is a very effective cooling technique for high thermal loaded components like gas turbine blades.

As a first step, a generic swirl tube with tangential inlets at the beginning of the tube was investigated to gain a better understanding of the complex physical mechanisms in swirl tube flows. Second, a novel application-oriented swirl tube geometry with multiple tangential inlet jets in axial direction was examined. In a comprehensive study, the flow field, the heat transfer and the pressure loss for several Reynolds numbers (mass flow rates), swirl numbers and outlet geometries were investigated experimentally and numerically. For this purpose, the flow field is measured via stereo- and tomographic-PIV (Particle Image Velocimetry) and the heat transfer is measured by applying a transient technique using thermochromic liquid crystals. The numerical simulations are performed via Detached Eddy Simulation. The results were used to analyze the vortex breakdown phenomenon and the stability of swirling

flows. Moreover, the thermal performance parameters (ratio of heat transfer to pressure loss) for all investigated swirl tube configurations were evaluated. The experimental and numerical results of the generic swirl tube provided a comprehensive insight in the occurring physical mechanisms in swirling flows. In strong swirling flows (swirl number $S = 5.3$), the flow field is dominated by the circumferential velocity which is characterized by a Rankine vortex with a solid body vortex in the tube center and a potential vortex in the outer region. A stability analysis revealed that the solid body vortex is unstable according to the thermal criterion by Maršík [150]. This analysis explained the transformation of the solid body vortex into the stable potential vortex towards the tube outlet. However, the thermal instability is compensated by the mechanical stability, which means that the vortex system is entirely stable in terms of minimum total enthalpy. Furthermore, the numerical simulations provided a detailed insight in the turbulent flow structures and revealed a stable double helix vortex structure in the swirl tube.

In addition, the axial velocity shows a backflow region in the tube center over the entire tube length. This axial backflow (vortex breakdown) has been studied extensively by simulating swirl tubes with low swirl numbers between 0.5 and 1.0. The results could confirm the analytically estimated swirl number limit $S_{limit} = 0.928$ by Kobiela [113], for which the axial pressure gradient in the tube center vanishes and a backflow occurs. Furthermore, it is shown that in swirl dominated flows, a vortex breakdown is possible for Rossby numbers (ratio between axial and circumferential velocity) below 0.65 in accordance with Spall et al. [203]. In addition, a comparison between the local mean axial Reynolds number and the local mean circumferential Reynolds number illustrates that vortex breakdown occurs in flow regions with higher circumferential than axial Reynolds number. Consequently, in axial dominated flows no backflow appears.

The measurements indicated that the heat transfer in swirl tubes increases with increasing Reynolds number and swirl number, respectively. Near the inlet region, the maximum heat transfer occurs due to the large circumferential velocity component. For the highest swirl number, the highest heat transfer is up to ten times higher than the one in an axial tube flow. With decreasing swirl and velocity towards the tube outlet, the heat transfer decreases continuously. The normalized heat transfer results overlap for all investigated Reynolds numbers, so that the swirling flow is proportional to $Re^{0.8}$ analogous to an axial tube flow. This is a very important result as it allows to scale the obtained heat transfer data.

The investigation of various outlet geometries (straight, tangential and 180° bend outlet) showed that an outlet redirection has no significant influence on the upstream flow structure and the heat transfer. Thus, the here investigated

swirl tube is characterized by a robust design regarding inflow and outflow conditions and is well applicable for the cooling of high thermal loaded components like gas turbine blades.

The investigation of the swirl tubes with multiple tangential inlet jets revealed a very complex axial velocity which changes after each inlet due to the additional mass flow. However, the circumferential velocity stays almost constant since the swirl strength is re-enhanced with each inlet jet, respectively. For the swirl tube with one inlet jet, the highest heat transfer occurs in the inlet region and continuously decreases towards the tube outlet analogous to the generic swirl tube. For the multiple inlet swirl tubes, the highest heat transfer can be observed at each inlet jet. Downstream between the tangential jets, the heat transfer decreases until the next inlet. However, the maximum heat transfer is lower than for the swirl tube with only one inlet because of the lower inlet jet velocities. On the other hand, due to the additional tangential jets, and thus enhanced swirl strength, the heat transfer distribution is more homogeneous over the entire tube length at a much lower pressure loss than with only one inlet.

For the investigated swirl tubes with one, three or five inlets, the thermal performance parameter is in the same order of magnitude. This means that all swirl tube configurations are suitable for cooling. It strongly depends on the application, if one is interested in a maximum heat transfer, paid by a high pressure loss, or a lower but more homogeneous heat transfer with a low pressure loss. For the first case, one should choose the swirl tube with only one inlet. For the second case, the swirl tube with five inlets would be the better choice.

Bibliography

[1] Ahlborn, B. and Groves, S., 1997. Secondary flow in a vortex tube. *Fluid Dynamics Research* **21**(2), pp. 73–86.

[2] Ahlborn, B., Keller, J. U., Staudt, R., Treitz, G., and Rebhan, E., 1994. Limits of temperature separation in a vortex tube. *Journal of Physics D: Applied Physics* **27**(3), pp. 480–488.

[3] Al-Ajmi, R. M., Syred, N., Bowen, P. J., Khalatov, A., and Al-Shagh-dari, M. A., 1998. A comparison of CFD and LDA studies of internal vortex cooling systems for turbine blades. *Journal of Flow Visualization and Image Processing* **5**(3), pp. 197–210. DOI: `10.1615/JFlowVisImage Proc.v5.i3.20`.

[4] Akiyama, T. and Ikeda, M., 1986. Fundamental Study of the Fluid Mechanics of Swirling Pipe Flow with Air Suction. *Industrial & Engineering Chemistry Process Design and Development* **25**(4), pp. 907–913.

[5] Alekseenko, S. V., Kuibin, P. A., Okulov, V. L., and Shtork, S. I., 1999. Helical vortices in swirl flow. *Journal of Fluid Mechanics* **382**, pp. 195–243.

[6] Althaus, W., Krause, E., Hofhaus, J., and Weimer, M., 1994. Vortex breakdown: Transition between bubble- and spiral-type breakdown. *Meccanica* **29**(4), pp. 373–382. DOI: `10.1007/BF00987572`.

[7] Balmer, R. T., 1988. Pressure-Driven Ranque-Hilsch Temperature Separation in Liquids. *Journal of Fluids Engineering* **110**(2), pp. 161–164. DOI: `10.1115/1.3243529`.

[8]   Batchelor, G. K., 2000. An Introduction to Fluid Dynamics. Cambridge University Press.

[9]   Behera, U., Paul, P. J., Dinesh, K., and Jacob, S., 2008. Numerical investigation of the thermal separation in a Ranque–Hilsch vortex tube. *International Journal of Heat and Mass Transfer* **51**, pp. 6077–6089. DOI: `10.1016/j.ijheatmasstransfer.2008.03.029`.

[10]   Behera, U., Paul, P. J., Kasthurirengan, S., Karunanithi, R., Ram, S. N., Dinesh, K., and Jacob, S., 2005. CFD analysis and experimental investigations towards optimizing the parameters of Ranque–Hilsch vortex tube. *International Journal of Heat and Mass Transfer* **48**(10), pp. 1961–1973. DOI: `10.1016/j.ijheatmasstransfer.2004.12.046`.

[11]   Ben Hmidene, M., 2015. Stabilitätsanalyse der Strömungsphänomene in einem Wirbelrohr. Bachelor Thesis, Institute of Aerospace Thermodynamics (ITLR), University of Stuttgart.

[12]   Benjamin, T. B., 1962. Theory of the vortex breakdown phenomenon. *Journal of Fluid Mechanics* **14**(4), pp. 593–629. DOI: `10.1017/S002211 2062001482`.

[13]   Benjamin, T. B., 1965. Significance of the Vortex Breakdown Phenomenon. *Journal of Basic Engineering* **87**(2), pp. 518–522. DOI: `10 .1115/1.3650590`.

[14]   Benjamin, T. B., 1967. Some developments in the theory of vortex breakdown. *Journal of Fluid Mechanics* **28**(1), pp. 65–84. DOI: `10.1 017/S0022112067001909`.

[15]   Bernhard, F., 2003. Technische Temperaturmessung. Springer.

[16]   Biegger, C., Cabitza, A., and Weigand, B., 2013. Three Components- and Tomographic-PIV Measurements of a Cyclone Cooling Flow in a Swirl Tube. *ASME Turbo Expo GT2013-94424*. DOI: `10.1115/GT2013 -94424`.

[17]   Biegger, C., Sotgiu, C., and Weigand, B., 2015. Numerical investigation of flow and heat transfer in a swirl tube. *International Journal of Thermal Sciences* **96**, pp. 319–330. DOI: `10.1016/j.ijthermalsci.2014.1 2.001`.

[18]   Biegger, C. and Weigand, B., 2014. Heat Transfer Measurements in a Swirl Chamber Using the Transient Liquid Crystal Technique. *15th International Heat Transfer Conference, IHTC15-9231.*

[19] Biegger, C. and Weigand, B., 2015. Flow and heat transfer measurements in a swirl chamber with different outlet geometries. *Experiments in Fluids* **56**(78). DOI: `10.1007/s00348-015-1937-3`.

[20] Biegger, C. and Weigand, B., 2016. Detached Eddy Simulation of Flow and Heat Transfer in Swirl Tubes. *High Performance Computing in Science and Engineering ´15*, pp. 449–461. DOI: `10.1007/978-3-319-24633-8_29`.

[21] Boussinesq, J., 1877. Essai sur la théorie des eaux courantes. *Mémoires présentés par divers savants à l'Académie des Sciences* **23**(1), pp. 1–680.

[22] Brethauer, S., 2014. Wärmeübergangsmessungen in einer Zyklonkühlkammer mit der transienten Flüssigkristallmesstechnik. Master Thesis (Diplomarbeit), Institute of Aerospace Thermodynamics (ITLR), University of Stuttgart.

[23] Brown, G. L. and Lopez, J. M., 1990. Axisymmetric vortex breakdown Part 2. Physical mechanisms. *Journal of Fluid Mechanics* **221**, pp. 553–576. DOI: `10.1017/S0022112090003676`.

[24] Bruschewski, M., Scherhag, C., Grundmann, S., and Schiffer, H.-P., 2014. Swirl Flow Formations in Cooling Ducts. *Proceedings of CONV-14*. DOI: `10.1615/ICHMT.2014.IntSympConvHeatMassTransf.840`.

[25] Bruschewski, M., Scherhag, C., Schiffer, H.-P., and Grundmann, S., 2015. Influence of channel geometry and flow variables on cyclone cooling of turbine blades. *ASME Turbo Expo GT2015-42860*. DOI: `10.1115/GT2015-42860`.

[26] Bruun, H. H., 1969. Experimental Investigation of the Energy Separation in Vortex Tubes. *Journal of Mechanical Engineering Science* **11**(6), pp. 567–582. DOI: `10.1243/JMES_JOUR_1969_011_070_02`.

[27] Buttsworth, D. R. and Jones, T. V., 1997. Radial conduction effects in transient heat transfer experiments. *The Aeronautical Journal of the Royal Aeronautical Society*, pp. 209–212.

[28] Cabitza, A., 2012. 3C- and Tomographic-PIV Measurements of a Swirl Cooling Flow in a Vortex Chamber. Master Thesis, Institute of Aerospace Thermodynamics (ITLR), University of Stuttgart.

[29] Carslaw, H. S. and Jaeger, J. C., 1959. Conduction of Heat in Solids. Second Edition. Oxford University Press.

Bibliography

[30] Cassidy, J. J. and Falvey, H. T., 1970. Observations of unsteady flow arising after vortex breakdown. *Journal of Fluid Mechanics* **41**(4), pp. 727–736. DOI: 10.1017/S0022112070000873.

[31] Chanaud, R. C., 1965. Observations of oscillatory motion in certain swirling flows. *Journal of Fluid Mechanics* **21**(1), pp. 111–127. DOI: 10.1017/S0022112065000083.

[32] Chandrasekhar, S., 1961. Hydrodynamic and hydromagnetic stability. Oxford: Clarendon Press.

[33] Chang, C.-Y., Jakirlić, S., Dietrich, K., Basara, B., and Tropea, C., 2014. Swirling flow in a tube with variably-shaped outlet orifices: An LES and VLES study. *International Journal of Heat and Fluid Flow* **49**, pp. 28–42. DOI: 10.1016/j.ijheatfluidflow.2014.05.008.

[34] Chang, F. and Dhir, V. K., 1994. Turbulent flow field in tangentially injected swirl flows in tubes. *International Journal of Heat and Fluid Flow* **15**, pp. 346–356.

[35] Chang, F. and Dhir, V. K., 1995. Mechanisms of heat transfer enhancement and slow decay of swirl in tubes using tangential injection. *International Journal of Heat and Fluid Flow* **16**(2), pp. 78–87.

[36] Chen, J. C. and Lin, C. A., 1999. Computations of strongly swirling flows with second-moment closures. *International Journal for Numerical Methods in Fluids* **30**, pp. 493–508. DOI: 10.1002/(SICI)1097-0363(19990715)30:5<493::AID-FLD849>3.0.CO;2-3.

[37] De Villiers, E., 2006. The potential of Large Eddy Simulation for the modeling of wall bounded flows. PhD thesis. Imperial College London.

[38] Deissler, R. G. and Perlmutter, M., 1960. Analysis of the Flow and Energy Separation in a Turbulent Vortex. *International Journal of Heat and Mass Transfer* **1**, pp. 173–191. DOI: 10.1016/0017-9310(60)90021-1.

[39] Dhir, V. K., 1994. Heat transfer enhancement using tangential injection. *U.S. Patent No. 5291943*.

[40] Dhir, V. K. and Chang, F., 1992. Heat transfer enhancement using tangential injection. *ASHRAE Trans.* **98**, pp. 383–390.

[41] Dincer, K., Baskaya, S., and Uysal, B. Z., 2008. Experimental investigation of the effects of length to diameter ratio and nozzle number on

the performance of counter flow Ranque–Hilsch vortex tubes. *Heat and Mass Transfer* **44**(3), pp. 367–373. DOI: `10.1007/s00231-007-0241-z`.

[42] Dittus, F. W. and Boelter, L. M. K., 1930. Heat Transfer in Automobile Radiators of the Tubular Type. *Publications of Engineering* **2**, p. 443. University of California, Berkeley.

[43] Eckert, E. R. G., 1986. Energy separation in fluid streams. *International Communications in Heat and Mass Transfer* **13**(2), pp. 127–143. DOI: `10.1016/0735-1933(86)90053-9`.

[44] Eiamsa-ard, S. and Promvonge, P., 2006. Numerical investigation of the thermal separation in a Ranque–Hilsch vortex tube. *Journal of Zhejiang University SCIENCE A* **7**(8), pp. 1406–1415. DOI: `10.1631/jzus.2006.A1406`.

[45] Eiamsa-ard, S. and Promvonge, P., 2007. Numerical investigation of the thermal separation in a Ranque–Hilsch vortex tube. *International Journal of Heat and Mass Transfer* **50**, pp. 821–832. DOI: `10.1016/j.ijheatmasstransfer.2006.08.018`.

[46] Eiamsa-ard, S. and Promvonge, P., 2008. Review of Ranque-Hilsch effects in vortex tubes. *Renewable and Sustainable Energy Reviews* **12**, pp. 1822–1842. DOI: `10.1016/j.rser.2007.03.006`.

[47] Ekkad, S. V., Pamula, G., and Acharya, S., 2000. Influence of Cross-flow-Induced Swirl and Impingement on Heat Transfer in an Internal Coolant Passage of a Turbine Airfoil. *Journal of Heat Transfer* **122**(3), pp. 587–597. DOI: `10.1115/1.1289020`.

[48] Elser, K. and Hoch, M., 1951. Das Verhalten verschiedener Gase und die Trennung von Gasgemischen in einem Wirbelrohr. *Z. Naturforschg.* **6a**, pp. 25–31.

[49] Elsinga, G. E., Oudheusden, B. W. van, and Scarano, F., 2006a. Experimental assessment of Tomographic-PIV accuracy. *13th Int Symp on Applications of Laser Techniques to Fluid Mechanics, Lisbon, Portugal.*

[50] Elsinga, G. E., Scarano, F., Wieneke, B., and Oudheusden, B. W. van, 2006b. Tomographic particle image velocimetry. *Experiments in Fluids* **41**, pp. 933–947.

[51] Erdélyi, I., 1962. Wirkung des Zentrifugalkraftfeldes auf den Wärmezustand der Gase, Erklärung der Ranque-Erscheinung. *Forschung auf dem Gebiet des Ingenieurwesens A* **28**(6), pp. 181–186. DOI: `10.1007/BF02557439`.

[52] Escudier, M., 1988. Vortex breakdown: Observations and explanations. *Prog. Aerospace Sci.* **25**(2), pp. 189–229. DOI: `10.1016/0376-0421(88)90007-3`.

[53] Escudier, M. P., 1983. Vortex breakdown in the absence of an endwall boundary layer. *Experiments in Fluids* **1**(4), pp. 193–194. DOI: `10.1007/BF00266467`.

[54] Escudier, M. P., 1984. Observations of the flow produced in a cylindrical container by a rotating endwall. *Experiments in Fluids* **2**(4), pp. 189–196. DOI: `10.1007/BF00571864`.

[55] Escudier, M. P., Bornstein, J., and Maxworthy, T., 1982. The dynamics of confined vortices. *Proceedings of the Royal Society A* **382**, pp. 335–360.

[56] Escudier, M. P. and Keller, J. J., 1983. Vortex Breakdown: A Two-Stage Transition. *AGARD CP No. 342*.

[57] Escudier, M. P. and Keller, J. J., 1985. Recirculation in Swirling Flow: A Manifestation of Vortex Breakdown. *AIAA Journal* **23**(1), pp. 111–116.

[58] Escudier, M. P., Nickson, A. K., and Poole, R. J., 2006. Influence of outlet geometry on strongly swirling turbulent flow through a circular tube. *Phys. Fluids* **18**. DOI: `10.1063/1.2400075`.

[59] Escudier, M. P. and Zehnder, N., 1982. Vortex-flow regimes. *Journal of Fluid Mechanics* **115**, pp. 105–121. DOI: `10.1017/S0022112082000676`.

[60] Faler, J. H. and Leibovich, S., 1977. Disrupted states of vortex flow and vortex breakdown. *Phys. Fluids* **20**, pp. 1385–1400. DOI: `10.1063/1.862033`.

[61] Ferziger, J. H. and Perić, M., 2002. Computational Methods for Fluid Dynamics. Third Edition. Springer.

[62] Foroutan, H. and Yavuzkurt, S., 2014. A partially-averaged Navier–Stokes model for the simulation of turbulent swirling flow with vortex breakdown. *International Journal of Heat and Fluid Flow* **50**, pp. 402–416. DOI: `10.1016/j.ijheatfluidflow.2014.10.005`.

[63] Fröhlich, J., 2006. Large Eddy Simulation turbulenter Strömungen. B.G. Teubner Verlag.

[64] Fröhlich, J. and Terzi, D. von, 2008. Hybrid LES/RANS methods for the simulation of turbulent flows. *Prog. Aerospace Sci.* **44**, pp. 349–377.

[65] Führer, U., 2013. Die experimentelle Untersuchung eines Ranque-Hilsch Rohres. Master Thesis (Diplomarbeit), Institute of Aerospace Thermodynamics (ITLR), University of Stuttgart.

[66] Gao, C. M., Bosschaart, K. J., Zeegers, J. C. H., and Waele, A. T. A. M. de, 2005. Experimental study on a simple Ranque–Hilsch vortex tube. *Cryogenics* **45**(3), pp. 173–183. DOI: `10.1016/j.cryogenics.2004.09.004`.

[67] Garg, A. K. and Leibovich, S., 1979. Spectral characteristics of vortex breakdown flowfields. *Phys. Fluids* **22**(11), pp. 2053–2064. DOI: `10.1063/1.862514`.

[68] Glezer, B., Lin, T., and Moon, H. K., 1997. Turbine cooling system. *U.S. Patent No. 5603606.*

[69] Glezer, B., Moon, H. K., Kerrebrock, J., Bons, J., and Guenette, G., 1998. Heat transfer in a rotating radial channel with swirling internal flow. *ASME Paper No. 98-GT-214.*

[70] Glezer, B., Moon, H. K., and O'Connell, T., 1996. A novel technique for the internal blade cooling. *ASME Paper No. 96-GT-181.*

[71] Grundmann, S., Wassermann, F., Lorenz, R., Jung, B., and Tropea, C., 2012. Experimental investigation of helical structures in swirling flows. *International Journal of Heat and Fluid Flow* **37**, pp. 51–63.

[72] Gulyaev, A. I., 1965. Ranque Effect at Low Temperatures. *Inzhenerno-Fizicheskii Zhurnal* **9**(3), pp. 354–357.

[73] Gupta, A. K., Lilley, D. G., and Syred, N., 1984. Swirl Flows. Energy and Engineering Science Series. Abacus Press.

[74] Gupta, A. and Kumar, R., 2007. Three-dimensional turbulent swirling flow in a cylinder: Experiments and computations. *International Journal of Heat and Fluid Flow* **28**, pp. 249–261. DOI: `10.1016/j.ijheatfluidflow.2006.04.005`.

[75] Gursul, I., 1996. Effect of Nonaxisymmetric Forcing on a Swirling Jet With Vortex Breakdown. *Journal of Fluids Engineering* **118**(2), pp. 316–321. DOI: `10.1115/1.2817379`.

[76] Gutsol, A. F., 1997. The Ranque effect. *Physics - Uspekhi* **40**(6), pp. 639–658.

[77] Gutsol, A. and Bakken, J. A., 1998. A new vortex method of plasma insulation and explanation of the Ranque effect. *Journal of Physics D:*

Applied Physics **31**(6), pp. 704–711. DOI: `10.1088/0022-3727/31/6/0` `18`.

[78] Hall, M. G., 1966. The structure of concentrated vortex cores. *Progress in Aerospace Sciences* **7**. DOI: `10.1016/0376-0421(66)90006-6`.

[79] Hall, M. G., 1967. A new approach to vortex breakdown. *Proceedings of the 1967 Heat Transfer and Fluid Mechanics Institute* **20**, pp. 319–340.

[80] Hall, M. G., 1972. Vortex Breakdown. *Annual Review of Fluid Mechanics* **4**, pp. 195–218. DOI: `10.1146/annurev.fl.04.010172.001211`.

[81] Harvey, J. K., 1962. Some observations of the vortex breakdown phenomenon. *Journal of Fluid Mechanics* **14**(4), pp. 585–592. DOI: `10.101` `7/S0022112062001470`.

[82] Harvey, N. W., Ling, C. W. J. P., and Ireland, P. T., 2006. Turbine components. *U.S. Patent No. 7137781 B2*.

[83] Hay, N. and West, P. D., 1975. Heat Transfer in Free Swirling Flow in a Pipe. *Journal of Heat Transfer* **97**(3), pp. 411–416.

[84] Hedlund, C. R. and Ligrani, P. M., 2000. Local Swirl Chamber Heat Transfer and Flow Structure at Different Reynolds Numbers. *Journal of Turbomachinery* **122**, pp. 375–385.

[85] Hedlund, C. R., Ligrani, P. M., Glezer, B., and Moon, H.-K., 1999a. Heat transfer in a swirl chamber at different temperature ratios and Reynolds numbers. *International Journal of Heat and Mass Transfer* **42**(22), pp. 4081–4091. DOI: `10.1016/S0017-9310(99)00086-1`.

[86] Hedlund, C. R., Ligrani, P. M., Moon, H.-K., and Glezer, B., 1999b. Heat transfer and flow phenomena in a swirl chamber simulating turbine blade internal cooling. *Journal of Turbomachinery* **121**, pp. 804–813.

[87] Hilsch, R., 1946. Die Expansion von Gasen im Zentrifugalfeld als Kälteprozeß. *Z. Naturforschg.* **1**, pp. 208–214.

[88] Hogg, S. and Leschziner, M. A., 1989. Computation of highly swirling confined flow with a Reynolds stress turbulence model. *AIAA Journal* **27**(1), pp. 57–63. DOI: `10.2514/3.10094`.

[89] Howard, L. N. and Gupta, A. S., 1962. On the hydrodynamic and hydromagnetic stability of swirling flows. *Journal of Fluid Mechanics* **14**(3), pp. 463–476. DOI: `10.1017/S0022112062001366`.

[90] Hwang, J.-J. and Cheng, C.-S., 1999. Augmented Heat Transfer in a Tri-angular Duct by Using Multiple Swirling Jets. *Journal of Heat Transfer* **121**(3), pp. 683–690. DOI: `10.1115/1.2826033`.

[91] Iida, O. and Kasagi, N., 2001. Test Case: Heat transfer of fully devel-oped turbulent channel flow with iso-thermal walls. Turbulence and Heat Transfer Laboratory, University of Tokyo. URL: `http://thtlab.jp/DNS/dns_database.html`.

[92] Ireland, P. T. and Jones, T. V., 2000. Liquid crystal measurements of heat transfer and surface shear stress. *Meas. Sci. Technol.* **11**, pp. 969–986.

[93] Iwamoto, K., Suzuki, Y., and Kasagi, N., 2002. Test Case: Fully De-veloped 2-D Channel Flow at Re_tau = 400. Turbulence and Heat Transfer Laboratory, University of Tokyo. URL: `http://thtlab.jp/DNS/dns_database.html`.

[94] Jakirlić, S., Hanjalić, K., and Tropea, C., 2002. Modeling Rotating and Swirling Turbulent Flows: A Perpetual Challenge. *AIAA Journal* **40**(10), pp. 1984–1996.

[95] Jasak, H., 1996. Error Analysis and Estimation for the Finite Volume Method with Applications to Fluid Flows. PhD thesis. Imperial College London.

[96] Jasak, H., Jemcov, A., and Maruszewski, J. P., 2007a. Preconditioned Linear Solvers for Large Eddy Simulation. *CFD 2007 Conference, CFD Society of Canada.*

[97] Jasak, H., Jemcov, A., and Tukovic, Z., 2007b. OpenFOAM: A C++ Library for Complex Physics Simulations. *International Workshop on Coupled Methods in Numerical Dynamics*, pp. 1–20.

[98] Jeong, J. and Hussain, F., 1995. On the identification of a vortex. *Jour-nal of Fluid Mechanics* **285**, pp. 69–94. DOI: `10.1017/S0022112095000462`.

[99] Jiang, Y., Zheng, Q., Yue, G., Dong, P., and Jiang, Y., 2014. Numerical Investigation of Swirl Cooling Heat Transfer Enhancement on Blade Leading Edge by Adding Water Mist. *ASME Turbo Expo GT2014-25697.* DOI: `10.1115/GT2014-25697`.

[100] Kays, W. M., Crawford, M. E., and B.Weigand, 2004. Convective Heat and Mass Transfer. Fourth Edition. McGraw-Hill.

Bibliography

[101] Kazantseva, O. V., Piralishvili, Sh. A., and Fuzeeva, A. A., 2005. Numerical Simulation of Swirling Flows in Vortex Tubes. *High Temperature* **43**(4), pp. 608–613.

[102] Keller, J. J., Egli, W., and Exley, J., 1985. Force- and loss-free transitions between flow states. *Journal of Applied Mathematics and Physics (ZAMP)* **36**(6), pp. 854–889. DOI: 10.1007/BF00944899.

[103] Khalatov, A. A., 1989. Swirl Flows: Fundamentals and Applications. Naukova Dumka, Kiev, Ukraine (in Russian).

[104] Khalatov, A. A., Borisov, I. I., Severin, S. D., Romanov, V. V., Spitsyn, V. Y., and Dashevskyy, Y. Y., 2011. Heat Transfer, Hydrodynamics and Pressure Drop in the Model of a Blade Leading Edge Cyclone Cooling. *ASME Turbo Expo GT2011-45150.*

[105] Khalatov, A. A. and Nam, C.-D., 2003. Aerothermal Vortex Technologies in Aerospace Engineering. *Journal of the Korean Society of Marine Engineering* **28**(2), pp. 163–184.

[106] Khalatov, A. A. and Schukin, V. K., 1982. Heat, Mass Transfer and Hydrodynamics of Swirl Flows in Axisymmetrical Channels (in Russian). *Mashinostroenie, Moscow, Russia.*

[107] Khalatov, A., Syred, N., Bowen, P., and Al-Ajmi, R., 2001. Quasi Two-Dimensional Cyclone-Jet Cooling Configuration: Evaluation of Heat Transfer and Pressure Loss. *ASME Turbo Expo 2001-GT-0182.*

[108] Khalatov, A., Syred, N., Bowen, P., and Al-Ajmi, R., 2002. Enhanced Cyclone Cooling Technique for High Performance Gas Turbine Blades. *Proceedings of the Twelfth International Heat Transfer Conference.*

[109] Khalatov, A., Syred, N., Bowen, P., Al-Ajmi, R., Kozlov, A., and Schukin, A., 2000. Innovative Cyclone Cooling Scheme for Gas Turbine Blade: Thermal-Hydraulic Performance Evaluation. *ASME Turbo Expo 2000-GT-0237.* DOI: 10.1115/2000-GT-0237.

[110] King, M. K., Rothfus, R. R., and Kermode, R. I., 1969. Static pressure and velocity profiles in swirling incompressible tube flow. *AIChE Journal* **15**, pp. 837–842.

[111] Kitoh, O., 1991. Experimental study of turbulent swirling flow in a straight pipe. *Journal of Fluid Mechanics* **225**, pp. 445–479. DOI: 10.1017/S0022112091002124.

[112] Knoernschild, E., 1948. Friction Laws and Energy Transfer in Circular Flow. Part II - Energy Transfer in Circular Flow and Possible Applications (Explanation of the Hilsch or Ranque Effect). *Technical Report No. F-TR-2198-ND, GS-USAF Wright-Patterson Air Force Base No. 78.*

[113] Kobiela, B., 2014. Wärmeübertragung in einer Zyklonkühlkammer einer Gasturbinenschaufel. PhD thesis. University of Stuttgart.

[114] Kolmogorov, A. N., 1941. The local structure of turbulence in incompressible viscous fluid for very large Reynolds numbers. *Dokl. Akad. Nauk SSSR* **30**(4).

[115] Kreith, F. and Margolis, D., 1959. Heat transfer and friction in turbulent vortex flow. *Appl. Sci. Research* **8**, pp. 457–473.

[116] Kreith, F. and Sonju, O. K., 1965. The decay of a turbulent swirl in a pipe. *Journal of Fluid Mechanics* **22**(2), pp. 257–271. DOI: `10.1017/S0022112065000733`.

[117] Kumar, R. and Conover, T., 1993. Flow visualization studies of a swirling flow in a cylinder. *Experimental Thermal and Fluid Science* **7**, pp. 254–262.

[118] Kurosaka, M., 1982. Acoustic streaming in swirling flow and the Ranque-Hilsch (vortex-tube) effect. *Journal of Fluid Mechanics* **124**, pp. 139–172. DOI: `10.1017/S0022112082002444`.

[119] Kusterer, K., Lin, G., Bohn, D., Sugimoto, T., Tanaka, R., and Kazari, M., 2013. Heat transfer enhancement for gas turbine internal cooling by application of double swirl cooling chambers. *ASME Turbo Expo GT2013-94774.* DOI: `10.1115/GT2013-94774`.

[120] Kusterer, K., Lin, G., Bohn, D., Sugimoto, T., Tanaka, R., and Kazari, M., 2014. Leading Edge Cooling of a Gas Turbine Blade With Double Swirl Chambers. *ASME Turbo Expo GT2014-25851.* DOI: `10.1115/GT2014-25851`.

[121] Kusterer, K., Lin, G., Sugimoto, T., Bohn, D., Tanaka, R., and Kazari, M., 2015. Novel Gas Turbine Blade Leading Edge Cooling Configuration Using Advanced Double Swirl Chambers. *ASME Turbo Expo GT2015-42400.* DOI: `10.1115/GT2015-42400`.

[122] Lee, C.-P., 2008. Turbine airfoil with integrated impingement and serpentine cooling circuit. *U.S. Patent No. 7377747 B2.*

Bibliography

[123] Leibovich, S., 1978. The Structure of Vortex Breakdown. *Annual Review of Fluid Mechanics* **10**, pp. 221–246. DOI: `10.1146/annurev.fl.10.010178.001253`.

[124] Leibovich, S., 1984. Vortex stability and breakdown - Survey and extension. *AIAA Journal* **22**(9), pp. 1192–1206. DOI: `10.2514/3.8761`.

[125] Leibovich, S. and Stewartson, K., 1983. A sufficient condition for the instability of columnar vortices. *Journal of Fluid Mechanics* **126**, pp. 335–356. DOI: `10.1017/S0022112083000191`.

[126] Leonard, A., 1974. Energy cascade in large-eddy simulations of turbulent fluid flows. *Advances in Geophysics* **18**(Part A), pp. 237–248. DOI: `10.1016/S0065-2687(08)60464-1`.

[127] Lerch, A., Klaubert, D., and Schiffer, H.-P., 2011. Impact on adiabatic film cooling effectiveness using internal cyclone cooling. *ASME Turbo Expo GT2011-45120*.

[128] Lerch, A. and Schiffer, H.-P., 2009. Influence of internal cyclone flow on adiabatic film cooling effectiveness. *Proceedings of the International Symposium on Heat Transfer in Gas Turbine Systems (TURBINE-09), Antalya, Turkey.* DOI: `10.1615/ICHMT.2009.HeatTransfGasTurbSyst.140`.

[129] Lerch, A. and Schiffer, H.-P., 2011. Influence of internal cyclone flow on adiabatic film cooling effectiveness. *Heat Transfer Research* **42**(2).

[130] Liew, R., Zeegers, J. C. H., Kuerten, J. G. M., and Michałek, W. R., 2012a. Maxwell's Demon in the Ranque-Hilsch Vortex Tube. *Physical Review Letters* **109**(5). DOI: `10.1103/PhysRevLett.109.054503`.

[131] Liew, R., Zeegers, J. C. H., Kuerten, J. G. M., and Michałek, W. R., 2012b. Temperature, Pressure and Velocity measurements on the Ranque-Hilsch Vortex Tube. *Journal of Physics: Conference Series* **395**. DOI: `10.1088/1742-6596/395/1/012066`.

[132] Ligrani, P. M., 2013. Heat Transfer Augmentation Technologies for Internal Cooling of Turbine Components of Gas Turbine Engines. *International Journal of Rotating Machinery* **2013**, p. 32. DOI: `10.1155/2013/275653`.

[133] Ligrani, P. M., Hedlund, C. R., Babinchak, B. T., Thambu, R., Moon, H.-K., and Glezer, B., 1998. Flow phenomena in swirl chambers. *Experiments in Fluids* **24**, pp. 254–264.

[134] Ligrani, P. M., Oliveira, M. M., and Blaskovich, T., 2003. Comparison of heat transfer augmentation techniques. *AIAA Journal* **41**(3), pp. 337–362.

[135] Lin, G., Kusterer, K., Ayed, A. H., Bohn, D., Sugimoto, T., Tanaka, R., and Kazari, M., 2015. Numerical investigation on heat transfer in an advanced new leading edge impingement cooling configuration. *Propulsion and Power Research* **4**(4), pp. 179–189. DOI: `10.1016/j.jppr.2015.10.003`.

[136] Lin, G., Kusterer, K., Bohn, D., Sugimoto, T., Tanaka, R., and Kazari, M., 2013. Investigation on heat transfer enhancement and pressure loss of double swirl chambers cooling. *Propulsion and Power Research* **2**(3), pp. 177–187. DOI: `0.1016/j.jppr.2013.07.003`.

[137] Lin, G., Kusterer, K., Bohn, D., Sugimoto, T., Tanaka, R., and Kazari, M., 2014. Impingement Cooling with Spent Flow in the Blade Leading Edge Using Double Swirl Chambers. *15th International Heat Transfer Conference, IHTC15-8669.*

[138] Linderstrøm-Lang, C. U., 1971. The three-dimensional distributions of tangential velocity and total-temperature in vortex tubes. *Journal of Fluid Mechanics* **45**(1), pp. 161–187. DOI: `10.1017/S0022112071003057`.

[139] Ling, J. P. C. W., 2005. Development of Heat Transfer Measurement Techniques and Cooling Strategies for Gas Turbines. PhD thesis. University of Oxford.

[140] Ling, J. P. C. W., Ireland, P. T., and Harvey, N. W., 2006. Measurement of Heat Transfer Coefficient Distributions and Flow Field in a Model of a Turbine Blade Cooling Passage with Tangential Injection. *ASME Turbo Expo GT2006-90352.*

[141] Liu, Z., Feng, Z., and Song, L., 2011. Numerical Study on Flow and Heat Transfer Characteristics of Swirl Cooling on Leading Edge Model of Gas Turbine Blade. *ASME Turbo Expo GT2011-46125.* DOI: `10.1115/GT2011-46125`.

[142] Liu, Z., Li, J., and Feng, Z., 2013. Numerical Study on the Effect of Jet Slot Height on Flow and Heat Transfer of Swirl Cooling in Leading Edge Model for Gas Turbine Blade. *ASME Turbo Expo GT2013-94819.* DOI: `10.1115/GT2013-94819`.

[143]   Lopez, J. M., 1990. Axisymmetric vortex breakdown Part 1. Confined swirling flow. *Journal of Fluid Mechanics* **221**, pp. 533–552. DOI: `10.1017/S0022112090003664`.

[144]   Lopez, J. M., 1994. On the bifurcation structure of axisyrnmetric vortex breakdown in a constricted pipe. *Phys. Fluids* **6**(11), pp. 3683–3693. DOI: `10.1063/1.868359`.

[145]   Lopez, J. M. and Perry, A. D., 1992. Axisymmetric vortex breakdown Part 3. Onset of periodic flow and chaotic advection. *Journal of Fluid Mechanics* **234**, pp. 449–471. DOI: `10.1017/S0022112092000867`.

[146]   Lord Rayleigh, O. M., F. R. S., 1916. On the Dynamics of Revolving Fluids. *Proceedings of the Royal Society A* **93**, pp. 148–154. DOI: `10.1098/rspa.1917.0010`.

[147]   Lucca-Negro, O. and O'Doherty, T., 2001. Vortex breakdown: a review. *Progress in Energy and Combustion Science* **27**, pp. 431–481.

[148]   Ludwieg, H., 1962. Zur Erklärung der Instabilität der über angestellten Deltaflügeln auftretenden freien Wirbelkerne. *Z. Flugwiss.* **10**(6), pp. 242–249.

[149]   Mager, A., 1971. Incompressible, viscous, swirling flow through a nozzle. *AIAA Journal* **9**(4), pp. 649–655. DOI: `10.2514/3.6243`.

[150]   Maršík, F., 1989. Consequences of Thermodynamical Conditions of Stability for Thermoviscous Fluids and Thermoviscoelastic Solids. *Acta Physica Hungarica* **66**(1-4), pp. 195–202.

[151]   Maršík, F., 1999. Termodynamika Kontinua. Academia, Praha.

[152]   Maršík, F., Kobiela, B., Novotny, P., and Weigand, B., 2010a. Thermodynamic Analysis and Experimental Investigation of Swirl Tube Flow. *21st Int Symp on Transport Phenomena, Kaohsiung City, Taiwan.*

[153]   Maršík, F., Travnicek, Z., Novotny, P., and Werner, E., 2010b. Stability of a swirling annular flow. *Journal of Flow Visualization and Image Processing* **17**(3), pp. 267–279.

[154]   Menter, F. R. and Kuntz, M., 2004. Adaptation to eddy-viscosity turbulence models to unsteady separated flow behind vehicles. *Symposium on the aerodynamics of heavy vehicles: trucks, buses and trains* **19**, pp. 339–352. DOI: `10.1007/978-3-540-44419-0_30`.

[155]   Miloh, T., 1991. Mathematical Approaches in Hydrodynamics. Society for Industrial and Applied Mathematics.

[156] Mischner, J. and Bespalov, V. I., 2002. Zur Entropieproduktion im Ranque-Hilsch-Rohr. *Forschung im Ingenieurwesen* **67**, pp. 1–10. DOI: `10.1007/S10010-002-0070-7`.

[157] Mitchell, A. M. and Délery, J., 2001. Research into vortex breakdown control. *Progress in Aerospace Sciences* **37**(4), pp. 385–418. DOI: `10.1016/S0376-0421(01)00010-0`.

[158] Mitrofanova, O. V., 2003. Hydrodynamics and Heat Transfer in Swirling Flows in Channels with Swirlers (Analytical Review). *High Temperature* **41**(4), pp. 518–559. DOI: `10.1023/A:1025172018351`.

[159] Moffat, R. J., 1988. Describing the Uncertainties in Experimental Results. *Experimental Thermal and Fluid Science* **1**(1), pp. 3–17.

[160] Moon, H. K., O'Connell, T., and Glezer, B., 1998. Heat transfer enhancement in a circular channel using lengthwise continuous tangential injection. *Heat Transfer 1998, Proceedings of 11th IHTC* **6**, pp. 559–564.

[161] Murakhtina, T. O. and Okulov, V. L., 2000. Changes in the topology and symmetry of a vorticity field upon turbulent vortex breakdown. *Technical Physics Letters* **26**, pp. 432–435. DOI: `10.1134/1.1262870`.

[162] Neitzel, G. P. and Watson, J. P., 1991. Computational Studies of Vortex Breakdown. *AFOSR 91-0047*.

[163] Nissan, A. H. and Bresan, V. P., 1961. Swirling flow in cylinders. *AIChE Journal* **7**(4), pp. 543–547. DOI: `10.1002/aic.690070404`.

[164] Oertel jr., H., 2004. Prandtl's Essentials of Fluid Mechanics. Springer. DOI: `10.1007/b97538`.

[165] Okulov, V. L., 1996. Transition from right to left helical symmetry during vortex breakdown. *Technical Physics Letters* **22**, pp. 798–800.

[166] OpenFOAM, 2013. The Open Source CFD Toolbox, User Guide, Version 2.2.0.

[167] Paik, J. and Sotiropoulos, F., 2010. Numerical simulation of strongly swirling turbulent flows through an abrupt expansion. *International Journal of Heat and Fluid Flow* **31**, pp. 390–400. DOI: `10.1016/j.ijheatfluidflow.2010.02.025`.

[168] Parchen, R. R., 1993. Decay of swirl in turbulent pipe flows. PhD thesis. Eindhoven University of Technology.

[169] Piralishvili, Sh. A. and Fuzeeva, A. A., 2005. Hydraulic Characteristics of Ranque–Hilsch Energy Separators. *High Temperature* **43**(6), pp. 900–907.

[170] Piralishvili, Sh. A. and Fuzeeva, A. A., 2006. Similarity of the Energy-Separation Process in Vortex Ranque Tubes. *Journal of Engineering Physics and Thermophysics* **79**(1), pp. 27–32.

[171] Pope, S. B., 2000. Turbulent Flows. Cambridge University Press.

[172] Poser, R., 2010. Transient Heat Transfer Experiments in Complex Geometries Using Liquid Crystal Thermography. PhD thesis. University of Stuttgart.

[173] Poser, R., Wolfersdorf, J. von, and Lutum, E., 2007. Advanced Evaluation of Transient Heat Transfer Experiments Using Thermochromic Liquid Crystals. *Proc. IMechE Vol. 221 Part A: J. Power and Energy.*

[174] Qian, C., Flannery, K., Saito, K., Downs, J. P., and Soechting, F. O., 1997. Innovative vortex cooling concept and its application to turbine airfoil trailing edge cooling design. *33rd Joint Propulsion Conference and Exhibit, Paper no. 97-3013.* DOI: `10.2514/6.1997-3013`.

[175] Quast, C., 2015. Stereo-PIV Measurements in a Swirl Tube with Multiple Tangential Injections. Bachelor Thesis, Institute of Aerospace Thermodynamics (ITLR), University of Stuttgart.

[176] Raffel, M., Willert, C. E., Wereley, S. T., and Kompenhans, J., 2007. Particle Image Velocimetry: A Practical Guide. Second Edition. Springer.

[177] Ranque, G., 1933. Experiences sur la detente giratoire avec productions simultanees d'un echappement d'air chaud et d'un echappement d'air froid. *Journal de Physique et Radium* **4**(7), pp. 112–114.

[178] Rao, Y., Biegger, C., and Weigand, B., 2017. Heat transfer and pressure loss in swirl tubes with one and multiple tangential jets pertinent to gas turbine internal cooling. *International Journal of Heat and Mass Transfer* **106**, pp. 1356–1367. DOI: `10.1016/j.ijheatmasstransfer.2016.10.119`.

[179] Reader-Harris, M. J., 1994. The decay of swirl in a pipe. *International Journal of Heat and Fluid Flow* **15**(3), pp. 212–217. DOI: `10.1016/0142-727X(94)90040-X`.

[180] Reynolds, A. J., 1961. Energy Flows in a Vortex Tube. *Zeitschrift für Angewandte Mathematik und Physik* **12**(4), pp. 343–357.

[181] Richardson, L. F., 1922. Weather Prediction by Numerical Process. Cambridge University Press.

[182] Roache, P. J., 1994. Perspective: A Method for Uniform Reporting of Grid Refinement Studies. *Journal of Fluids Engineering* **116**, pp. 405–413.

[183] Sagaut, P., 2006. Large Eddy Simulation for Incompressible Flows. Third Edition. Springer.

[184] Sarpkaya, T., 1971a. On stationary and travelling vortex breakdowns. *Journal of Fluid Mechanics* **45**(3), pp. 545–559. DOI: `10.1017/S002211 2071000181`.

[185] Sarpkaya, T., 1971b. Vortex Breakdown in Swirling Conical Flows. *AIAA Journal* **9**(9), pp. 1792–1799. DOI: `10.2514/3.49981`.

[186] Sarpkaya, T., 1974. Effect of the Adverse Pressure Gradient on Vortex Breakdown. *AIAA Journal* **12**(5), pp. 602–607. DOI: `10.2514/3.49305`.

[187] Scherhag, C., Bruschewski, M., and Schiffer, H.-P., 2014. Influence of Internal Swirl Flow on Heat Transfer. *Proceedings of CONV-14*. DOI: `10.1615/ICHMT.2014.IntSympConvHeatMassTransf.540`.

[188] Schlichting, H. and Gersten, K., 2000. Boundary-Layer Theory. Eighth Edition. Springer.

[189] Schlösser, P., 2013. Stereo-PIV Messungen einer Drallströmung in einer Zyklonkühlkammer. Bachelor Thesis, Institute of Aerospace Thermodynamics (ITLR), University of Stuttgart.

[190] Secchiaroli, A., Ricci, R., Montelpare, S., and D'Alessandro, V., 2009. Numerical simulation of turbulent flow in a Ranque–Hilsch vortex tube. *International Journal of Heat and Mass Transfer* **52**(23-24), pp. 5496–5511. DOI: `10.1016/j.ijheatmasstransfer.2009.05.031`.

[191] Seiler, P., 2014. Heat Transfer Measurements in a Swirl Chamber using the Transient Liquid Crystal Technique. Master Thesis (Diplomarbeit), Institute of Aerospace Thermodynamics (ITLR), University of Stuttgart.

[192] Shannak, B. A., 2004. Temperature separation and friction losses in vortex tube. *Heat and Mass Transfer* **40**(10), pp. 779–785. DOI: `10.10 07/s00231-003-0485-1`.

[193] Shur, M., Spalart, P. R., Strelets, M., and Travin, A., 1999. Detached-eddy simulation of an airfoil at high angle of attack. *Engineering Turbulence Modelling and Experiments. W. Rodi, D. Laurence, editors. Elsevier* **4**, pp. 669–678.

[194] Sibulkin, M., 1962. Unsteady, viscous, circular flow Part 3. Application to the Ranque-Hilsch vortex tube. *Journal of Fluid Mechanics* **12**(2), pp. 269–293. DOI: 10.1017/S0022112062000191.

[195] Smagorinsky, J., 1963. General circulation experiments with the primitive equations, I. The basic experiment. *Monthly Weather Review* **91**(3), pp. 99–164. DOI: 10.1175/1520-0493(1963)091<0099:GCEWTP>2.3.CO;2.

[196] Sohn, C.-H., Kim, C.-S., Jung, U.-H., and Gowda, B. H. L. L., 2006. Experimental and Numerical Studies in a Vortex Tube. *Journal of Mechanical Science and Technology* **20**(3), pp. 418–425. DOI: 10.1007/BF02917525.

[197] Sotgiu, C., 2013. Detached Eddy Simulation of the Cyclone Flow and the Heat Transfer in a Swirl Tube with OpenFOAM. Master Thesis, Institute of Aerospace Thermodynamics (ITLR), University of Stuttgart.

[198] Spalart, P. R. and Allmaras, S. R., 1994. A one-equation turbulence model for aerodynamic flows. *La recherche Aérospatiale* **1**, pp. 5–21.

[199] Spalart, P. R., Deck, S., Shur, M. L., Squires, K. D., Strelets, M. Kh., and Travin, A., 2006. A new version of Detached Eddy Simulation, resistant to ambiguous grid densities. *Theor. Comput. Fluid Dyn.* **20**, pp. 181–195.

[200] Spalart, P. R., Jou, W-H., Strelets, M., and Allmaras, S. R., 1997. Comments on the feasibility of LES for wings, and on a hybrid RANS/LES approach. *Advances in DNS/LES. C. Liu, Z. Liu, editors. Greyden Press.*

[201] Spall, R. E. and Ashby, B. M., 1999. A Numerical Study of Vortex Breakdown in Turbulent Swirling Flows. *Journal of Fluids Engineering* **122**(1), pp. 179–183. DOI: 10.1115/1.483247.

[202] Spall, R. E. and Gatski, T. B., 1995. Numerical calculations of three-dimensional turbulent vortex breakdown. *International Journal for Numerical Methods in Fluids* **20**(4), pp. 307–318. DOI: 10.1002/fld.1650200404.

[203] Spall, R. E., Gatski, T. B., and Grosch, C. E., 1987. A criterion for vortex breakdown. *Phys. Fluids* **30**(11), pp. 3434–3440. DOI: `10.1063/1.866475`.

[204] Speziale, C. G., 1998. Turbulence Modeling for Time-Dependent RANS and VLES: A Review. *AIAA Journal* **36**(2), pp. 173–184. DOI: `10.2514/2.7499`.

[205] Squire, H. B., 1960. Analysis of the "vortex breakdown" phenomenon. Part I. *Aero. Dept., Imperial College, London, Rep. 102*.

[206] Steenbergen, W., 1995. Turbulent Pipe Flow with Swirl. PhD thesis. Eindhoven University of Technology.

[207] Steenbergen, W. and Voskamp, J., 1998. The rate of decay of swirl in turbulent pipe flow. *Flow Measurement and Instrumentation* **9**, pp. 67–78.

[208] Stephan, K., Lin, S., Durst, M., Huang, F., and Seher, D., 1983. An investigation of energy separation in a vortex tube. *International Journal of Heat and Mass Transfer* **26**(3), pp. 341–348. DOI: `10.1016/0017-9310(83)90038-8`.

[209] Stephan, K., Lin, S., Durst, M., Huang, F., and Seher, D., 1984. A similarity relation for energy separation in a vortex tube. *International Journal of Heat and Mass Transfer* **27**(6), pp. 911–920. DOI: `10.1016/0017-9310(84)90012-7`.

[210] Takahama, H. and Yokosawa, H., 1981. Energy Separation in Vortex Tubes with a Divergent Chamber. *Journal of Heat Transfer* **103**(2), pp. 196–203. DOI: `10.1115/1.3244441`.

[211] Taylor, G. I., 1935. Statistical Theory of Turbulence: Parts I-III. *Proc. R. Soc. London Ser. A 164*, pp. 476–490.

[212] Teitel, M. and Antonia, R. A., 1993. Heat transfer in fully developed turbulent channel flow: comparison between experiment and direct numerical simulation. *International Journal of Heat and Mass Transfer* **36**, pp. 1701–1706.

[213] Thakare, H. R., Monde, A., and Parekh, A. D., 2015. Experimental, computational and optimization studies of temperature separation and flow physics of vortex tube: A review. *Renewable and Sustainable Energy Reviews* **52**, pp. 1043–1071. DOI: `10.1016/j.rser.2015.07.198`.

[214] Thambu, R., Babinchak, B. T., Ligrani, P. M., Hedlund, C. R., Moon, H.-K., and Glezer, B., 1999. Flow in a simple swirl chamber with and without controlled inlet forcing. *Experiments in Fluids* **26**, pp. 347–357.

[215] Uzol, O. and Camci, C., 2001. The Effect of Sample Size, Turbulence Intensity and the Velocity Field on the Experimental Accuracy of Ensemble Averaged PIV Measurements. *4th International Symposium an Particle Image Velocimetry, Göttingen, Germany.*

[216] Vogel, G. and Weigand, B., 2001. A New Evaluation Method for Transient Liquid Crystal Experiments. *ASME National Heat Transfer Conference, NHTC2001-20250.*

[217] Vogler, P., 2015. Numerische Simulation einer Wirbelrohrströmung mit Expliziten Algebraischen Reynoldsspannungsmodellen (EARSM) in OpenFOAM. Master Thesis, Institute of Aerospace Thermodynamics (ITLR), University of Stuttgart.

[218] Wassermann, F., Grundmann, S., Kloss, M., and Schiffer, H.-P., 2012. Swirl flow investigations on the enhancement of heat transfer processes in cyclone cooling ducts. *ASME Turbo Expo GT2012-69395.*

[219] Wenzel, C., 2014. Implementierung und Validierung des YSC-Skalarflussmodells für eine DES Wirbelrohrströmung in OpenFOAM. Master Thesis, Institute of Aerospace Thermodynamics (ITLR), University of Stuttgart.

[220] Weske, D. R. and Sturov, G. Y., 1974. Experimental study of turbulent swirled flows in a cylindrical tube. *Fluid Mechanics - Soviet Research* **3**, pp. 77–82.

[221] Winter, N. and Schiffer, H.-P., 2009. Effect of rotation on the cyclone cooling method: Mass transfer measurements. *Proceedings of the International Symposium on Heat Transfer in Gas Turbine Systems (TURBINE-09), Antalya, Turkey.* DOI: `10.1615/ICHMT.2009.HeatTransfGasTurbSyst.440`.

[222] Wolf, S., 2015. Wärmeübergangsmessungen in einer Zyklonkühlkammer mit Mehrfacheinblasung mit der transienten Flüssigkristallmesstechnik. Bachelor Thesis, Institute of Aerospace Thermodynamics (ITLR), University of Stuttgart.

[223] Xue, Y. and Arjomandi, M., 2008. The effect of vortex angle on the efficiency of the Ranque–Hilsch vortex tube. *Experimental Thermal and*

Fluid Science **33**(1), pp. 54–57. DOI: 10.1016/j.expthermflusci.2008.07.001.

[224]   Xue, Y., Arjomandi, M., and Kelso, R., 2010. A critical review of temperature separation in a vortex tube. *Experimental Thermal and Fluid Science* **34**, pp. 1367–1374. DOI: 10.1016/j.expthermflusci.2010.06.010.

[225]   Xue, Y., Arjomandi, M., and Kelso, R., 2013. Experimental study of the thermal separation in a vortex tube. *Experimental Thermal and Fluid Science* **46**, pp. 175–182. DOI: 10.1016/j.expthermflusci.2012.12.009.

[226]   Xue, Y., Arjomandi, M., and Kelso, R., 2014. Energy analysis within a vortex tube. *Experimental Thermal and Fluid Science* **52**, pp. 139–145. DOI: 10.1016/j.expthermflusci.2013.09.004.

[227]   Yilmaz, M., Çomakli, Ö., and Yapici, S., 1999. Enhancement of heat transfer by turbulent decaying swirl flow. *Energy Conversion and Management* **40**(13), pp. 1365–1376. DOI: 10.1016/S0196-8904(99)00030-8.

[228]   Yilmaz, M., Çomakli, Ö., Yapici, S., and Sara, N., 2003. Heat transfer and friction characteristics in decaying swirl flow generated by different radial guide vane swirl generators. *Energy Conversion and Management* **44**(2), pp. 283–300. DOI: 10.1016/S0196-8904(02)00053-5.

[229]   Yilmaz, M., Kaya, M., Karagoz, S., and Erdogan, S., 2009. A review on design criteria for vortex tubes. *Heat and Mass Transfer* **45**(5), pp. 613–632. DOI: 10.1007/s00231-008-0447-8.

[230]   Younis, B. A., Speziale, C. G., and Clark, T. T., 2005. A rational model for the turbulent scalar fluxes. *Proceedings of the Royal Society A* **461**, pp. 575–594. DOI: 10.1098/rspa.2004.1380.

[231]   Zin, K. K., Hansske, A., and Ziegler, F., 2010. Modeling and Optimization of the Vortex Tube with Computational Fluid Dynamic Analysis. *Energy Research Journal* **1**(2), pp. 193–196.

OpenFOAM Setup

For the here shown DES swirl tube simulations, the OpenFOAM setup is presented in terms of the discretization schemes and the solution settings for the used solver `rhoPimpleFoam`. Then, a representative overview of the used boundary conditions is given. In addition, the mesh quality with respect to the mesh non-orthogonality, the cell aspect ratio and the skewness is summarized for all used swirl tube grids. Finally, the OpenFOAM code for the Spalart-Allmaras DDES model for a compressible flow is given.

Table A.1: `fvSchemes` dictionary for the swirl tube simulations

```
ddtSchemes
{
    default         backward;
}

gradSchemes
{
    default         Gauss linear;
```

```
    grad(p)         Gauss linear;
    grad(U)         Gauss linear;
}

divSchemes
{
    default           none;
    div(phi,U)        Gauss limitedCubicV 0;
    div(phi,muTilda)  Gauss limitedLinear 1;
    div(phi,h)        Gauss limitedCubic  0;
    div(phi,k)        Gauss limitedLinear 1;
    div(phi,B)        Gauss limitedLinear 1;
    div(phi,K)        Gauss linear;
    div(B)            Gauss linear;
    div((muEff*dev2(T(grad(U))))) Gauss linear;
}

laplacianSchemes
{
    default                       none;
    laplacian(muEff,U)            Gauss linear corrected;
    laplacian(Dp,p)               Gauss linear corrected;
    laplacian((rho*(1|A(U))),p)   Gauss linear corrected;
    laplacian(alphaEff,h)         Gauss linear corrected;
    laplacian(DkEff,k)            Gauss linear corrected;
    laplacian(DBEff,B)            Gauss linear corrected;
    laplacian(DmuTildaEff,muTilda) Gauss linear corrected;
}

interpolationSchemes
{
    default       linear;
    interpolate(U)  linear;
}

snGradSchemes
{
    default       corrected;
}
```

Table A.2: `fvSolution` dictionary for the swirl tube simulations

```
solvers
{
    p
    {
        solver                  GAMG;
        tolerance               1e-5;
        relTol                  1e-4;
        nVcycles                2;
        smoother                DICGaussSeidel;
        nPostSweeps             1;
        cacheAgglomeration      true;
        nCellsInCoarsestLevel   100;
        agglomerator            faceAreaPair;
        mergeLevels             2;
    }
    pFinal
    {
        solver                  GAMG;
        tolerance               1e-7;
        relTol                  0;
        nVcycles                2;
        smoother                DICGaussSeidel;
        nPostSweeps             2;
        cacheAgglomeration      true;
        nCellsInCoarsestLevel   100;
        agglomerator            faceAreaPair;
        mergeLevels             2;
    }
    "rho.*"
    {
        solver          PCG;
        preconditioner  DIC;
        tolerance       1e-06;
        relTol          0.01;
    }
    "(U|h|k|omega|epsilon|R|nuTilda)"
    {
        solver                  GAMG;
```

```
            tolerance                   1e-5;
            relTol                      1e-3;
            nVcycles                    2;
            smoother                    DILUGaussSeidel;
            nPostSweeps                 1;
            cacheAgglomeration          false;
            nCellsInCoarsestLevel       100;
            agglomerator                faceAreaPair;
            mergeLevels                 2;
        }
        "(U|h|k|omega|epsilon|R|nuTilda)Final"
        {
            solver                      GAMG;
            tolerance                   1e-7;
            relTol                      0;
            nVcycles                    2;
            smoother                    DILUGaussSeidel;
            nPostSweeps                 2;
            nFinestSweeps    2;
            cacheAgglomeration          true;// false;
            nCellsInCoarsestLevel       100;
            agglomerator                faceAreaPair;
            mergeLevels                 2;
      }
}
PIMPLE
{
    nOuterCorrectors 4;
    nCorrectors      2;
    nNonOrthogonalCorrectors 0;
    turbOnFinalIterOnly      no;
    pRefCell 0;
    pRefValue 1e5;
    rhoMin          rhoMin [ 1 -3 0 0 0 ] 0.9;
    rhoMax          rhoMax [ 1 -3 0 0 0 ] 1.4;
    pRefCell 0;
    pRefValue 0;
}
```

Table A.3: Boundary conditions (BC) for the swirl tube simulation for a compressible flow for $S = 5.3$ and $Re = 20{,}000$

variable	dimensions	patch	BC	value
U	m/s	inlets	`fixedValue`	($\pm$ `38.24 0 0`)
		outlet	`zeroGradient`	`-`
		walls	`fixedValue`	`uniform (0 0 0)`
p	$kg/m/s^2$	inlets	`zeroGradient`	`-`
		outlet	`fixedMean`	`uniform 1e5`
		walls	`zeroGradient`	`-`
nuTilda	m^2/s	inlets	`zeroGradient`	`-`
		outlet	`zeroGradient`	`-`
		walls	`fixedValue`	`uniform 0`
muSgs	$kg/m/s$	inlets	`zeroGradient`	`-`
		outlet	`zeroGradient`	`-`
		walls	`zeroGradient`	`-`
alphaSgs	$kg/m/s$	inlets	`zeroGradient`	`-`
		outlet	`zeroGradient`	`-`
		walls	`zeroGradient`	`-`
T	K	inlets	`fixedValue`	`uniform 333`
		outlet	`zeroGradient`	`-`
		walls	`fixedValue`	`uniform 293`

Table A.4: Mesh quality in terms of mesh non-orthogonality, cell aspect ratio and skewness for all used swirl tube grids

mesh	mesh non-orthogonality	cell aspect ratio	skewness
BSL $Re = 10{,}000$	48.8	36.5	0.89
BSL $Re = 20{,}000$	79.8	162.4	1.10
BSL $Re = 40{,}000$	77.7	203.7	1.48
MI5 $Re = 10{,}000$	46.9	36.0	0.92
MI5 $Re = 50{,}000$	48.5	50.7	0.93

Spalart-Allmaras DDES

The standard OpenFOAM 2.2.x library contains the Spalart-Allmaras DDES model for the simulation of incompressible flows. Since this model is not available for the simulation of compressible flows, the compressible formulation has been implemented as part of this work. The following OpenFOAM code shows the implemented and here used Spalart-Allmaras DDES model for a compressible flow.

Listing A.1: SpalartAllmarasDDEScomp.C

```
#include "SpalartAllmarasDDEScomp.H"
#include "addToRunTimeSelectionTable.H"

// * * * * * * * * * * * * * * * * * * * * * * * * * * * //

namespace Foam
{
namespace compressible
{
namespace LESModels
{

// * * * * * * * * * Static Data Members * * * * * * * //

defineTypeNameAndDebug(SpalartAllmarasDDEScomp, 0);
addToRunTimeSelectionTable(LESModel,
    SpalartAllmarasDDEScomp, dictionary);

// * * * * * * * Protected Member Functions  * * * * * //

tmp<volScalarField> SpalartAllmarasDDEScomp::rd
(
    const volScalarField& visc,
    const volScalarField& S
) const
{
    return min
    (
        visc
```

```cpp
        / (
            max
            (
                S,
                dimensionedScalar ("SMALL",
                    S. dimensions () , SMALL)
            ) * sqr (kappa_ * wallDist (mesh_) . y () )
          + dimensionedScalar
            (
                "ROOTVSMALL" ,
                dimensionSet (0 , 2 , -1, 0, 0) ,
                ROOTVSMALL
            )
        ) ,
        scalar (10)
    ) ;
}

tmp<volScalarField> SpalartAllmarasDDEScomp :: fd ( const
    volScalarField& S) const
{
    return 1 - tanh (pow3(8* rd (muEff () / rho () , S) ) ) ;
}

tmp<volScalarField> SpalartAllmarasDDEScomp :: S ( const
    volTensorField& gradU) const
{
    return sqrt (2.0) * mag(symm( gradU) ) ;
}

tmp<volScalarField>
    SpalartAllmarasDDEScomp :: dTilda ( const
    volScalarField& S) const
{
    return max
    (
        wallDist (mesh_) . y ()
      - fd (S)
        * max ( wallDist (mesh_) . y () - CDES_ * delta () ,
            dimensionedScalar ("zero", dimLength , 0) ) ,
        dimensionedScalar (" small " , dimLength , SMALL)
```

```
    ) ;
}

// * * * * * * * * * * Constructors  * * * * * * * * //

SpalartAllmarasDDEScomp : : SpalartAllmarasDDEScomp
(
    const volScalarField& rho ,
    const volVectorField& U,
    const surfaceScalarField& phi ,
    const fluidThermo& thermoPhysicalModel ,
    const word& turbulenceModelName ,
    const word& modelName
)
:
    SpalartAllmaras ( rho , U, phi , thermoPhysicalModel ,
        turbulenceModelName , modelName )
{}

// * * * * * * * * * * * * * * * * * * * * * * * * * //

} // End namespace LESModels
} // End namespace incompressible
} // End namespace Foam

// ************************************************* //
```

APPENDIX B

PIV Results

For completeness, the non-dimensional PIV results for the baseline single inlet swirl tube for all investigated outlet geometries (straight, tangential and 180° bend) are given. Additionally, the non-dimensional PIV results for the multiple inlet swirl tube for higher Reynolds numbers 20,000, 30,000 and 50,000 are presented.

B.1 Single Inlet Swirl Tube

B.1.1 Velocity Field
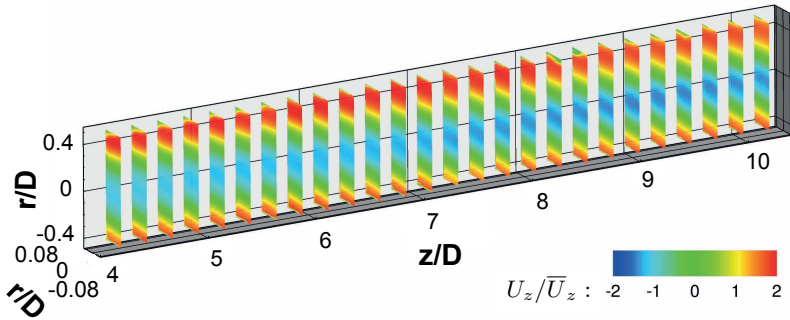
Figure B.1: Tomographic-PIV axial velocity at $S = 5.3$ and $Re = 10{,}000$, baseline straight outlet
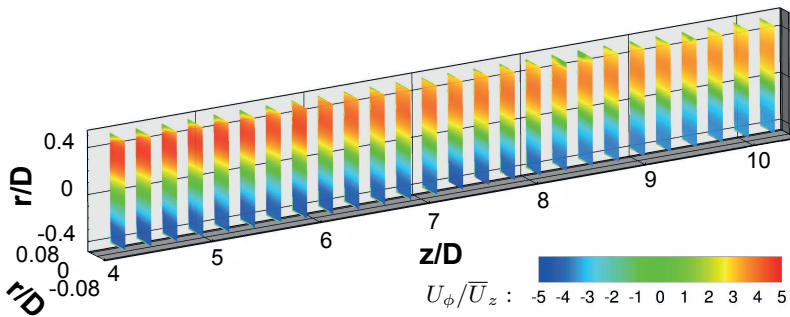
Figure B.2: Tomographic-PIV circumferential velocity at $S = 5.3$ and $Re = 10{,}000$, baseline straight outlet
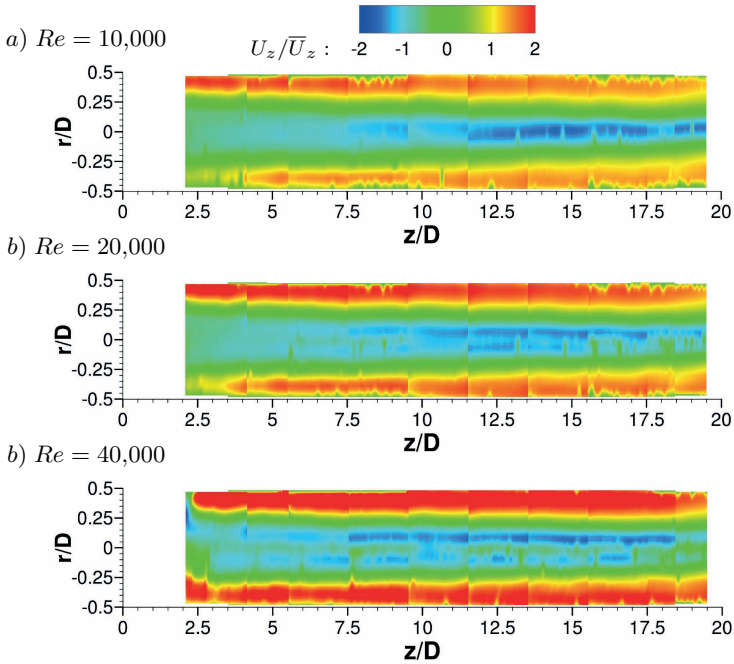
Figure B.3: Axial velocity ($S = 5.3$), baseline swirl tube with straight outlet

a) $Re = 10,000$ $U_z/\overline{U}_z$:

b) $Re = 20,000$
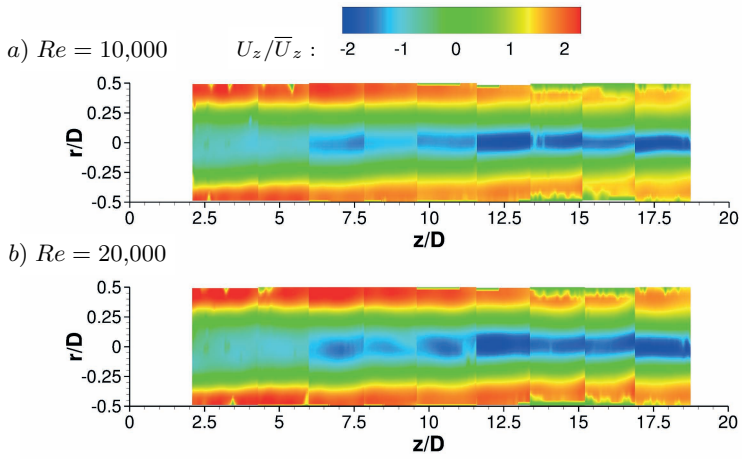
Figure B.4: Axial velocity ($S = 5.3$), $180°$ bend outlet

a) $Re = 10,000$ $U_z/\overline{U}_z$:

b) $Re = 20,000$
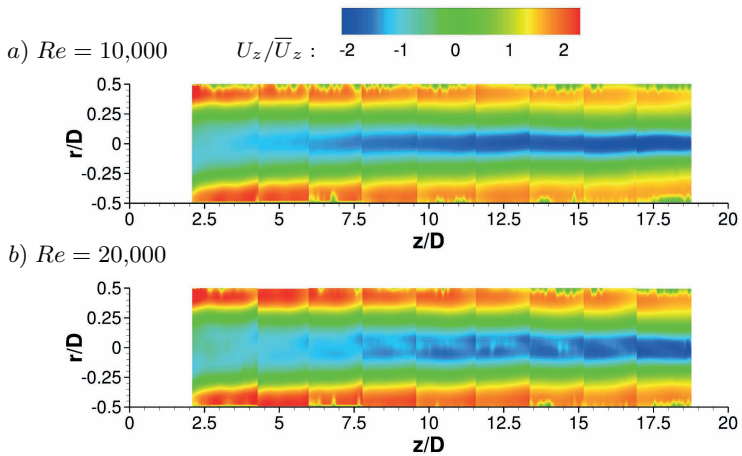
Figure B.5: Axial velocity ($S = 5.3$), tangential outlet
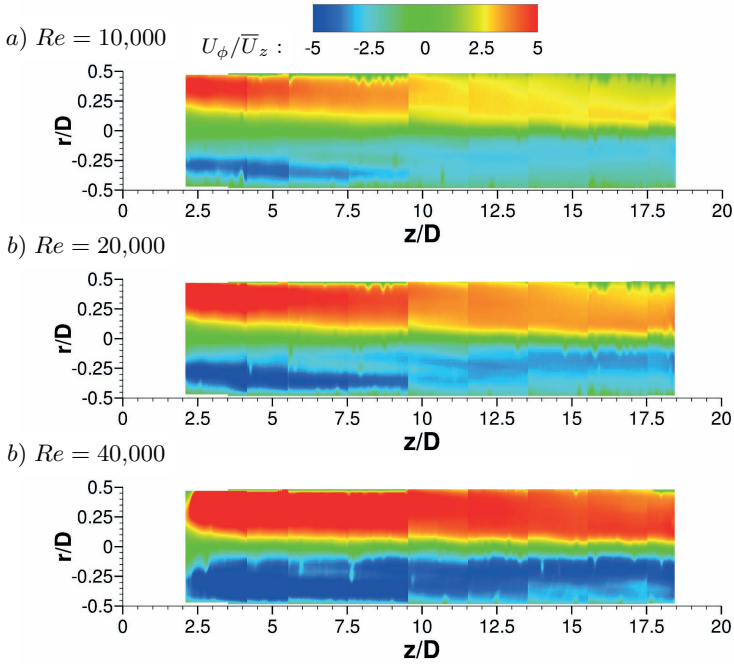
Figure B.6: Circumferential velocity ($S = 5.3$), baseline swirl tube with straight outlet
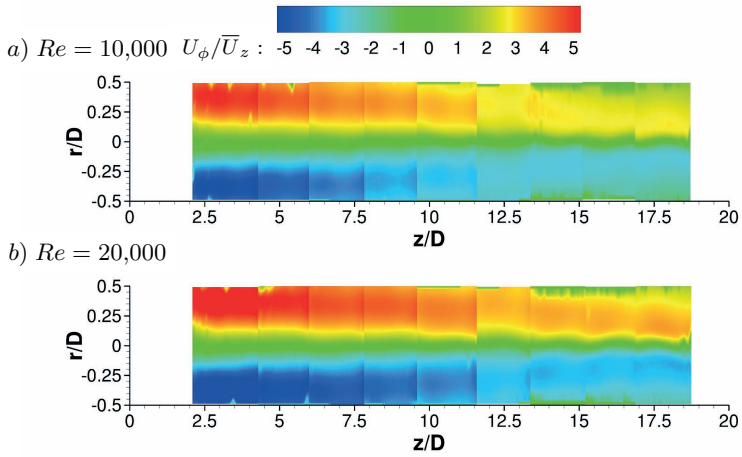
Figure B.7: Circumferential velocity ($S = 5.3$), $180°$ bend outlet
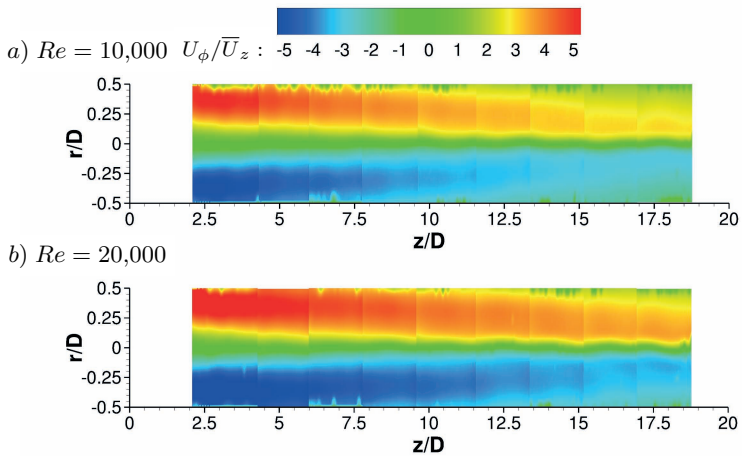
Figure B.8: Circumferential velocity ($S = 5.3$), tangential outlet

B.1.2 Turbulence Kinetic Energy
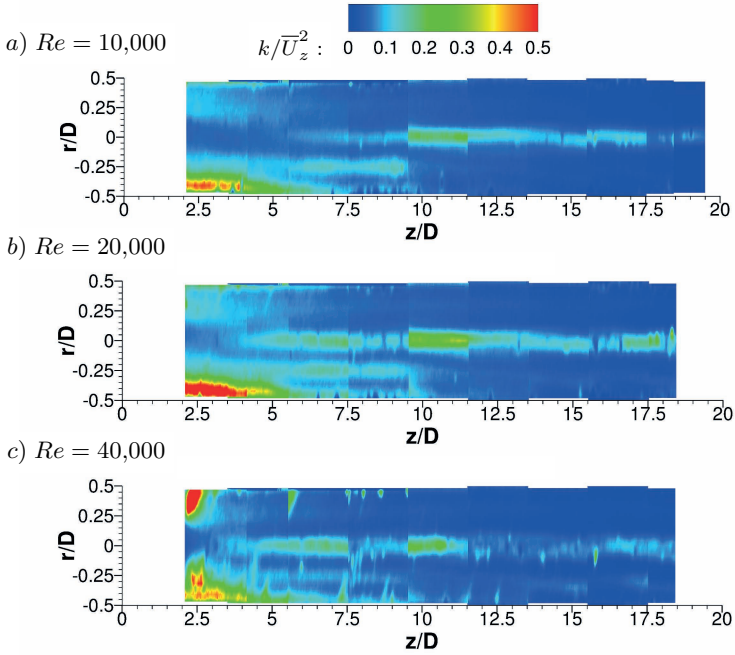
Figure B.9: Turbulence kinetic energy ($S = 5.3$), baseline straight outlet
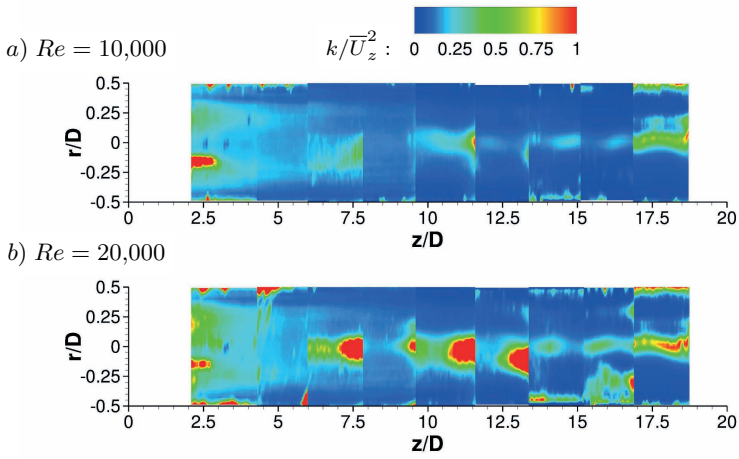
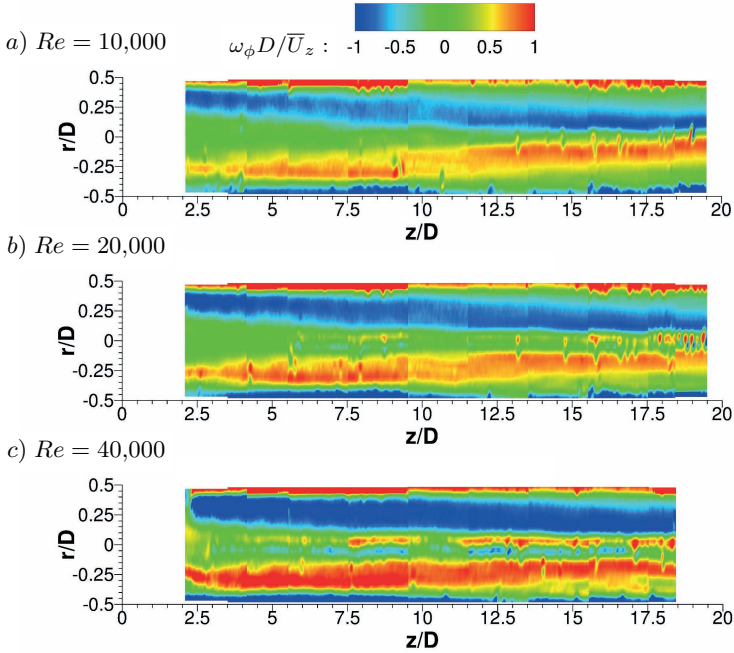**Figure B.10:** Turbulence kinetic energy ($S = 5.3$), $180°$ bend outlet
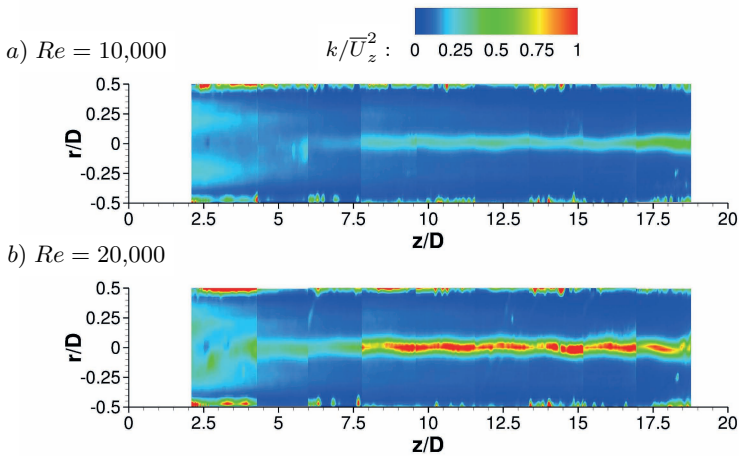
Figure B.11: Turbulence kinetic energy ($S = 5.3$), tangential outlet

B.1.3 Vorticity

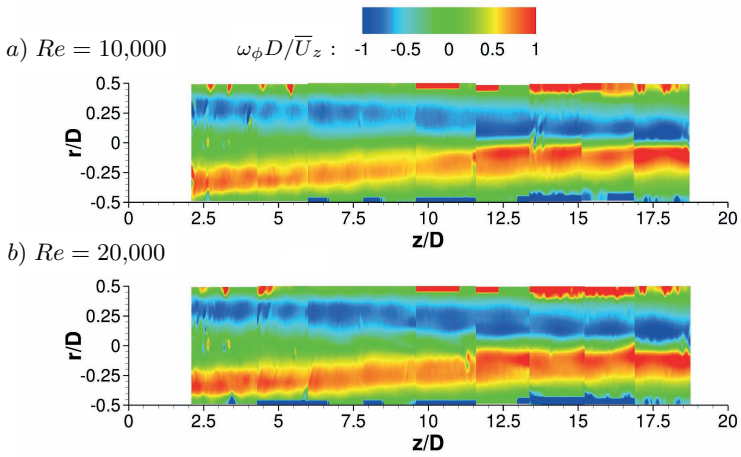**Figure B.12:** Vorticity ($S = 5.3$), baseline straight outlet

a) $Re = 10,000$

b) $Re = 20,000$

Figure B.13: Vorticity ($S = 5.3$), 180° bend outlet

a) $Re = 10,000$
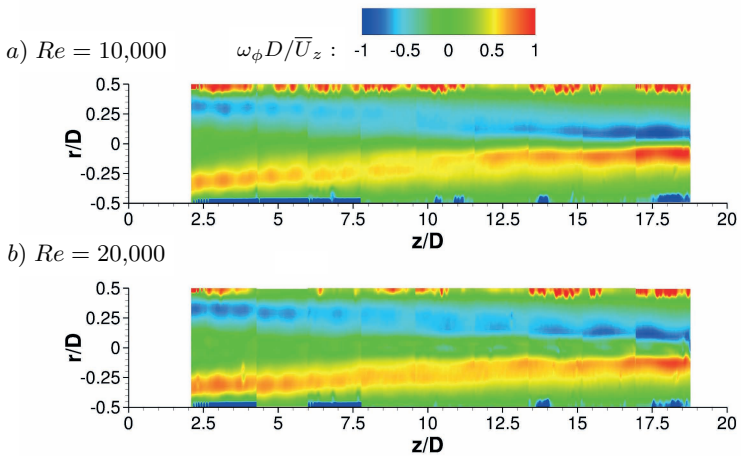
b) $Re = 20,000$

Figure B.14: Vorticity ($S = 5.3$), tangential outlet

B.2 Multiple Inlet Swirl Tube

B.2.1 Velocity Field
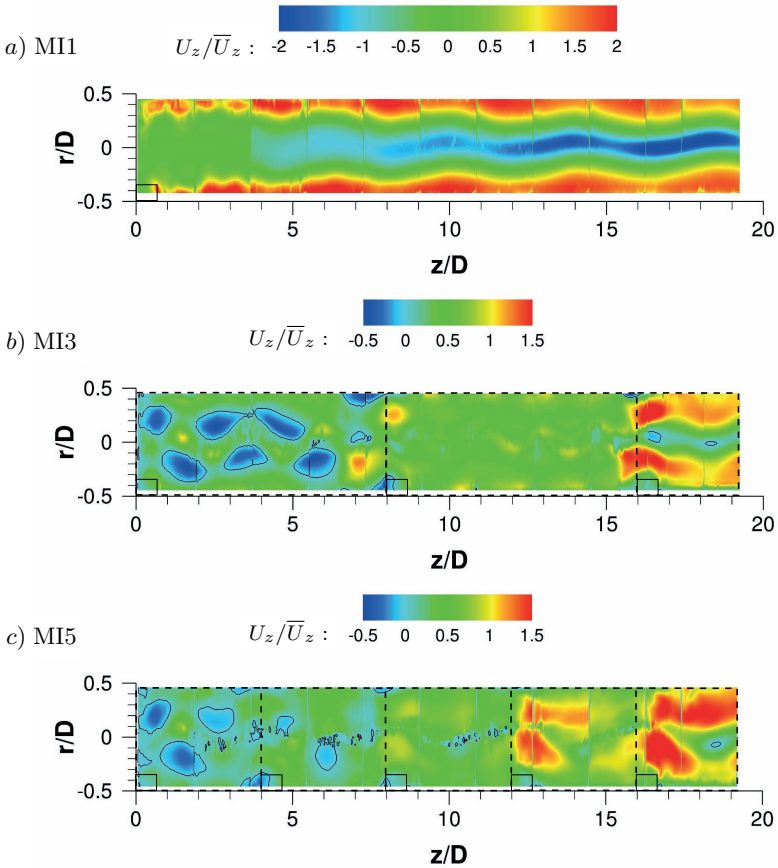
Figure B.15: Axial velocity for MI1, MI3 and MI5 at $Re = 20,000$, $30,000$ and $50,000$, respectively

a) MI1

$U_\phi/\overline{U}_z$: -6 -4 -2 0 2 4 6

b) MI3

$U_\phi/\overline{U}_z$: -2 -1.5 -1 -0.5 0 0.5 1 1.5 2

c) MI5

$U_\phi/\overline{U}_z$: -2 -1.5 -1 -0.5 0 0.5 1 1.5 2

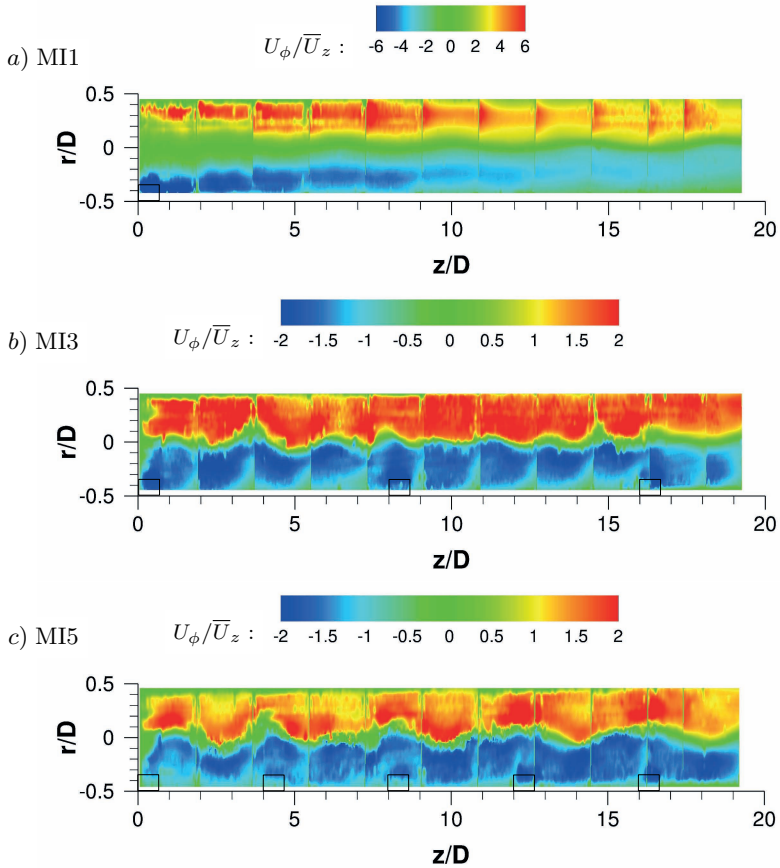**Figure B.16:** Circumferential velocity for MI1, MI3 and MI5 at Re = 20,000, 30,000 and 50,000, respectively
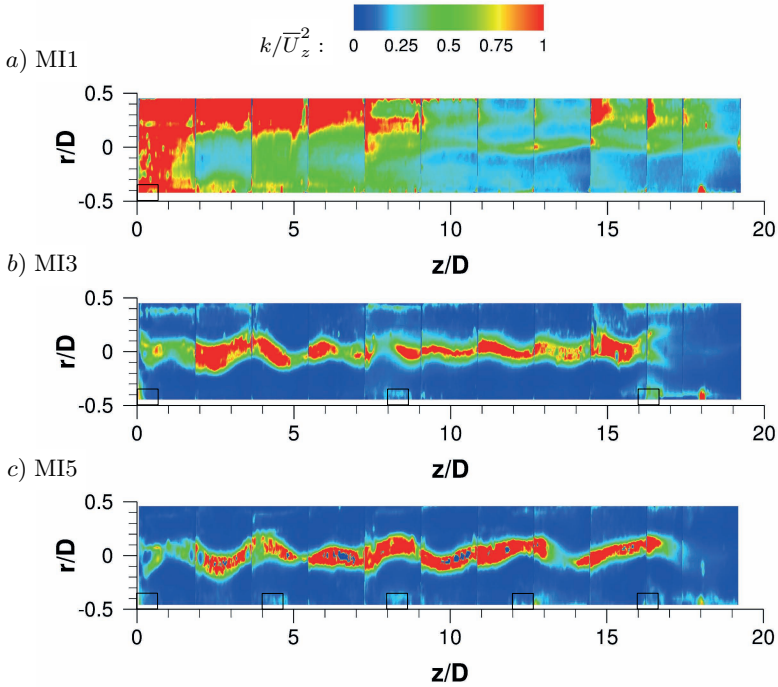
B.2.2 Turbulence Kinetic Energy

Figure B.17: Turbulence kinetic energy for MI1, MI3 and MI5 at $Re = $ 20,000, 30,000 and 50,000, respectively
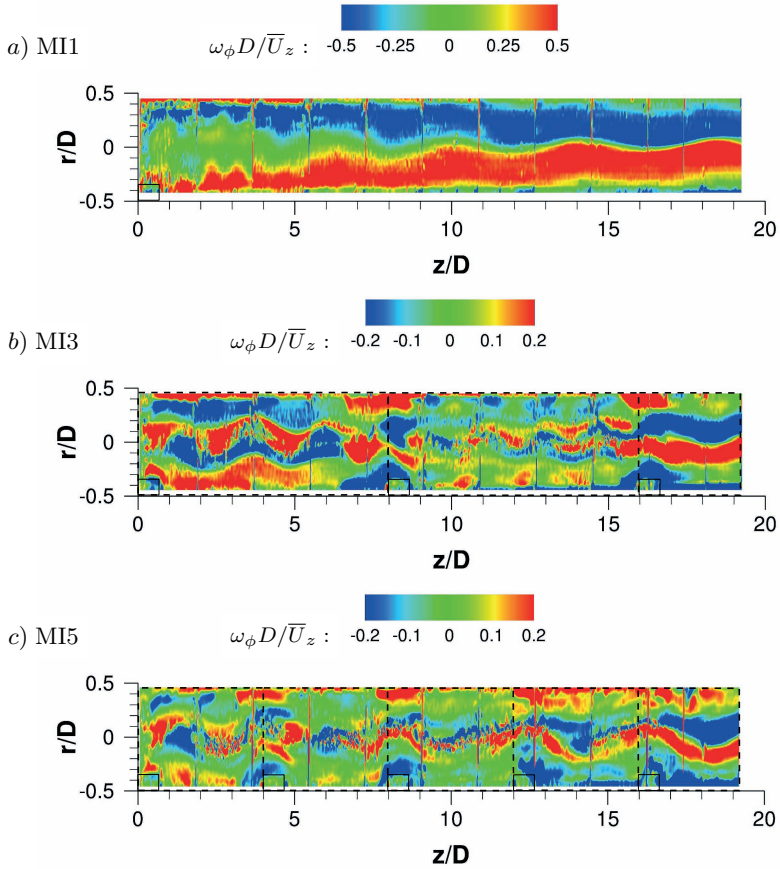
B.2.3 Vorticity

Figure B.18: Vorticity for MI1, MI3 and MI5 at $Re = 20{,}000$, $30{,}000$ and $50{,}000$, respectively

Name:	Christoph Biegger
Date:	09.05.1984
Place of birth:	Weingarten
Nationality:	German

Professional Career

since 10/2016	Development engineer at Daimler AG, Stuttgart
08/2011-07/2016	Research assistant at the Institute of Aerospace Thermodynamics, University of Stuttgart

Studies

10/2005-03/2011	Diploma studies of mechanical engineering, Karlsruhe Institute of Technology (KIT)
10/2010-03/2011	Diploma thesis at the Institute for Thermal Turbomachinery, KIT
10/2008-03/2009	Studienarbeit at the French-German Research Institute of Saint-Louis (ISL), France

Education

11/1999-06/2004	Welfen Gymnasium, Ravensburg
09/1995-10/1999	Lessing Gymnasium, Neu-Ulm

Internships

04/2009-09/2009	Rolls-Royce plc, Derby, United Kingdom
06/2005-07/2005	Voith, Ravensburg